Precision calculations for
$\gamma\gamma \to$ 4 fermions
and H $\to$ WW/ZZ $\to$ 4 fermions

Axel Bredenstein

SIGILL: UNIVERSITAT: LUDOVIC: MAXIM:

Februar 2006

Precision calculations for $\gamma\gamma \to$ 4 fermions and H $\to$ WW/ZZ $\to$ 4 fermions

Dissertation
an der Fakultät für Physik
der Ludwig–Maximilians–Universität
München

vorgelegt von
Axel Bredenstein
aus Hamburg

München, den 14.2.2006

Erstgutachter: PD Dr. Stefan Dittmaier
Zweitgutachter: Prof. Dr. Gerhard Buchalla
Tag der mündlichen Prüfung: 8.5.2006

Contents

Zusammenfassung

In dieser Arbeit werden Präzisionsrechnungen für die Prozesse $\gamma\gamma \to 4\,\mathrm{Fermionen}$ und $\mathrm{H} \to \mathrm{WW/ZZ} \to 4\,\mathrm{Fermionen}$ vorgestellt.

An einem $\gamma\gamma$-Collider werden wegen des großen Wirkungsquerschnitts genaue theoretische Vorhersagen für die Prozesse $\gamma\gamma \to \mathrm{WW} \to 4f$ benötigt. Mittels dieser Prozesse lassen sich unter anderem die Eichboson-Kopplungen $\gamma\mathrm{WW}$ und $\gamma\gamma\mathrm{WW}$ messen. Außerdem wird über virtuelle geladene, massive Teilchen die Reaktion $\gamma\gamma \to \mathrm{H} \to \mathrm{WW/ZZ} \to 4f$ ermöglicht. Auf diese Weise läßt sich die Kopplung $\gamma\gamma\mathrm{H}$ messen, und relativ schwere Higgs-Bosonen könnten erzeugt werden.

Für Massen $M_\mathrm{H} \gtrsim 135\,\mathrm{GeV}$ zerfällt das Higgs-Boson hauptsächlich über W- und Z-Bosonen in vier Fermionen. Bei der kinematischen Rekonstruktion dieser Zerfälle spielen Quanten-Korrekturen, insbesondere Photon-Bremsstrahlung, eine wichtige Rolle. Die Einbeziehung der Zerfälle der Eichbosonen in Fermionen ist zum einen wichtig, weil unterhalb von $M_\mathrm{H} \approx 2M_\mathrm{W/Z}$ „off-shell“-Effekte der Eichbosonen berücksichtigt werden müssen. Zum anderen lassen sich mit Hilfe von Winkel- und Energie-Verteilungen der Fermionen der Spin und die CP-Eigenschaften des Higgs-Bosons bestimmen.

Besonders geeignet für den Vergleich theoretischer Vorhersagen mit experimentellen Daten sind Monte-Carlo-Generatoren. Für die Prozesse $\gamma\gamma \to 4f$ und $\mathrm{H} \to \mathrm{WW/ZZ} \to 4f$ werden solche Programme konstruiert. Sie liefern zum einen die kompletten Vorhersagen in niedrigster Ordnung der Störungstheorie. Zum anderen enthalten sie Quanten-Korrekturen, die sich unterteilen lassen in reelle Korrekturen, welche durch Photon-Bremsstrahlung gegeben sind, und virtuelle Korrekturen. Während die virtuellen Quanten-Korrekturen zu $\gamma\gamma \to \mathrm{WW} \to 4f$ in der Doppel-Pol-Näherung berechnet werden, in der nur die doppelt resonanten Beiträge berücksichtigt werden, werden zu den Prozessen $\mathrm{H} \to \mathrm{WW/ZZ} \to 4f$ die kompletten Quantenkorrekturen der Ordnung $\mathcal{O}(\alpha)$ berechnet. Für die Behandlung der in den virtuellen und reellen Korrekturen auftretenden infraroten Divergenzen („soft“ und „collinear“) wird wahlweise die Dipol-Subtraktions-Methode oder die Phase-Space-Slicing-Methode verwendet. Nicht bei allen Observablen müssen sich die bei kollinearer Photon-Abstrahlung auftretenden Massen-Singularitäten gegenseitig aufheben. Um auch solche nicht-kollinear-sichere Observablen untersuchen zu können, wird die Dipol-Subtraktions-Methode diesbezüglich erweitert.

Die Diskussion der numerischen Ergebnisse umfasst den Einfluss eines realistischen Photon-Spektrums auf die Wirkungsquerschnitte, das Potential eines $\gamma\gamma$-Colliders, Grenzen an anomale Eichboson-Kopplungen zu setzen, sowie verschiedene Verteilungen in der Invarianten Masse, in der Energie und in Winkeln, die für eine Rekonstruktion der Eichbosonen und die Bestimmung der Eigenschaften des Higgs-Bosons genutzt werden können.

Abstract

In this work we provide precision calculations for the processes $\gamma\gamma \to 4\,\mathrm{fermions}$ and $\mathrm{H} \to \mathrm{WW/ZZ} \to 4\,\mathrm{fermions}$.

At a $\gamma\gamma$ collider precise theoretical predictions are needed for the $\gamma\gamma \to \mathrm{WW} \to 4f$ processes because of their large cross section. These processes allow a measurement of the gauge-boson couplings $\gamma\mathrm{WW}$ and $\gamma\gamma\mathrm{WW}$. Furthermore, the reaction $\gamma\gamma \to \mathrm{H} \to \mathrm{WW/ZZ} \to 4f$ arises through loops of virtual charged, massive particles. Thus, the coupling $\gamma\gamma\mathrm{H}$ can be measured and Higgs bosons with a relatively large mass could be produced.

For masses $M_\mathrm{H} \gtrsim 135\,\mathrm{GeV}$ the Higgs boson predominantly decays into W- or Z-boson pairs and subsequently into four leptons. The kinematical reconstruction of these decays is influenced by quantum corrections, especially real photon radiation. Since off-shell effects of the gauge bosons have to be taken into account below $M_\mathrm{H} \approx 2M_{\mathrm{W/Z}}$, the inclusion of the decays of the gauge bosons is important. In addition, the spin and the CP properties of the Higgs boson can be determined by considering angular and energy distributions of the decay fermions.

For a comparison of theoretical predictions with experimental data Monte Carlo generators are useful tools. We construct such programs for the processes $\gamma\gamma \to \mathrm{WW} \to 4f$ and $\mathrm{H} \to \mathrm{WW/ZZ} \to 4f$. On the one hand, they provide the complete predictions at lowest order of perturbation theory. On the other hand, they contain quantum corrections, which can be classified into real corrections, connected with photon bremsstrahlung, and virtual corrections. Whereas the virtual quantum corrections to $\gamma\gamma \to \mathrm{WW} \to 4f$ are calculated in the double-pole approximation, i.e. only doubly-resonant contributions are taken into account, we calculate the complete $\mathcal{O}(\alpha)$ corrections for the $\mathrm{H} \to \mathrm{WW/ZZ} \to 4f$ processes. The infrared (soft and collinear) divergences in the virtual and real corrections are treated either with the dipole-subtraction method or with the phase-space slicing method. The mass singularities that occur due to collinear photon emission do not cancel for all observables. In order to treat also such non-collinear-safe observables we apply an extension of the dipole-subtraction method.

The discussion of numerical results comprises the impact of a realistic beam spectrum on cross sections, the potential of a $\gamma\gamma$ collider to constrain anomalous couplings, and various angular, energy, and invariant-mass distributions, which can be used for a kinematical reconstruction of the gauge bosons and for determining the properties of the Higgs boson.

Chapter 1

Introduction

1.1 Outline of the thesis

In the introduction we will give an overview of the construction and the essential ingredients of the Standard Model (SM) of elementary particles, which describes all fundamental particles that we know today and the interactions between them. In addition, we will mention some remaining questions, especially the existence of the Higgs boson, and the reasons why there should be physics beyond the SM. In this context we will stress the importance of quantum corrections in the search for the Higgs boson and for new physics.

The next chapter starts with a brief description of the $\gamma\gamma$ collider, an optional experiment at the International $\mathrm{e}^+\mathrm{e}^-$-Linear Collider (ILC), and some interesting processes that could be studied there. Focusing on four-fermion production, especially through W-boson pair production, we describe the strategy for performing a precision calculation for these processes. To this end, also subtleties occurring in the treatment of unstable particles are discussed. The pole expansion is presented as a means of introducing the width of an unstable particle in a gauge-invariant way and for calculating quantum corrections in an economic manner. In Chapter 4 the results will be used in order to calculate quantum corrections to $\gamma\gamma \to \mathrm{WW} \to 4f$ in the double-pole approximation.

In Chapter 3, which is mainly based on Ref. [1], we present the lowest-order results for $\gamma\gamma \to 4f(\gamma)$, first in the SM and then including anomalous couplings, which parametrize possible new physics phenomena. As a preparation for the next chapter, the double-pole approximation is applied to the lowest-order calculation and compared to the complete result. After discussing the appearance of a Higgs boson as s-channel resonance, we briefly describe how the convolution over the photon spectrum is performed. We conclude the chapter with a discussion of numerical results that include integrated cross sections, distributions, the influence of the Higgs resonance, and the potential of the $\gamma\gamma$ collider to set bounds on anomalous couplings.

In Chapter 4, which is mainly based on Ref. [2], quantum corrections to the process $\gamma\gamma \to \mathrm{WW} \to 4f$ are calculated in the double-pole approximation, which classifies the virtual corrections into factorizable and non-factorizable corrections. The infrared divergences occurring in the virtual and real corrections are treated either with the dipole subtraction or with the phase-space slicing method, which are explained in some detail. For the case of non-collinear-safe observables these methods are generalized. The numerical impact of the results is discussed in terms of integrated cross sections and distributions. This also includes an estimate of the remaining theoretical uncertainty and a comparison with an improved Born approximation, which only contains universal effects of the quantum corrections.

In Chapter 5 we discuss the Higgs-boson decays into W or Z bosons, which are the most relevant decay channels for $M_{\mathrm{H}} \gtrsim 140\,\mathrm{GeV}$. This decay type is, of course, not only important for the $\gamma\gamma$ collider but also for the LHC and the $\mathrm{e}^+\mathrm{e}^-$ mode of the ILC. After having presented the analytical formulae for the lowest-order processes $\mathrm{H} \to \mathrm{WW/ZZ} \to 4f(\gamma)$, the complete virtual $\mathcal{O}(\alpha)$ corrections are calculated in the complex-mass scheme, which allows a gauge-invariant treatment of width effects of the gauge bosons. The implementation into a Monte Carlo generator proceeds along the same lines as for the processes $\gamma\gamma \to 4f(\gamma)$. The chapter concludes with a presentation of decay widths and distributions that can be used to determine the properties of the Higgs boson such as spin and parity.

In the appendices we explain how the phase-space integration over the momenta of the final-state particles is done with the multi-channel Monte Carlo method. Furthermore, we present the structure of the infrared (soft and collinear) singularities, which are similar for both processes $\gamma\gamma \to \mathrm{WW} \to 4f$ and $\mathrm{H} \to \mathrm{WW/ZZ} \to 4f$. Finally, some details that are necessary for a stable evaluation of the virtual corrections to $\gamma\gamma \to \mathrm{WW}$ are presented.

The numerical calculations in this thesis have been performed using Fortran, and many of the algebraic calculations were done using the program *Mathematica*. The computer codes are available so that they can be used for experimental studies or as a reference for future Monte Carlo generators.

1.2 The Standard Model of elementary particle physics

In this section we will give a brief account of the SM. More details can, for example, be found in Ref. [4].

The SM is a quantum field theory in which interactions between particles are governed by gauge (or local) symmetries. It is most conveniently formulated in terms of the Lagrange formalism, i.e. all the ingredients of the theory, such as kinetic, mass, and interaction terms of the fields, are incorporated into a single local functional, the Lagrangian density. Integrating the Lagrangian density over space-time yields the action of the theory. The form of the Lagrangian density is dictated by symmetry principles and the requirement of renormalizability.

A quantum field theory is called renormalizable if all ultraviolet divergences can be absorbed into a redefinition of the parameters and fields of the Lagrangian. Ultraviolet divergences may appear if observables are calculated by a perturbative expansion. The higher-order terms of this expansion usually involve loop integrals that do not yield a UV-finite result. The procedure of regularizing these UV divergences, e.g. by calculating the integrals in $D \neq 4$ dimensions, and absorbing them into the parameters of the Lagrangian, is called renormalization. The redefinition of the bare parameters of the Lagrangian results in so-called counterterms. Power counting shows that all operators in the Lagrangian that have four or less mass dimensions are renormalizable, i.e. the divergences can be cancelled by counterterms that also have four or less dimensions. However, the Lagrangian including the counterterms has to obey the underlying symmetries restricting the form of the counterterms. Nevertheless, it can be shown that non-abelian gauge theories with spontaneous symmetry breaking, and hence the SM, are renormalizable [5].

One class of symmetries are space-time symmetries. For example, the SM is invariant under Poincare transformations (excluding time and space inversions). Mathematically, these transformation form the Poincare group, which is made up of Lorentz boosts, rotations, and translations in the Minkowski space. All irreducible representations of the Poincare group can be classified by a real positive number m and a half-integer s that can be identified with mass and spin of a given particle type.

On the other hand, there are internal symmetries, which are symmetries among the fields. The Lagrangian density of the SM is invariant under the transformations of the group $\mathrm{SU}(3)_c \otimes \mathrm{SU}(2)_W \otimes \mathrm{U}(1)_Y$. These transformations are local, i.e. they may depend on space-time. When changing a symmetry from a global to a local symmetry, new fields have to be introduced in order to keep the Lagrangian density invariant. The reason is that the Lagrangian density of a quantum field theory contains derivatives of fields. Since the derivatives behave differently under local transformations than the fields themselves, a covariant derivative is defined by minimal substitution as

$$\partial_\mu \to D_\mu = \partial_\mu - ig_s G^a_\mu t^a - ig_W W^i_\mu I^i + ig_Y B_\mu \frac{Y}{2}, \tag{1.2.1}$$

where $t_a = \frac{\lambda^a}{2}$, I^i, and Y are the generators of the corresponding Lie group of the SM, and g_s, g_W, and g_Y are constants. The new vector fields $G^a_\mu (a = 1, .., 8)$, $W^i_\mu (i = 1, 2, 3)$, and B_μ that have to be introduced in order to construct a locally symmetric theory are called gauge fields. They transform in the adjoint representation of the gauge group of the SM. Thus, kinetic terms for fermions can be constructed that are gauge invariant, i.e. invariant under the SM group transformations. These kinetic terms read

$$\begin{aligned}\mathcal{L}_{\text{fermionic}} = {} & \bar{\Psi}^l_L i\gamma^\mu D_\mu \Psi^l_L + \bar{\Psi}^q_L i\gamma^\mu D_\mu \Psi^q_L \\ & + \bar{\Psi}^e_R i\gamma^\mu D_\mu \Psi^e_R + \bar{\Psi}^u_R i\gamma^\mu D_\mu \Psi^u_R + \bar{\Psi}^d_R i\gamma^\mu D_\mu \Psi^d_R,\end{aligned} \tag{1.2.2}$$

where the summation over the three generations is suppressed in the notation. The fermion fields, which are classified into leptons and quarks, are summarized in Table 1.1. They are characterized by their transformation properties under the SM group. With respect to $\mathrm{SU}(3)_c$, leptons are uncharged, and quarks transform in the fundamental representation, i.e. they have three so-called colour degrees of freedom which we also suppress in the notation. With respect to $\mathrm{SU}(2)_W$ the fermions are left-chiral doublets Ψ_L or right-chiral singlets Ψ_R. In the massless case they can be identified with left-handed and right-handed particles. The corresponding quantum numbers of $\mathrm{SU}(2)_W$, the third component of the weak isospin I_3, and of $\mathrm{U}(1)_Y$, the weak hypercharge Y, are given in Table 1.1. The weak hypercharge is fixed by the identification of the photon in the theory, as explained below.

					I_3	Y	Q
leptons	Ψ^l_L	$\begin{pmatrix}\nu_\mathrm{e}\\ \mathrm{e}\end{pmatrix}_L$	$\begin{pmatrix}\nu_\mu\\ \mu\end{pmatrix}_L$	$\begin{pmatrix}\nu_\tau\\ \tau\end{pmatrix}_L$	$\frac{1}{2}$ $-\frac{1}{2}$	-1 -1	0 -1
	Ψ^e_R	e_R	μ_R	τ_R	0	-2	-1
quarks	Ψ^q_L	$\begin{pmatrix}\mathrm{u}\\ \mathrm{d}\end{pmatrix}_L$	$\begin{pmatrix}\mathrm{c}\\ \mathrm{s}\end{pmatrix}_L$	$\begin{pmatrix}\mathrm{t}\\ \mathrm{b}\end{pmatrix}_L$	$\frac{1}{2}$ $-\frac{1}{2}$	$\frac{1}{3}$ $\frac{1}{3}$	$\frac{2}{3}$ $-\frac{1}{3}$
	Ψ^u_R	u_R	c_R	t_R	0	$\frac{4}{3}$	$\frac{2}{3}$
	Ψ^d_R	d_R	s_R	b_R	0	$-\frac{2}{3}$	$-\frac{1}{3}$

Table 1.1: Fermions of the SM and their quantum numbers weak isospin I_3, weak hypercharge Y, and electromagnetic charge Q.

After introducing a local symmetry, the Lagrangian density (1.2.2) also contains interaction terms between fermions and gauge fields in addition to the purely kinetic terms of the fermions. This is the guiding principle in the construction of gauge theories.

Besides the kinetic terms of the fermions, gauge-invariant kinetic terms of the gauge fields can be constructed from the field-strength tensors

$$\begin{aligned} G^a_{\mu\nu} &= \partial_\mu G^a_\nu - \partial_\nu G^a_\mu - g_s f^{abc} G^b_\mu G^c_\nu, \\ W^i_{\mu\nu} &= \partial_\mu W^i_\nu - \partial_\nu W^i_\mu - g_W \epsilon^{ijk} W^j_\mu W^k_\nu, \\ B_{\mu\nu} &= \partial_\mu B_\nu - \partial_\nu B_\mu, \end{aligned} \tag{1.2.3}$$

where f^{abc} and ϵ^{ijk} are the structure constants of the Lie algebras su(3) and su(2), respectively. The field-strength tensors can be expressed in terms of the commutator $[D_\mu, D_\nu]$, which transforms covariantly. Taking the trace of the squared field strengths, a gauge-invariant Lagrangian density can be constructed as

$$\mathcal{L}_\mathrm{YM} = -\frac{1}{4} G^a_{\mu\nu} G^{a,\mu\nu} - \frac{1}{4} W^i_{\mu\nu} W^{i,\mu\nu} - \frac{1}{4} B_{\mu\nu} B^{\mu\nu}. \tag{1.2.4}$$

It contains kinetic terms (hence, the gauge fields are propagating physical fields), and, in the case of the non-abelian groups, also interaction terms among the gauge fields.

However, there are no mass terms in the theory yet, because these terms would violate gauge invariance. A solution is provided by the Higgs mechanism for spontaneous symmetry breaking. To this end, the Higgs field,

$$\Phi(x) = \begin{pmatrix} \phi^+(x) \\ \phi^0(x) \end{pmatrix}, \tag{1.2.5}$$

is introduced, which has a weak hypercharge $Y = 1$ and transforms as an $\mathrm{SU}(2)_W$ doublet. Its contribution to the Lagrangian density reads

$$\mathcal{L}_\mathrm{Higgs} = (D_\mu \Phi)^\dagger (D^\mu \Phi) + \mu^2 (\Phi^\dagger \Phi) - \frac{\lambda}{4} (\Phi^\dagger \Phi)^2, \qquad \mu^2, \lambda > 0. \tag{1.2.6}$$

The last two terms constitute the most general form of a renormalizable self-interaction. For the classical ground state Φ_0 of the Higgs field we have

$$|\langle\Phi_0\rangle|^2 = \frac{2\mu^2}{\lambda} = \frac{v^2}{2}, \tag{1.2.7}$$

i.e. the Higgs field acquires a non-vanishing vacuum expectation value, which breaks the $\mathrm{SU}(2)_W \otimes \mathrm{U}(1)_Y$ symmetry. According to the Goldstone theorem, there is a massless boson for every spontaneously broken continuous symmetry. These Goldstone bosons appear in an expansion of the Higgs field around its vacuum expectation value,

$$\Phi = \begin{pmatrix} \phi^+ \\ \frac{v+H+i\chi}{\sqrt{2}} \end{pmatrix}, \quad \phi^- = (\phi^+)^\dagger. \tag{1.2.8}$$

The fields ϕ^+, ϕ^-, and χ can be eliminated by a suitable gauge transformation, and are, thus, unphysical degrees of freedom (would-be Goldstone bosons). However, they deliver the longitudinal degrees of freedom of the three massive gauge bosons corresponding to the broken symmetries of $\mathrm{SU}(2)_W \otimes \mathrm{U}(1)_Y$.

Inserting Eq. (1.2.8) into Eq. (1.2.6), we observe that the vacuum expectation value of the Higgs field gives rise to mass terms for the electroweak gauge bosons. However, the fields that correspond to mass eigenstates are mixtures of the fields W^i_μ and B_μ and can be obtained by diagonalizing the mass matrix,

$$\begin{aligned} W^\pm_\mu &= \tfrac{1}{\sqrt{2}}(W^1_\mu \mp iW^2_\mu), \\ \begin{pmatrix} Z_\mu \\ A_\mu \end{pmatrix} &= \begin{pmatrix} \cos\theta_W & \sin\theta_W \\ -\sin\theta_W & \cos\theta_W \end{pmatrix} \begin{pmatrix} W^3_\mu \\ B_\mu \end{pmatrix}, \end{aligned} \tag{1.2.9}$$

with

$$c_\mathrm{w} \equiv \cos\theta_W \equiv \frac{g_W}{\sqrt{g_W^2+g_Y^2}}, \qquad s_\mathrm{w} \equiv \sin\theta_W \equiv \frac{g_Y}{\sqrt{g_W^2+g_Y^2}}, \tag{1.2.10}$$

where θ_W is called weak mixing angle. Since after spontaneous symmetry breaking a $U(1)$ symmetry with the generator $Q = I_3 + \frac{Y}{2}$ remains unbroken, one gauge boson stays massless. This is the field A_μ, which can be identified with the photon. According to (1.2.2) its coupling to fermions is proportional to eQ with the elementary charge

$$e \equiv \sqrt{4\pi\alpha} \equiv \frac{g_W g_Y}{\sqrt{g_W^2+g_Y^2}}. \tag{1.2.11}$$

The fermion charges relativ to the elementary charge, which are the eigenvalues of the charge operator Q, are given in Table 1.1. To summarize, the electroweak gauge bosons consist of two electrically neutral gauge bosons A and Z and two charged gauge bosons $\mathrm{W}^\pm$. Their masses read

$$M_{\mathrm{W}^\pm} = \frac{1}{2} v g_W, \qquad M_\mathrm{Z} = \frac{1}{2} v \sqrt{g_W^2+g_Y^2}, \qquad M_\mathrm{A} = 0. \tag{1.2.12}$$

The mechanism of spontaneous symmetry breaking also allows for incorporating the fermion masses into the theory. A naive construction of fermion-mass terms $m(\bar{\Psi}_L\Psi_R + h.c.)$, where $h.c.$ denotes the hermitian conjugate expression, is not possible, because left- and right-chiral fermions belong to different representations of the gauge group and have different quantum numbers. However, fermion mass terms can be obtained by coupling the fermions to the Higgs field. The vacuum expectation value then yields the desired mass terms. The corresponding contribution to the Lagrangian density reads

$$\mathcal{L}_{\text{Yukawa}} = -\sum_{l,\text{e}} \bar{\Psi}^l_L G_{l\text{e}} \Psi^{\text{e}}_R \Phi - \sum_{q,d} \bar{\Psi}^q_L G_{qd} \Psi^d_R \Phi - \sum_{q,u} \bar{\Psi}^q_L G_{qu} \Psi^u_R \tilde{\Phi} + h.c., \tag{1.2.13}$$

where $\tilde{\Phi} = i\sigma_2\Phi^*$ is the charge conjugate Higgs field [1]. The coupling constants that are contained in the matrices $G_{l\text{e}}, G_{qd}$, and G_{qu} are called Yukawa couplings. The mass eigenstates of the fermions are obtained by diagonalizing these matrices via field transformations. For massless neutrinos the diagonalization matrices can be absorbed into the fields so that there is no difference between mass eigenstates and eigenstates of the weak interactions. However, for quarks the change from the weak eigenstates to the mass eigenstates is described by the Cabibbo-Kobayashi-Maskawa (CKM) matrix. If the quark masses are neglected, the CKM matrix can be set to the unit matrix in most applications.

Finally, in order to quantize the theory in the path-integral formalism, a gauge has to be specified to avoid an integration over equivalent field configurations. This is achieved by adding gauge-fixing terms to the Lagrangian density. In an R_ξ gauge, gauge-fixing functionals are chosen as

$$\begin{aligned} F^G &= \tfrac{1}{\sqrt{\xi^G}}\partial^\mu G^a_\mu, & F^{\text{W}^\pm} &= \tfrac{1}{\sqrt{\xi^{\text{W}}_1}}\partial^\mu \text{W}^\pm_\mu \mp \text{i}M_{\text{W}}\sqrt{\xi^{\text{W}}_2}\phi^\pm, \\ F^A &= \tfrac{1}{\sqrt{\xi^A}}\partial^\mu A_\mu, & F^{\text{Z}} &= \tfrac{1}{\sqrt{\xi^{\text{Z}}_1}}\partial^\mu \text{Z}_\mu - \text{i}M_{\text{Z}}\sqrt{\xi^{\text{Z}}_2}\chi, \end{aligned} \tag{1.2.14}$$

where the case of $\xi^G = \xi^A = \xi^{\text{W}} = \xi^{\text{Z}} = 1$ is called 't Hooft–Feynman gauge. The corresponding contributions to the Lagrangian density are

$$\mathcal{L}_{\text{fix}} = -\frac{1}{2}|F^\alpha|^2, \tag{1.2.15}$$

where we implicitly sum over the parameter α. The gauge fixing as it is done in Eq. (1.2.15) changes the measure of the path integral, which can be accounted for by introducing another term in the Lagrangian density,

$$\mathcal{L}_{FP} = -\bar{u}^\alpha(x)\frac{\delta F^\alpha}{\delta\theta^\beta(x)}u^\beta(x), \tag{1.2.16}$$

where $u^\alpha(x)$ are called Faddeev–Popov ghosts, and $\delta\theta^\beta(x)$ denotes an infinitesimal gauge transformation. The Faddeev–Popov ghosts represent unphysical degrees of freedom and

---

[1] In principle it is possible to include also right-chiral neutrinos in Table 1.1 and to add a corresponding Yukawa coupling in Eq. (1.2.13). Also a Majorana mass term is then possible, because the right-chiral neutrinos are uncharged under the SM group. In fact, neutrino oscillation experiments have shown that neutrinos have a mass. However, their mass is very small and can be neglected in this context.

cancel the degrees of freedom of the gauge bosons that were over-counted by the gauge fixing.

From the Lagrangian density Feynman rules for calculating scattering amplitudes perturbatively can be inferred. For example, the couplings of the fermions to the electroweak gauge bosons $V = \gamma, \mathrm{Z}, \mathrm{W}$ are obtained by inserting the above definitions into Eq. (1.2.2). With the operators $\omega_\pm = \frac{1}{2}(1 \pm \gamma^5)$, which project onto the right- and left-handed components of the fermions, respectively, the corresponding Feynman rule reads

$$i\Gamma^{V\bar{f}_1 f_2}_{\mu} = ie\gamma_\mu (g^{+}_{V\bar{f}_1 f_2}\omega_+ + g^{-}_{V\bar{f}_1 f_2}\omega_-) \tag{1.2.17}$$

with

$$g^{\sigma}_{\gamma\bar{f}f} = -Q_f, \qquad g^{\sigma}_{\mathrm{Z}\bar{f}f} = -\frac{s_\mathrm{W}}{c_\mathrm{W}}Q_f + \frac{I^3_f}{c_\mathrm{W}s_\mathrm{W}}\delta_{\sigma-}, \qquad g^{\sigma}_{\mathrm{W}\bar{f}f'} = \frac{1}{\sqrt{2}s_\mathrm{W}}\delta_{\sigma-}, \tag{1.2.18}$$

where f and f' denote the two components of an $SU(2)_W$ doublet. In our calculations we adopt the particle masses as input parameters, from which we derive the weak mixing angle via the on-shell condition

$$s^2_\mathrm{w} = 1 - c^2_\mathrm{w} = 1 - \frac{M^2_\mathrm{W}}{M^2_\mathrm{Z}}. \tag{1.2.19}$$

The Feynman rule for the coupling of the gluon to quarks reads

$$i\Gamma^{g\bar{f}_i f_j}_{\mu} = ig_\mathrm{s}\gamma_\mu \frac{\lambda^a_{ij}}{2}, \tag{1.2.20}$$

where i and j are colour indices and λ^a are the Gell-Mann matrices. From Eq. (1.2.6) we obtain the coupling of the gauge bosons to the Higgs boson,

$$i\Gamma^{\mathrm{H}VV}_{\mu\nu} = ieg_{\mu\nu}g_{\mathrm{H}VV}, \tag{1.2.21}$$

with

$$g_\mathrm{HZZ} = \frac{M_\mathrm{W}}{s_\mathrm{W}c^2_\mathrm{W}}, \qquad g_\mathrm{HWW} = \frac{M_\mathrm{W}}{s_\mathrm{W}}. \tag{1.2.22}$$

The other Feynman rules that are relevant for this thesis can, e.g., be found in Ref. [6, 7].

1.3 Open questions and the role of quantum corrections

The most obvious question concerns the existence of the Higgs boson. Determining whether the Higgs mechanism or some other model to introduce particle masses is realised in nature is one of the most outstanding questions in high-energy physics. The Large Hadron Collider (LHC), which will start operation in 2007 at CERN, will probably settle this issue. The LHC is able to discover the Higgs boson for the whole range of masses that are theoretically conceivable. This mass range is determined by a lower bound of $M_\mathrm{H} > 114.4\,\mathrm{GeV}$ at 95% confidence level [8] by the direct searches at the previous experiment at CERN, LEP, and an upper bound by electroweak precision observables of

$M_{\mathrm{H}} \lesssim 260\,\mathrm{GeV}$ at 95% confidence level [9] and the observation that unitarity would be violated for a Higgs mass of $M_{\mathrm{H}} \gtrsim 1$ TeV [10].

However, the SM, as formulated in the previous section, cannot be an ultimate theory, because it does not incorporate gravity. It might be possible to formulate a theory that describes the phenomena at very high energies, close to the Planck scale, where the gravitational force becomes as strong as the forces of the SM.

But there are also other reasons why there should be new physics, i.e. physics beyond the SM. For example, the SM is not able to explain the dark matter of the universe. Furthermore, as already mentioned in the previous section, neutrinos have a very small mass whose origin is not clear up to now.

Besides these obvious problems, there are conceptual problems such as the question why the Higgs mass is so small compared to the Planck scale (hierarchy problem). And also the origin of other SM parameters, especially the fermion masses, is unclear. The fermion masses have to be inserted “by hand” through the Yukawa couplings in Eq. (1.2.13). However, their values differ by several orders of magnitude from each other. This immediately rises the question where this hierarchy comes from. Moreover, it is not clear why there are exactly three generations of quarks and leptons.

Many models have been constructed that can solve some of these problems, such as supersymmetry or models with new gauge groups or extra dimensions. A common feature of these models is that they contain the SM as an effective theory that is valid at least up to the electroweak scale. At some higher energy the predictions of the new models deviate from the SM predictions. This is one reason why precise theoretical predictions are so important. If the energy of a collider is not large enough to directly see new particles, it might still be possible to see a deviation from the SM prediction in certain observables. However, this is only possible if the accuracy of experimental and theoretical results is high enough.

Precise theoretical predictions for scattering processes are usually obtained by a perturbative expansion in the coupling constants. The expansion can be visualized by so-called Feynman diagrams, which are classified into tree-level diagrams and loop diagrams. The higher-order contributions of the expansion are called quantum (or radiative, or loop) corrections.

For the LHC the quantum corrections of QCD are the most relevant ones. They make up a substantial part of the predictions. In some cases the lowest-order uncertainty can be up to 100%, but the next-to-leading order reduces it to the order of some 10% or better. For the ILC the situation is different. Quantum corrections are typically smaller, and the experimental environment is much cleaner allowing for a much higher precision. The ILC can be seen as a window to higher energies because of virtual effects of heavy particles which only occur in quantum corrections.

During the past years a lot of progress has been made in the calculation of quantum corrections. For example, the calculation of one-loop corrections to $2 \to 2$ processes has become a standard task, and various tools exist for this purpose. However, many things remain to be done. On the one hand, two-loop or even three-loop corrections are needed for many high-precision observables. On the other hand, most searches for new physics involve processes with many particles in the final state so that corrections to $2 \to 3$ or

$2 \to 4$ processes have to be calculated. Usually, this is not possible by a brute force computer calculation, but new techniques have to be developed. This is the case, e.g., for the reduction of tensor integrals, for the phase-space integration, and for the treatment of soft and collinear divergences. But also conceptual problems arise, e.g., the question how to treat resonances of unstable particles.

This thesis will touch some of these issues, and the chosen solutions will be presented.

Chapter 2

Four-fermion production at the $\gamma\gamma$ collider

2.1 The $\gamma\gamma$ collider

As a design option at the ILC, a photon (or $\gamma\gamma$) collider found considerable interest in recent years. The idea, though, was already discussed more than 20 years ago (see, e.g., Refs. [11, 12] and references therein). High-energy photons can be produced by focusing a laser beam on the electron beam. The photons, which have an energy at the order of $1\,\mathrm{eV}$, are Compton backscattered, and most of the energy of the electrons is transferred to the photons. Detailed simulations of the resulting energy spectra of polarized photons have been performed in Ref. [13]. Based on these simulations and assuming that the $\gamma\gamma$ luminosity spectrum can be written as the product of the two photon-energy spectra, a parametrization of the photon-energy spectra has been suggested in Ref. [14]. We will use the computer code CompAZ, introduced in this reference. For an electron beam energy of $250\,\mathrm{GeV}$ the photon energy spectrum is shown in Figure 2.1, where the laser polarization is $P_c = -1$ and the electron polarization $\lambda_\mathrm{e} = +0.85$. For $\lambda_\mathrm{e} P_c < 0$, the high-energy peak of the spectrum is very pronounced. Apart from the simple Compton scattering, which gives rise to the peak at $E_\gamma/E_\mathrm{e} \sim 0.8$, different contributions can be seen. The small high-energy end of the spectrum is due to the scattering of two incoming photons at one electron, whereas as the low-energy part is dominated by secondary scattering of electrons.

There is a vast number of phenomena that could be studied at the $\gamma\gamma$ collider, and the information that could be obtained is complementary to the $\mathrm{e}^+\mathrm{e}^-$ mode in many cases. One of the most interesting reactions is $\gamma\gamma \to \mathrm{H}$, i.e. the production of a Higgs boson as an s-channel resonance, which extends the discovery reach of the linear collider for heavy Higgs bosons. It also allows a direct measurement of the $\gamma\gamma\mathrm{H}$ coupling. This coupling is loop induced (i.e. due to quantum corrections) in the SM and sensitive to heavy charged particles that receive their mass through the Higgs mechanism and that might not be produced directly.

Another intriguing property of the $\gamma\gamma$ collider is the large cross section for pair production of charged particles. This especially applies to W-boson pair production so that

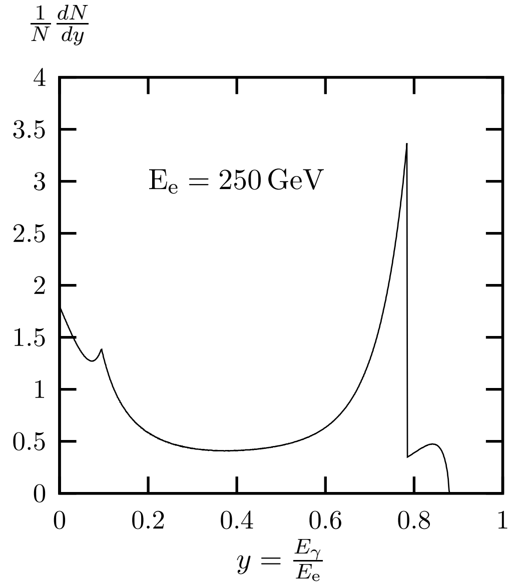

Figure 2.1: Photon energy spectrum obtain with the program CompAZ for a laser polarization $P_c = -1$ and an electron polarization $\lambda_e = +0.85$.

the $\gamma\gamma$ collider can be considered as a W-boson factory. For instance, it can be used for precision tests of the gauge sector of the SM. While the reaction $e^+e^- \to$ WW depends on the gauge-boson couplings ZWW and γWW, the corresponding reaction at a $\gamma\gamma$ collider, $\gamma\gamma \to$ WW, is sensitive to the gauge-boson couplings γWW and $\gamma\gamma$WW. At an e^+e^- collider the coupling $\gamma\gamma$WW is only directly accessible through the bremsstrahlung process $e^+e^- \to$ WWγ, which is suppressed by a factor $\alpha(0)/\pi$ w.r.t. the non-radiative process $e^+e^- \to$ WW. Therefore, the sensitivity to the anomalous $\gamma\gamma$WW coupling in the $\gamma\gamma$ mode is expected to be an order of magnitude better than in the e^+e^- mode. The precision for the measurement of the γWW coupling is comparable in both modes [15].

2.2 Four-fermion production in $\gamma\gamma$ collisions

2.2.1 Precision calculations for $\gamma\gamma \to \mathrm{WW} \to 4f$

Since W bosons decay into fermion–anti-fermion pairs, the actually observed final states of $\gamma\gamma \to$ WW involve four fermions. A theoretical prediction can be obtained by multiplying the cross section for the process $\gamma\gamma \to$ WW with the corresponding branching ratios for the two W-boson decays. This approach is called narrow-width approximation (NWA), because it is assumed that the W bosons are stable, i.e. that they have a negligible width (the NWA is actually a zero-width approximation). If more information than the total cross section is needed, the kinematics and spin correlations between the W-boson production and the subsequent decays have to be taken into account. This can be done, e.g., in the leading-pole approximation. However, this procedure neglects terms that are of the order $\mathcal{O}(\frac{\Gamma_W}{M_W})$, where $\frac{\Gamma_W}{M_W} \sim 2.6\%$. A theoretical uncertainty of at least 2.6% is clearly not sufficient. Consequently the full process $\gamma\gamma \to 4f$ should be considered, which involves not only the so-called "signal diagrams" but also "background diagrams". The former are related to the process $\gamma\gamma \to \mathrm{WW} \to 4f$, where two W bosons can become resonant for a specific region in phase space. The latter involve only one or no W resonance. Compared to the doubly-resonant diagrams, such singly-resonant and non-resonant diagrams are suppressed by roughly a factor $\Gamma_\mathrm{W}/M_\mathrm{W}$ and $(\Gamma_\mathrm{W}/M_\mathrm{W})^2$, respectively. Lowest-order predictions for $\gamma\gamma \to 4f$ processes (with monochromatic photon beams and leptonic or semi-leptonic final states) were discussed in Refs. [16, 17].

In addition to the "background diagrams" from the full four-fermion process, which are of the order $\mathcal{O}(\frac{\Gamma_\mathrm{W}}{M_\mathrm{W}})$, there are radiative corrections to the "signal diagrams", which are of the order $\mathcal{O}(\alpha)$. Since $\alpha \sim \frac{\Gamma_\mathrm{W}}{M_\mathrm{W}}$, the size of both contributions is comparable. This suggests to calculate the full four-fermion lowest-order cross section and the $\mathcal{O}(\alpha)$ corrections to the resonant parts of the W-pair process in order to obtain a precise theoretical description of the process $\gamma\gamma \to \mathrm{WW} \to 4f$. The resulting theoretical uncertainty is $\mathcal{O}(\frac{\alpha}{\pi}\frac{\Gamma_\mathrm{W}}{M_\mathrm{W}})$, because radiative corrections to the background diagrams are neglected. Introducing a safety factor for possibly enhanced higher-order contributions, the remaining theoretical uncertainty is $\lesssim 0.5\%$. For the similar process $\mathrm{e}^+\mathrm{e}^- \to \mathrm{WW} \to 4f$ this programme has been carried through in Refs. [18, 19, 20, 21, 22, 23] by applying the double-pole approximation (DPA). The error estimate of 0.5% was confirmed in Ref. [24] through a calculation of the full $\mathcal{O}(\alpha)$ corrections to $\mathrm{e}^+\mathrm{e}^- \to 4f$. Calculating the full $\mathcal{O}(\alpha)$ corrections to $\gamma\gamma \to 4f$ clearly exceeds the scope of this work, because the occurring tensors integrals can have an even higher rank than in $\mathrm{e}^+\mathrm{e}^- \to 4f$. Furthermore, due to the complexity of such a calculation, the run-time of the corresponding computer code would be rather long. Therefore, a calculation of the $\mathcal{O}(\alpha)$ corrections in DPA is a valuable step in a precise description of the process $\gamma\gamma \to \mathrm{WW} \to 4f$.

Close to the production threshold of W pairs, the error estimate of 0.5% is not reliable anymore, because the background diagrams are not suppressed by Γ/M_W with respect to the signal diagrams anymore. Hence, in this region the DPA cannot be trusted. Below the threshold, only one W-boson propagator can become resonant. Thus, a single-pole approximation could be used. However, since the cross section is relatively small in this region, we only use an improved Born approximation for the corrections. The exact details will be given in Chapter 4.

Calculating the $\mathcal{O}(\alpha)$ corrections to the resonance process $\gamma\gamma \to \mathrm{WW} \to 4f$ is, however, not straightforward. First of all, this would mean singling out a specific set of diagrams which causes a violation of gauge invariance, and, thus, a violation of Ward identities. In principle, these effects are of higher order, but they can be enhanced, because the unitarity cancellations are spoiled. This is a problem especially at large energies, because of the appearance of ratios of different scales, such as a momentum of the scattering process and a mass [18, 25, 26]. A solution is provided by the DPA in which only the leading contribution of an expansion around the resonances of the propagators (pole expansion) is taken into account. This expansion also provides a natural way for implementing the width of the W bosons, a problem that will be discussed in the next section. The pole expansion will be explained in Section 2.4 while the details of the calculation of the radiative corrections to $\gamma\gamma \to \mathrm{WW} \to 4f$ in DPA will be given in Chapter 4.

In applying the DPA we basically follow the strategy of Ref. [19], i.e. we calculate only the virtual corrections in DPA, and use the exact matrix elements for the lowest order and for the real corrections. On the one hand, this requires the calculation of the complete lowest-order matrix elements of the process $\gamma\gamma \to 4f\gamma$. On the other hand, it avoids the distinction between different regions of photon momenta. For example, if $E_\gamma \sim \Gamma_{\mathrm{W}}$ a photon that is emitted from a resonant W boson might lead to two overlapping resonances, and it is difficult to estimate the resulting theoretical uncertainty. Furthermore, depending on the definition of the observable, the photonic corrections can be large so that a calculation of them without approximation is desirable.

2.2.2 Anomalous couplings

The process $\gamma\gamma \to \mathrm{WW}$ offers the possibility to measure the gauge couplings $\gamma\mathrm{WW}$ and $\gamma\gamma\mathrm{WW}$ very precisely. Thus, it is possible to search for the effect of new physics at an energy Λ that is larger than the electroweak scale. The influence of the high-energy theory can be described by an effective theory that is valid at the energy scale that can be accessed by colliders. This effective theory would break down at the energy Λ so that it need not be renormalizable and can contain higher-dimensional operators. Not knowing the high-energy theory, a reasonable approach is to guess these new operators, guided by symmetry principles, and to put limits on the size of the couplings in these operators. The corresponding couplings are called anomalous couplings as they deviate from the SM couplings.

With the exception of Ref. [27], the existing analyses on anomalous couplings at a $\gamma\gamma$ collider, which focus on anomalous triple gauge-boson couplings (ATGC) [15, 28], on anomalous quartic gauge-boson couplings (AQGC) [29, 30], on CP-violating gauge-boson couplings [31], and on effects of strongly interacting longitudinal W bosons [32], treat W bosons as stable. In the above studies radiative corrections were not fully taken into account either.

In our calculation anomalous couplings are introduced in the lowest-order matrix elements for the processes $\gamma\gamma \to 4f$. The coefficients of the corresponding anomalous operators are already constrained from the LEP2 analysis to be small. Therefore, the inclusion of anomalous couplings can be viewed as an expansion in these coefficients which are of $\mathcal{O}(\alpha)$.

2.2.3 Higgs production

As already mentioned in Section 2.1, the process $\gamma\gamma \to \mathrm{H}$ is one of the most interesting processes at a $\gamma\gamma$ collider. For Higgs masses of $M_{\mathrm{H}} \gtrsim 135\,\mathrm{GeV}$, the Higgs boson dominantly decays into W and Z bosons. Thus, the processes $\gamma\gamma \to \mathrm{H} \to \mathrm{WW/ZZ} \to 4f$ can be observed. In Section 3.3 we take this reaction into account in our lowest-order calculation by defining an effective $\gamma\gamma\mathrm{H}$ coupling that is derived from the loop-induced SM vertex. On the other hand, the process $\gamma\gamma \to \mathrm{H} \to \mathrm{WW}$ is contained in the one-loop corrections to $\gamma\gamma \to \mathrm{WW}$, which will be discussed in Chapter 4. In Section 4.2.2.4 we describe how the Higgs resonance is separated in a gauge-invariant way allowing for the inclusion of higher-order corrections to the Higgs signal in the future.

2.3 Problems with unstable particles in field theory

An overview of unstable particles in field theory can be found in Ref. [33]. In the following we will sketch the issue of unitarity, the definition of the mass and width of an unstable particle, the implementation of the width in perturbative calculations, and the pole expansion.

The first problem that can be encountered with unstable particles is the validity of unitarity, and related to this, of causality. The scattering of particles is described by the S-matrix

$$S_{fi} = \langle \Psi_f^- | \Psi_i^+ \rangle, \tag{2.3.1}$$

which is related to the probability amplitude for an “in” state $|\Psi_i^+\rangle$ to evolve to an “out” state $|\Psi_f^-\rangle$. These asymptotic states are defined via the limit

$$|\Psi_\alpha^\pm\rangle = \lim_{t\to\mp\infty} U(t,t_0)|\mathbf{p}_\alpha\rangle \tag{2.3.2}$$

with the time-evolution operator in the interaction picture $U(t,t_0)$ and the momentum eigenstates $|\mathbf{p}_\alpha\rangle$. The origin of the problem obviously lies in the fact that unstable particles cannot be defined as asymptotic states. Hence, unstable particles should only be considered as virtual intermediate states, and should not be contained in the Hilbert space of asymptotic states. In Ref. [34] it was shown that such a theory respects unitarity and causality.

Another problem is the finite width of unstable particles. The propagator of an unstable particle involves a factor $1/(p^2-m^2)$, where p is the momentum and m the mass of the particle. If p^2 is not fixed but must be integrated over like in the process $\gamma\gamma \to \mathrm{WW} \to 4f$, this would lead to an infinite result at lowest order of perturbation theory. This can be cured by including higher-order contributions from the self-energy $\Sigma(p^2)$ of the unstable particle. Performing a Dyson summation, i.e. summing up the self-energies to all orders, the propagator of a scalar particle becomes

$$\begin{aligned} P(p^2) &= \frac{i}{p^2-m^2}\sum_{n=0}^{\infty}\left(\frac{-\Sigma(p^2)}{p^2-m^2}\right)^n \\ &= \frac{i}{p^2-m^2+\Sigma(p^2)}. \end{aligned} \tag{2.3.3}$$

Close to the resonance, the self-energy behaves as $\Sigma(p^2) \sim im\Gamma$. The constant Γ can be viewed as width of the particle. This becomes clear when squaring the propagator,

$$|P(p^2)|^2 \underset{p^2\to m^2}{\sim} \frac{1}{(p^2-m^2)^2+m^2\Gamma^2}, \tag{2.3.4}$$

which yields a Breit-Wigner profile. When the Fourier transform is taken, an exponential decay can be observed

$$|P(x)|^2 \propto \exp(-\frac{m\Gamma}{E_p}t), \tag{2.3.5}$$

where E_p is the energy of the particle.

Using the Dyson summation of Eq. (2.3.3) mixes different orders of perturbation theory. In the beginning of this section we already mentioned that selecting specific diagrams of the $\mathcal{O}(\alpha)$ corrections to the process $\gamma\gamma \to 4f$ potentially violates gauge invariance. This is also the case if the width is included by a Dyson summation. A possible solution is provided by taking into account even more higher-order terms in order to obtain a gauge-invariant set of diagrams. In Ref. [25] it was noted that the contribution to the imaginary part of the gauge-boson self-energy near the resonance and, hence, to the width, originates from fermion loops. Consequently, also vertex corrections with closed fermion loops were taken into account which leads to a gauge-invariant result. In a more general way this can be done in the background-field method [7, 35] so that also bosonic loops can be taken into account. The drawback of this method is the large calculational effort that is necessary, because the width calculated at n-loop level only yields a description of the resonance that is accurate at the $(n-1)$-loop level.

A simpler way is provided by the naive fixed-width scheme, were a fixed width is included in all propagators, also in space-like propagators. In principle, it is not necessary to include a width in space-like propagators. However, compared to the step-width scheme, where the width is only included in time-like propagators, the fixed-width scheme has the advantage that it respects U(1) gauge invariance. Both schemes violate SU(2) symmetry and the corresponding Ward identities. A more accurate description of the self-energy close to resonance is provided by the running-width scheme, where $\mathrm{i}m\Gamma$ is replaced by $\mathrm{i}p^2(\Gamma/m)\theta(p^2)$. The step function indicates that the width is only introduced in time-like propagators. This scheme also violates both U(1) and SU(2) invariance, and now these effects can even be enhanced by the factor p^2 at large energies. Examples for this phenomenon were found, e.g., in Refs. [18, 25, 26].

Finally, the complex-mass scheme [18], where the mass is replaced by $m \to \sqrt{m^2 - \mathrm{i}m\Gamma}$ at the level of the Lagrangian density, respects all Ward identities. At lowest oder this scheme is similar to the fixed-width scheme. The only difference is that the width also appears in other quantities that are defined through the mass, such as the weak mixing angle.

The application of the fixed-width, the step-width, the running-width, and the complex-mass scheme for the lowest-order processes $\gamma\gamma \to 4f(\gamma)$ will be discussed in Section 3.1.4. For the processes $\mathrm{e^+e^-} \to 4f(\gamma)$ this has, e.g., been done in Ref. [18]. In Chapter 5 the generalization of the complex-mass scheme to the one-loop order [24] will be used for the calculation of the $\mathcal{O}(\alpha)$ corrections to $\mathrm{H} \to \mathrm{WW/ZZ} \to 4f$ without resonance expansion.

Until now, we did not specify how to renormalize the mass of an unstable particle. This will be important for the next section, where we need the concept of the complex-pole mass in contrast to the more common on-shell mass. In Eq. (2.3.3) the ultraviolet divergence of the self-energy has to be absorbed into a redefinition of the mass. However, the exact form of the redefinition involves some arbitrariness, which is fixed by a renormalization condition. In the case of stable particles, where the self-energy is a real quantity near $p^2 = m^2$, the square of the mass is defined as the location of the pole of the propagator.

In analogy, the on-shell mass for an unstable particle is defined as the zero of the real part of the inverse propagator,

$$m_{\rm OS}^2 = m_0^2 - {\rm Re}\,\Sigma(m_{\rm OS}^2), \tag{2.3.6}$$

where m_0 is the bare mass. The corresponding on-shell width is obtained from the propagator in Eq. (2.3.3),

$$P(p^2) = {\rm i}\frac{1+{\rm Re}\,\Sigma'(m_{\rm OS}^2)}{p^2 - m_{\rm OS}^2 + {\rm i}\frac{{\rm Im}\,\Sigma(p^2)}{1+{\rm Re}\,\Sigma'(m_{\rm OS}^2)}} + \mathcal{O}(p^2 - m_{\rm OS}^2), \tag{2.3.7}$$

as

$$m_{\rm OS}\Gamma_{\rm OS} = \frac{{\rm Im}\,\Sigma(m_{\rm OS})}{1+{\rm Re}\,\Sigma'(m_{\rm OS}^2)}. \tag{2.3.8}$$

Alternatively, the complex pole position can be used as renormalization condition, resulting in

$$M^2 = m_0^2 - \Sigma(M^2), \qquad M^2 = m_{\rm pole}^2 - {\rm i}m_{\rm pole}\Gamma_{\rm pole}, \tag{2.3.9}$$

where $m_{\rm pole}$ is called pole mass and M is the complex-pole mass. Since the location of the complex pole is a property of the S-matrix, the pole mass is gauge invariant, whereas the on-shell mass becomes gauge dependent beyond one-loop order [36]. Unfortunately, $m_{\rm OS}$ is sometimes called pole mass in the literature. It is, however, important to note, that $m_{\rm OS}$ and $m_{\rm pole}$ in fact differ by 2-loop terms. This can be seen by expanding the real and complex parts of Eq. (2.3.9) separately in terms of $\Gamma \sim m_{\rm pole}\mathcal{O}(\alpha)$, resulting in

$$\begin{aligned} m_{\rm pole}^2 &= m_0^2 - {\rm Re}\,\Sigma(m_{\rm pole}^2) - m_{\rm pole}\Gamma_{\rm pole}\,{\rm Im}\,\Sigma'(m_{\rm pole}^2) + \mathcal{O}(\alpha^3), \\ m_{\rm pole}\Gamma_{\rm pole} &= {\rm Im}\,\Sigma(m_{\rm pole}^2) - m_{\rm pole}\Gamma_{\rm pole}\,{\rm Re}\,\Sigma'(m_{\rm pole}^2) + \mathcal{O}(\alpha^3). \end{aligned} \tag{2.3.10}$$

We can now determine the difference of the on-shell and the pole mass,

$$\begin{aligned} m_{\rm OS}^2 &= m_{\rm pole}^2 + {\rm Im}\,\Sigma(m_{\rm pole}^2)\,{\rm Im}\,\Sigma'(m_{\rm pole}^2) + \mathcal{O}(\alpha^3) \\ &\approx m_{\rm pole}^2 + \Gamma_{\rm pole}^2 + \mathcal{O}(\alpha^3). \end{aligned} \tag{2.3.11}$$

In the second line it is assumed that the main contribution to the width originates from light fermions. For the W boson the difference corresponds to $m_{\rm OS} - m_{\rm pole} \approx 28\,{\rm MeV}$.

2.4 The pole expansion

The pole expansion is an expansion around the pole of the propagator. It can be viewed as an expansion in terms of Γ/m. Performing a calculation in the double-pole approximation (DPA) means to calculate the first term of a (double-)pole expansion. As already mentioned in the previous sections, the reason to use the DPA to calculate the radiative corrections to the process $\gamma\gamma \to {\rm WW} \to 4f$ is twofold. Since each term of the pole expansion is gauge invariant, the DPA provides a means of calculating a reduced set of diagrams, the W-pair signal diagrams in our case, in a gauge-invariant way. Second,

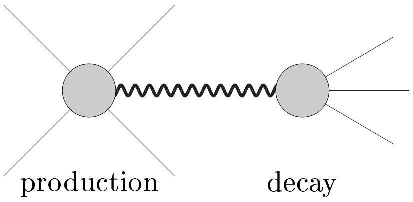

Figure 2.2: A generic factorizable diagram.

the pole expansion naturally enables us to incorporate also the finite gauge-boson width in a gauge-invariant way.

The terms with the highest degree of resonance in the pole expansion can be expressed by the complex pole position and the residue at this pole, which are properties of the S-matrix, and they are therefore gauge invariant. The resonant terms consist in two different kinds of contributions. First, there are factorizable contributions. The corresponding diagrams factorize into the production process of the unstable particle and the subsequent decay process. The generic structure is shown in Figure 2.2.

After Dyson summation the matrix elements of the factorizable diagrams can be expanded around the square of the complex-pole mass M^2 as

$$\mathcal{M}_{\text{fact}} = \frac{W(p^2)}{p^2 - m^2 + \Sigma(p^2)} = \frac{\omega(M^2)}{p^2 - M^2} + n(p^2), \tag{2.4.1}$$

with

$$w(M^2) = \frac{W(M^2)}{1 + \Sigma'(M^2)}, \tag{2.4.2}$$

where $W(p^2)$ contains the parts of the matrix elements that are related to the production and the decay processes. Equation (2.4.1) separates resonant and non-resonant terms in a gauge-invariant way. Yet, the definition of $W(M^2)$ is unclear, because with a complex argument it would involve complex momenta. This problem can be circumvented by an alternative expansion around a real mass m. If m is the pole mass, the following relations hold exactly, otherwise they hold up to higher-order terms. Assuming that this mass has been renormalized, the expansion reads

$$\mathcal{M} = \frac{W(p^2)}{p^2 - m^2} \sum_{n=0}^{\infty} \left(\frac{-\Sigma(p^2)}{p^2 - m^2} \right)^2 = \bar{N}(p^2) + \frac{W_{-1}(m^2)}{p^2 - m^2} + \sum_{n=2}^{\infty} \frac{W_{-n}}{(p^2 - m^2)^n}, \tag{2.4.3}$$

with

$$W_{-1}(m^2) = W(m^2) + \sum_{n=1}^{\infty} \frac{1}{n!} \left[\frac{d^n}{(dp^2)^n} W(p^2) \left(-\Sigma(p^2) \right)^n \right]_{p^2 = m^2}. \tag{2.4.4}$$

The quantities $\bar{N}(p^2)$ and W_{-n} can be defined accordingly. In Ref. [37] it was shown to all orders that

$$\omega(M^2) = W_{-1}(m^2), \qquad n(p^2) = \bar{N}(p^2). \tag{2.4.5}$$

With this relation we are now able to calculate the one-loop corrections to the first term of the pole expansion,

$$W_{-1}^{(1)}(m^2) = W^{(1)}(m^2) - W^{(0)}(m^2)\Sigma^{(1)\prime}(m^2) - W^{(0)\prime}(m^2)\Sigma^{(1)}(m^2), \tag{2.4.6}$$

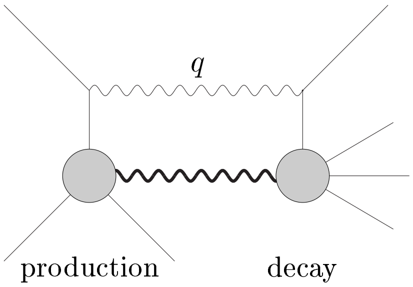

Figure 2.3: A manifestly non-factorizable diagram.

where the superscripts denote the order of perturbation theory. The second term corresponds to the wave-function renormalization of the resonant field. Since the last term of Eq. (2.4.6) is already contained in the complete leading order result, we can write the factorizable one-loop corrections in the pole approximation as

$$\begin{aligned}\mathcal{M}_{\text{PA,fact}} &= \frac{W^{(1)}(m^2)}{p^2-M^2} - \frac{W^{(0)}(m^2)\Sigma^{(1)\prime}(m^2)}{p^2-M^2} \\ &= \sum_{\text{pol}} \frac{1}{p^2-M^2}\left(\mathcal{M}^{(1)}_{\text{production}}\mathcal{M}^{(0)}_{\text{decay}} + \mathcal{M}^{(0)}_{\text{production}}\mathcal{M}^{(1)}_{\text{decay}}\right), \qquad (2.4.7)\end{aligned}$$

where we sum over the polarizations of the unstable particle. The matrix element $\mathcal{M}_{\text{PA,fact}}$ depends on the complete on-shell matrix elements for the production and the decay, which are gauge invariant, and on the complex pole position M^2. Consequently, it is also gauge invariant.

Second, there are non-factorizable diagrams where the production and decay processes are linked by a massless particle like the photon in our case. A generic diagram of this kind is shown in Figure 2.3. If this linking particle was massive, the position of the resonance in phase space would be changed with respect to the lowest-order diagram. After squaring the matrix element, these diagrams do not contribute to the first terms in the pole expansion. For the same reasoning only soft photons contribute, so that the non-factorizable contributions can be written as a correction factor times the leading-order resonant cross section. Power counting reveals that in the limit $p^2 \to m^2$ and $q \to 0$, where q is the photon momentum, the non-factorizable diagrams develop a linear singularity (a quadratic singularity in the case of two resonances). Remote from the resonance, the singularity is mitigated to a logarithmic singularity. Hence, the linear singularity is characteristic for the contribution of the non-factorizable diagrams to the first term in the pole expansion and can be used to split off non-resonant terms.

But there are also diagrams that contain both a factorizable and a non-factorizable contribution. An example is shown in Figure 2.4, where the photon is attached to the resonant particle and an external particle. Alternatively, it may be emitted and reabsorbed by the resonant particle. Taking the on-shell limit ($p^2 \to m^2$ everywhere but in the resonant propagator) before $\lambda \to 0$, where λ is the photon mass, obviously yields a factorizable contribution. However, these two limits do not commute, and performing an off-shell calculation with $\lambda \to 0$ and then taking $p^2 \to m^2$ gives a different result. This

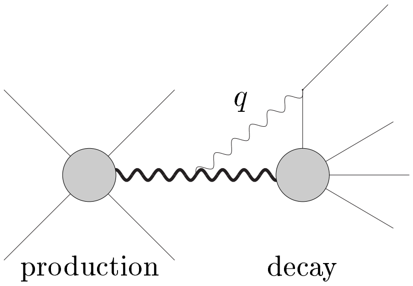

Figure 2.4: A diagram that contains both factorizable and non-factorizable contributions.

shows that these diagrams, which are neither manifestly factorizable nor manifestly non-factorizable, contain both types of contributions. We also arrive at this conclusion when we try to define a gauge-invariant contribution from the non-factorizable diagrams. This can be done by subtracting the factorizable resonant contribution (defined by $p^2 \to m^2$) from the complete resonant contribution. Since these terms are both gauge invariant, as explained above, the result is gauge invariant as well. While the diagram depicted in Figure 2.4 receives contributions from the whole range of the photon momenta q, after subtracting the factorizable contribution, only soft photons contribute. Thus, the non-factorizable contribution, defined in this way, can still be written as a correction factor to the Born cross section.

In Ref. [38] the possible impact of non-factorizable contributions was discussed. It was proven that for inclusive quantities their effect is suppressed by Γ/m. Inclusive in this context means, that the invariant mass of the unstable particle has to be integrated over completely. Since we only take into account the first term of the pole expansion, the non-factorizable contributions vanish for inclusive quantities in the pole approximation. However, they become important, e.g., in invariant-mass distributions of the unstable particle.

Chapter 3

Lowest-order predictions for $\gamma\gamma \to 4f(\gamma)$

3.1 Analytical results for amplitudes in the Standard Model

3.1.1 Notation and conventions

We consider reactions of the types

$$\gamma(k_1,\lambda_1)+\gamma(k_2,\lambda_2) \to f_1(p_1,\sigma_1)+\bar{f}_2(p_2,\sigma_2)+f_3(p_3,\sigma_3)+\bar{f}_4(p_4,\sigma_4), \tag{3.1.1}$$
$$\gamma(k_1,\lambda_1)+\gamma(k_2,\lambda_2) \to f_1(p_1,\sigma_1)+\bar{f}_2(p_2,\sigma_2)+f_3(p_3,\sigma_3)+\bar{f}_4(p_4,\sigma_4)+\gamma(p_5,\sigma_5). \tag{3.1.2}$$

The arguments label the momenta k_i, p_j and helicities λ_k, σ_l (which take the values $\pm 1/2$ in the case of fermions and ± 1 in the case of photons) of the corresponding particles. We often use only the signs to denote the helicities. The fermion masses are neglected everywhere assuming that all mass singularities are avoided by appropriate phase-space cuts. In Section 4.3.2, however, we will restore the mass logarithms for non-collinear-safe observables.

For the Feynman rules we follow the conventions of Ref. [6]. We extend the usual linear gauge-fixing term (1.2.15) in the 't Hooft–Feynman gauge by a term that is non-linear in the gauge fields according to Refs. [18, 39, 40]. In this way the vertex $\gamma \mathrm{W}\phi$ vanishes, where ϕ are the would-be Goldstone bosons corresponding to the W bosons. Note that this also affects the gauge-boson couplings $\gamma\gamma\mathrm{WW}$ and $\gamma\mathrm{WW}$. The corresponding Feynman rules relevant for $\gamma\gamma \to 4f(\gamma)$ in lowest order can be found in Ref. [18]. Since we neglect fermion masses, the would-be Goldstone bosons do not couple to fermions and do not occur in the Feynman graphs of the SM amplitudes to $\gamma\gamma \to 4f(\gamma)$, which leads to a considerable reduction of the number of Feynman diagrams.

3.1.2 Classification of final states for $\gamma\gamma \to 4f(\gamma)$

The final states for $\gamma\gamma \to 4f$ and $\gamma\gamma \to 4f\gamma$ can be classified similarly to the processes $\mathrm{e^+e^-} \to 4f$ and $\mathrm{e^+e^-} \to 4f\gamma$ [18]. In the following, f and F are different fermions ($f \neq F$), and f' and F' denote their weak-isospin partners, respectively. We distinguish between states that are produced via charged-current (CC, corresponding to W bosons), via neutral-current (NC, corresponding to photons or Z bosons) interactions, or via both interaction types:

(i) CC reactions:

$\gamma\gamma \to f\bar{f}'F\bar{F}'$ (*CC31* family),

(ii) NC reactions:

(a) $\gamma\gamma \to f\bar{f}F\bar{F}$ (*NC40* family),
(b) $\gamma\gamma \to f\bar{f}f\bar{f}$ (*NC2·40* family),

(iii) Mixed CC/NC reactions:

$\gamma\gamma \to f\bar{f}f'\bar{f}'$ (*mix71* family).

The radiation of an additional photon does not change this classification. Following Ref. [41] we give the names of the process families in parentheses where the numbers correspond to the number of Feynman diagrams involved in unitary or non-linear gauge (for processes without neutrinos in the final state, not counting gluon-exchange diagrams).

Since the matrix elements depend on the colour structure of the final state, we further distinguish between leptonic, semi-leptonic, and hadronic final states. Keeping in mind that we neglect fermion masses, omitting four-neutrino final states, and suppressing reactions that are equivalent by CP symmetry we end up with 17 different representative processes which we have listed in Table 3.1.

Since the photons are polarized after Compton backscattering, final states that are flavour equivalent up to a CP transformation need not necessarily yield the same cross section if the convolution over a realistic photon beam spectrum is included. However, as we neglect fermion masses, this is only relevant for the semi-leptonic CC processes $\gamma\gamma \to \mathrm{e}^-\bar{\nu}_\mathrm{e}\mathrm{u}\bar{\mathrm{d}}(\gamma)$ and $\gamma\gamma \to \nu_\mathrm{e}\mathrm{e}^+\mathrm{d}\bar{\mathrm{u}}(\gamma)$.

3.1.3 Lowest-order amplitudes for $\gamma\gamma \to 4f$

3.1.3.1 Construction of matrix elements

The amplitudes for the processes $\gamma\gamma \to 4f$ are constructed by attaching the two incoming photons in all possible ways to the corresponding diagrams with four external fermions as shown in Figure 3.1. The matrix element of the generic diagram in Figure 3.1, where two fermion lines are linked by a gauge boson V, can be written as

$$\mathcal{M}^{\sigma_1\sigma_2\sigma_3\sigma_4}_{\lambda_1\lambda_2,V}(k_i,p_j,Q_j) = 4e^4\delta_{\sigma_1,-\sigma_2}\delta_{\sigma_3,-\sigma_4}\, g^{\sigma_1}_{V\bar{f}_1f_2}g^{\sigma_3}_{V\bar{f}_3f_4}A^{\sigma_1\sigma_3}_{\lambda_1\lambda_2,V}(k_i,p_j,Q_j), \qquad (3.1.3)$$

where k_i, p_j, and Q_j $(i=1,2; j=1,..,4)$ stand for the momenta and relative electric charges of the particles, respectively. The coupling factors g have been introduced in (1.2.18). For the gluon coupling we define

$$g^{\sigma}_{\mathrm{g}\bar{f}_if_i} = \frac{g_\mathrm{s}}{e}. \qquad (3.1.4)$$

final state	reaction type	$\gamma\gamma \to$
leptonic	CC	$\mathrm{e}^-\bar{\nu}_\mathrm{e}\nu_\mu\mu^+$
	NC(a)	$\mathrm{e}^-\mathrm{e}^+\nu_\mu\bar{\nu}_\mu$
		$\mathrm{e}^-\mathrm{e}^+\mu^-\mu^+$
	NC(b)	$\mathrm{e}^-\mathrm{e}^+\mathrm{e}^-\mathrm{e}^+$
	CC/NC	$\mathrm{e}^-\mathrm{e}^+\nu_\mathrm{e}\bar{\nu}_\mathrm{e}$
semi-leptonic	CC(c)	$\mathrm{e}^-\bar{\nu}_\mathrm{e}\mathrm{u}\bar{\mathrm{d}}$
	NC(a)	$\nu_\mathrm{e}\bar{\nu}_\mathrm{e}\mathrm{u}\bar{\mathrm{u}}$
		$\nu_\mathrm{e}\bar{\nu}_\mathrm{e}\mathrm{d}\bar{\mathrm{d}}$
		$\mathrm{e}^-\mathrm{e}^+\mathrm{u}\bar{\mathrm{u}}$
		$\mathrm{e}^-\mathrm{e}^+\mathrm{d}\bar{\mathrm{d}}$
hadronic	CC	$\mathrm{u}\bar{\mathrm{d}}\mathrm{s}\bar{\mathrm{c}}$
	NC(a)	$\mathrm{u}\bar{\mathrm{u}}\mathrm{c}\bar{\mathrm{c}}$
	NC(a)	$\mathrm{u}\bar{\mathrm{u}}\mathrm{s}\bar{\mathrm{s}}$
	NC(a)	$\mathrm{d}\bar{\mathrm{d}}\mathrm{s}\bar{\mathrm{s}}$
	NC(b)	$\mathrm{u}\bar{\mathrm{u}}\mathrm{u}\bar{\mathrm{u}}$
	NC(b)	$\mathrm{d}\bar{\mathrm{d}}\mathrm{d}\bar{\mathrm{d}}$
	CC/NC	$\mathrm{u}\bar{\mathrm{u}}\mathrm{d}\bar{\mathrm{d}}$

Table 3.1: Set of representative processes for $\gamma\gamma \to 4f(\gamma)$.

Quark mixing is neglected everywhere, i.e. we set the CKM matrix equal to the unit matrix. The auxiliary functions $A^{\sigma_1\sigma_3}_{\lambda_1\lambda_2,V}$ are calculated within the Weyl–van-der-Waerden (WvdW) formalism following the conventions of Ref. [42]. The WvdW spinor products are defined by

$$\langle pq\rangle = \epsilon^{AB} p_A q_B = 2\sqrt{p_0 q_0}\left(\mathrm{e}^{-\mathrm{i}\phi_p}\cos\frac{\theta_p}{2}\sin\frac{\theta_q}{2} - \mathrm{e}^{-\mathrm{i}\phi_q}\cos\frac{\theta_q}{2}\sin\frac{\theta_p}{2}\right), \tag{3.1.5}$$

where p_A, q_A are the associated momentum spinors for the momenta

$$\begin{aligned} p^\mu &= p_0(1, \sin\theta_p\cos\phi_p, \sin\theta_p\sin\phi_p, \cos\theta_p), \\ q^\mu &= q_0(1, \sin\theta_q\cos\phi_q, \sin\theta_q\sin\phi_q, \cos\theta_q). \end{aligned} \tag{3.1.6}$$

Moreover, we define the shorthands

$$\begin{aligned} \langle p_i P_k p_j\rangle &= p_{i,\dot{A}} P_k^{\dot{A}B} p_{j,B} = p_{i,\dot{A}} p_k^{\dot{A}} p_k^B p_{j,B} = \langle p_i p_k\rangle^* \langle p_j p_k\rangle, \\ \langle p_i [P_l + P_m] p_j\rangle &= \langle p_i P_l p_j\rangle + \langle p_i P_m p_j\rangle, \end{aligned} \tag{3.1.7}$$

where $p_{k,l,m}$ are light-like momenta, i.e., $p_k^2 = p_l^2 = p_m^2 = 0$. In the following, the denominators of the gauge-boson propagators are abbreviated by

$$P_V(p) = \frac{1}{p^2 - M_V^2}, \qquad V = \gamma, \mathrm{Z}, \mathrm{W}, \mathrm{g}, \qquad M_\gamma = M_\mathrm{g} = 0. \tag{3.1.8}$$

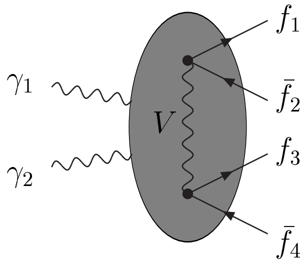

Figure 3.1: Generic diagram for the process $\gamma\gamma \to 4f$ where the photons γ_1, γ_2 couple to the fermions $f_1, \dots, \bar{f}_4$ and the gauge boson V in all possible ways.

The introduction of the finite width is described in Section 3.1.4 below.

The auxiliary functions $A^{\sigma_1\sigma_3}_{\lambda_1\lambda_2,V}$ explicitly read

$$
\begin{aligned}
A^{--}_{++,V}(k_i,p_j,Q_j) &= (\langle p_2p_4\rangle^*)^2 \\
\times \Bigg\{ &-Q_1^2 \frac{\langle p_1p_2\rangle^*\langle p_3p_4\rangle P_V(p_3+p_4)}{\langle k_1p_1\rangle^*\langle k_1p_2\rangle^*\langle k_2p_1\rangle^*\langle k_2p_2\rangle^*} - Q_1Q_3 \frac{(p_1+p_2-k_1)^2 P_V(p_1+p_2-k_1)}{\langle k_1p_1\rangle^*\langle k_1p_2\rangle^*\langle k_2p_3\rangle^*\langle k_2p_4\rangle^*} \\
&+ Q_3(Q_1-Q_2)P_V(p_1+p_2) \\
&\quad \times \left[\frac{-\langle p_2p_4\rangle^*\langle p_1p_2\rangle + \langle k_1p_4\rangle^*\langle k_1p_1\rangle M_V^2 P_V(p_1+p_2-k_1)}{\langle k_1p_2\rangle^*\langle k_1p_4\rangle^*\langle k_2p_3\rangle^*\langle k_2p_4\rangle^*} + (k_1 \leftrightarrow k_2)\right] \\
&+ (Q_1-Q_2)^2 P_V(p_1+p_2)P_V(p_3+p_4)\Bigg[-\langle p_2p_4\rangle^* \frac{\langle p_2p_4\rangle^*\langle p_1p_2\rangle\langle p_3p_4\rangle + M_V^2\langle p_1p_3\rangle}{2\langle k_1p_2\rangle^*\langle k_1p_4\rangle^*\langle k_2p_2\rangle^*\langle k_2p_4\rangle^*} \\
&\quad + M_V^2 P_V(p_1+p_2-k_1)\frac{\langle k_1p_1\rangle\langle k_2p_3\rangle}{\langle k_1p_2\rangle^*\langle k_2p_4\rangle^*}\Bigg] \\
+ \Big(&\{p_1,Q_1;p_2,Q_2\} \leftrightarrow \{p_3,Q_3;p_4,Q_4\}\Big)\Bigg\},
\end{aligned}
$$

$$
\begin{aligned}
A^{--}_{+-,V}(k_i,p_j,Q_j) &= Q_1^2 P_V(p_3+p_4)\frac{\langle p_2p_4\rangle^*\langle k_1p_1\rangle\langle k_2[P_2+P_4]p_3\rangle}{\langle k_1p_1\rangle^*\langle k_2p_1\rangle(p_2+p_3+p_4)^2} \\
&+ Q_2^2 P_V(p_3+p_4)\frac{\langle k_2p_2\rangle^*\langle p_1p_3\rangle\langle p_4[P_1+P_3]k_1\rangle}{\langle k_1p_2\rangle^*\langle k_2p_2\rangle(p_1+p_3+p_4)^2} \\
&+ Q_1Q_2 P_V(p_3+p_4)\frac{\langle p_2[K_1-P_1]p_3\rangle\langle p_4[K_1-P_3]p_1\rangle}{\langle k_1p_1\rangle^*\langle k_1p_2\rangle^*\langle k_2p_1\rangle\langle k_2p_2\rangle} \\
&+ (Q_2-Q_1)P_V(p_3+p_4)\frac{\langle p_2p_4\rangle^*\langle p_1p_3\rangle}{\langle k_1p_2\rangle^*\langle k_2p_1\rangle}\left[Q_2\frac{\langle p_4[K_1-P_3]p_1\rangle}{\langle k_1p_4\rangle^*\langle k_2p_2\rangle} + Q_1\frac{\langle p_2[K_1-P_1]p_3\rangle}{\langle k_1p_1\rangle^*\langle k_2p_3\rangle}\right] \\
&+ \frac{1}{2}(Q_2-Q_1)^2 P_V(p_1+p_2)P_V(p_3+p_4) \\
&\quad \times \frac{\langle p_2p_4\rangle^*\langle p_1p_3\rangle\Big(\langle p_2[K_1-P_1]p_3\rangle\langle p_4[K_1-P_3]p_1\rangle - M_V^2\langle p_2p_4\rangle^*\langle p_1p_3\rangle\Big)}{\langle k_1p_2\rangle^*\langle k_1p_4\rangle^*\langle k_2p_1\rangle\langle k_2p_3\rangle}
\end{aligned}
$$

$$
\begin{aligned}
&+ [-Q_1 + (Q_1 - Q_2) 2(k_1p_1) P_V(p_1+p_2)]\,[Q_4 + (Q_3 - Q_4) 2(k_2p_4) P_V(p_3+p_4)] \\
&\quad \times \frac{(\langle p_2[K_1 - P_1]p_3\rangle)^2 P_V(p_1+p_2-k_1)}{\langle k_1p_1\rangle^* \langle k_1p_2\rangle^* \langle k_2p_3\rangle \langle k_2p_4\rangle} \\
&+ \Bigl(\{p_1, Q_1; p_2, Q_2\} \leftrightarrow \{p_3, Q_3; p_4, Q_4\}\Bigr). \qquad (3.1.9)
\end{aligned}
$$

The other auxiliary functions $A^{\sigma_1\sigma_3}_{\lambda_1\lambda_2,V}$ follow from the relations

$$
\begin{aligned}
A^{-\sigma_1,\sigma_3}_{\lambda_1\lambda_2,V}(k_i, p_j, Q_j) &= \Bigl[A^{\sigma_1\sigma_3}_{\lambda_1\lambda_2,V}(k_i, p_j, Q_j)\Bigr]_{\{p_1,Q_1\} \leftrightarrow \{p_2,-Q_2\}}, \\
A^{\sigma_1,-\sigma_3}_{\lambda_1\lambda_2,V}(k_i, p_j, Q_j) &= \Bigl[A^{\sigma_1\sigma_3}_{\lambda_1\lambda_2,V}(k_i, p_j, Q_j)\Bigr]_{\{p_3,Q_3\} \leftrightarrow \{p_4,-Q_4\}}, \qquad (3.1.10)
\end{aligned}
$$

and

$$
A^{-\sigma_1,-\sigma_3}_{-\lambda_1,-\lambda_2,V}(k_i, p_j, Q_j) = \Bigl[A^{\sigma_1\sigma_3}_{\lambda_1\lambda_2,V}(k_i, p_j, Q_j)\Bigr]^*. \qquad (3.1.11)
$$

The last relation expresses a parity transformation. Note that the operation of complex conjugation in Eq. (3.1.11) must not affect the gauge-boson widths in the propagator functions P_V which will be introduced in Section 3.1.4.

The calculation of the helicity amplitudes for $\gamma\gamma \to 4f\gamma$ proceeds along the same lines. The result, however, is quite lengthy so that we do not write it down explicitly.

3.1.3.2 Squared amplitudes for leptonic and semi-leptonic final states

The result for leptonic and semi-leptonic final states follows immediately from the generic amplitude (3.1.3). The gauge boson cannot be a gluon in this case, and the sum over the colour degrees of freedom in the squared matrix elements trivially leads to the global factors $N^{\mathrm{c}}_{\mathrm{lept}} = 1$ and $N^{\mathrm{c}}_{\mathrm{semilept}} = 3$. Note that for NC diagrams the result for the amplitude is much simpler than for CC diagrams, since all terms in Eq. (3.1.9) involving a factor $(Q_1 - Q_2)$ or $(Q_3 - Q_4)$ drop out. Most of these terms originate from diagrams where a photon couples to a virtual W boson.

The explicit results for the colour-summed squared matrix elements read

$$
\sum_{\text{colour}} |\mathcal{M}_{\mathrm{CC}}|^2 = N^{\mathrm{c}} |\mathcal{M}_{\mathrm{W}}|^2, \qquad (3.1.12)
$$

$$
\sum_{\text{colour}} |\mathcal{M}_{\mathrm{NC(a)}}|^2 = N^{\mathrm{c}} \left|\mathcal{M}_{\mathrm{NC}}\right|^2, \qquad (3.1.13)
$$

$$
\sum_{\text{colour}} |\mathcal{M}_{\mathrm{NC(b)}}|^2 = N^{\mathrm{c}} \left|\mathcal{M}_{\mathrm{NC}} - [\mathcal{M}_{\mathrm{NC}}]_{\{p_1,Q_1,\sigma_1\} \leftrightarrow \{p_3,Q_3,\sigma_3\}}\right|^2, \qquad (3.1.14)
$$

$$
\sum_{\text{colour}} |\mathcal{M}_{\mathrm{CC/NC}}|^2 = N^{\mathrm{c}} \left|\mathcal{M}_{\mathrm{NC}} - [\mathcal{M}_{\mathrm{W}}]_{\{p_1,Q_1,\sigma_1\} \leftrightarrow \{p_3,Q_3,\sigma_3\}}\right|^2, \qquad (3.1.15)
$$

where we use the shorthand

$$
\mathcal{M}_{\mathrm{NC}} = \sum_{V=\gamma,\mathrm{Z}} \mathcal{M}_V \qquad (3.1.16)
$$

and suppress the helicity indices and the dependence on momenta and relative charges. The relative signs account for interchanging external fermion lines.

3.1.3.3 Squared amplitudes for hadronic final states

Next we consider purely hadronic final states, i.e., the cases where all final-state fermions are quarks. This renders the summation of the squared matrix elements over the colour degrees of freedom non-trivial, and in addition gluon-exchange diagrams appear. Since gluon-exchange diagrams require two quark–anti-quark pairs in the final state they do not appear in CC processes. For CC processes there is only one possibility for the colour flow, and the summation over the colour degrees of freedom leads to an overall factor $N^{\mathrm{c}}_{\mathrm{had,CC}} = 3^2 = 9$ to the squared matrix elements as given in Eq. (3.1.12).

For NC reactions we have to compute the sum of pure electroweak (ew) and gluon-exchange (QCD) matrix elements,

$$\mathcal{M}^{c_1c_2c_3c_4}_{\mathrm{had}} = \mathcal{M}^{c_1c_2c_3c_4}_{\mathrm{had,ew}} + \mathcal{M}^{c_1c_2c_3c_4}_{\mathrm{had,QCD}}, \tag{3.1.17}$$

where c_i denotes the colour indices of the quarks. The electroweak diagrams are diagonal in colour space and therefore read

$$\begin{aligned}
\mathcal{M}^{c_1c_2c_3c_4}_{\mathrm{NC(a),had,ew}} &= \mathcal{M}_{\mathrm{NC}}\delta_{c_1c_2}\delta_{c_3c_4}, \\
\mathcal{M}^{c_1c_2c_3c_4}_{\mathrm{NC(b),had,ew}} &= \mathcal{M}_{\mathrm{NC}}\delta_{c_1c_2}\delta_{c_3c_4} - [\mathcal{M}_{\mathrm{NC}}]_{\{p_1,Q_1,\sigma_1\}\leftrightarrow\{p_3,Q_3,\sigma_3\}}\, \delta_{c_3c_2}\delta_{c_1c_4}.
\end{aligned} \tag{3.1.18}$$

The gluon-exchange diagrams are obtained from the generic formula (3.1.3) by inserting the corresponding generators, $\lambda^a/2$, of the gauge group SU(3),

$$\begin{aligned}
\mathcal{M}^{c_1c_2c_3c_4}_{\mathrm{NC(a),had,QCD}} &= \mathcal{M}_{\mathrm{g}}\frac{1}{4}\lambda^a_{c_1c_2}\lambda^a_{c_3c_4}, \\
\mathcal{M}^{c_1c_2c_3c_4}_{\mathrm{NC(b),had,QCD}} &= \mathcal{M}_{\mathrm{g}}\frac{1}{4}\lambda^a_{c_1c_2}\lambda^a_{c_3c_4} - [\mathcal{M}_{\mathrm{g}}]_{\{p_1,Q_1,\sigma_1\}\leftrightarrow\{p_3,Q_3,\sigma_3\}}\, \frac{1}{4}\lambda^a_{c_3c_2}\lambda^a_{c_1c_4}.
\end{aligned} \tag{3.1.19}$$

The matrix element $\mathcal{M}_{\mathrm{g}}$ is defined by Eq. (3.1.3) with $V = \mathrm{g}$.

Carrying out the colour sum using the completeness relation for the Gell-Mann matrices,

$$\lambda^a_{ij}\lambda^a_{kl} = -\frac{2}{3}\delta_{ij}\delta_{kl} + 2\delta_{il}\delta_{jk}, \tag{3.1.20}$$

yields

$$\begin{aligned}
\sum_{\mathrm{colour}} |\mathcal{M}_{\mathrm{NC(a),had}}|^2 &= 9|\mathcal{M}_{\mathrm{NC}}|^2 + 2|\mathcal{M}_{\mathrm{g}}|^2, \\
\sum_{\mathrm{colour}} |\mathcal{M}_{\mathrm{NC(b),had}}|^2 &= 9|\mathcal{M}_{\mathrm{NC}}|^2 + 9\left|[\mathcal{M}_{\mathrm{NC}}]_{\{p_1,Q_1,\sigma_1\}\leftrightarrow\{p_3,Q_3,\sigma_3\}}\right|^2 + 2|\mathcal{M}_{\mathrm{g}}|^2 \\
&\quad + 2\left|[\mathcal{M}_{\mathrm{g}}]_{\{p_1,Q_1,\sigma_1\}\leftrightarrow\{p_3,Q_3,\sigma_3\}}\right|^2 - 6\,\mathrm{Re}\left\{\mathcal{M}_{\mathrm{NC}}\,[\mathcal{M}^*_{\mathrm{NC}}]_{\{p_1,Q_1,\sigma_1\}\leftrightarrow\{p_3,Q_3,\sigma_3\}}\right\} \\
&\quad + \frac{4}{3}\,\mathrm{Re}\left\{\mathcal{M}_{\mathrm{g}}\left[\mathcal{M}^*_{\mathrm{g}}\right]_{\{p_1,Q_1,\sigma_1\}\leftrightarrow\{p_3,Q_3,\sigma_3\}}\right\} - 8\,\mathrm{Re}\left\{\mathcal{M}_{\mathrm{NC}}\left[\mathcal{M}^*_{\mathrm{g}}\right]_{\{p_1,Q_1,\sigma_1\}\leftrightarrow\{p_3,Q_3,\sigma_3\}}\right\} \\
&\quad - 8\,\mathrm{Re}\left\{\mathcal{M}_{\mathrm{g}}\,[\mathcal{M}^*_{\mathrm{NC}}]_{\{p_1,Q_1,\sigma_1\}\leftrightarrow\{p_3,Q_3,\sigma_3\}}\right\}.
\end{aligned} \tag{3.1.21}$$

All squared matrix elements of this section have been compared numerically with results obtained with the program MADGRAPH [43] at several phase-space points, and perfect agreement has been found.

3.1.4 Implementation of finite gauge-boson widths

We have implemented the finite widths of the W- and Z-boson propagators[1] in four different ways:

- *fixed width* in all propagators:

$$P_V(p) = \frac{1}{p^2 - M_V^2 + \mathrm{i}M_V\Gamma_V}, \tag{3.1.22}$$

- *step width* (fixed width in time-like propagators):

$$P_V(p) = \frac{1}{p^2 - M_V^2 + \mathrm{i}M_V\Gamma_V\theta(p^2)}, \tag{3.1.23}$$

- *running width* in time-like propagators:

$$P_V(p) = \frac{1}{p^2 - M_V^2 + \mathrm{i}p^2(\Gamma_V/M_V)\theta(p^2)}, \tag{3.1.24}$$

- *complex-mass scheme* [18]: complex gauge-boson masses are used everywhere, i.e. $\sqrt{M_V^2 - \mathrm{i}M_V\Gamma_V}$ instead of M_V in all propagators and couplings. This results in a constant width in all propagators,

$$P_V(p) = \frac{1}{p^2 - M_V^2 + \mathrm{i}M_V\Gamma_V}, \tag{3.1.25}$$

  and in a complex weak mixing angle

$$c_{\mathrm{w}}^2 = 1 - s_{\mathrm{w}}^2 = \frac{M_{\mathrm{W}}^2 - \mathrm{i}M_{\mathrm{W}}\Gamma_{\mathrm{W}}}{M_{\mathrm{Z}}^2 - \mathrm{i}M_{\mathrm{Z}}\Gamma_{\mathrm{Z}}}. \tag{3.1.26}$$

The virtues and drawbacks of the first three schemes were mentioned in Section 2.3 and are discussed in more detail in Ref. [25]. All but the complex-mass scheme, in general, violate SU(2) gauge invariance, the step- and the running-width schemes also violate electromagnetic $\mathrm{U(1)_{em}}$ gauge invariance, which is preserved by using a fixed width. As known from many examples in $\mathrm{e^+e^-}$ physics [18, 25, 26], gauge-invariance-violating effects, in particular when enhanced by factors p^2/M_V^2 as in the running-width scheme, can lead to totally wrong results. Furthermore, the violation of $\mathrm{U(1)_{em}}$ gauge invariance also causes a dependence of matrix elements and cross sections on the gauge chosen for external photons. In $\mathrm{e^+e^-} \to 4f$ and $\mathrm{e^+e^-} \to 6f$ this problem does not occur since no external photons are involved.

---

[1] We have also supplemented the explicit gauge-boson masses appearing in the numerators of Eq. (3.1.9) by the corresponding widths, because these mass terms originate from denominators upon combining different diagrams.

The complex-mass scheme, which was introduced in Ref. [18] for tree-level calculations, preserves gauge invariance and thus all Ward identities which rule gauge cancellations. Its application is particularly simple for $\gamma\gamma \to 4f(\gamma)$ in the non-linear gauge. In this case, no couplings involving explicit gauge-boson masses appear, and it is sufficient to introduce the finite gauge-boson widths in the propagators [cf. Eq. (3.1.25)] and to introduce the complex weak mixing angle (3.1.26) in the couplings.

For CC processes $\gamma\gamma \to 4f(\gamma)$ with massless fermions, the fixed-width (FW) approach in the non-linear gauge and the complex-mass scheme (CMS) are practically equivalent, because all Feynman graphs are proportional to e^4/s_w^2 (e^5/s_w^2) and gauge-boson masses appear only in propagator denominators. In this case the corresponding amplitudes in the two schemes differ only in the global factor $s^2_\mathrm{w,FW}/s^2_\mathrm{w,CMS}$, where $s_\mathrm{w,FW}$ and $s_\mathrm{w,CMS}$ are the values of s_w in the different schemes, i.e., $s_\mathrm{w,FW}$ is derived from the ratio of real gauge-boson masses and $s_\mathrm{w,CMS}$ from complex masses. Thus, both squared amplitudes are gauge invariant and are equal up to the factor $|s_\mathrm{w,FW}/s_\mathrm{w,CMS}|^4$ which is equal to 1 up to terms of $\mathcal{O}(\Gamma_\mathrm{W}^2/M_\mathrm{W}^2)$.

For NC and CC/NC processes a similar reasoning can be used to show that the fixed-width approach does not violate gauge invariance in $\gamma\gamma \to 4f(\gamma)$ for massless fermions. The trick is to apply the above argument to gauge-invariant subsets of diagrams. For NC diagrams with photon exchange, which is the (gauge-invariant) QED subset of diagrams (Figure 3.1 with $V = \gamma$), there is nothing to show. The sum of NC diagrams of type NC(a) with Z-boson exchange (Figure 3.1 with $V = \mathrm{Z}$) again involves c_w and s_w only in a global coupling factor (per helicity channel); the remaining dependence on the gauge-boson masses is located in the propagator denominators. Thus, the subamplitudes of the fixed-width and the complex-mass scheme are again identical up to a global factor and both preserve gauge invariance and Ward identities. For NC processes of type NC(b) a second class of diagrams exists (Figure 3.1 with $V = \gamma, \mathrm{Z}$ and external fermions interchanged). This new class of diagrams forms a gauge-invariant subset because of the different flow of fermion numbers. Thus, the reasoning for type NC(a) applies to both classes of diagrams of NC(b) reactions. The same argument is also valid for the subset of CC diagrams in mixed CC/NC reactions.

In summary, we have argued that the use of naive fixed gauge-boson widths does not lead to gauge-invariance violations in amplitudes for $\gamma\gamma \to 4f(\gamma)$ as long as fermions are massless and the non-linear gauge with vanishing $\gamma\mathrm{W}\phi$ coupling (or the complex W-boson mass in this coupling if the 't Hooft–Feynman gauge is chosen) is used. The corresponding squared amplitudes agree with the ones of the (gauge-invariant) complex-mass scheme up to terms of $\mathcal{O}(\Gamma_\mathrm{W}/M_\mathrm{W})$, for CC processes even up to terms of $\mathcal{O}(\Gamma_\mathrm{W}^2/M_\mathrm{W}^2)$.

3.1.5 W-pair signal diagrams and double-pole approximation

The diagrams to CC and CC/NC processes comprise graphs with two, one, or no internal W-boson lines that can become resonant, similar to the situation for $\mathrm{e}^+\mathrm{e}^- \to \mathrm{WW} \to 4f$ (see Refs. [44, 45] and references therein). It is interesting to investigate the possibility to define an amplitude for the W-pair signal based on doubly-resonant contributions only, because such an amplitude is much simpler than the full amplitudes for four-fermion production and is universal (up to colour factors) for all relevant $4f$ final states. Moreover, this study is an important exercise for the calculation of radiative corrections to $\gamma\gamma \to \mathrm{WW} \to 4f$ in the double-pole approximation (DPA), which is done in the next chapter. Taking simply all doubly-resonant diagrams, of course, yields a result that is not gauge invariant. Nevertheless in the $\mathrm{e}^+\mathrm{e}^-$ case the lowest-order cross section based on such a gauge-dependent amplitude (defined in the 't Hooft–Feynman gauge), known as "CC03 cross section", is a very useful quantity that is very close to the full $4f$ calculation if both W bosons are close to resonance. The CC03 amplitude can be rendered gauge invariant upon deforming the momenta of the four outgoing fermions in such a way that the intermediate W-boson states become on shell, because the residues of the W resonances are gauge-invariant quantities. This "on-shell projection" is part of the pole expansion (2.4.1) and is needed in the construction of the DPA. The definition of the "on-shell projection" involves some freedom, and different versions, which have been described in Refs. [20, 22], differ by contributions of relative order $\mathcal{O}(\Gamma_\mathrm{W}/M_\mathrm{W})$, which is the uncertainty of the DPA for leading-order predictions.

We want to perform the exercise to study the usefulness of a possible "CC03"[2] off-shell cross section for $\gamma\gamma \to \mathrm{WW} \to 4f$. To this end, we define the amplitude for the off-shell W-pair signal by evaluating the three W-pair diagrams in the non-linear gauge with polarization vectors $\varepsilon_i(k_i)$ for the incoming photons, which obey the gauge conditions

$$\varepsilon_1(k_1)\cdot k_2 = \varepsilon_2(k_2)\cdot k_1 = 0. \tag{3.1.27}$$

In terms of WvdW spinors, this means that the gauge spinors g_1 and g_2 of the photons are identified with the spinors of the momenta k_2 and k_1, respectively. With this choice the auxiliary functions for the matrix elements (3.1.3) read

$$\begin{aligned}
A^{--}_{++,\mathrm{WW}}(k_i,p_j,Q_j) &= P_\mathrm{W}(p_1+p_2)P_\mathrm{W}(p_3+p_4)\frac{\langle p_2p_4\rangle^*}{\langle k_1k_2\rangle^*}\\
&\times\Biggl\{\Bigl[P_\mathrm{W}(p_1+p_2-k_1)\Bigr]_{\Gamma_\mathrm{W}=0}\Bigl[\langle k_2p_1\rangle\langle k_2p_3\rangle\langle k_2[P_1+P_2]k_1\rangle+\langle k_1p_1\rangle\langle k_1p_3\rangle\langle k_1[P_3+P_4]k_2\rangle\\
&\qquad+\frac{\langle p_1p_3\rangle}{\langle k_1k_2\rangle^*}\langle k_2[P_1+P_2]k_1\rangle\langle k_1[P_3+P_4]k_2\rangle-2(k_1\cdot k_2)\langle k_1p_1\rangle\langle k_2p_3\rangle\Bigr]\\
&\quad-\frac{1}{2}\langle p_1p_3\rangle\langle k_1k_2\rangle\Biggr\}+(k_1\leftrightarrow k_2),\\
A^{--}_{+-,\mathrm{WW}}(k_i,p_j,Q_j) &= P_\mathrm{W}(p_1+p_2)P_\mathrm{W}(p_3+p_4)\\
&\times\Bigl[P_\mathrm{W}(p_1+p_2-k_1)+P_\mathrm{W}(p_1+p_2-k_2)\Bigr]_{\Gamma_\mathrm{W}=0}\\
&\times\Biggl\{\langle k_2[P_1+P_2]k_1\rangle\Biggl[\frac{\langle k_2p_2\rangle^*\langle k_2p_4\rangle^*\langle p_1p_3\rangle}{\langle k_1k_2\rangle^*}-\frac{\langle p_2p_4\rangle^*\langle k_1p_1\rangle\langle k_1p_3\rangle}{\langle k_1k_2\rangle}\Biggr]\\
&\quad-\frac{\langle p_2p_4\rangle^*\langle p_1p_3\rangle}{2(k_1k_2)}\langle k_2[P_1+P_2]k_1\rangle^2+\langle k_2p_2\rangle^*\langle k_2p_4\rangle^*\langle k_1p_1\rangle\langle k_1p_3\rangle\Biggr\}.
\end{aligned}\tag{3.1.28}$$

---

[2] The name also fits to the $\gamma\gamma$ case where three W-pair diagrams exist in unitary or non-linear gauge.

Note that $A^{\sigma_1\sigma_3}_{\lambda_1\lambda_2,\mathrm{WW}}$ do not coincide with the parts of the functions $A^{\sigma_1\sigma_3}_{\lambda_1\lambda_2,\mathrm{W}}$ of Eq. (3.1.9) that are proportional to $P_\mathrm{W}(p_1+p_2)P_\mathrm{W}(p_3+p_4)$ because the derivation of Eq. (3.1.9) involves rearrangements of various singly-resonant contributions. We point out that the definition (3.1.28) is neither independent of the gauge fixing used to define gauge-boson propagators nor of the gauge of the external photons. The definition is gauge invariant after the outgoing fermion momenta p_i are on-shell projected as described above, while leaving the resonant propagators $P_\mathrm{W}(p_1+p_2)P_\mathrm{W}(p_3+p_4)$ untouched. This defines the lowest-order amplitude in DPA. Finally, we stress that the t- and u-channel W propagators in Eq. (3.1.28) do not receive a finite W width; otherwise the gauge invariance of the DPA would be spoiled.

3.2 Inclusion of anomalous gauge-boson couplings

In this section we introduce the most important anomalous gauge-boson couplings accessible by the process $\gamma\gamma\to 4f$ and give explicit analytical results for the corresponding helicity amplitudes.

3.2.1 The effective Lagrangians

First we consider anomalous triple gauge-boson couplings (ATGC) in the charged-current sector, i.e., anomalous γWW and the related $\gamma\gamma$WW couplings. Instead of using rather general parametrizations of non-standard couplings [46], we follow the approach already used at LEP2 to reduce the number of free parameters by requiring that all symmetries of the SM are respected. From the resulting operators we only keep those that appear in the lowest-order cross section of $\gamma\gamma\to 4f$. Specifically, we start from the gauge-invariant CP-conserving effective Lagrangian with dimension-6 operators [47]

$$\begin{aligned}\mathcal{L}^{\mathrm{ATGC}}_{\mathrm{CC}} = {} & \mathrm{i}g_Y\frac{\alpha_{\mathrm{B}\phi}}{M_\mathrm{W}^2}(D_\mu\Phi)^\dagger B^{\mu\nu}(D_\nu\Phi) - \mathrm{i}g_W\frac{\alpha_{\mathrm{W}\phi}}{M_\mathrm{W}^2}(D_\mu\Phi)^\dagger\boldsymbol{\sigma}\cdot\mathbf{W}^{\mu\nu}(D_\nu\Phi) \\ & -g_W\frac{\alpha_\mathrm{W}}{6M_\mathrm{W}^2}\mathbf{W}^\mu{}_\nu\cdot(\mathbf{W}^\nu{}_\rho\times\mathbf{W}^\rho{}_\mu),\end{aligned} \tag{3.2.1}$$

where Φ is the Higgs doublet field and

$$\begin{aligned} B^{\mu\nu} &= \partial^\mu B^\nu - \partial^\nu B^\mu, \\ \mathbf{W}^{\mu\nu} &= (W_1^{\mu\nu}, W_2^{\mu\nu}, W_3^{\mu\nu}) = \partial^\mu\mathbf{W}^\nu - \partial^\nu\mathbf{W}^\mu + g_W\mathbf{W}^\mu\times\mathbf{W}^\nu \end{aligned} \tag{3.2.2}$$

are the field strengths of the U(1) and SU(2) gauge fields, respectively. The Pauli matrices are combined into the vector $\boldsymbol{\sigma}=(\sigma_1,\sigma_2,\sigma_3)$, and the parameters g_Y, g_W denote the gauge couplings.[3] Inserting the vacuum expectation value of the Higgs field Φ, we can relate the coefficients $\alpha_{\mathrm{B}\phi}$, $\alpha_{\mathrm{W}\phi}$, and α_W to the coefficients of the Lagrangian considered in the LEP2 analysis [47],

$$\Delta g_1^\mathrm{Z} = \frac{\alpha_{\mathrm{W}\phi}}{c_\mathrm{w}^2}, \qquad \Delta\kappa_\gamma = -\frac{c_\mathrm{w}^2}{s_\mathrm{w}^2}(\Delta\kappa_\mathrm{Z}-\Delta g_1^\mathrm{Z}) = \alpha_{\mathrm{W}\phi}+\alpha_{\mathrm{B}\phi}, \qquad \lambda_\gamma=\lambda_\mathrm{Z}=\alpha_\mathrm{W}. \tag{3.2.3}$$

---

[3] In order to be compatible with the conventions of Ref. [6] used for the SM amplitudes above, we had to change the sign of the SU(2) coupling g_W w.r.t. Ref. [47].

In contrast to the pure anomalous γWW coupling [46], the SU(2)×U(1) symmetry of the effective Lagrangian (3.2.1) induces additional anomalous $\gamma\gamma$WW and $\gamma \mathrm{W}\phi$ couplings. The corresponding Feynman rules are

$$\begin{aligned}
\mathrm{i}\Gamma^{\gamma \mathrm{W}^+\mathrm{W}^-}_{\mu\nu\rho}(k_0,k_+,k_-) ={}& -\mathrm{i}e\biggl\{\Delta\kappa_\gamma(k_{0\nu}g_{\mu\rho}-k_{0\rho}g_{\mu\nu}) \\
&-\frac{\lambda_\gamma}{M_\mathrm{W}^2}\Bigl[k_{+\mu}k_{-\nu}k_{0\rho}-k_{-\mu}k_{+\rho}k_{0\nu}+g_{\nu\rho}(k_{-\mu}(k_+k_0)-k_{+\mu}(k_-k_0)) \\
&\quad+g_{\mu\rho}(k_{0\nu}(k_+k_-)-k_{-\nu}(k_+k_0))+g_{\mu\nu}(k_{+\rho}(k_-k_0)-k_{0\rho}(k_+k_-))\Bigr]\biggr\},
\end{aligned}$$

$$\begin{aligned}
\mathrm{i}\Gamma^{\gamma\gamma \mathrm{W}^+\mathrm{W}^-}_{\mu\nu\rho\sigma}(k_1,k_2,k_+,k_-) ={}& -\mathrm{i}e^2\frac{\lambda_\gamma}{M_\mathrm{W}^2}\biggl\{g_{\mu\nu}g_{\rho\sigma}(k_1+k_2)^2+g_{\mu\rho}g_{\nu\sigma}(k_2k_++k_1k_-) \\
&+g_{\nu\rho}g_{\mu\sigma}(k_1k_++k_2k_-)+g_{\mu\nu}\Bigl[(k_1+k_2)_\rho k_{+\sigma}+(k_1+k_2)_\sigma k_{-\rho}\Bigr] \\
&+g_{\rho\sigma}\Bigl[(k_++k_-)_\mu k_{1\nu}+(k_++k_-)_\nu k_{2\mu}\Bigr]+g_{\mu\rho}\Bigl[(k_1-k_2)_\sigma k_{+\nu}-k_{1\nu}k_{+\sigma}-k_{1\sigma}k_{-\nu}\Bigr] \\
&+g_{\mu\sigma}\Bigl[(k_1-k_2)_\rho k_{-\nu}-k_{1\nu}k_{-\rho}-k_{1\rho}k_{+\nu}\Bigr]+g_{\nu\rho}\Bigl[(k_2-k_1)_\sigma k_{+\mu}-k_{2\mu}k_{+\sigma}-k_{2\sigma}k_{-\mu}\Bigr] \\
&+g_{\nu\sigma}\Bigl[(k_2-k_1)_\rho k_{-\mu}-k_{2\mu}k_{-\rho}-k_{2\rho}k_{+\mu}\Bigr]\biggr\},
\end{aligned}$$

$$\mathrm{i}\Gamma^{\gamma \mathrm{W}\phi}_{\mu\nu}(k_0,k_\mathrm{W},k_\phi) = -\mathrm{i}e\frac{\Delta\kappa_\gamma}{M_\mathrm{W}}\Bigl\{(k_\phi k_0)g_{\mu\nu}-k_{\phi,\mu}k_{0,\nu}\Bigr\}, \tag{3.2.4}$$

where all fields and momenta are considered incoming. Note that the neglect of the contribution to the quartic coupling $\gamma\gamma$WW, which is proportional to λ_γ, would lead to a violation of electromagnetic gauge invariance in predictions for $\gamma\gamma \to \mathrm{WW}(\to 4f)$. In contrast, neglecting the $\gamma \mathrm{W}\phi$ coupling, which is proportional to $\Delta\kappa_\gamma$, would not spoil the electromagnetic gauge invariance of the predictions.

Next we consider anomalous triple gauge-boson couplings involving only the neutral gauge bosons γ and Z. Assuming Lorentz invariance and electromagnetic gauge invariance, the most general effective dimension-6 Lagrangian for $\gamma\gamma$Z, γZZ, and ZZZ couplings can be written as [48][4]

$$\begin{aligned}
\mathcal{L}^\mathrm{ATGC}_\mathrm{NC} ={}& \frac{e}{M_\mathrm{Z}^2}\Bigl\{[f_4^\gamma(\partial_\mu F^{\mu\nu})-f_4^\mathrm{Z}(\partial_\mu Z^{\mu\nu})]Z_{\nu\rho}Z^\rho+[f_5^\gamma(\partial_\mu F^{\mu\nu})-f_5^\mathrm{Z}(\partial_\mu Z^{\mu\nu})]\tilde{Z}_{\nu\rho}Z^\rho \\
&+[h_1^\gamma(\partial_\mu F^{\mu\nu})-h_1^\mathrm{Z}(\partial_\mu Z^{\mu\nu})]F_{\nu\rho}Z^\rho+[h_3^\gamma(\partial_\mu F^{\mu\nu})-h_3^\mathrm{Z}(\partial_\mu Z^{\mu\nu})]\tilde{F}_{\nu\rho}Z^\rho\Bigr\}
\end{aligned} \tag{3.2.5}$$

with the abelian field-strength tensors

$$F^{\mu\nu}=\partial^\mu A^\nu-\partial^\nu A^\mu, \qquad Z^{\mu\nu}=\partial^\mu Z^\nu-\partial^\nu Z^\mu, \tag{3.2.6}$$

and the dual field-strength tensors ($\epsilon^{0123}=+1$)

$$\tilde{F}^{\mu\nu}=\frac{1}{2}\epsilon^{\mu\nu\rho\sigma}F_{\rho\sigma}, \qquad \tilde{Z}^{\mu\nu}=\frac{1}{2}\epsilon^{\mu\nu\rho\sigma}Z_{\rho\sigma}. \tag{3.2.7}$$

---

[4] Note that our conventions differ from those of Ref. [48] by a minus sign in the Z-boson field.

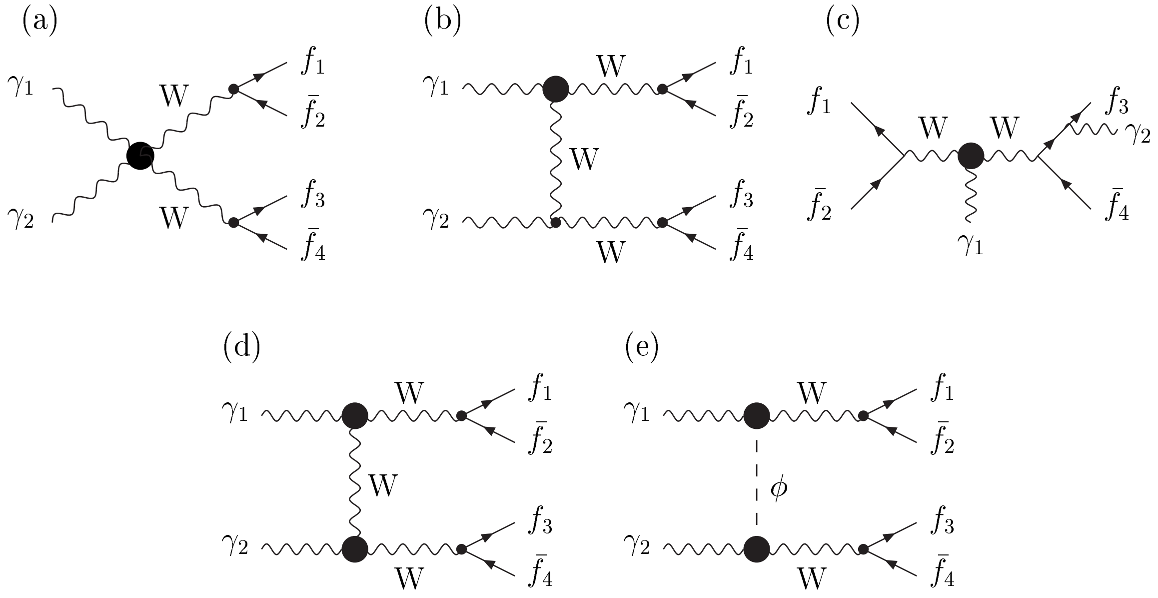

Figure 3.2: Representative diagrams with anomalous γWW and $\gamma\gamma$WW couplings (black blobs) contributing to CC processes $\gamma\gamma \to 4f$.

An operator inducing a $\gamma\gamma\gamma$ coupling does not appear in Eq. (3.2.5) since it violates electromagnetic gauge invariance.

Apart from the $\gamma\gamma$WW coupling which is induced by symmetries in the Lagrangian (3.2.1), we also include genuine anomalous quartic gauge-boson couplings (AQGC) in our analysis, whose lowest dimension is 6. In Refs. [49, 50] all genuine dimension-6 AQGC that involve photons and that are allowed by electromagnetic gauge invariance and custodial $\mathrm{SU}(2)_\mathrm{c}$ have been classified; more general AQGC have been discussed in Ref. [51]. Following Ref. [50] we use the effective Lagrangian

$$\mathcal{L}^{\mathrm{AQGC}}_{\gamma\gamma VV} = -\frac{e^2}{16\Lambda^2}\Big\{a_0\, F^{\mu\nu}F_{\mu\nu}\overline{\mathbf{W}}_\alpha\overline{\mathbf{W}}^\alpha + a_\mathrm{c}\, F^{\mu\alpha}F_{\mu\beta}\overline{\mathbf{W}}^\beta\overline{\mathbf{W}}_\alpha + \tilde{a}_0\, F^{\mu\nu}\tilde{F}_{\mu\nu}\overline{\mathbf{W}}_\alpha\overline{\mathbf{W}}^\alpha\Big\} \quad (3.2.8)$$

with the definition

$$\overline{\mathbf{W}}_\mu = \left(\overline{W}^1_\mu, \overline{W}^2_\mu, \overline{W}^3_\mu\right) = \left(\frac{1}{\sqrt{2}}(W^+ + W^-)_\mu, \frac{\mathrm{i}}{\sqrt{2}}(W^+ - W^-)_\mu, \frac{1}{c_\mathrm{w}}Z_\mu\right). \quad (3.2.9)$$

The scale of new physics, Λ, is introduced in Eq. (3.2.8) to render the coupling coefficients $a_0, a_\mathrm{c}, \tilde{a}_0$ dimensionless. The effective Lagrangian $\mathcal{L}^{\mathrm{AQGC}}_{\gamma\gamma VV}$ contains $\gamma\gamma$WW and $\gamma\gamma$ZZ couplings, whose Feynman rules can be found in Ref. [50]. The other coupling structures $\mathcal{L}_\mathrm{n}$ and $\tilde{\mathcal{L}}_\mathrm{n}$ considered in Ref. [50] induce γZWW couplings that are not relevant for $\gamma\gamma \to 4f$.

3.2.2 Amplitudes with triple gauge-boson couplings

Before we write down the helicity amplitudes including ATGC explicitly, we discuss the impact of these couplings w.r.t. the SM cross section. The diagrams containing ATGC and the corresponding quartic couplings in CC diagrams are shown in Figure 3.2. We quantify the size of the anomalous contributions in terms of powers of anomalous coupling factors (generically denoted by a_3) or suppression factors $\Gamma_\mathrm{W}/M_\mathrm{W}$. Considering the SM process $\gamma\gamma \to \mathrm{WW} \to 4f$ as the leading contribution, i.e., regarding anomalous-coupling effects as small, we get non-standard contributions to CC and CC/NC cross sections from CC ATGC of the following orders:

- $\mathcal{O}(a_3)$:
  The matrix elements of diagrams (a) and (b) in Figure 3.2 involve one power of a_3. Both diagrams are not suppressed by $\Gamma_\mathrm{W}/M_\mathrm{W}$ since they are doubly resonant.

- $\mathcal{O}(a_3\Gamma_\mathrm{W}/M_\mathrm{W})$:
  The diagram (c) of Figure 3.2 has one power of a_3 and one resonant W-boson propagator, i.e., it is only singly resonant. Thus, it is of $\mathcal{O}(a_3\Gamma_\mathrm{W}/M_\mathrm{W})$.

- $\mathcal{O}(a_3^2)$:
  The diagrams (d) and (e) of Figure 3.2 involve two anomalous couplings a_3 and are doubly resonant. Therefore, they are of $\mathcal{O}(a_3^2)$. Note that the squares of the diagrams (a) and (b), as well as their products with one another, are of the same order as the interference of diagrams (d) and (e) with the SM amplitude.

There are no diagrams containing CC ATGC for NC processes.

Next we consider the impact of NC ATGC, as defined in the effective Lagrangian (3.2.5). The by far largest SM cross sections of the process class $\gamma\gamma \to 4f$ belong to diagrams with two resonant W bosons in CC and CC/NC reactions. Thus, the largest effect of NC ATGC could be expected from an interference of "anomalous diagrams" with the SM amplitude for CC or CC/NC processes. The only candidate of this kind is a diagram where an off-shell s-channel Z boson is produced by an anomalous $\gamma\gamma\mathrm{Z}$ coupling that subsequently produces a W-boson pair. However, the effective $\gamma\gamma\mathrm{Z}$ coupling of Eq. (3.2.5) vanishes for two on-shell photons, so that this diagram does not contribute. No other CC diagram exists that includes a NC ATGC.

We now turn to the effects of NC ATGC in NC amplitudes, i.e., in diagrams without W bosons. The corresponding SM amplitudes involve at most a single resonance of the Z boson, which leads already to a suppression of NC cross sections w.r.t. CC cross sections by a factor $(\Gamma_\mathrm{Z}/M_\mathrm{Z})^2$. This suppression is clearly visible in the numerical results presented in Section 3.5.2.1 below. Diagrams with one NC ATGC also possess at most one resonant Z boson and, therefore, show a suppression by a factor $a_3(\Gamma_\mathrm{Z}/M_\mathrm{Z})^2$ w.r.t. the CC signal diagrams. This suppression is not changed by interferences with doubly-resonant CC diagrams in CC/NC processes because the Z- and W-boson resonances are located at different regions in phase space and do not enhance each other. Diagrams with two NC ATGC can involve two Z-boson resonances resulting in a suppression of $\mathcal{O}(a_3^2\Gamma_\mathrm{Z}/M_\mathrm{Z})$, which is also small compared to the CC case owing to the squared ATGC. In summary, we conclude that the sensitivity of the processes $\gamma\gamma \to 4f$ to NC ATGC is much smaller than to CC ATGC. Therefore, we restrict our investigation on ATGC to CC couplings in the following.

As explained above, the diagrams of Figure 3.2 induce contributions to the amplitude that are either linear or quadratic in the CC ATGC. We give the explicit contributions to the helicity amplitudes in a way similar to the SM case (3.1.3),

$$\mathcal{M}^{\sigma_1\sigma_2\sigma_3\sigma_4}_{\lambda_1\lambda_2,\mathrm{CCATGC}}(k_i,p_j,Q_j) = e^4\delta_{\sigma_1,-}\delta_{\sigma_2,+}\delta_{\sigma_3,-}\delta_{\sigma_4,+}\, g^-_{\mathrm{W}\bar{f}_1f_2}g^-_{\mathrm{W}\bar{f}_3f_4}\,\delta_3A^{\sigma_1\sigma_3}_{\lambda_1\lambda_2}(k_i,p_j,Q_j) \qquad (3.2.10)$$

with the auxiliary functions $\delta_3A^{\sigma_1\sigma_3}_{\lambda_1\lambda_2}$. The generic amplitude $\mathcal{M}^{\sigma_1\sigma_2\sigma_3\sigma_4}_{\lambda_1\lambda_2,\mathrm{CCATGC}}$ is coherently added to the SM amplitude $\mathcal{M}^{\sigma_1\sigma_2\sigma_3\sigma_4}_{\lambda_1\lambda_2,\mathrm{W}}$ of Eq. (3.1.3). The colour summation of the squared amplitudes for the various process types proceeds as described in Sections 3.1.3.2 and 3.1.3.3.

The terms in $\delta_3A^{\sigma_1\sigma_3}_{\lambda_1\lambda_2}$ that are quadratic and linear in ATGC explicitly read

$$\begin{aligned}
\delta_3A^{--}_{++}\Big|_{\mathrm{quad}} &= -P_{\mathrm{W}}(p_1+p_2)P_{\mathrm{W}}(p_3+p_4)P_{\mathrm{W}}(p_1+p_2-k_1)\langle k_1p_1\rangle\langle k_2p_3\rangle \\
&\times\Bigg\{\Delta\kappa_\gamma^2\Big[\langle p_2p_4\rangle^*\langle k_1k_2\rangle+\frac{1}{2M_{\mathrm{W}}^2}\langle p_1p_2\rangle^*\langle p_3p_4\rangle^*\langle k_1p_1\rangle\langle k_2p_3\rangle\Big] \\
&\quad+\Delta\kappa_\gamma\frac{\lambda_\gamma}{M_{\mathrm{W}}^2}\Big[\langle p_1p_2\rangle^*\langle p_3p_4\rangle^*\Big(\langle k_1p_3\rangle\langle k_2p_1\rangle-\langle k_1k_2\rangle\langle p_1p_3\rangle\Big) \\
&\quad+\langle k_1k_2\rangle\Big(\langle p_3p_4\rangle^*\langle k_1p_2\rangle^*\langle k_1p_3\rangle-\langle p_1p_2\rangle^*\langle k_2p_4\rangle^*\langle k_2p_1\rangle\Big)\Big] \\
&\quad+\frac{\lambda_\gamma^2}{M_{\mathrm{W}}^4}\langle p_1p_2\rangle^*\langle p_3p_4\rangle^*\frac{1}{2}(p_1+p_2-k_1)^2\Big[\langle k_1p_3\rangle\langle k_2p_1\rangle-\langle k_1k_2\rangle\langle p_1p_3\rangle\Big]\Bigg\} \\
&+(k_1\leftrightarrow k_2),
\end{aligned}$$

$$\begin{aligned}
\delta_3A^{--}_{+-}\Big|_{\mathrm{quad}} &= -P_{\mathrm{W}}(p_1+p_2)P_{\mathrm{W}}(p_3+p_4)P_{\mathrm{W}}(p_1+p_2-k_1)\langle k_2p_4\rangle^*\langle k_1p_1\rangle \\
&\times\Bigg\{-\Delta\kappa_\gamma^2\Big[\langle k_2p_2\rangle^*\langle k_1p_3\rangle+\frac{1}{2M_{\mathrm{W}}^2}\langle p_1p_2\rangle^*\langle k_2p_4\rangle^*\langle k_1p_1\rangle\langle p_3p_4\rangle\Big] \\
&\quad+\Delta\kappa_\gamma\frac{\lambda_\gamma}{M_{\mathrm{W}}^2}\Big[-2(p_1+p_2-k_1)^2\langle k_2p_2\rangle^*\langle k_1p_3\rangle \\
&\qquad+\langle p_2[K_2-K_1]p_3\rangle\langle k_2[P_1+P_2]k_1\rangle-\langle p_1p_2\rangle^*\langle k_2p_4\rangle^*\langle p_3p_4\rangle\langle k_1p_1\rangle\Big] \\
&\quad+\frac{\lambda_\gamma^2}{M_{\mathrm{W}}^4}\langle p_1p_2\rangle^*\langle p_3p_4\rangle\Big[-\frac{1}{2}(p_1+p_2-k_1)^2\langle k_2p_4\rangle^*\langle k_1p_1\rangle \\
&\qquad+\langle p_4[K_2-P_3]k_1\rangle\langle k_2[K_1-P_2]p_1\rangle\Big]\Bigg\} \\
&+\Big(\{p_1,Q_1;p_2,Q_2\}\leftrightarrow\{p_3,Q_3;p_4,Q_4\}\Big),
\end{aligned}$$

$$\begin{aligned}
\delta_3A^{--}_{++}\Big|_{\mathrm{lin}} &= 2P_{\mathrm{W}}(p_1+p_2)P_{\mathrm{W}}(p_3+p_4)\langle k_2p_1\rangle\langle k_2p_3\rangle \\
&\times\frac{\langle p_2p_4\rangle^*}{\langle k_1p_2\rangle^*\langle k_1p_4\rangle^*}\Big[\Delta\kappa_\gamma\langle p_2p_4\rangle^*-\frac{\lambda_\gamma}{M_{\mathrm{W}}^2}\langle p_3p_4\rangle^*\langle p_1p_2\rangle^*\langle p_1p_3\rangle\Big] \\
&+\Big\{2(Q_4-Q_3)\left[-Q_1+(Q_1-Q_2)2(k_1p_1)P_{\mathrm{W}}(p_1+p_2)\right]P_{\mathrm{W}}(p_3+p_4)
\end{aligned}$$

$$
\begin{aligned}
&\times P_{\mathrm{W}}(p_3+p_4-k_2)\frac{\langle k_2p_3\rangle\langle p_2[P_1-K_1]k_2\rangle}{\langle k_1p_1\rangle^*\langle k_1p_2\rangle^*}\\
&\times\left[\Delta\kappa_\gamma\langle p_2p_4\rangle^*+\frac{\lambda_\gamma}{M_{\mathrm{W}}^2}\langle p_3p_4\rangle^*\langle p_2[P_4-K_2]p_3\rangle\right]\\
&+\Big(\{p_1,Q_1;p_2,Q_2\}\leftrightarrow\{p_3,Q_3;p_4,Q_4\}\Big)\Bigg\}+(k_1\leftrightarrow k_2),
\end{aligned}
$$

$$
\begin{aligned}
\delta_3 A^{--}_{+-}\Big|_{\mathrm{lin}} ={}& -2P_{\mathrm{W}}(p_1+p_2)P_{\mathrm{W}}(p_3+p_4)\langle p_1p_3\rangle\frac{\langle k_1p_1\rangle\langle k_1p_3\rangle}{\langle k_2p_1\rangle\langle k_2p_3\rangle}\\
&\times\left[-\Delta\kappa_\gamma\langle p_2p_4\rangle^*+\frac{\lambda_\gamma}{M_{\mathrm{W}}^2}\Big(\langle p_1p_2\rangle^*\langle k_2p_4\rangle^*\langle k_2p_1\rangle-\langle p_3p_4\rangle^*\langle k_2p_2\rangle^*\langle k_2p_3\rangle\right.\\
&\qquad\left.+\langle p_1p_2\rangle^*\langle p_3p_4\rangle^*\langle p_1p_3\rangle\Big)\right]\\
&-\Bigg\{2(Q_1-Q_2)P_{\mathrm{W}}(p_1+p_2)\Big[[Q_4+(Q_3-Q_4)2(k_2p_4)P_{\mathrm{W}}(p_3+p_4)]\\
&\qquad\times P_{\mathrm{W}}(p_1+p_2-k_1)\frac{\langle k_1p_1\rangle\langle k_1p_3\rangle}{\langle k_2p_3\rangle\langle k_2p_4\rangle}\Big(-\Delta\kappa_\gamma\langle p_2[P_4-K_2]p_3\rangle\\
&\qquad\quad+\frac{\lambda_\gamma}{M_{\mathrm{W}}^2}\langle p_1p_2\rangle^*\langle p_1p_3\rangle(p_3+p_4-k_2)^2\Big)\Big]\\
&\qquad+\Big(\{p_1,Q_1;p_2,Q_2\}\leftrightarrow\{p_3,Q_3;p_4,Q_4\}\Big)\Bigg\}\\
&+\Big(\text{c.c. and }\{p_1,Q_1;p_3,Q_3;k_1\}\leftrightarrow\{p_2,Q_2;p_4,Q_4;k_2\}\Big),
\end{aligned}
\tag{3.2.11}
$$

where "c.c. and $\{\ldots\}\leftrightarrow\{\ldots\}$" indicates that the complex conjugate of the preceding expression has to be added after some substitutions. The auxiliary functions for the remaining polarizations follow from the relations (3.1.10) and (3.1.11).

In order to check our results, we have implemented the ATGC of the effective Lagrangian (3.2.1) into the program MADGRAPH [43] and compared our amplitudes with the MADGRAPH results for various phase-space points. We found perfect numerical agreement.

3.2.3 Amplitudes with genuine quartic gauge-boson couplings

Figure 3.3 shows the only diagram with an AQGC (generically denoted by a_4) that contributes to $\gamma\gamma\to 4f$. For CC processes the "anomalous diagram" contributes in $\mathcal{O}(a_4)$ to the cross section, because it is (as the SM contribution) doubly resonant. For NC processes, the diagram involves one power of a_4 and two Z-boson resonances and interferes with the singly-resonant SM amplitude. In this case, the contribution to the corresponding cross section is suppressed by $a_4\Gamma_{\mathrm{Z}}/M_{\mathrm{Z}}$ w.r.t. CC cross sections, i.e., the suppression factor involves one factor in the anomalous coupling or in $\Gamma_{\mathrm{Z}}/M_{\mathrm{Z}}$ less than we counted for NC ATGC. In the following we take both CC and NC AQGC into account.

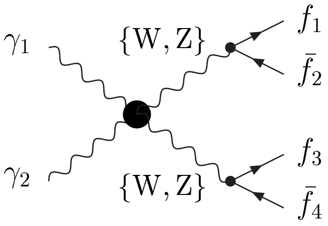

Figure 3.3: Diagram with AQGC (black blob) contributing to $\gamma\gamma \to 4f$.

The AQGC contributions to the amplitudes read

$$\begin{aligned}\mathcal{M}^{\sigma_1\sigma_2\sigma_3\sigma_4}_{\lambda_1\lambda_2,\gamma\gamma VV} = {} & \frac{e^4}{8\Lambda^2}\delta_{\sigma_1,-\sigma_2}\delta_{\sigma_3,-\sigma_4}\, g_{\gamma\gamma VV}\, g^{\sigma_1}_{V\bar{f}_1 f_2} g^{\sigma_3}_{V\bar{f}_3 f_4} P_V(p_1+p_2)P_V(p_3+p_4) \\ & \times \delta_4 A^{\sigma_1\sigma_3}_{\lambda_1\lambda_2}(k_1,k_2,p_1,p_2,p_3,p_4) \qquad (3.2.12)\end{aligned}$$

with

$$g_{\gamma\gamma\mathrm{WW}} = 1, \qquad g_{\gamma\gamma\mathrm{ZZ}} = \frac{1}{c_\mathrm{w}^2} \qquad (3.2.13)$$

and

$$\begin{aligned}\delta_4 A^{--}_{++}(k_1,k_2,p_1,p_2,p_3,p_4) &= (4a_0 - 4\mathrm{i}\tilde{a}_0 + a_\mathrm{c})\langle p_2 p_4\rangle^* \langle k_1 k_2\rangle^2 \langle p_1 p_3\rangle, \\ \delta_4 A^{--}_{+-}(k_1,k_2,p_1,p_2,p_3,p_4) &= -2a_\mathrm{c}\langle k_2 p_2\rangle^* \langle k_2 p_4\rangle^* \langle k_1 p_1\rangle \langle k_1 p_3\rangle. \qquad (3.2.14)\end{aligned}$$

The remaining auxiliary functions $\delta_4 A^{\sigma_1\sigma_3}_{\lambda_1\lambda_2}$ can be obtained via the substitutions

$$\begin{aligned}\delta_4 A^{\sigma_1,+}_{\lambda_1\lambda_2}(k_1,k_2,p_1,p_2,p_3,p_4) &= \delta_4 A^{\sigma_1,-}_{\lambda_1\lambda_2}(k_1,k_2,p_1,p_2,p_4,p_3), \\ \delta_4 A^{+,\sigma_3}_{\lambda_1\lambda_2}(k_1,k_2,p_1,p_2,p_3,p_4) &= \delta_4 A^{-,\sigma_3}_{\lambda_1\lambda_2}(k_1,k_2,p_2,p_1,p_3,p_4), \\ \delta_4 A^{\sigma_1\sigma_3}_{\lambda_1\lambda_2}(k_1,k_2,p_1,p_2,p_3,p_4) &= \Big(\delta_4 A^{-\sigma_1,-\sigma_3}_{-\lambda_1,-\lambda_2}(k_1,k_2,p_1,p_2,p_3,p_4)\Big)^*. \qquad (3.2.15)\end{aligned}$$

The generic amplitude $\mathcal{M}^{\sigma_1\sigma_2\sigma_3\sigma_4}_{\lambda_1\lambda_2,\gamma\gamma VV}$ is coherently added to the SM amplitude $\mathcal{M}^{\sigma_1\sigma_2\sigma_3\sigma_4}_{\lambda_1\lambda_2,V}$ of Eq. (3.1.3) for $V = \mathrm{W},\mathrm{Z}$, respectively. The colour summation of the squared amplitudes for the various process types proceeds as in the SM case.

Again we have checked the amplitudes against results obtained with MADGRAPH, as explained at the end of the previous section.

3.3 Effective $\gamma\gamma$H coupling and Higgs resonance

In order to incorporate a possible Higgs resonance in $\gamma\gamma \to \mathrm{H} \to VV \to 4f$ with $V = \mathrm{W},\mathrm{Z}$, as depicted in Figure 3.4, we consider an effective coupling of the Higgs boson to two photons. In the SM this coupling is mediated via fermion (mainly top-quark) and W-boson loops. We define the effective Lagrangian for the $\gamma\gamma$H vertex [52] by

$$\mathcal{L}_{\gamma\gamma\mathrm{H}} = -\frac{g_{\gamma\gamma\mathrm{H}}}{4} F^{\mu\nu} F_{\mu\nu} \frac{H}{v}, \qquad (3.3.1)$$

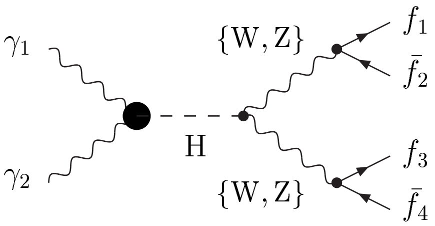

Figure 3.4: Diagram with effective $\gamma\gamma$H coupling (black blob).

where $v = 2M_W s_w/e$ is the vacuum expectation value of the Higgs field H. Up to normalization, $\mathcal{L}_{\gamma\gamma\mathrm{H}}$ is the lowest-dimensional, CP-conserving, electromagnetically gauge-invariant operator for two photons and the scalar field H. The corresponding Feynman rule reads

$$\mathrm{i}\Gamma^{\gamma\gamma\mathrm{H}}_{\mu\nu}(k_1,k_2,k_\mathrm{H}) = \frac{\mathrm{i}g_{\gamma\gamma\mathrm{H}}}{v}\left[g_{\mu\nu}(k_1k_2) - k_{1,\nu}k_{2,\mu}\right], \tag{3.3.2}$$

where k_1, k_2 are the incoming photon momenta. Comparing this Feynman rule to the loop-induced SM vertex with the external fields on shell, which has, e.g., been given in Refs. [39, 52], we obtain

$$\begin{aligned} g_{\gamma\gamma\mathrm{H}}\Big|_{\mathrm{SM}} = \frac{\alpha}{\pi}\Bigg\{ & \frac{6M_\mathrm{W}^2}{M_\mathrm{H}^2} + 1 + \frac{6M_\mathrm{W}^2}{M_\mathrm{H}^2}(2M_\mathrm{W}^2 - M_\mathrm{H}^2)C_0(M_\mathrm{H}, M_\mathrm{W}) \\ & - 2\sum_f N_f^\mathrm{c} Q_f^2 \frac{m_f^2}{M_\mathrm{H}^2}\left[2 + (4m_f^2 - M_\mathrm{H}^2)C_0(M_\mathrm{H}, m_f)\right]\Bigg\}, \end{aligned} \tag{3.3.3}$$

where the colour factor N_f^c in the sum over all fermions f is equal to 3 for quarks and 1 for leptons. The scalar 3-point integral C_0 is given by

$$C_0(M_\mathrm{H}, m) = \frac{1}{2M_\mathrm{H}^2}\ln^2\left(\frac{\beta_m + 1}{\beta_m - 1}\right), \qquad \beta_m = \sqrt{1 - \frac{4m^2}{M_\mathrm{H}^2} + \mathrm{i}0}. \tag{3.3.4}$$

The complete matrix elements for the diagrams with a Higgs resonance (as shown in Figure 3.4) can then be written as

$$\begin{aligned} \mathcal{M}^{\sigma_1\sigma_2\sigma_3\sigma_4}_{\lambda_1\lambda_2,HVV} = & -\frac{e^4}{2s_\mathrm{w}^2}\,\delta_{\sigma_1,-\sigma_2}\delta_{\sigma_3,-\sigma_4}\, g_{\gamma\gamma\mathrm{H}}\, g_{\gamma\gamma VV}\, g^{\sigma_1}_{V\bar{f}_1f_2} g^{\sigma_3}_{V\bar{f}_3f_4} P_V(p_1+p_2)P_V(p_3+p_4) \\ & \times M_\mathrm{H}^2 P_\mathrm{H}(k_1+k_2)\,\delta_\mathrm{H}A^{\sigma_1\sigma_3}_{\lambda_1\lambda_2}(k_1,k_2,p_1,p_2,p_3,p_4) \end{aligned} \tag{3.3.5}$$

with $g_{\gamma\gamma VV}$ defined in Eq. (3.2.13) and

$$\delta_\mathrm{H}A^{--}_{++}(k_1,k_2,p_1,p_2,p_3,p_4) = \frac{\langle k_1k_2\rangle}{\langle k_1k_2\rangle^*}\langle p_2p_4\rangle^*\langle p_1p_3\rangle, \qquad \delta_\mathrm{H}A^{\sigma_1\sigma_3}_{\pm\mp} = 0. \tag{3.3.6}$$

The other expressions for $\delta_\mathrm{H}A^{\sigma_1\sigma_3}_{\lambda_1\lambda_2}$ follow in the same way as described in Eq. (3.2.15) for $\delta_4A^{\sigma_1\sigma_3}_{\lambda_1\lambda_2}$. The width in the Higgs-boson propagator P_H is introduced in the same way as in Section 3.1.4 for the gauge bosons.

3.4 Phase-space integration and convolution over the photon spectrum

The squared matrix element is integrated over the phase space following the strategy described in Refs. [18, 26, 53], where the multi-channel Monte Carlo technique [54] was applied. This method cures problems that occur due to the very complex peaking structure of the integrand induced by various diagram types. More precisely, appropriate mappings of the pseudo-random numbers into the momenta of the outgoing particles are constructed and combined in such a way that the integrand is widely smoothened everywhere. The details are presented in App. A.

The convolution over the photon spectrum is given by

$$\mathrm{d}\sigma = \int_0^1 \mathrm{d}x_1 \int_0^1 \mathrm{d}x_2 \, f_\gamma(x_1)\, f_\gamma(x_2)\, \mathrm{d}\sigma_{\gamma\gamma}(x_1 P_1, x_2 P_2), \tag{3.4.1}$$

where $\mathrm{d}\sigma_{\gamma\gamma}$ is the differential $\gamma\gamma$ cross section. The function $f_\gamma(x_i)$ denotes the probability density for obtaining a photon with momentum $k_i = x_i P_i$, and P_i is the electron momentum before Compton backscattering. In order to reduce the statistical error of this integration we use a simple way of stratified sampling. The integration region for x_i of each photon spectrum is divided into a fixed number of bins. We choose bin i with a probability α_i and divide the corresponding weight by α_i. In this way the integration remains formally unchanged if we normalize $\sum_i \alpha_i = 1$. The parameters α_i can be used to improve the convergence of the numerical integration. By choosing the α_i proportional to the cross section of the corresponding bin i, more events are sampled in regions where the photon spectrum is large. Care has to be taken that the α_i do not become too small because this might lead to rare events with very large weights that render the error estimate unreliable. This optimization typically reduces the Monte Carlo integration error by a factor 2–5.

3.5 Numerical results

3.5.1 Input parameters

We use the following set of input parameters [55]:

$$\begin{aligned}
M_\mathrm{W} &= 80.423\,\mathrm{GeV}, & \Gamma_\mathrm{W} &= 2.118\,\mathrm{GeV},\\
M_\mathrm{Z} &= 91.1876\,\mathrm{GeV}, & \Gamma_\mathrm{Z} &= 2.4952\,\mathrm{GeV},\\
M_\mathrm{H} &= 170\,\mathrm{GeV}, & \Gamma_\mathrm{H} &= 0.3834\,\mathrm{GeV},\\
\alpha(0) &= 1/137.03599976, & \alpha_\mathrm{s} &= 0.1172,\\
G_\mu &= 1.16639 \times 10^{-5}\,\mathrm{GeV}^{-2}, & &
\end{aligned} \tag{3.5.1}$$

where the Higgs mass is chosen well above the W-pair threshold so that intermediate Higgs bosons decay rapidly into W pairs; the corresponding decay width Γ_H has been obtained with the program HDECAY [56].

Furthermore, we apply the separation cuts

$$\begin{array}{llll} E_\gamma > 10\,\mathrm{GeV}, & \theta(\gamma,\mathrm{beam}) > 5^\circ, & \theta(l,\gamma) > 5^\circ, & \theta(q,\gamma) > 5^\circ, \\ E_l > 10\,\mathrm{GeV}, & \theta(l,\mathrm{beam}) > 5^\circ, & \theta(l,l') > 5^\circ, & \theta(l,q) > 5^\circ, \\ E_q > 10\,\mathrm{GeV}, & \theta(q,\mathrm{beam}) > 5^\circ, & m(q,q') > 10\,\mathrm{GeV}, & \end{array} \tag{3.5.2}$$

where q and l denote quarks and charged leptons, respectively, and $m(q,q')$ is the invariant mass of an outgoing quark pair. The energies E_X and angles $\theta(X,Y)$ are defined in the laboratory frame. Using these cuts all infrared, i.e., soft or collinear, singularities are removed from the phase space.

In order to account for leading universal corrections, we use two different values for the coupling constant $\alpha = e^2/(4\pi)$. Since on-shell photons couple to charged particles with the coupling constant $\alpha(0)$ (effective electromagnetic coupling at zero-momentum transfer), we take this coupling for each external photon in the processes $\gamma\gamma \to 4f$ and $\gamma\gamma \to 4f\gamma$. For CC reactions, the remaining couplings correspond to $\mathrm{W}f\bar{f}$ vertices. For these vertices a large part of the electroweak radiative corrections [57] (the running of the electromagnetic coupling and the universal corrections related to the ρ parameter) are absorbed into an effective electromagnetic coupling α_{G_μ} which is derived from the Fermi constant G_μ by

$$\alpha_{G_\mu} = \frac{\sqrt{2}G_\mu M_\mathrm{W}^2 s_\mathrm{w}^2}{\pi}. \tag{3.5.3}$$

Therefore, in the following numerical studies, we replace α^4 by $\alpha(0)^2\alpha_{G_\mu}^2$ for the processes $\gamma\gamma \to 4f$ and α^5 by $\alpha(0)^3\alpha_{G_\mu}^2$ for $\gamma\gamma \to 4f\gamma$.

For the evaluation of the photon spectrum we use the program CompAZ [14] with the polarization of the laser beams -1 (i.e. photon helicity -1)[5] and the polarization of the electron beams $+0.85$. This choice for the relative signs in the polarizations yields a sharper peak at the upper end of the photon spectrum. Results for monochromatic photon beams are shown for unpolarized photons if not stated otherwise.

The results are obtained in the fixed-width scheme, except from Section 3.5.2.5, where we compare different schemes.

The numerical integration over the phase space is carried out applying the multi-channel Monte Carlo technique as described in App. A. We use 10^7 events leading to a runtime of our Monte Carlo program on a PC with 2 GHz that varies from 30 minutes to 6 hours depending on the considered process.

3.5.2 Results for integrated cross sections

3.5.2.1 Survey of cross sections

In order to illustrate the reliability of our Monte Carlo generator we compare our results on cross sections for a representative set of the processes $\gamma\gamma \to 4f$ and $\gamma\gamma \to 4f\gamma$ with the results obtained with the Monte Carlo program Whizard (version 1.28)

---

[5] Internally in CompAZ the polarization of the laser light is defined as the negative of the photon helicity.

	present work		Whizard/Madgraph	
$\gamma\gamma \to$	$\sigma_{4f}[\,\mathrm{fb}]$	$\sigma_{4f}[\,\mathrm{fb}](\mathrm{conv})$	$\sigma_{4f}[\,\mathrm{fb}]$	$\sigma_{4f}[\,\mathrm{fb}](\mathrm{conv})$
$\mathrm{e}^-\bar{\nu}_\mathrm{e}\nu_\mu\mu^+$	826.47(21)	190.87(10)	826.39(26)	191.05(16)
$\mathrm{e}^-\mathrm{e}^+\nu_\mu\bar{\nu}_\mu$	1.75460(62)	0.90525(61)	1.75518(78)	0.9050(11)
$\mathrm{e}^-\mathrm{e}^+\mu^-\mu^+$	19.400(33)	19.129(61)	19.342(21)	19.188(48)
$\mathrm{e}^-\mathrm{e}^+\mathrm{e}^-\mathrm{e}^+$	9.469(17)	9.357(32)	9.453(11)	9.383(25)
$\mathrm{e}^-\mathrm{e}^+\nu_\mathrm{e}\bar{\nu}_\mathrm{e}$	828.34(21)	191.72(10)	828.29(26)	191.55(17)
$\mathrm{e}^-\bar{\nu}_\mathrm{e}\mathrm{u}\bar{\mathrm{d}}$	2351.11(68)	565.05(33)	2351.79(84)	565.07(51)
$\nu_\mathrm{e}\mathrm{e}^+\mathrm{d}\bar{\mathrm{u}}$	2350.84(68)	558.39(32)	2353.21(84)	558.41(50)
$\nu_\mathrm{e}\bar{\nu}_\mathrm{e}\mathrm{u}\bar{\mathrm{u}}$	1.19761(50)	0.61256(50)	1.19684(57)	0.61083(71)
$\nu_\mathrm{e}\bar{\nu}_\mathrm{e}\mathrm{d}\bar{\mathrm{d}}$	0.095981(44)	0.049092(45)	0.096011(48)	0.049118(57)
$\mathrm{e}^-\mathrm{e}^+\mathrm{u}\bar{\mathrm{u}}$	14.036(21)	10.597(26)	14.016(15)	10.574(21)
$\mathrm{e}^-\mathrm{e}^+\mathrm{d}\bar{\mathrm{d}}$	4.7406(29)	2.6614(32)	4.7377(28)	2.6651(38)
$\mathrm{u}\bar{\mathrm{d}}\mathrm{s}\bar{\mathrm{c}}$	6659.6(2.1)	1603.8(1.0)	6663.5(2.7)	1605.0(1.5)
$\mathrm{u}\bar{\mathrm{u}}\mathrm{c}\bar{\mathrm{c}}$	10.469(14)	6.111(12)	10.4531(88)	6.113(10)
with QCD	1543.6(2.9)	1071.3(2.9)	—	—
$\mathrm{u}\bar{\mathrm{u}}\mathrm{s}\bar{\mathrm{s}}$	3.3282(21)	1.6569(18)	3.3310(20)	1.6595(23)
with QCD	412.97(75)	288.79(72)	—	—
$\mathrm{d}\bar{\mathrm{d}}\mathrm{s}\bar{\mathrm{s}}$	0.49807(29)	0.23232(24)	0.49804(30)	0.23252(32)
with QCD	96.34(18)	66.80(18)	—	—
$\mathrm{u}\bar{\mathrm{u}}\mathrm{u}\bar{\mathrm{u}}$	5.1846(69)	3.0298(57)	5.1900(45)	3.0419(53)
with QCD	772.6(1.5)	538.9(1.4)	—	—
$\mathrm{d}\bar{\mathrm{d}}\mathrm{d}\bar{\mathrm{d}}$	0.24683(15)	0.11581(12)	0.24665(17)	0.11579(17)
with QCD	48.252(96)	33.685(88)	—	—
$\mathrm{u}\bar{\mathrm{u}}\mathrm{d}\bar{\mathrm{d}}$	6663.5(2.3)	1606.1(1.1)	6664.8(2.8)	1604.6(1.6)
with QCD	7075.8(3.7)	1896.4(2.9)	—	—

Table 3.2: Total cross sections for $\gamma\gamma \to 4f$ at $\sqrt{s} = 500\,\mathrm{GeV}$ for various final states with and without convolution over the photon spectrum.

	present work		WHIZARD/MADGRAPH	
$\gamma\gamma \to$	$\sigma_{4f\gamma}$[fb]	$\sigma_{4f\gamma}$[fb](conv)	$\sigma_{4f\gamma}$[fb]	$\sigma_{4f\gamma}$[fb](conv)
$\mathrm{e}^-\bar{\nu}_\mathrm{e}\nu_\mu\mu^+\gamma$	39.234(44)	6.188(11)	39.218(29)	6.2040(87)
$\mathrm{e}^-\mathrm{e}^+\nu_\mu\bar{\nu}_\mu\gamma$	0.10157(10)	0.028612(40)	0.101556(88)	0.028548(52)
$\mathrm{e}^-\mathrm{e}^+\mu^-\mu^+\gamma$	1.0567(35)	0.5083(28)	1.0547(20)	0.5091(29)
$\mathrm{e}^-\mathrm{e}^+\mathrm{e}^-\mathrm{e}^+\gamma$	0.5085(18)	0.2433(13)	0.5091(10)	0.2461(12)
$\mathrm{e}^-\mathrm{e}^+\nu_\mathrm{e}\bar{\nu}_\mathrm{e}\gamma$	39.301(46)	6.213(11)	39.332(30)	6.2069(89)
$\mathrm{e}^-\bar{\nu}_\mathrm{e}\mathrm{u}\bar{\mathrm{d}}\gamma$	96.61(13)	14.216(27)	96.575(75)	14.159(21)
$\nu_\mathrm{e}\mathrm{e}^+\mathrm{d}\bar{\mathrm{u}}\gamma$	96.60(13)	15.459(30)	96.520(76)	15.429(22)
$\nu_\mathrm{e}\bar{\nu}_\mathrm{e}\mathrm{u}\bar{\mathrm{u}}\gamma$	0.030818(35)	0.008640(14)	0.030756(28)	0.008609(16)
$\nu_\mathrm{e}\bar{\nu}_\mathrm{e}\mathrm{d}\bar{\mathrm{d}}\gamma$	0.00061753(75)	0.00017313(31)	0.00061731(56)	0.00017358(34)
$\mathrm{e}^-\mathrm{e}^+\mathrm{u}\bar{\mathrm{u}}\gamma$	0.6446(17)	0.25463(99)	0.6477(10)	0.2579(10)
$\mathrm{e}^-\mathrm{e}^+\mathrm{d}\bar{\mathrm{d}}\gamma$	0.26653(36)	0.08137(17)	0.26689(28)	0.08166(21)
$\mathrm{u}\bar{\mathrm{d}}\mathrm{s}\bar{\mathrm{c}}\gamma$	229.86(36)	32.621(81)	229.52(19)	32.531(49)
$\mathrm{u}\bar{\mathrm{u}}\mathrm{c}\bar{\mathrm{c}}\gamma$	0.30556(69)	0.10718(34)	0.30563(47)	0.10836(43)
with QCD	34.73(14)	13.801(77)	—	—
$\mathrm{u}\bar{\mathrm{u}}\mathrm{s}\bar{\mathrm{s}}\gamma$	0.08791(13)	0.026278(59)	0.087935(98)	0.026271(65)
with QCD	6.362(23)	2.493(13)	—	—
$\mathrm{d}\bar{\mathrm{d}}\mathrm{s}\bar{\mathrm{s}}\gamma$	0.0046253(71)	0.0014842(37)	0.0046191(52)	0.0014832(36)
with QCD	0.5427(22)	0.2165(11)	—	—
$\mathrm{u}\bar{\mathrm{u}}\mathrm{u}\bar{\mathrm{u}}\gamma$	0.15081(33)	0.05301(16)	0.15082(21)	0.05332(16)
with QCD	17.377(71)	6.964(35)	—	—
$\mathrm{d}\bar{\mathrm{d}}\mathrm{d}\bar{\mathrm{d}}\gamma$	0.0022893(37)	0.0007421(21)	0.0022878(25)	0.0007398(18)
with QCD	0.2716(11)	0.10863(53)	—	—
$\mathrm{u}\bar{\mathrm{u}}\mathrm{d}\bar{\mathrm{d}}\gamma$	229.86(40)	32.85(15)	229.65(19)	32.518(51)
with QCD	236.31(42)	35.14(11)	—	—

Table 3.3: Total cross sections for $\gamma\gamma \to 4f\gamma$ at $\sqrt{s} = 500\,\mathrm{GeV}$ for various final states with and without convolution over the photon spectrum.

[58] which uses the matrix-element generator MADGRAPH [43][6]. In Tables 3.2 and 3.3 we list the results for the 17 different final states defined in Table 3.1. The numbers in parentheses correspond to the Monte Carlo error. For the final states that can be produced via intermediate gluons we compute the cross section both with and without gluon-exchange contributions. Since the version of MADGRAPH implemented in WHIZARD is not able to deal with interferences of electroweak and QCD diagrams, we give only the pure electroweak WHIZARD/MADGRAPH results for these processes. Furthermore, we list the corresponding cross sections with and without convolution over the photon beam spectrum. For this study, we have implemented the program COMPAZ into WHIZARD.

As explained in Section 3.1.2, the cross sections for the CP-equivalent final states $\mathrm{e}^-\bar{\nu}_\mathrm{e}\mathrm{u}\bar{\mathrm{d}}(\gamma)$ and $\nu_\mathrm{e}\mathrm{e}^+\mathrm{d}\bar{\mathrm{u}}(\gamma)$ are not identical if the convolution over the photon beam spectrum is carried out. Therefore, we give results for both final states. In all other cases, the cross sections for a given final state and for the CP-conjugated one coincide.

CC and CC/NC processes possess the largest cross sections because of the dominance of W-pair production. The convolution over the photon spectrum reduces these cross sections significantly since low-energy photons cannot produce on-shell W pairs. NC processes are affected less, and in some cases, such as $\gamma\gamma \to \mathrm{e}^+\mathrm{e}^-\mu^+\mu^-$, the cross section is only slightly reduced. Owing to the colour factors of the quarks, hadronic and semi-leptonic cross sections differ by roughly a factor 3, hadronic and leptonic cross sections by roughly a factor $3^2 = 9$. For CC processes $\gamma\gamma \to 4f$ we obtain a rough estimate of the cross sections by multiplying the cross section of $\gamma\gamma \to \mathrm{WW}$ with the branching ratios of the W bosons into leptons or quarks depending on the final state. Note that this estimate, which is only good within 10−20%, does not take into account contributions from background diagrams, width effects, and cuts on final-state fermions. The difference of cross sections for CC processes and the corresponding processes of mixed type reflects the size of the background contributions induced by NC diagrams.

The results of WHIZARD, which are also generated with 10^7 events, and of our program typically agree within 1–2 standard errors. The size of the statistical errors obtained with WHIZARD and our program is comparable. The runtime of WHIZARD is usually somewhat bigger than the one of our program. Depending on the process class, the speed of our program is 1−7 times higher, where the largest difference occurs for NC processes.

3.5.2.2 Energy dependence of integrated cross sections

In Figure 3.5 we show the cross sections for the processes $\gamma\gamma \to \mathrm{e}^-\bar{\nu}_\mathrm{e}\mathrm{u}\bar{\mathrm{d}}(\gamma)$ as a function of the centre-of-mass (CM) energy $\sqrt{s}$ with and without convolution over the photon spectrum. Here and in the following, with convolution over the photon spectrum $\sqrt{s}$ stands for the CM energy $\sqrt{s_{\mathrm{ee}}}$ of the incoming electron beams, without convolution it is the CM energy $\sqrt{s_{\gamma\gamma}}$ of the incoming photons. In the case without photon spectrum, the rise of the cross section is clearly visible at the W-pair threshold, $\sqrt{s_{\gamma\gamma}} \gtrsim 160\,\mathrm{GeV}$. For $\gamma\gamma \to \mathrm{e}^-\bar{\nu}_\mathrm{e}\mathrm{u}\bar{\mathrm{d}}$ the cross section increases roughly proportional to $\beta = \sqrt{1 - 4M_\mathrm{W}^2/s_{\gamma\gamma}}$

---

[6] For a tuned comparison we rescaled the WHIZARD/MADGRAPH results by a factor $\alpha(0)^2\alpha_{G_\mu}^2/\alpha^4$ for $\gamma\gamma \to 4f$ and $\alpha(0)^3\alpha_{G_\mu}^2/\alpha^5$ for $\gamma\gamma \to 4f\gamma$.

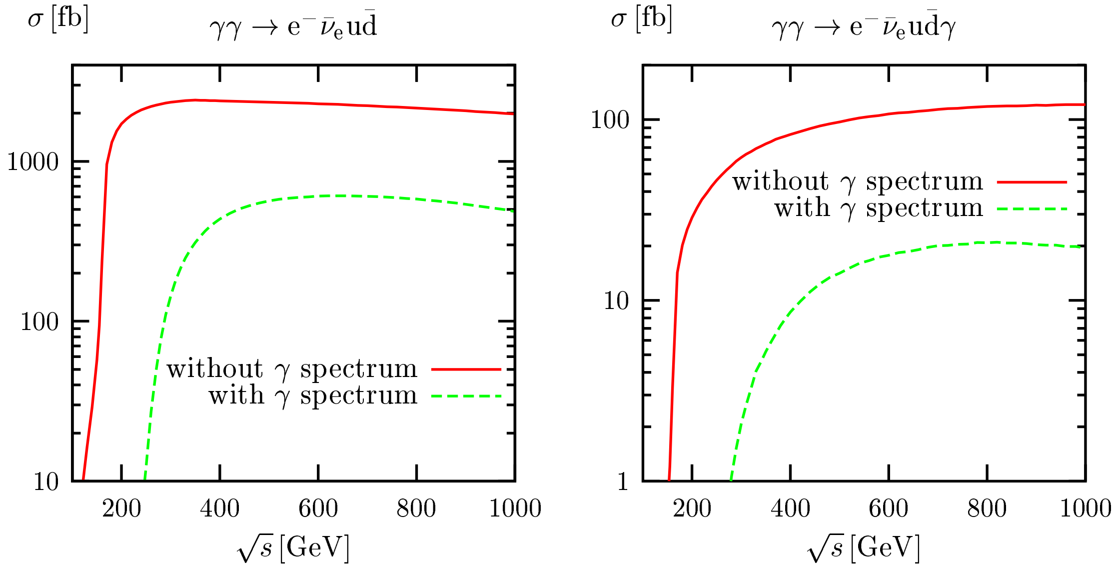

Figure 3.5: Integrated cross sections of the processes $\gamma\gamma \to \mathrm{e}^-\bar{\nu}_\mathrm{e}\mathrm{u}\bar{\mathrm{d}}(\gamma)$ with and without convolution over the photon spectrum as a function of the CM energy $\sqrt{s}$.

above the threshold, as expected from the two-particle phase space of the W pairs. For $\gamma\gamma \to \mathrm{e}^-\bar{\nu}_\mathrm{e}\mathrm{u}\bar{\mathrm{d}}\gamma$ the rise of the cross section is not as steep because of the higher-dimensional WWγ phase space. The convolution over the photon spectrum reduces the available energy for W-pair production and shifts the onset of the cross section to higher CM energies.

The cross sections for $\gamma\gamma \to 4f$ as well as $\gamma\gamma \to 4f\gamma$ decrease at high energies, even though the total cross section of the $\gamma\gamma \to$ WW process approaches a constant in the high-energy limit if no cuts are imposed, i.e., if the W bosons are allowed to go in the beam directions. At high energies, however, forward and backward scattering of W bosons is restricted due to the cuts applied to the outgoing fermions, because the decay fermions mainly follow the direction of the decaying W boson.

3.5.2.3 Contributions from CC, NC, and gluon-exchange diagrams

In Figure 3.6 we show the impact of CC, NC, and gluon-exchange diagrams on the CC/NC processes $\gamma\gamma \to \mathrm{u}\bar{\mathrm{u}}\mathrm{d}\bar{\mathrm{d}}$ and $\gamma\gamma \to \mathrm{u}\bar{\mathrm{u}}\mathrm{d}\bar{\mathrm{d}}\gamma$. We do not include the photon spectrum in this analysis. Above the W-pair threshold, $\sqrt{s_{\gamma\gamma}} > 160\,\mathrm{GeV}$, the CC diagrams are clearly dominating, while the contributions from gluon-exchange diagrams are one or two orders of magnitude smaller. The impact of the gluon-exchange diagrams strongly depends on the choice of the invariant-mass cut between two quarks, and gluon-exchange diagrams are more important if the invariant-mass cut is small. The contributions from pure NC diagrams are totally negligible as long as W-pair production is possible.

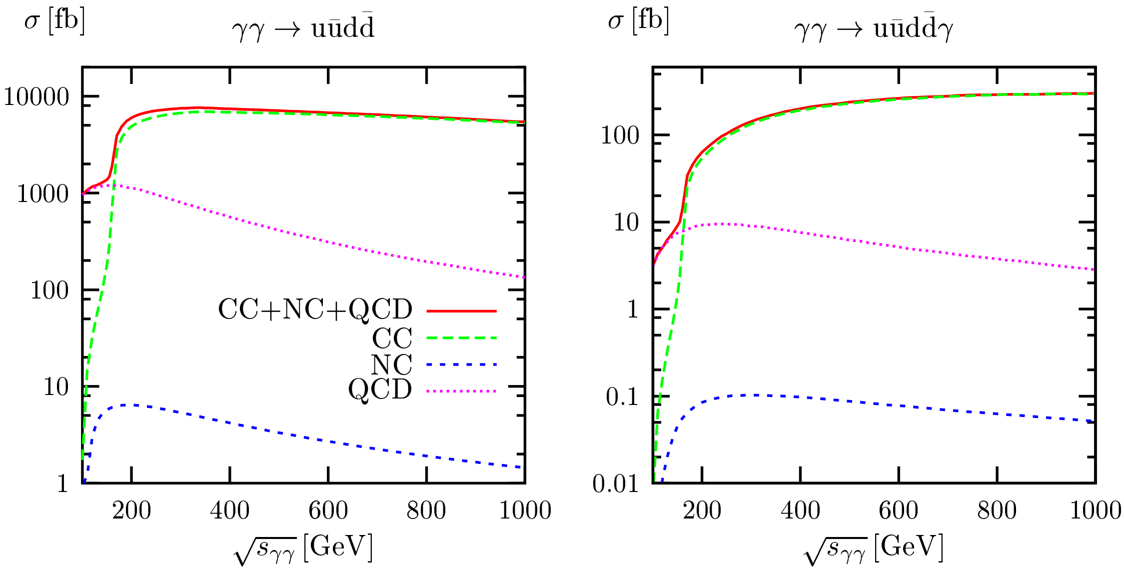

Figure 3.6: Different contributions to the integrated cross sections for the processes $\gamma\gamma \to \mathrm{u}\bar{\mathrm{u}}\mathrm{d}\bar{\mathrm{d}}(\gamma)$ as a function of the CM energy without photon spectrum.

3.5.2.4 W-pair signal diagrams and double-pole approximation

In Figure 3.7 the cross sections of the W-pair signal diagrams and the DPA for $\gamma\gamma \to \mathrm{WW} \to 4f$ (see Section 3.1.5 for definitions) are compared with the complete lowest-order cross section for several processes. The plots on the l.h.s. show the cross sections for various final states calculated from the full set of (electroweak) diagrams, from the signal diagrams only, and in DPA separately for hadronic, semi-leptonic, and leptonic final states, while the plots on the r.h.s. show the relative deviation from the corresponding DPA. We do not include the convolution over the photon spectrum and gluon-exchange diagrams in this analysis so that effects of the approximation are clearly visible. For energies not too close to the W-pair threshold, the DPA agrees with the full lowest-order cross section within 1–3%, which is of the expected order of $\Gamma_\mathrm{W}/M_\mathrm{W}$. Near threshold, i.e. for $\sqrt{s_{\gamma\gamma}} - 2M_\mathrm{W} = \mathcal{O}(\Gamma_\mathrm{W})$, the reliability of the DPA breaks down, since background diagrams become more and more important and small scales γ, such as $\sqrt{s_{\gamma\gamma} - 4M_\mathrm{W}^2}$, can increase the naive error estimate from $\Gamma_\mathrm{W}/M_\mathrm{W}$ to Γ_W/γ. The cross sections of the W-pair signal diagrams, however, shows large deviations from the full $\gamma\gamma \to 4f$ cross sections for the whole energy range, in particular, at high energies. As explained in Section 3.1.5, the W-pair signal diagrams are not gauge invariant, and thus the reliability and usefulness of the resulting predictions should be investigated carefully. The results of Figure 3.7 clearly show that a naive signal definition is a bad concept for $\gamma\gamma \to \mathrm{WW} \to 4f$, since deviations from the full process $\gamma\gamma \to 4f$ even reach 5–10% in the TeV range. This is in contrast to the situation at $\mathrm{e}^+\mathrm{e}^-$ colliders where the naive W-pair signal (defined in 't Hooft–Feynman gauge) was a reasonable approximation (see, e.g., Ref. [44]).

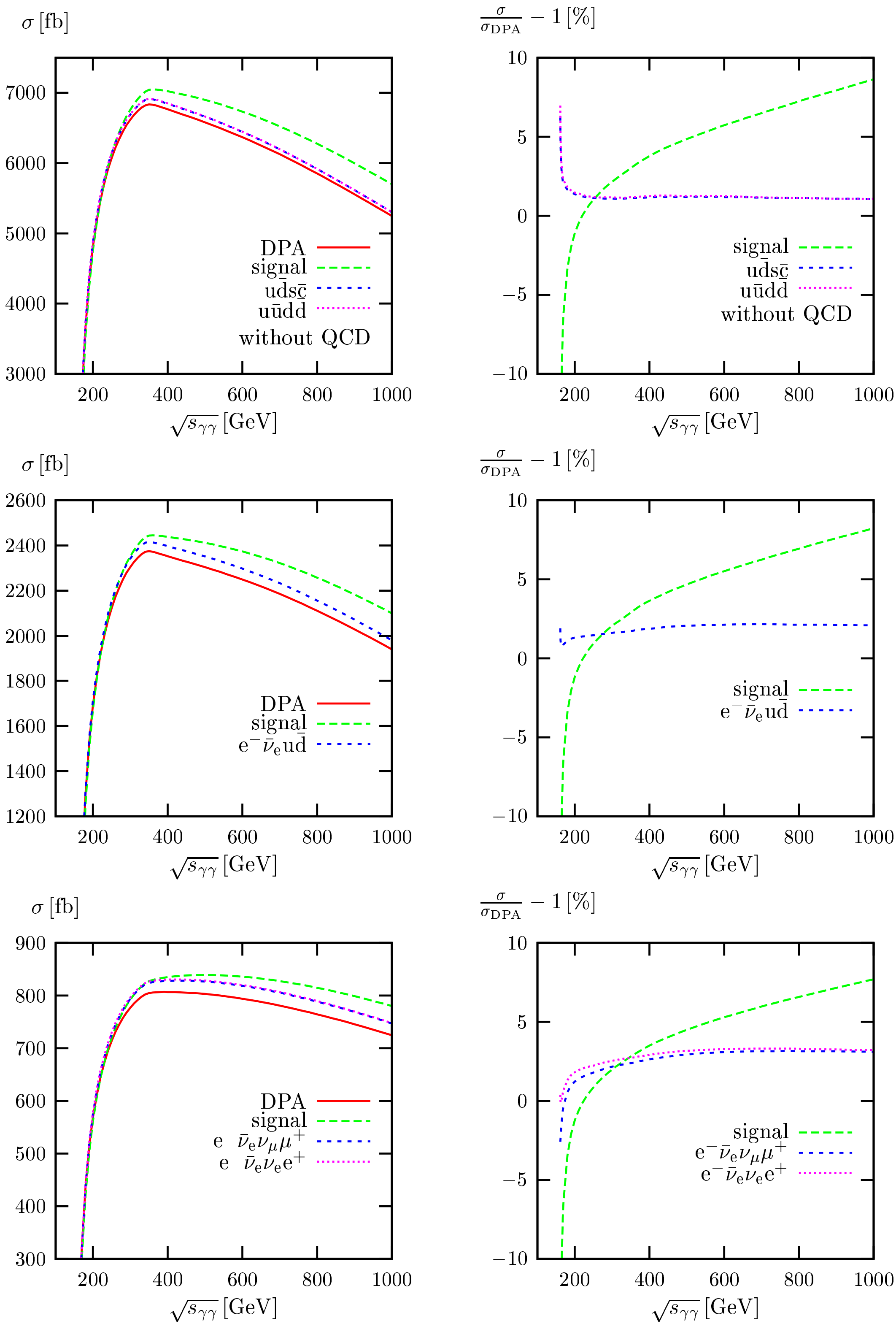

Figure 3.7: Cross sections of various processes including all diagrams, only W-pair signal diagrams, and in DPA as a function of the CM energy (l.h.s.), and the corresponding relative deviations from the DPA (r.h.s.); photon spectrum and gluon-exchange diagrams are not included.

$\sigma(\gamma\gamma \to \mathrm{e}^-\bar{\nu}_\mathrm{e}\nu_\mu\mu^+)$					
$\sqrt{s_{\gamma\gamma}}$ [GeV]	500	800	1000	2000	10000
fixed width	826.40(21)	788.35(21)	746.94(21)	500.70(20)	31.745(68)
step width	827.45(22)	789.34(21)	748.17(23)	501.41(21)	31.746(68)
running width	827.43(23)	789.29(21)	748.11(23)	501.32(21)	31.715(68)
complex mass	826.23(21)	788.18(21)	746.78(21)	500.59(20)	31.738(68)

$\sigma(\gamma\gamma \to \mathrm{e}^-\bar{\nu}_\mathrm{e}\nu_\mu\mu^+\gamma)$					
$\sqrt{s_{\gamma\gamma}}$ [GeV]	500	800	1000	2000	10000
fixed width	39.230(45)	47.740(73)	49.781(91)	43.98(18)	4.32(23)
step width	39.253(45)	47.781(73)	49.881(96)	44.01(18)	4.31(24)
running width	39.251(49)	47.781(74)	49.898(95)	44.48(22)	10.83(28)
complex mass	39.221(45)	47.730(73)	49.770(91)	43.97(18)	4.31(23)

Table 3.4: Cross sections for the processes $\gamma\gamma \to \mathrm{e}^-\bar{\nu}_\mathrm{e}\nu_\mu\mu^+$ and $\gamma\gamma \to \mathrm{e}^-\bar{\nu}_\mathrm{e}\nu_\mu\mu^+\gamma$ for various CM energies and various width schemes without convolution over the photon spectrum.

The failure of the naive W-pair signal definition for $\gamma\gamma$ collisions was also pointed out in Refs. [16, 17] before. In Ref. [17] an "improved narrow-width approximation" was presented which provides another variant for a gauge-invariant W-pair signal definition. It is based on the factorization of production and decay matrix elements, while retaining W-spin correlations.

3.5.2.5 Comparison of schemes for introducing finite gauge-boson widths

In this section we compare the different implementations of gauge-boson widths described in Section 3.1.4 numerically. As explained in Section 3.1.4, the complex-mass scheme is the only scheme that yields gauge-invariant results in general, but for the process classes $\gamma\gamma \to 4f(\gamma)$ the fixed-width approach (in the non-linear gauge) also yields amplitudes that respect Ward identities and gauge cancellations. Table 3.4 lists the cross sections for the processes $\gamma\gamma \to \mathrm{e}^-\bar{\nu}_\mathrm{e}\nu_\mu\mu^+$ and $\gamma\gamma \to \mathrm{e}^-\bar{\nu}_\mathrm{e}\nu_\mu\mu^+\gamma$ obtained with the fixed W width, the step-width, the running-width, and with the complex-mass scheme. The results of all four schemes for the process $\gamma\gamma \to \mathrm{e}^-\bar{\nu}_\mathrm{e}\nu_\mu\mu^+$ agree within the expected accuracy of $\mathcal{O}(\Gamma_\mathrm{W}/M_\mathrm{W})$ up to energies in the TeV range. However, for $\gamma\gamma \to \mathrm{e}^-\bar{\nu}_\mathrm{e}\nu_\mu\mu^+\gamma$ the running-width scheme yields totally wrong results for several TeV, while the other schemes are still in good agreement. Although the gauge-invariance-breaking effects in the running-width scheme are formally of $\mathcal{O}(\Gamma_\mathrm{W}/M_\mathrm{W})$, they are enhanced by spoiling gauge cancellations, thereby ruining the reliability of the prediction completely.

θ_e	$E_\mathrm{e}[\,\mathrm{GeV}]$	$\sigma_{++}[\,\mathrm{fb}]$	
		$\gamma\gamma \to \mathrm{e}^-\bar{\nu}_\mathrm{e}\mathrm{u}\bar{\mathrm{d}}$	$\gamma\gamma \to \nu_\mathrm{e}\mathrm{e}^+\mathrm{d}\bar{\mathrm{u}}$
1°	10	2557.2(1.6)	2618.6(1.6)
5°	10	2492.0(1.6)	2505.6(1.6)
10°	10	2413.2(1.6)	2258.5(1.5)
5°	1	2611.4(1.6)	2505.7(1.6)
5°	10	2492.0(1.6)	2505.6(1.6)
5°	20	2181.1(1.4)	2505.1(1.6)

Table 3.5: Polarized cross sections for the processes $\gamma\gamma \to \mathrm{e}^-\bar{\nu}_\mathrm{e}\mathrm{u}\bar{\mathrm{d}}$ and $\gamma\gamma \to \nu_\mathrm{e}\mathrm{e}^+\mathrm{d}\bar{\mathrm{u}}$ without convolution over the photon spectrum at $\sqrt{s_{\gamma\gamma}} = 500\,\mathrm{GeV}$ for different angular and energy cuts of e^- and e^+.

For the semi-leptonic $\gamma\gamma \to 4f$ process it was already observed in Ref. [17] that the cross section does not vary significantly if the fixed-width, the running-width, or a so-called "fudge-factor" scheme is used for introducing finite widths.

3.5.2.6 Effect of phase-space cuts on $\gamma\gamma \to \mathrm{e}^-\bar{\nu}_\mathrm{e}\mathrm{u}\bar{\mathrm{d}}$ *and* $\gamma\gamma \to \nu_\mathrm{e}\mathrm{e}^+\mathrm{d}\bar{\mathrm{u}}$

As observed in Section 3.5.2.1, the CP-related final states $\mathrm{e}^-\bar{\nu}_\mathrm{e}\mathrm{u}\bar{\mathrm{d}}$ and $\nu_\mathrm{e}\mathrm{e}^+\mathrm{d}\bar{\mathrm{u}}$ do not yield the same cross section if the photon spectrum is included. A CP transformation not only transforms the two final states into each other, but also flips the polarization of the photons. Thus, for unpolarized photons the two processes have the same cross section. However, the photon spectrum induces an effective polarization of the photons so that CP invariance does not require the two cross sections to be equal anymore. Which cross section is larger in this case depends on the applied phase-space cuts [17].

In fact, there are two competing influences. On the one hand, there is the angular cut of e^- and e^+ w.r.t. the beam axis, on the other hand, the cross sections are sensitive to the energy cut of e^- and e^+. In this context it is important to note that two photons with polarization $(\lambda_1\lambda_2) = (++)$ mainly produce W bosons with helicities $(++)$ (see, e.g., Refs. [17, 59]). Since W bosons decay into left-handed particles and right-handed anti-particles, helicity conservation requires that the largest part of the cross section (for positive photon helicities) comes from a region of the phase space where the $\bar{\nu}_\mathrm{e}$ in the final state $\mathrm{e}^-\bar{\nu}_\mathrm{e}\mathrm{u}\bar{\mathrm{d}}$ is emitted in the direction of flight of the W^- boson. In the rest frame of the W boson the e^- is emitted in the opposite direction. However, the cuts are applied in the laboratory frame so that the Lorentz boost tends to push the e^- out of the angular cut w.r.t. the beam axis (remember that the W bosons are preferably produced in a direction close to the beam axis). For the $\bar{\nu}_\mathrm{e}$ no cuts are applied, thus, the Lorentz boost of the $\bar{\nu}_\mathrm{e}$ does not have any effect. In the process $\gamma\gamma \to \nu_\mathrm{e}\mathrm{e}^+\mathrm{d}\bar{\mathrm{u}}$ the e^+ is emitted in the forward direction of the W^+ boson, while the ν_e is emitted in the backward direction. In this case, more events are subject to the phase-space cut. As a result, the angular cut of $\mathrm{e}^+/\mathrm{e}^-$

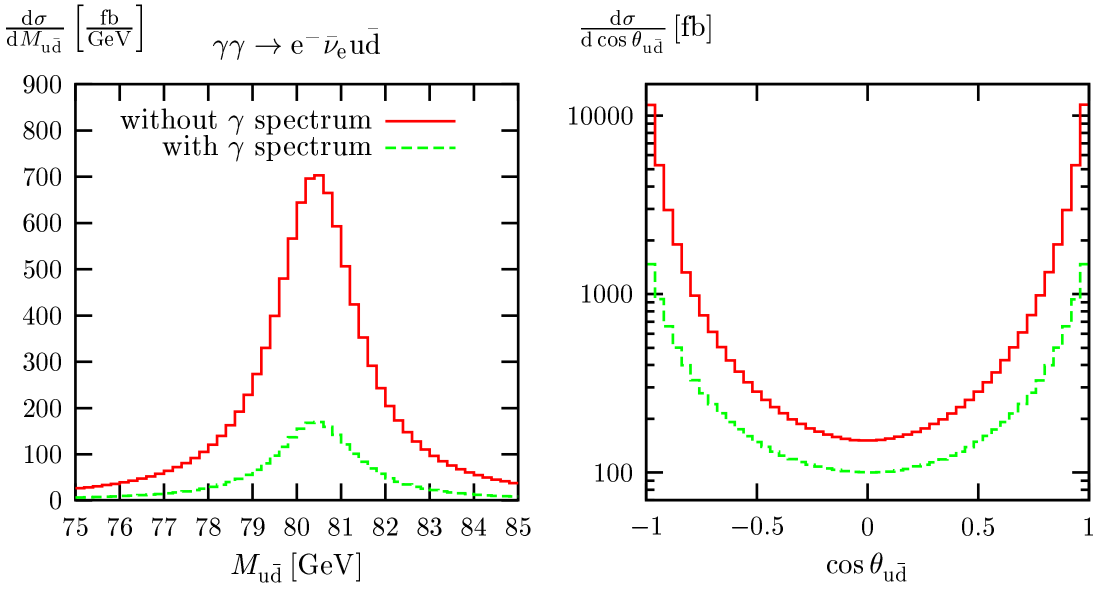

Figure 3.8: Invariant-mass distribution of the W^+ boson reconstructed from the $u\bar{d}$ quark pair (l.h.s.) as well as its production-angle distribution (r.h.s.) in the reaction $\gamma\gamma \to e^-\bar{\nu}_e u\bar{d}$ at $\sqrt{s} = 500\,\text{GeV}$ with and without convolution over the photon spectrum.

reduces the cross section of the process $\gamma\gamma \to \nu_e e^+ d\bar{u}$ more than the cross section of the process $\gamma\gamma \to e^-\bar{\nu}_e u\bar{d}$. This is illustrated in Table 3.5, where we compare the polarized cross sections for both processes for different values of the angular cut.

On the other hand, the cross sections also depend on the energy cut that is applied to e^- and e^+. As explained above, the largest part of the cross section for $\gamma\gamma \to e^-\bar{\nu}_e u\bar{d}$ comes from a phase-space region where the $\bar{\nu}_e$ is emitted parallel to the W^- boson and the e^- anti-parallel. Since the $\bar{\nu}_e$ carries most of the energy of the W^- boson and the e^- only a small fraction, the energy cut of e^- disfavours this process. For the CP-conjugate final state $\nu_e e^+ d\bar{u}$ the energy cut has almost no effect on the cross section, because the e^+ carries most of the energy and the ν_e is not subject to an energy cut. This situation is also illustrated in Table 3.5, where we show the cross sections for different energy and fixed angular cut in the lower part of the table.

3.5.3 Results for differential cross sections

3.5.3.1 Invariant-mass and angular distributions for W bosons

In Figure 3.8 we show the invariant-mass and angular distributions of the intermediate W^+ boson for the process $\gamma\gamma \to e^-\bar{\nu}_e u\bar{d}$ at $\sqrt{s} = 500\,\text{GeV}$. The momentum of the W^+ boson is reconstructed from the outgoing quark pair in the decay $W^+ \to u\bar{d}$. Figure 3.8 also illustrates the effect of the convolution over the photon spectrum.

The resonance in the invariant-mass distribution (l.h.s. of Figure 3.8) has the typical Breit-Wigner shape and can be used to determine the W-boson mass and width at a $\gamma\gamma$ collider. Moreover, owing to its large cross section, the W reconstruction in this reaction seems to be a promising possibility for detector calibration at a $\gamma\gamma$ collider. Similarly to the integrated cross sections discussed in the previous sections, the convolution qualitatively rescales the distribution by roughly a factor 4.

The r.h.s. of Figure 3.8 shows the distribution in the angle $\theta_{\mathrm{u\bar{d}}}$ between the W^+ boson and the beam axis. Since the incoming $\gamma\gamma$ state is symmetric w.r.t. interchange of the two photons, the angular distribution is symmetric in the production angle $\theta_{\mathrm{u\bar{d}}}$. W bosons are predominantly produced in forward or backward direction owing to diagrams with t- and u-channel exchange of W bosons. For the process $\gamma\gamma \to \mathrm{WW}$ with on-shell W bosons, the forward and backward peaks are integrable and lead to a constant cross section in the high-energy limit. As already pointed out in Section 3.5.2.2, the angular cuts (3.5.2) restrict the available phase space of the intermediate W bosons and lead to a reduction of the forward and backward peaks for high energies. Note that the reduction induced by the convolution over the photon spectrum is not uniform, but tends to flatten the shape of the angular distribution slightly. This is mainly due to the reduced CM energy in the photon spectrum, leading to a less pronounced peaking behaviour in the forward and backward directions.

3.5.3.2 Energy and production-angle distributions of fermions

In Figure 3.9 we show the energy and angular distributions of the outgoing fermions e^-, u, and $\mathrm{\bar{d}}$ in the reaction $\gamma\gamma \to \mathrm{e}^-\bar{\nu}_\mathrm{e}\mathrm{u\bar{d}}$ at $\sqrt{s} = 500\,\mathrm{GeV}$ with and without convolution over the photon spectrum.

For monochromatic, unpolarized incoming γ beams (i.e. without convolution over the photon spectrum), the energy distributions (l.h.s. of Figure 3.9) of the fermions e^-, u, and $\mathrm{\bar{d}}$ almost coincide and are maximal at their largest and smallest kinematical limits. These regions are dominated by the situations where the respective W boson emits the considered fermion parallel or anti-parallel to its direction of flight. The convolution over the photon spectrum changes the shapes of the energy distributions considerably. Since the photon spectrum falls off rapidly for energies above 80% of the incoming electron energy, energies of the final-state fermions larger than 200 GeV become practically impossible. For fermion energies below 200 GeV the shapes of the distributions of the outgoing fermions e^- and u look rather different from the one for the anti-fermion $\mathrm{\bar{d}}$. This effect is due to the effective γ beam polarization in the photon spectrum; for unpolarized γ beams the energy distributions would look almost identical. In detail, the effective polarization of the $\gamma\gamma$ system is mainly $(\lambda_1\lambda_2) = (++)$, leading predominantly to $\mathrm{W}^+\mathrm{W}^-$ production with effective helicities $(++)$. Following the line of thought of Section 3.5.2.6 W bosons with helicity $+1$ cannot decay into fermion–anti-fermion pairs with a fermion (which must have helicity $-\frac{1}{2}$) parallel to the flight direction of the W boson. Thus, much more anti-fermions (which have helicity $+\frac{1}{2}$) than fermions follow the directions of the decaying W bosons, which qualitatively explains the reduction (enhancement) of the fermion (anti-fermion) energy distributions at the upper kinematical energy limit. The above arguments are nicely illustrated in Ref. [17], where the fermion energy distributions are shown for fully polarized, monochromatic photon beams.

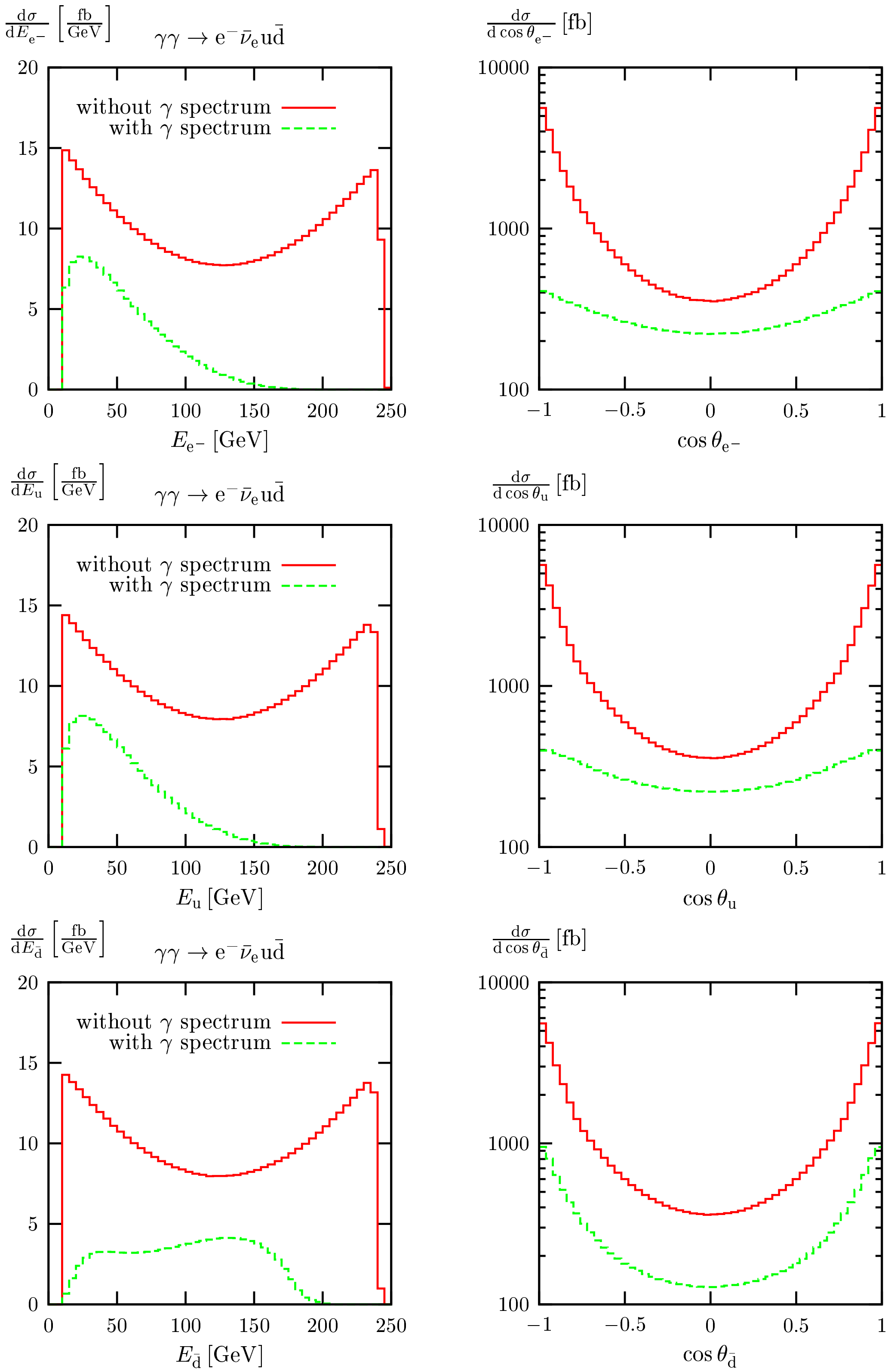

Figure 3.9: Energy (l.h.s.) and production-angle (r.h.s.) distributions of the outgoing fermions e^-, u, and $\bar{d}$ in the process $\gamma\gamma \to e^-\bar{\nu}_e u\bar{d}$ at $\sqrt{s} = 500\,\text{GeV}$ with and without convolution over the photon spectrum.

The r.h.s. of Figure 3.9 shows the distributions in the angles θ_f of the (anti-)fermions $f = \mathrm{e}^-, \mathrm{u}, \bar{\mathrm{d}}$ to the beam axis. Because of the symmetry of the incoming $\gamma\gamma$ state w.r.t. interchange of the two photons, the angular distribution is symmetric in θ_f. The forward and backward peaks originate from two sources. The by far largest contribution to the differential cross section comes from signal diagrams and thus from configurations where the W bosons as well as the decay fermions are nearly parallel to the beam. The second source, which is widely suppressed by the applied cuts, is related to collinear singularities of background diagrams where an incoming photon splits into an fermion–anti-fermion pair $f\bar{f}$, with the fermion or anti-fermion directly going into the final state. If the phase space of the outgoing (anti-)fermion is not restricted by cuts, such collinear or mass singularities lead to logarithms of the form $\ln(s/m_f^2)$, where m_f is the fermion mass. Since our calculation is done for massless fermions, the collinear singularities must be excluded by phase-space cuts and the fermion mass in $\ln(s/m_f^2)$ is replaced by the corresponding cut parameter.

The photon spectrum reduces the differential cross section over the whole range and again flattens the angular distributions, especially in the cases of outgoing fermions. The significant difference between the outgoing fermions and anti-fermions is again due to the effective γ polarization in the photon spectrum. As explained above, more anti-fermions than fermions follow the flight directions of the W bosons, which are mainly produced in the forward and backward directions. This is the reason why the θ_{e^-} and θ_{u} distributions are flattened, while the peaking behaviour in the $\theta_{\bar{\mathrm{d}}}$ distribution is more pronounced after the convolution over the photon spectrum.

3.5.3.3 Higgs-boson resonance

In Figure 3.10 we show the invariant-mass distribution of the Higgs boson for the process $\gamma\gamma \to \mathrm{H} \to \mathrm{WW} \to \mathrm{u}\bar{\mathrm{d}}\mathrm{s}\bar{\mathrm{c}}$ for a Higgs mass of $M_{\mathrm{H}} = 170\,\mathrm{GeV}$. The CM energy of the electron beams is chosen to be $\sqrt{s_{\mathrm{ee}}} = 260\,\mathrm{GeV}$ which maximizes the $\gamma\gamma$ luminosity in the region $\sqrt{s_{\gamma\gamma}} \sim M_{\mathrm{H}}$. The invariant mass $M_{\mathrm{u}\bar{\mathrm{d}}\mathrm{s}\bar{\mathrm{c}}}$ of the Higgs boson is reconstructed from its decay products which are the four outgoing quarks. This means that $M_{\mathrm{u}\bar{\mathrm{d}}\mathrm{s}\bar{\mathrm{c}}}$ is equal to the photonic CM energy, $M_{\mathrm{u}\bar{\mathrm{d}}\mathrm{s}\bar{\mathrm{c}}} = \sqrt{s_{\gamma\gamma}}$. Thus, the shape of the distribution depends on the form of the photon spectrum very strongly. The effective $\gamma\gamma\mathrm{H}$ coupling is set to the SM value (3.3.3). For comparison the situation without Higgs resonance is also included in Figure 3.10, illustrating the significance of the Higgs signal. The different peak heights in the two plots simply result from different bin sizes.

3.5.4 Anomalous couplings

In this section we study the impact of possible anomalous gauge-boson couplings on CC cross sections of the process class $\gamma\gamma \to 4f$. In order to estimate the full sensitivity of a future $\gamma\gamma$ collider, such as the $\gamma\gamma$ option at the ILC, on anomalous couplings, in addition differential distributions and realistic event selections should be taken into account. Such a study goes beyond the scope of this work, but our Monte Carlo generator can serve as a tool in this task.

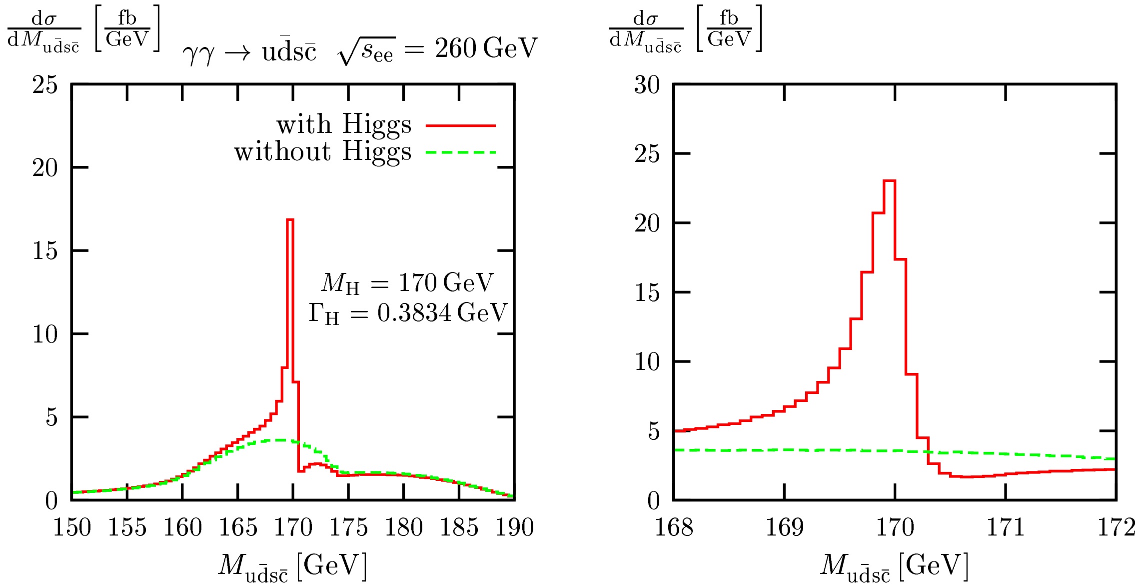

Figure 3.10: Invariant-mass distribution of the four-quark final state for the process $\gamma\gamma \to \mathrm{u\bar{d}s\bar{c}}$ at $\sqrt{s_{\mathrm{ee}}} = 260\,\mathrm{GeV}$ including convolution over the photon spectrum.

We consider only semi-leptonic final states, since these have the cleanest experimental signal. The cross section for semi-leptonic final states is obtained from the sum over all reactions $\gamma\gamma \to l^-\bar{\nu}_l q\bar{q}'$, with $q = \mathrm{u}, \mathrm{c}$ and $l = \mathrm{e}, \mu, \tau$, and their corresponding charge-conjugated processes $\gamma\gamma \to \nu_l l^+ q'\bar{q}$. The results are shown in Figure 3.11 for ATGC and in Figure 3.12 for AQGC. In the left plot of Figure 3.11 and the upper plot of Figure 3.12 we show the cross section as a function of the anomalous coupling constant normalized to the SM cross section. As can be seen in the insert of Figure 3.11, the minimum in the $\Delta\kappa_\gamma$ curve is shifted to negative values which is caused by contributions to the cross section that are linear in $\Delta\kappa_\gamma$. These contributions result from the interference between matrix elements linear in the ATGC $\Delta\kappa_\gamma$ with the SM amplitude. On the other hand, the interferences for the ATGC λ_γ are small. In the case of AQGC, such interferences are relatively large for a_{c}.

In order to examine the sensitivity of a linear collider to anomalous couplings, we consider a $\gamma\gamma$ collider with an integrated luminosity of $\mathcal{L} = 100\,\mathrm{fb}^{-1}$ and a CM energy of $\sqrt{s_{\mathrm{ee}}} = 500\,\mathrm{GeV}$ [11]. We define

$$\chi^2 \equiv \frac{(N(a_i) - N)^2}{N} \qquad \text{with} \quad N = \sigma_{\mathrm{SM}}\mathcal{L}, \quad N(a_i) = \sigma(a_i)\mathcal{L}, \tag{3.5.4}$$

where N is the expected number of events in the SM and $N(a_i)$ the number of events in the SM extended by the non-standard couplings. In Figures 3.11 and 3.12 the 1σ contours corresponding to $\chi^2 = 1$ are shown. Note that the 1σ contour can result from $N(a_i) > N$ and $N(a_i) < N$. While $\chi^2 = 1$ with $N(a_i) > N$ is always possible for sufficiently large anomalous couplings, $\chi^2 = 1$ with $N(a_i) < N$ requires large interference effects of matrix elements with anomalous couplings. In our case, both branches of the 1σ contours are

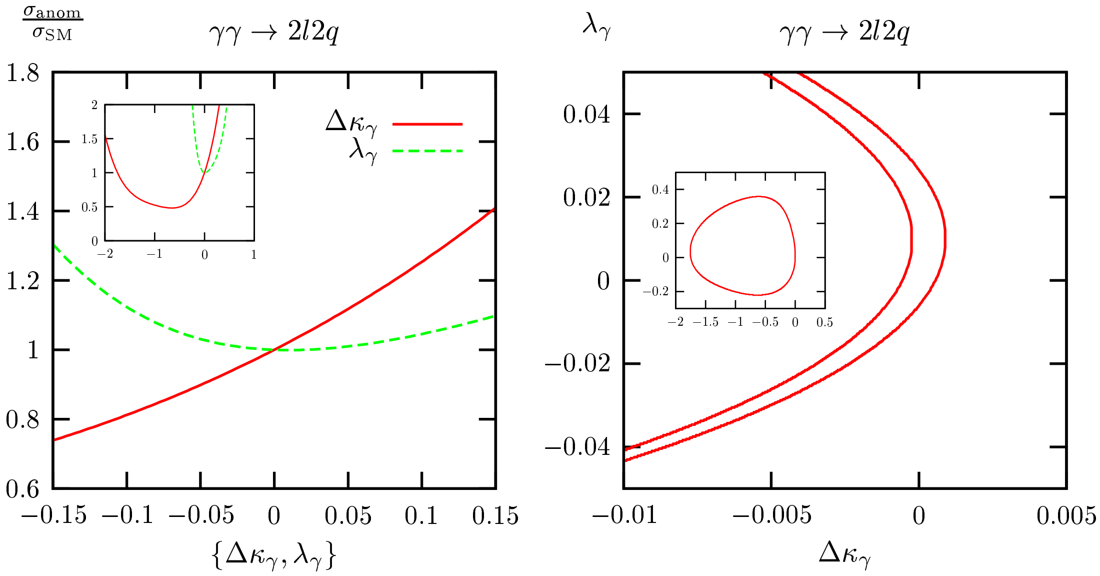

Figure 3.11: Combined cross section for semi-leptonic final states as a function of the ATGC $\Delta\kappa_\gamma$ and λ_γ (l.h.s.) and 1σ contours (r.h.s.) in the $(\Delta\kappa_\gamma, \lambda_\gamma)$ plane at $\sqrt{s_{\rm ee}} = 500\,{\rm GeV}$ including the convolution over the photon spectrum.

realized. In Figure 3.11 the plot on the r.h.s. shows the 1σ contours in the $(\Delta\kappa_\gamma, \lambda_\gamma)$ plane. Since the cross section is a polynomial up to fourth power in the ATGC, the contours are not of elliptic form. The allowed region lies between the two contours that are rather close to each other so that they cannot be distinguished in the insert which shows the contours on a larger scale. Note that in the limit of large luminosity the contour in the insert of the r.h.s. of Figure 3.11 does not shrink to a point, but reduces to a line in the $(\Delta\kappa_\gamma, \lambda_\gamma)$ plane on which $\sigma_{\rm anom} = \sigma_{\rm SM}$. In order to resolve this correlation between $\Delta\kappa_\gamma$ and λ_γ, anomalous effects on distributions should be considered, or other constraints from the e^+e^- or $e^-\gamma$ modes should be included.

In case of AQGC the cross section is at most quadratic in the AQGC, and the $\chi^2 = 1$ surface consists of two ellipsoids in the $(a_0, a_{\rm c}, \tilde{a}_0)$ space. The existence of two branches is again due to large interferences of anomalous contributions. In the lower left plot of Figure 3.12 we show the projections of the outer ellipsoid into the coordinate planes of two AQGC (where the third AQGC is zero). In the lower right plot the sections of both ellipsoids with these planes are given. Since the centre of the ellipsoids is shifted in the $a_{\rm c}$ and a_0 directions, the terms in $\sigma(a_i)$ linear in these couplings are significant; they result from interferences of the diagram with the AQGC with the SM amplitude. Interferences that are proportional to $\tilde{a}_0$ turn out to be small. From Eq. (3.2.14) it is obvious that there are no $a_0\tilde{a}_0$ and $a_{\rm c}\tilde{a}_0$ terms in $\sigma(a_i)$. Consequently, the projection into and the section with the $(a_0, a_{\rm c})$ plane coincide. On the other hand, the two other projections and sections differ, signalling that the $a_{\rm c}a_0$ term in $\sigma(a_i)$ is significant.

The allowed 1σ region ($\chi^2 < 1$) in the $(a_0, a_{\rm c}, \tilde{a}_0)$ space is the shell at the boundary of the shown ellipsoid. Similar to the observation made above for the ATGC, the size

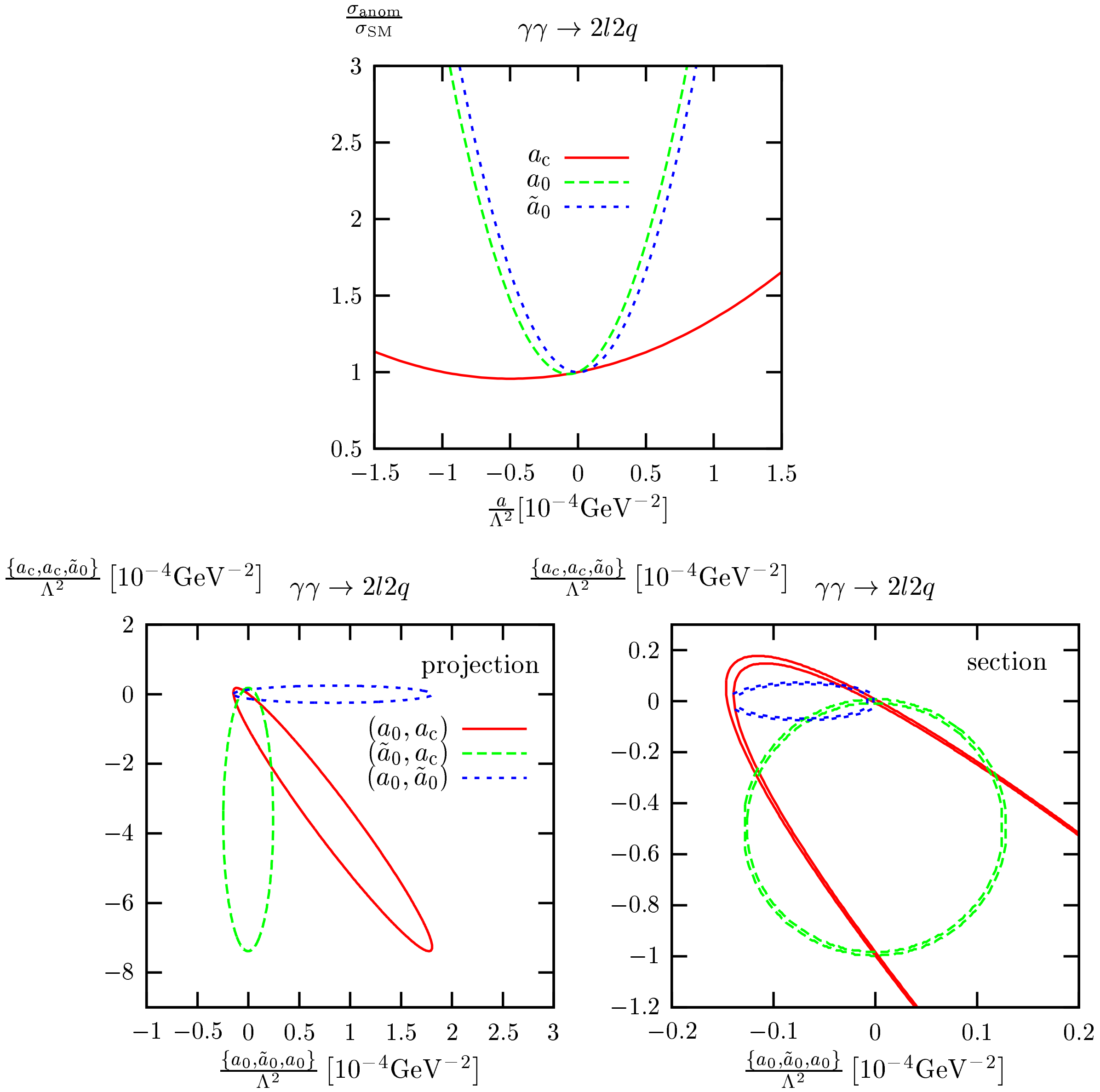

Figure 3.12: Combined cross section for semi-leptonic final states as a function of the AQGC a_0, a_c, and $\tilde{a}_0$ (upper plot) and 1σ contours (l.h.s. projection, r.h.s. section) in the coordinate planes at $\sqrt{s_{ee}} = 500\,\text{GeV}$ including the convolution over the photon spectrum.

of the ellipsoid does not shrink for larger luminosity, only the thickness of the shell will decrease. This means that the size of the projections shown in the lower left plot of Figure 3.12 will not reduce for larger luminosity. Thus, using only information on an integrated cross section (for a fixed energy) could not improve the bounds on AQGC w.r.t. the ones resulting from $e^+e^- \to WW\gamma \to 4f\gamma$ [50]. However, the thinness of the shell of the ellipsoid, as illustrated in the lower right plot of Figure 3.12, shows that the bounds can be drastically tightened if the correlation between the three AQGC is resolved. Differential distributions will certainly provide this information, so that a $\gamma\gamma$ collider should be able to constrain AQGC by an order of magnitude better than an e^+e^- collider operating at comparable energy.

Chapter 4

Quantum corrections to $\gamma\gamma \to \mathrm{WW} \to 4f$ in double-pole approximation

4.1 Strategy of the calculation

We consider the process

$$\begin{aligned}\gamma(k_1,\lambda_1)+\gamma(k_2,\lambda_2) &\to \mathrm{W}^+(k_+,\lambda_+)+\mathrm{W}^-(k_-,\lambda_-)\\ &\to f_1(p_1,\sigma_1)+\bar{f}_2(p_2,\sigma_2)+f_3(p_3,\sigma_3)+\bar{f}_4(p_4,\sigma_4),\end{aligned}\qquad(4.1.1)$$

where k_i and p_i denote the momenta and λ_i and σ_i the helicities of the corresponding particles.

The lowest-order cross section $\mathrm{d}\sigma_{\mathrm{Born}}^{\gamma\gamma\to 4f}$, based on the complete matrix elements $\mathcal{M}_{\mathrm{Born}}^{\gamma\gamma\to 4f}$ with massless fermions, has been discussed in the previous chapter. Suppressing the averaging over the photon polarizations and the spin and colour summation for the final state in the notation, it reads

$$\int \mathrm{d}\sigma_{\mathrm{Born}}^{\gamma\gamma\to 4f} = \frac{1}{2s}\int \mathrm{d}\Phi_{4f}|\mathcal{M}_{\mathrm{Born}}^{\gamma\gamma\to 4f}|^2,\qquad(4.1.2)$$

with

$$s=(k_1+k_2)^2,\qquad s_{ij}=(p_i+p_j)^2,\quad i,j=1,2,3,4.\qquad(4.1.3)$$

The variables s_{ij} are introduced for later use.

In the following we focus on the radiative corrections of $\mathcal{O}(\alpha)$ which consist of virtual corrections $\mathrm{d}\sigma_{\mathrm{virt}}^{\gamma\gamma\to 4f}$ to the process (4.1.1) and real-photonic corrections $\mathrm{d}\sigma^{\gamma\gamma\to 4f\gamma}$, originating from the process

$$\begin{aligned}\gamma(k_1,\lambda_1)+\gamma(k_2,\lambda_2) &\to \mathrm{W}^+(k_+,\lambda_+)+\mathrm{W}^-(k_-,\lambda_-)\ (+\gamma)\\ &\to f_1(p_1,\sigma_1)+\bar{f}_2(p_2,\sigma_2)+f_3(p_3,\sigma_3)+\bar{f}_4(p_4,\sigma_4)+\gamma(k,\lambda_\gamma).\end{aligned}\qquad(4.1.4)$$

Combining the different contributions we obtain the $\mathcal{O}(\alpha)$-corrected prediction for the cross section,

$$\int \mathrm{d}\sigma = \int \mathrm{d}\sigma_{\mathrm{Born}}^{\gamma\gamma\to 4f} + \int \mathrm{d}\sigma_{\mathrm{virt}}^{\gamma\gamma\to 4f} + \int \mathrm{d}\sigma^{\gamma\gamma\to 4f\gamma}.\qquad(4.1.5)$$

The real-photonic corrections $\mathrm{d}\sigma^{\gamma\gamma\to 4f\gamma}$ are based on the full lowest-order matrix elements $\mathcal{M}_{\mathrm{Born}}^{\gamma\gamma\to 4f\gamma}$ of the process $\gamma\gamma \to 4f\gamma$ for massless fermions, which were calculated in the previous chapter . In the limit of vanishing photon momentum k (soft limit) or when the photon becomes collinear to an external charged fermion (collinear limit), the cross section diverges. Considering the process $\gamma\gamma \to 4f\gamma$ with a visible photon (which is neither soft nor collinear), these soft and collinear singularities are removed by imposing appropriate phase-space cuts which are justified by the finite experimental resolution. For predictions of the $\gamma\gamma \to 4f(\gamma)$ processes, i.e. with or without photon radiation, the singular phase-space regions of soft or collinear emission have to be integrated over. In this case the real corrections are combined with the virtual corrections which contain exactly the same singularities with opposite sign. The regularization of the singularities in the real corrections by small photon and fermion masses, λ and m_f, as well as the matching with the singularities in the virtual corrections, is described in detail in Section 4.3. The starting point is a separation into a finite and a singular part,

$$\mathrm{d}\sigma^{\gamma\gamma\to 4f\gamma} = \mathrm{d}\sigma_{\mathrm{finite}}^{\gamma\gamma\to 4f\gamma} + \mathrm{d}\sigma_{\mathrm{sing}}^{\gamma\gamma\to 4f\gamma}, \tag{4.1.6}$$

where the soft and collinear singularities appear in $\mathrm{d}\sigma_{\mathrm{sing}}^{\gamma\gamma\to 4f\gamma}$ as $\ln\lambda$ and $\ln m_f$ terms, respectively.

The virtual corrections to the process (4.1.1) are calculated in the DPA, which is explained in Section 4.2. Since the real corrections are based on complete $\gamma\gamma \to 4f\gamma$ matrix elements (i.e. they are not calculated in DPA), the cancellation of soft and collinear singularities in Eq. (4.1.5) requires particular care. To this end, we apply the DPA only to the finite part of the virtual corrections,

$$\mathrm{d}\sigma_{\mathrm{virt}}^{\gamma\gamma\to 4f} \to \mathrm{d}\sigma_{\mathrm{virt,finite,DPA}}^{\gamma\gamma\to\mathrm{WW}\to 4f} + \mathrm{d}\sigma_{\mathrm{virt,sing}}^{\gamma\gamma\to 4f}. \tag{4.1.7}$$

Technically this is achieved by subtracting the singular part in DPA from the DPA virtual corrections and adding the exact singular part $\mathrm{d}\sigma_{\mathrm{virt,sing}}^{\gamma\gamma\to 4f}$. Of course, this procedure involves some freedom, because finite terms can be shifted between $\mathrm{d}\sigma_{\mathrm{virt,finite,DPA}}^{\gamma\gamma\to 4f}$ and $\mathrm{d}\sigma_{\mathrm{virt,sing}}^{\gamma\gamma\to 4f}$. This arbitrariness is, however, of the order of the uncertainty $\mathcal{O}(\alpha\Gamma_{\mathrm{W}}/(\pi M_{\mathrm{W}}))$ of our calculation. In the $\mathrm{e}^+\mathrm{e}^-$ case this has been checked numerically in Ref. [19].

Inserting these rearrangements into Eq. (4.1.5) we obtain

$$\int \mathrm{d}\sigma = \int \mathrm{d}\sigma_{\mathrm{Born}}^{\gamma\gamma\to 4f} + \int \mathrm{d}\sigma_{\mathrm{virt,finite,DPA}}^{\gamma\gamma\to\mathrm{WW}\to 4f} + \int \mathrm{d}\sigma_{\mathrm{virt+real,sing}}^{\gamma\gamma\to 4f} + \int \mathrm{d}\sigma_{\mathrm{finite}}^{\gamma\gamma\to 4f\gamma}, \tag{4.1.8}$$

where $\int \mathrm{d}\sigma_{\mathrm{virt+real,sing}}^{\gamma\gamma\to 4f} = \int \mathrm{d}\sigma_{\mathrm{virt,sing}}^{\gamma\gamma\to 4f} + \int \mathrm{d}\sigma_{\mathrm{real,sing}}^{\gamma\gamma\to 4f\gamma}$ does not contain any dependence on the photon mass anymore. Collinear singularities, appearing as $\ln m_f$ terms, also cancel if the observable is sufficiently inclusive. Such *collinear-safe* observables result if photons within cones collinear to any outgoing charged fermion are treated inclusively, i.e. if they are not separated from the nearly collinear fermion by any phase-space or event selection cuts. For non-collinear-safe observables logarithms of the fermion masses remain in the final result. This case demands a special treatment of the singular terms. We elaborate more on this issue in Section 4.3.2.

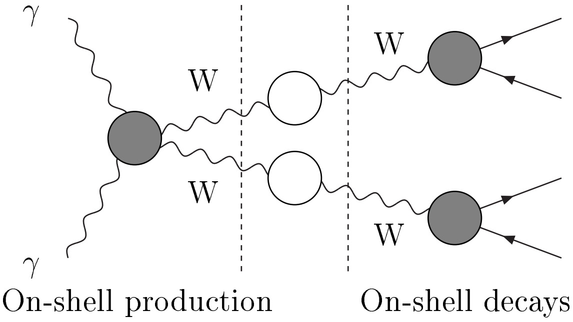

Figure 4.1: Generic Feynman diagram of the virtual factorizable corrections to $\gamma\gamma \to \mathrm{WW} \to 4f$. The shaded blobs stand for loop corrections to the production and decay processes.

4.2 Virtual corrections

4.2.1 Concept of the double-pole approximation

In Section 2.4 we described how to construct a pole expansion around a resonant propagator. In order to obtain the first term of this expansion factorizable and non-factorizable contributions have to be calculated. In the following, we apply the results to the case of two resonant propagators, i.e. we expand the matrix element for $\gamma\gamma \to 4f$ around the poles of the two resonant W propagators. For more details of the DPA, especially how a gauge-invariant decomposition into factorizable and non-factorizable contributions is obtained, we refer to Refs. [19, 37, 60, 61].

The generic Feynman diagram for the factorizable corrections is shown in Figure 4.1. It factorizes into the on-shell W-pair production, the off-shell W-boson propagators, and the subsequent on-shell W decays. The corrections can be attributed to either of these subprocesses. When integrating over the full $4f$ phase space, the W bosons usually are not on shell. However, a gauge-independent evaluation of the matrix elements for production and decay requires on-shell momenta for the W bosons. Therefore, we have to perform an on-shell projection, i.e. the momenta of the fermions are deformed in such a way that the W bosons become on shell. The deformation involves a certain freedom and introduces an error of $\mathcal{O}(\alpha\Gamma_{\mathrm{W}}/(\pi M_{\mathrm{W}}))$. We define the on-shell projection by fixing the directions of the W^+ boson and of the fermions f_1 and f_3. The explicit formulas can be found in Appendix A of Ref. [19]. For later use, we label the new momenta $\hat{k}_\pm$ and $\hat{p}_i$ and define the kinematic invariants

$$\hat{t} = (k_1 - \hat{k}_+)^2 = (k_1 - \hat{p}_1 - \hat{p}_2)^2, \qquad \hat{u} = 2M_{\mathrm{W}}^2 - s - \hat{t}. \tag{4.2.1}$$

Apart from the factorizable corrections there are additional doubly-resonant contributions. In the corresponding diagrams subprocesses are linked by a photon. These diagrams become doubly resonant in the limit of vanishing photon momentum, as can be seen from the soft-photon approximation in which the correction is proportional to the lowest-order cross section. The relative correction factor for these so-called non-factorizable corrections is, thus, not dependent of the actual production mechanism of the W pairs, but

(a) type (mf′) (b) type (ff′)

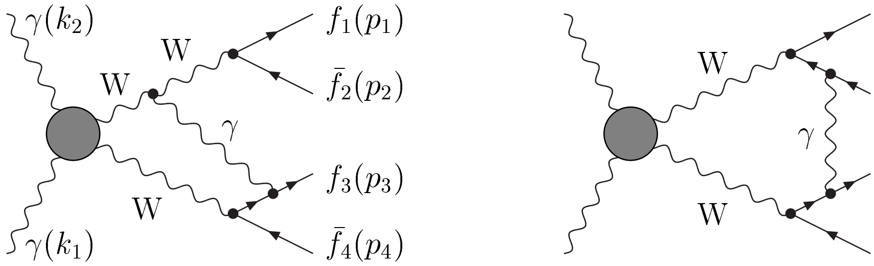

(c) type (mm′) (d) type (mf)

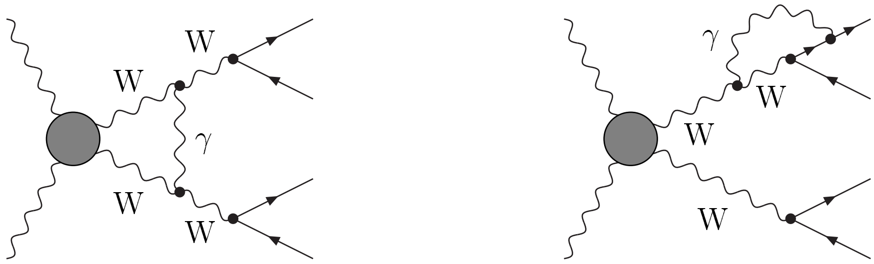

(e) type (mm)

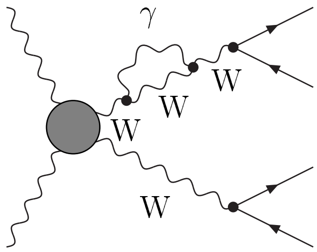

Figure 4.2: A representative set of diagrams contributing to the virtual non-factorizable corrections. The shaded blobs stand for all tree-level structures contributing to $\gamma\gamma \to \mathrm{WW}$.

only on the electric charges and kinematics of the external particles of the process. The non-factorizable corrections were calculated in Refs. [60, 61] for $\mathrm{e^+e^-} \to \mathrm{WW} \to 4f$. We can transfer the results for the $\mathrm{e^+e^-}$ case by simply omitting all contributions in which the exchanged photon is linked to an $\mathrm{e^\pm}$ from the initial state. The different types of relevant diagrams are depicted in Figure 4.2. The first two diagrams, labelled (a) and (b), are manifestly non-factorizable, i.e. the photon links different subprocesses so that the propagators in the diagrams cannot be factorized anymore. The diagrams (c), (d), and (e) contain both factorizable and non-factorizable contributions. Their factorizable parts are defined as the residues for on-shell W bosons times the off-shell W-boson propagators; note that this procedure introduces artificial soft IR divergences connected with the on-shellness of the W bosons in the loops. The non-factorizable parts of the diagrams are obtained from the difference of the doubly-resonant contribution of the full diagrams and their factorizable parts; the artificially introduced IR divergences of the factorizable parts are, thus, compensated by corresponding terms in the non-factorizable parts.

Following this strategy, the virtual corrections in DPA can be written as

$$\begin{aligned} \mathrm{d}\sigma^{\gamma\gamma\to\mathrm{WW}\to 4f}_{\mathrm{virt,DPA}} = \frac{1}{2s}\int \mathrm{d}\Phi_{4f}\Big(& 2\,\mathrm{Re}\{\delta\mathcal{M}_{\mathrm{virt,fact}}\mathcal{M}^{*}_{\mathrm{Born,DPA}}\} \\ & + \delta_{\mathrm{virt,nfact}}|\mathcal{M}_{\mathrm{Born,DPA}}|^2 + |\delta\mathcal{M}_{\mathrm{Higgs}}|^2\Big), \end{aligned} \qquad (4.2.2)$$

where $\mathcal{M}_{\mathrm{Born,DPA}}$ denotes the tree-level matrix element in DPA and $\delta_{\mathrm{virt,nfact}}$ contains the non-factorizable corrections. The factorizable corrections $\delta\mathcal{M}_{\mathrm{virt,fact}}$ also contain a contribution of the s-channel Higgs resonance, $\delta\mathcal{M}_{\mathrm{Higgs}}$. In order to describe this resonance properly, it is not sufficient to include the interference of $\delta\mathcal{M}_{\mathrm{Higgs}}$ with the Born matrix element, but the square of this matrix-element contribution has to be taken into account in addition. To this end, $\delta\mathcal{M}_{\mathrm{Higgs}}$ has to be defined in a gauge-invariant way. Our treatment of $\delta\mathcal{M}_{\mathrm{Higgs}}$ is described in Section 4.2.2.4 in detail.

4.2.2 Factorizable corrections

4.2.2.1 Calculation of the one-loop amplitudes

The factorizable corrections comprise the corrections to the on-shell production of the W bosons and their on-shell decay and can be expressed as

$$\begin{aligned} \delta\mathcal{M}_{\mathrm{virt,fact}} = \sum_{\lambda_+,\lambda_-}\frac{1}{K_+K_-}\Big(& \delta\mathcal{M}^{\gamma\gamma\mathrm{WW}}\mathcal{M}^{\mathrm{W}^+\to f_1\bar{f}_2}_{\mathrm{Born}}\mathcal{M}^{\mathrm{W}^-\to f_3\bar{f}_4}_{\mathrm{Born}} \\ & + \mathcal{M}^{\gamma\gamma\mathrm{WW}}_{\mathrm{Born}}\delta\mathcal{M}^{\mathrm{W}^+\to f_1\bar{f}_2}\mathcal{M}^{\mathrm{W}^-\to f_3\bar{f}_4}_{\mathrm{Born}} \\ & + \mathcal{M}^{\gamma\gamma\mathrm{WW}}_{\mathrm{Born}}\mathcal{M}^{\mathrm{W}^+\to f_1\bar{f}_2}_{\mathrm{Born}}\delta\mathcal{M}^{\mathrm{W}^-\to f_3\bar{f}_4}\Big), \end{aligned} \qquad (4.2.3)$$

where we introduced the abbreviations

$$K_{\pm} = k_{\pm}^2 - M_{\mathrm{W}}^2 + \mathrm{i}M_{\mathrm{W}}\Gamma_{\mathrm{W}}, \qquad (4.2.4)$$

and $\delta\mathcal{M}$ denote one-loop matrix elements. Note that all matrix elements on the r.h.s. of Eq. (4.2.3) depend on the on-shell projected momenta, but the momenta in $K_{\pm}$ remain unchanged. The results for the different one-loop corrections to the production [39, 59, 62] and the decay [57] are already known in the literature. Combining them in Eq. (4.2.3) is, however, non-trivial since the polarizations of the W bosons have to be defined consistently in a common reference frame.

The one-loop corrections $\delta\mathcal{M}^{\mathrm{W}\to f_i\bar{f}_j}$ to the W decays are rather simple. In the massless limit they are proportional to the respective Born matrix elements $\mathcal{M}^{\mathrm{W}\to f_i\bar{f}_j}_{\mathrm{Born}}$,

$$\delta\mathcal{M}^{\mathrm{W}\to f_i\bar{f}_j}(\lambda_{\mathrm{W}},\hat{p}_i,\hat{p}_j) = \delta^{\mathrm{W}\to f_i\bar{f}_j}\,\mathcal{M}^{\mathrm{W}\to f_i\bar{f}_j}_{\mathrm{Born}}(\lambda_{\mathrm{W}},\hat{p}_i,\hat{p}_j), \qquad (4.2.5)$$

where $\delta^{\mathrm{W}\to f_i\bar{f}_j}$ is a constant correction factor that neither depends on the kinematics nor on the helicity λ_{W} of the decaying W boson.

The one-loop correction $\delta\mathcal{M}^{\gamma\gamma\mathrm{WW}}$ to the W-pair production process contains the complicated part. Our calculation is based on the results of Ref. [39]. As in the previous chapter which use a non-linear gauge fixing term, so that the vertex $\gamma\mathrm{W}\phi$ of a photon, a W boson, and the would-be Goldstone boson of the W boson vanishes. This reduces the number of diagrams compared to the conventional 't Hooft–Feynman gauge.

In the following we describe an efficient way for calculating the contribution of $\delta\mathcal{M}^{\gamma\gamma\mathrm{WW}}$ to $\delta\mathcal{M}_{\mathrm{virt,fact}}$ of Eq. (4.2.3), taking into account all spin correlations. As described in Ref. [39], the matrix element $\delta\mathcal{M}^{\gamma\gamma\mathrm{WW}}$ for on-shell W-pair production is decomposed into a sum of products of form factors F_j, which only depend on the kinematic variables s and $\hat{t}$, and a set of standard matrix elements (SME) $\mathcal{M}_j^{\gamma\gamma\mathrm{WW}}$, which contain the polarizations and momenta of the external photons and W bosons,

$$\begin{aligned} &\delta\mathcal{M}^{\gamma\gamma\mathrm{WW}}(k_1,k_2,\lambda_1,\lambda_2;\hat{k}_+,\hat{k}_-,\lambda_+,\lambda_-) \\ &= \sum_{j=1}^{36} F_j(s,\hat{t})\mathcal{M}_j^{\gamma\gamma\mathrm{WW}}(k_1,k_2,\lambda_1,\lambda_2;\hat{k}_+,\hat{k}_-,\lambda_+,\lambda_-). \end{aligned} \tag{4.2.6}$$

The SME $\mathcal{M}_j^{\gamma\gamma\mathrm{WW}}$ are obtained from the 83 basic matrix elements given in Section 2 of Ref. [39] which are reduced to 36 matrix elements as described there[1]. The decay matrix elements $\mathcal{M}_{\mathrm{Born}}^{\mathrm{W}\to f_i\bar{f}_j}$, which multiply $\delta\mathcal{M}^{\gamma\gamma\mathrm{WW}}$ in Eq. (4.2.3), can be included by replacing the W polarization vectors $\varepsilon_\pm^*$ in the definitions of the SME $\mathcal{M}_j$ by the "effective polarization vectors"

$$\hat{\varepsilon}_+^{*\mu} = \frac{e}{\sqrt{2}s_\mathrm{w}}\frac{1}{K_+}\bar{u}(\hat{p}_1)\gamma^\mu\omega_- v(\hat{p}_2), \qquad \hat{\varepsilon}_-^{*\mu} = \frac{e}{\sqrt{2}s_\mathrm{w}}\frac{1}{K_-}\bar{u}(\hat{p}_3)\gamma^\mu\omega_- v(\hat{p}_4), \tag{4.2.7}$$

where $\bar{u}(\hat{p}_i)$ and $v(\hat{p}_i)$ are the Dirac spinors of the fermions and anti-fermions and $\omega_- = \frac{1}{2}(1-\gamma_5)$ is the left-handed chirality projector. The effective W-polarization vectors $\hat{\varepsilon}_\pm^*$ are formal shorthands for the W propagators and the tree-level decay matrix elements, which involve the usual SU(2) gauge coupling e/s_w. Upon substituting $\varepsilon_\pm^* \to \hat{\varepsilon}_\pm^*$ in the SME for on-shell W-pair production, we obtain a new set of SME $\mathcal{M}_j$ that correctly transfer the W polarization to the decay,

$$\begin{aligned} \mathcal{M}_j(k_1,k_2,\lambda_1,\lambda_2;k_+^2,k_-^2;\{\hat{p}_i\}) &= \mathcal{M}_j^{\gamma\gamma\mathrm{WW}}(k_1,k_2,\lambda_1,\lambda_2;\hat{k}_+,\hat{k}_-,\lambda_+,\lambda_-)\Big|_{\varepsilon_\pm^*\to\hat{\varepsilon}_\pm^*} \\ &= \sum_{\lambda_+,\lambda_-}\frac{1}{K_+K_-}\mathcal{M}_j^{\gamma\gamma\mathrm{WW}}(k_1,k_2,\lambda_1,\lambda_2;\hat{k}_+,\hat{k}_-,\lambda_+,\lambda_-) \\ &\qquad\times\mathcal{M}_{\mathrm{Born}}^{\mathrm{W}^+\to f_1\bar{f}_2}(\lambda_+,\hat{p}_1,\hat{p}_2)\,\mathcal{M}_{\mathrm{Born}}^{\mathrm{W}^-\to f_3\bar{f}_4}(\lambda_-,\hat{p}_3,\hat{p}_4). \end{aligned} \tag{4.2.8}$$

The new SME $\mathcal{M}_j$ can be easily evaluated with spinor methods, as e.g. described in Ref. [42].

---

[1] The on-shell momenta $\hat{k}_\pm$ and the helicities $\lambda_\pm$ of the W bosons are denoted $k_{3,4}$ and $\lambda_{3,4}$ in Ref. [39].

In summary the factorizable part of the virtual correction takes the form

$$\delta\mathcal{M}_{\mathrm{virt,fact}} = \sum_{j=1}^{36} F_j(s,\hat{t})\mathcal{M}_j(k_1,k_2,\lambda_1,\lambda_2;k_+^2,k_-^2;\{\hat{p}_i\}) \\ + \left(\delta^{\mathrm{W}^+\to f_1\bar{f}_2} + \delta^{\mathrm{W}^-\to f_3\bar{f}_4}\right)\mathcal{M}_{\mathrm{Born,DPA}}(k_1,k_2,\lambda_1,\lambda_2;k_+^2,k_-^2;\{\hat{p}_i\}). \quad (4.2.9)$$

4.2.2.2 Details of the numerical evaluation

The formulas for the coefficient functions F_j are rather lengthy and contain many one-loop integrals, which in turn involve many dilogarithmic functions, etc. Thus, to speed up the numerical evaluation it is desirable not to evaluate the F_j at each phase-space point. Moreover, numerical instabilities occur at the boundary of the phase space where the scattering angle θ between the W bosons and the beam axis tends to 0 or π. This is due to the inverse Gram determinants appearing in the Passarino–Veltman reduction [63] of the tensor integrals. The problems of speed and stability can be solved by expanding the functions $F_j(s,\hat{t})$ in terms of a generalized Fourier series in the variable $\hat{t}$ for fixed values of s. The coefficients of this expansion are calculated before the Monte Carlo integration. An appropriate system of orthogonal functions in the variable $x = \cos\theta$, which is equivalent to a function of $\hat{t}$ for fixed s, is provided by the Legendre polynomials

$$P_l(x) = \frac{1}{2^l l!}\frac{\mathrm{d}^l}{\mathrm{d}x^l}\left[(x^2-1)^l\right], \qquad l = 0,1,\dots \quad . \qquad (4.2.10)$$

For this basis functions, the coefficients read

$$c_{j,l}(s) = \frac{2l+1}{2}\int_{-1}^{+1} \mathrm{d}\cos\theta\,(\hat{t}-M_\mathrm{W}^2)(\hat{u}-M_\mathrm{W}^2)F_j(s,\hat{t})P_l(\cos\theta), \qquad (4.2.11)$$

where we have introduced the factor $(\hat{t}-M_\mathrm{W}^2)(\hat{u}-M_\mathrm{W}^2)$ in order to flatten the t- and u-channel poles in the functions F_j. This improves the efficiency of the expansion. The integration in Eq. (4.2.11) is carried out using Gaussian integration. With 40 integration points the region of instability is not entered (for energies up to a few TeV), and the integration is sufficiently precise. During the Monte Carlo integration the coefficient functions are recovered by the generalized Fourier series

$$F_j(s,\hat{t}) = \sum_{l=0}^{\infty}\frac{1}{(\hat{t}-M_\mathrm{W}^2)(\hat{u}-M_\mathrm{W}^2)}\,c_{j,l}(s)P_l(\cos\theta). \qquad (4.2.12)$$

In Ref. [19] the same concept was used to evaluate the factorizable corrections to $\mathrm{e}^+\mathrm{e}^- \to \mathrm{WW} \to 4f$; there it was sufficient to use the Legendre polynomials up to $l = 20$ for a good accuracy. In the case of $\gamma\gamma \to \mathrm{WW}$, however, the coefficient functions involve inverse Gram determinants $1/(\hat{t}\hat{u}-M_\mathrm{W}^4) \propto 1/\sin^2\theta$ which appear in the Passarino–Veltman reduction of the tensor integrals. As each step in this recursive reduction involves such an inverse determinant, $1/(\hat{t}\hat{u}-M_\mathrm{W}^4)$ can appear up to the fourth power. At $\cos\theta \approx \pm 1$ this factor leads to a behaviour of the $F_j(s,\hat{t})$ that is not well approximated by the Legendre expansion. Using higher-order Legendre polynomials is not a solution since this increases the calculation time and also requires more integration points for the Gaussian integration. The more points are used in the Gaussian integration, the closer some of these points approach the integration boundary where the numerical stability of the coefficient function breaks down. Therefore, we follow a different strategy based on the fact that the helicity amplitudes for the on-shell process $\gamma\gamma \to \mathrm{WW}$ are smooth functions of $\cos\theta$, apart from the t- and u-channel poles. Thus, within the full amplitude the factors $1/(\hat{t}\hat{u} - M_{\mathrm{W}}^4)$ have to cancel between contributions of different coefficient functions. To make use of this fact we change the basis of SME by a linear transformation in such a way that the new coefficient functions correspond to helicity amplitudes of the on-shell process $\gamma\gamma \to \mathrm{WW}$. Some details of this transformation can be found in App. C. After this transformation the uncertainty of the approximated matrix elements in Eq. (4.2.6) is well below 10^{-4} with respect to the Born matrix elements for all values of $\cos\theta$.

In contrast to the $\mathrm{e}^+\mathrm{e}^-$ case, the CM energy $\sqrt{s}$ of the photons is not fixed. Thus, we have to perform the Legendre expansions for different values of s. During the Monte Carlo integration we derive an approximate value of the coefficients $c_{j,l}(s)$ by interpolation. Since the $F_j(s,\hat{t})$ depend on s very smoothly, it is sufficient to calculate the $c_{j,l}(s)$ at intervals of $\Delta s \lesssim 1\,\mathrm{GeV}$. In these intervals we then interpolate with a polynomial of third order. We have checked that, up to 1 TeV, this yields a sufficient accuracy (i.e. better than the accuracy of the Legendre expansion).

4.2.2.3 Renormalization and imaginary parts of virtual corrections

For on-shell W-pair production, which was considered in Ref. [39], imaginary parts of counterterms, if included, do not influence the correction to the matrix element square. The reason is that for the $2 \to 2$ scattering process $\gamma\gamma \to \mathrm{WW}$ all SME, and thus also the Born matrix element, can be taken real by appropriate phase choices. Thus, the operation of taking the real part in the interference term $2\,\mathrm{Re}\{\mathcal{M}_{\mathrm{ct}}\mathcal{M}^*_{\mathrm{Born}}\}$ of the counterterm contribution $\mathcal{M}_{\mathrm{ct}}$ to the one-loop amplitude with the Born amplitude effectively acts on the renormalization constants themselves. The same argument shows that also imaginary parts of loop integrals drop out. These arguments are no longer true if the decay of the W bosons is taken into account, because the SME and the Born matrix element $\mathcal{M}_{\mathrm{Born,DPA}}$ become necessarily complex. Thus, imaginary parts of renormalization constants and of loop integrals in general matter. Considering the W-decay amplitudes in the DPA in more detail, as e.g. done in Ref. [22] for the $\mathrm{e}^+\mathrm{e}^-$ case, one can see that imaginary parts average to zero after the azimuthal decay angles of the W-decay products are integrated over.

We have calculated the virtual corrections taking into account the imaginary parts of all loop integrals. Comparing the virtual corrections with a second, independent calculation in the 't Hooft–Feynman gauge [6] and in the background-field gauge [7], we find agreement between the results obtained in these different gauges. This is, however, only true if we also take into account the imaginary parts of the loops that contribute to renormalization constants. In order to explain this fact, we consider the counterterm contributions to the one-loop matrix element in more detail.

Following Ref. [39], we write the Born matrix element in DPA as

$$\mathcal{M}_{\mathrm{Born,DPA}} = 8\pi\alpha \left\{ \frac{s}{M_\mathrm{W}^2 - \hat{t}} \mathcal{M}_{0,t} + \frac{s}{M_\mathrm{W}^2 - \hat{u}} \mathcal{M}_{0,u} - (\varepsilon_1\varepsilon_2)(\hat{\varepsilon}_+^*\hat{\varepsilon}_-^*) \right\}, \tag{4.2.13}$$

where $\mathcal{M}_{0,t}$ and $\mathcal{M}_{0,u}$ are abbreviations for specific combinations of momenta and polarization vectors defined as in Eq. (22) of Ref. [39] for on-shell W-pair production. In the 't Hooft–Feynman gauge, the counterterm contribution to the production part of the factorizable correction reads

$$\begin{aligned} \delta\mathcal{M}_{\mathrm{ct,prod}}^{\mathrm{tHF}} = {} & \mathcal{M}_{\mathrm{Born,DPA}} \left(2\delta Z_e + \delta Z_W + \delta Z_{AA} - \frac{c_\mathrm{w}}{s_\mathrm{w}} \delta Z_{ZA} \right) \\ & - 8\pi\alpha \left(\frac{s\delta M_\mathrm{W}^2}{(\hat{t} - M_\mathrm{W}^2)^2} \mathcal{M}_{0,t} + \frac{s\delta M_\mathrm{W}^2}{(\hat{u} - M_\mathrm{W}^2)^2} \mathcal{M}_{0,u} \right) \\ & - 4\pi\alpha \left(\frac{(\varepsilon_1\hat{\varepsilon}_+^*)(\varepsilon_2\hat{\varepsilon}_-^*)}{(\hat{t} - M_\mathrm{W}^2)} + \frac{(\varepsilon_1\hat{\varepsilon}_-^*)(\varepsilon_2\hat{\varepsilon}_+^*)}{(\hat{u} - M_\mathrm{W}^2)} \right) \left(2\delta M_\mathrm{W}^2 + \frac{M_\mathrm{W}^2}{s_\mathrm{w} c_\mathrm{w}} \delta Z_{ZA} \right) \\ & + 4\pi\alpha \frac{e M_\mathrm{W}}{2 s_\mathrm{w}} \left(\frac{(\varepsilon_1\hat{\varepsilon}_+^*)(\varepsilon_2\hat{\varepsilon}_-^*)}{(\hat{t} - M_\mathrm{W}^2)^2} + \frac{(\varepsilon_1\hat{\varepsilon}_-^*)(\varepsilon_2\hat{\varepsilon}_+^*)}{(\hat{u} - M_\mathrm{W}^2)^2} \right) \delta t, \end{aligned} \tag{4.2.14}$$

where we adopt the conventions of Ref. [6] for the renormalization constants δZ_e, δZ_W, etc. The explicit calculation of the constants in terms of self-energies is also described there. The counterterm contribution in the background-field gauge [7] can be obtained from $\delta\mathcal{M}_{\mathrm{ct,prod}}^{\mathrm{tHF}}$ by simply omitting the δZ_{ZA} terms, because δZ_{ZA} vanishes owing to the background-field gauge invariance. In the non-linear gauge the counterterm contribution reads

$$\begin{aligned} \delta\mathcal{M}_{\mathrm{ct,prod}}^{\mathrm{NL}} = {} & \mathcal{M}_{\mathrm{Born,DPA}} \left(2\delta Z_e + \delta Z_W + \delta Z_{AA} - \frac{c_\mathrm{w}}{s_\mathrm{w}} \delta Z_{ZA} \right) \\ & - 8\pi\alpha \left(\frac{s\delta M_\mathrm{W}^2}{(\hat{t} - M_\mathrm{W}^2)^2} \mathcal{M}_{0,t} + \frac{s\delta M_\mathrm{W}^2}{(\hat{u} - M_\mathrm{W}^2)^2} \mathcal{M}_{0,u} \right), \end{aligned} \tag{4.2.15}$$

as described in Ref. [39], which is different from its counterpart in 't Hooft–Feynman gauge. Note also that the explicit expressions of the renormalization constants in the different gauges are in general different.

Imaginary parts of loop and counterterm contributions that are proportional to the Born matrix element, $\delta\mathcal{M} = c\mathcal{M}_{\mathrm{Born}}$, cannot influence matrix element squares, because $2\,\mathrm{Re}\{\delta\mathcal{M}\mathcal{M}_{\mathrm{Born}}^*\} = 2\,\mathrm{Re}\{c\}|\mathcal{M}_{\mathrm{Born}}|^2$. Thus, the W-mass renormalization constant δM_W^2 is the only renormalization constant whose imaginary part plays a role, since the tadpole counterterm δt is a real quantity. From Eqs. (4.2.14) and (4.2.15), we see that δM_W^2, which is equal in all three considered gauges, enters the counterterm contributions in the 't Hooft–Feynman gauge and in the non-linear gauge in different ways. In fact, we have checked numerically that the virtual corrections in these two gauges are different (though finite) if the usual on-shell prescription $\delta M_\mathrm{W}^2 = \mathrm{Re}\{\Sigma_\mathrm{T}^W(M_\mathrm{W}^2)\}$ (see e.g. Ref. [6]) is applied, where $\Sigma_\mathrm{T}^W(k^2)$ is the transverse part of the W-boson self-energy with momentum transfer k. If we, on the other hand, use the definition $\delta M_\mathrm{W}^2 = \Sigma_\mathrm{T}^W(M_\mathrm{W}^2)$, i.e. without taking the real part of the self-energy, we find agreement for the results from the different gauges. This clearly shows that the imaginary part of a one-loop amplitude is in general gauge dependent if imaginary parts in renormalization constants are not taken into account. The reason for this fact, in other words, is that the decomposition of a renormalized transition matrix element into genuine loop parts and counterterm contributions depends on the gauge fixing. A consistent renormalization prescription with complex renormalization constants naturally leads to complex masses for unstable particles. Such a renormalization scheme was proposed in Ref. [24] in the context of a full $\mathcal{O}(\alpha)$ calculation for $\mathrm{e^+e^-} \to 4f$. We will apply this scheme in the next chapter for the calculation of the complete one-loop corrections to the process $\mathrm{H} \to \mathrm{WW/ZZ} \to 4f$.

In our Monte Carlo generator we have taken into account the imaginary parts of the virtual corrections (including the ones from counterterms); more precisely they can be switched on and off optionally. As explained above, they could only affect observables that are sensitive to the azimuthal decay angles of the fermions. In our numerical results, we could, however, find no significant effects.

4.2.2.4 Higgs resonance

The loop-induced Higgs resonance, $\gamma\gamma \to \mathrm{H} \to \mathrm{WW} \to 4f$, belongs to the class of factorizable contributions. Nevertheless, its treatment, especially the question of gauge invariance when including the Higgs decay width, deserves some care. In Ref. [39] the diagrams with an s-channel Higgs resonance were decomposed into a gauge-invariant resonant part and a gauge-dependent non-resonant part. If we write the contribution of the Higgs-exchange diagrams as

$$\delta\mathcal{M}^{\gamma\gamma\mathrm{H}} = \frac{F^H(s)}{s-M_\mathrm{H}^2}(\varepsilon_1\varepsilon_2)(\hat{\varepsilon}_+^*\hat{\varepsilon}_-^*), \tag{4.2.16}$$

with $F^H(s)$ given in Section 4.3 of Ref. [39], and ε_1 and ε_2 being the polarization vectors of the photons, then the Higgs decay width can be introduced by replacing

$$\delta\mathcal{M}^{\gamma\gamma\mathrm{H}} \to \left(\frac{F^H(M_\mathrm{H}^2)}{s-M_\mathrm{H}^2+\mathrm{i}M_\mathrm{H}\Gamma_\mathrm{H}} + \frac{F^H(s)-F^H(M_\mathrm{H}^2)}{s-M_\mathrm{H}^2}\right)(\varepsilon_1\varepsilon_2)(\hat{\varepsilon}_+^*\hat{\varepsilon}_-^*). \tag{4.2.17}$$

As the residue $F^H(M_\mathrm{H}^2)$ is gauge independent, we have introduced the Higgs decay width Γ_H in a gauge-invariant way. Recall that the choice of the polarization vectors of the photons is such that they obey

$$\varepsilon_i k_j = 0, \qquad i,j = 1,2. \tag{4.2.18}$$

Close to the resonance, the contribution of the Higgs-exchange diagrams is strongly enhanced. This is why we also take into account the square of the resonant part in Eq. (4.2.2),

$$\delta\mathcal{M}_\mathrm{Higgs} = \frac{F^H(M_\mathrm{H}^2)(\varepsilon_1\varepsilon_2)(\hat{\varepsilon}_+^*\hat{\varepsilon}_-^*)}{s-M_\mathrm{H}^2+\mathrm{i}M_\mathrm{H}\Gamma_\mathrm{H}}. \tag{4.2.19}$$

In this approach only the leading contribution to the Higgs resonance is taken into account. However, the gauge-invariant separation of $\delta\mathcal{M}_{\mathrm{Higgs}}$ from the remaining one-loop amplitude easily allows for specific improvements in predictions for the Higgs-production signal in the future. To this end, a pole expansion about the Higgs resonance would be an adequate first step. Conceptually this expansion again leads to factorizable and non-factorizable contributions, but the corresponding ingredients are not all available yet and their calculation is beyond the scope of this work. It should be mentioned that both the $\mathcal{O}(\alpha)$ electroweak and $\mathcal{O}(\alpha_{\mathrm{s}})$ QCD virtual factorizable corrections to (on-shell) Higgs production $\gamma\gamma \to \mathrm{H}$ can be deduced from the corresponding two-loop calculations [64] (see also references therein) for the decay $\mathrm{H} \to \gamma\gamma$.

4.2.3 Non-factorizable corrections

As explained in Section 4.2.1, we make use of the result for the non-factorizable corrections to $\mathrm{e}^+\mathrm{e}^- \to \mathrm{WW} \to 4f$. According to Refs. [19, 61] we write the correction factor to the lowest-order cross section as a sum over contributions that are associated with different pairs of fermions,

$$\delta_{\mathrm{virt,nfact}} = \sum_{a=1,2}\sum_{b=3,4}(-1)^{a+b+1}Q_aQ_b\frac{\alpha}{\pi}\,\mathrm{Re}\Big\{\Delta^{\mathrm{virt}}(k_+,p_a;k_-,p_b)\Big\}\,. \tag{4.2.20}$$

The function Δ^{virt} receives contributions from the different types of diagrams in Figure 4.2,

$$\Delta^{\mathrm{virt}} = \Delta^{\mathrm{virt}}_{\mathrm{mf}'} + \Delta^{\mathrm{virt}}_{\mathrm{ff}'} + \Delta^{\mathrm{virt}}_{\mathrm{mm}'} + \Delta^{\mathrm{virt}}_{\mathrm{mf}} + \Delta^{\mathrm{virt}}_{\mathrm{mm}}, \tag{4.2.21}$$

for which the results were given in terms of scalar integrals in Ref. [19]. The final result for $a=2, b=3$ (all other contributions can be derived by appropriate substitutions) is

$$\begin{aligned}
&\Delta^{\mathrm{virt}}_{\mathrm{mf}'} + \Delta^{\mathrm{virt}}_{\mathrm{ff}'} + \Delta^{\mathrm{virt}}_{\mathrm{mf}} \\
&\qquad \sim\; -\frac{K_+K_-s_{23}\det(Y_0)}{\det(Y)}D_0(-p_4,k_++p_3,p_2+p_3,0,M,M,0) \\
&\qquad\quad -\frac{K_+\det(Y_3)}{\det(Y)}F_3 - \frac{K_-\det(Y_2)}{\det(Y)}F_2 + \ln\left(\frac{\lambda^2}{M_{\mathrm{W}}^2}\right)\ln\left(-\frac{s_{23}}{M_{\mathrm{W}}^2}-\mathrm{i}\epsilon\right), \\
&\Delta^{\mathrm{virt}}_{\mathrm{mm}'} \sim (2M_{\mathrm{W}}^2-s)\Big\{C_0(k_+,-k_-,0,M,M) - C_0(k_+,-k_-,\lambda,M_{\mathrm{W}},M_{\mathrm{W}})\Big|_{k_\pm^2=M_{\mathrm{W}}^2}\Big\}, \\
&\Delta^{\mathrm{virt}}_{\mathrm{mm}} \sim 2\ln\left(\frac{\lambda M_{\mathrm{W}}}{-K_+}\right) + 2\ln\left(\frac{\lambda M_{\mathrm{W}}}{-K_-}\right) + 4,
\end{aligned} \tag{4.2.22}$$

where the sign "$\sim$" indicates that the limit $k_\pm^2 \to M_{\mathrm{W}}^2$ and $\Gamma_{\mathrm{W}} \to 0$ is carried out whenever this does not lead to a singularity. The matrices Y_0, Y_2, Y_3, and Y arise from the reduction of 5-point functions and can be found in Section 3.1 of Ref. [61]. The functions F_2 and F_3 are defined in Section 4.2, and the C_0 and D_0 functions in Appendix C.1 of the same reference. The contribution $\Delta^{\mathrm{virt}}_{\mathrm{mm}'}$ contains the difference of the full off-shell and on-shell Coulomb singularity, as described there in detail.

The full correction factor $\delta_{\mathrm{virt,nfact}}$ does not contain fermion-mass singularities [19], but involves IR-singular terms $\ln\lambda$, as explicitly visible in Eq. (4.2.22). The latter originate

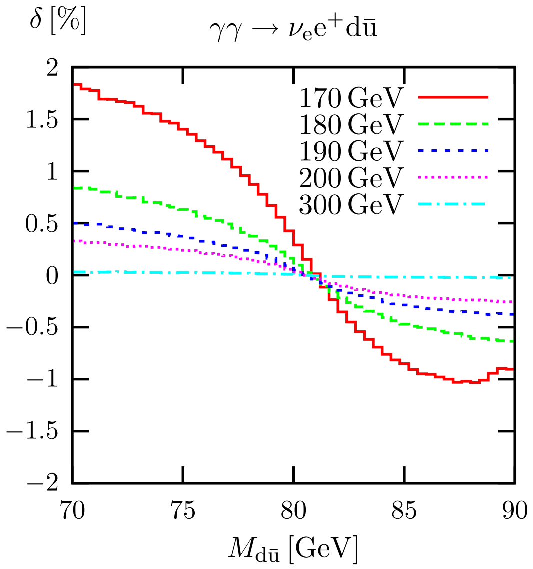

Figure 4.3: Relative correction factor of the non-factorizable virtual and real corrections to the invariant-mass distribution of the $\mathrm{d}\bar{\mathrm{u}}$ pair in the reaction $\gamma\gamma \to \nu_{\mathrm{e}}\mathrm{e}^{+}\mathrm{d}\bar{\mathrm{u}}$ for various CM energies $\sqrt{s_{\gamma\gamma}}$.

from the subtraction of the virtual factorizable correction, which involves the one-loop matrix elements for $\gamma\gamma \to \mathrm{WW}$ and $\mathrm{W} \to f\bar{f}'$ with on-shell W bosons, from the doubly-resonant part of the matrix element for the full $\gamma\gamma \to 4f$ process. Specifically, the $\ln\lambda$ terms stem from diagrams with photon exchange between an on-shell W boson and another on-shell particle. As already explained in Section 4.2.1, these singularities cancel in the sum of factorizable and non-factorizable contributions, since they are artificially introduced in the corresponding decomposition of the virtual correction. The explicit formulae for the soft and collinear singularities of the factorizable and non-factorizable contributions will be given in App. B.

In Section 2.4 we mentioned that the non-factorizable corrections vanish if the invariant mass of the W bosons is completely integrated over. However, they become important in invariant-mass distributions for the W bosons, which are needed for the kinematical reconstruction of the event. In order to demonstrate the size of the corrections we show the relative correction factor for the invariant-mass distribution of the $\mathrm{d}\bar{\mathrm{u}}$ pair in the reaction $\gamma\gamma \to \nu_{\mathrm{e}}\mathrm{e}^{+}\mathrm{d}\bar{\mathrm{u}}$ for the input parameters specified in Section 4.4.1. Since the virtual non-factorizable corrections are infrared divergent, we also included the corresponding non-factorizable real corrections. Note that this is only done in Figure 4.3. Later we will employ the real corrections based on the complete lowest-order matrix elements for $\gamma\gamma \to 4f\gamma$. The non-factorizable real corrections originate from interferences of diagrams where soft photons are emitted from different subprocesses. As in the case of the virtual corrections, there are diagrams that contain both factorizable and non-factorizable corrections. Their classification proceeds along the same line as for the virtual corrections. In Ref. [60] it was shown that all non-factorizable corrections connected with the initial state drop out in the sum of virtual and real corrections. Hence, we can simply take over the correction factor that was calculated in Ref. [61] for the process $e^-e^+ \to WW \to 4f$. Figure 4.3 shows that the corrections become larger for decreasing CM energy reaching almost 2% for $\sqrt{s_{\gamma\gamma}} = 170\,\mathrm{GeV}$. If a photon is emitted from the final state the invariant mass of the $d\bar{u}$ pair is smaller than the invariant mass of the resonant W boson. Therefore, the corrections result in a rearrangement of events in the resonance region. This also shows that a realistic prediction of the corrections very much depends on how the photons in the final state are treated experimentally. In the following, instead of employing the non-factorizable real corrections in DPA, we will make use of the complete matrix elements for $\gamma\gamma \to 4f\gamma$ as defined in Section 4.1. The experimental treatment of the photons can then be specified in the Monte Carlo generator. This issue will be discussed in more detail in Section 4.4.

4.2.4 Leading universal corrections and input-parameter scheme

We parametrize the cross section in such a way that the universal corrections arising from the running of the electromagnetic coupling α and from the ρ-parameter are absorbed in the lowest order. In Section 3.5.1 we argued that the relevant coupling for the $\gamma\gamma \to$ WW production process is the fine-structure constant $\alpha(0)$, because the external on-shell photons do not induce any running in their coupling to the W bosons. For the decay of the W bosons, it is, however, appropriate to derive α from the Fermi constant G_μ according to Eq. (3.5.3).

The definition of the electromagnetic coupling α has implications on the renormalization. For the $\gamma\gamma \to$ WW production process we can perform the on-shell renormalization precisely as described in Refs. [6]. For the decay of the W bosons, however, the modification of the coupling in the G_μ scheme induces an additional finite contribution to the charge renormalization constant,

$$\delta Z_{\mathrm{e}}|_{G_\mu} = \delta Z_{\mathrm{e}}|_{\alpha(0)} - \frac{1}{2}\Delta r, \tag{4.2.23}$$

where $\delta Z_{\mathrm{e}}|_{\alpha(0)}$ is the charge renormalization constant of the on-shell renormalization scheme [6] with $\alpha(0)$ as renormalized coupling. The quantity Δr contains the radiative corrections to muon decay; explicit expressions for Δr can, e.g., be found in Refs. [6, 65].

In summary, our lowest-order cross section scales like $\alpha(0)^2\alpha_{G_\mu}^2$. For the relative $\mathcal{O}(\alpha)$ corrections we use $\alpha(0)$, which is the correct effective coupling for real photon emission, so that the corrected cross section scales like $\alpha(0)^3\alpha_{G_\mu}^2$. For the loop-induced Higgs resonance we exceptionally take the scaling factor $\alpha(0)^2\alpha_{G_\mu}^3$, which accounts for the two "photonic" and the three "weak" couplings in the corresponding diagrams. We perform this rescaling, of course, only in the gauge-invariant resonant part $\delta\mathcal{M}_{\mathrm{Higgs}}$ of the one-loop amplitude, as defined in Eq. (4.2.19).

4.2.5 Improved Born approximation

The motivation for calculating the virtual corrections in DPA lies in the dominance of doubly-resonant diagrams. At threshold, however, singly-resonant and non-resonant diagrams become equally important, thus, rendering the naive error estimate of

$\mathcal{O}(\alpha\Gamma_\mathrm{W}/(M_\mathrm{W}\pi))$ unreliable. As a consequence, we decided to use the DPA only for a CM energy $\sqrt{s_{\gamma\gamma}} > 170\,\mathrm{GeV}$ when integrating over the photon spectrum. For $\sqrt{s_{\gamma\gamma}} < 170\,\mathrm{GeV}$ we make use of an improved Born approximation (IBA), i.e. we approximate the $\mathcal{O}(\alpha)$ corrections by universal contributions without any expansion about the W resonances. Assuming that the IBA accounts for all $\mathcal{O}(\alpha)$ corrections with pronounced enhancement factors, the relative uncertainty of the IBA is about ~ ±2%. For the corresponding $\mathrm{e}^+\mathrm{e}^-$ reaction this expectation was confirmed by the full $\mathcal{O}(\alpha)$ calculation [24] for $4f$ production.

In detail, we start from the Born cross section based on the full set of $\gamma\gamma \to 4f$ diagrams, which is parametrized as described in the previous section. We denote the resulting matrix element that includes the Higgs resonance with SM couplings, as described in Section 3.3, "Born+Higgs". In addition, we dress the resulting cross section with the off-shell Coulomb singularity,

$$\int \mathrm{d}\sigma^{\gamma\gamma\to 4f}_{\mathrm{IBA}} = \frac{1}{2s}\int \mathrm{d}\Phi_{4f}\,(1+\delta_{\mathrm{coul}})|\mathcal{M}^{\gamma\gamma\to 4f}_{\mathrm{Born+Higgs}}|^2. \tag{4.2.24}$$

The correction factor δ_coul for the Coulomb singularity was calculated in Ref. [66] to

$$\delta_{\mathrm{coul}} = \frac{\alpha(0)}{\bar\beta}\,\mathrm{Im}\left\{\ln\left(\frac{\beta+\Delta-\bar\beta}{\beta+\Delta+\bar\beta}\right)\right\}, \tag{4.2.25}$$

with the abbreviations

$$\begin{aligned}\bar\beta &= \frac{1}{s}\sqrt{s^2+(k_+^2)^2+(k_-^2)^2-2sk_+^2-2sk_-^2-2k_+^2k_-^2},\\ \beta &= \sqrt{1-\frac{4(M_\mathrm{W}^2-\mathrm{i}M_\mathrm{W}\Gamma_\mathrm{W})}{s}}, \qquad \Delta = \frac{|k_+^2-k_-^2|}{s}.\end{aligned} \tag{4.2.26}$$

4.3 Treatment of soft and collinear photon emission

We calculate the real photonic corrections from the full lowest-order matrix element of the process (4.1.4) without any expansion about the W-boson resonances. They are calculated from the integral

$$\int \mathrm{d}\sigma^{\gamma\gamma\to 4f\gamma} = \frac{1}{2s}\int \mathrm{d}\Phi_{4f\gamma}\,|\mathcal{M}^{\gamma\gamma\to 4f\gamma}|^2\,\Theta(\Phi_{4f\gamma}), \tag{4.3.1}$$

where we have made the implementation of phase-space cuts explicit by including the step function $\Theta(\Phi_{4f\gamma})$, which is equal to 1 if an event passes the cuts and 0 otherwise. Since we evaluate the real matrix element $\mathcal{M}^{\gamma\gamma\to 4f\gamma}$ with massless particles, the phase-space integral diverges in the soft and collinear regions, where the emitted photon is either soft or collinear to an outgoing external charged fermion. In these regions we reintroduce a formally infinitesimal photon mass λ and small fermion masses m_f as regulators.

To this end, we apply two different methods: the dipole subtraction and the (two-cutoff) phase-space slicing methods. In the case of collinear-safe observables we closely follow the approach of Ref. [19] and only give a brief description in Section 4.3.1 since the procedure is very similar to the $\mathrm{e}^+\mathrm{e}^-$ case. In Section 4.3.2 we describe how the two methods are extended to non-collinear-safe observables.

4.3.1 Collinear-safe observables

4.3.1.1 Phase-space slicing

In the phase-space slicing approach the phase space is divided into regions where the integrand is finite and can, thus, be integrated numerically, and regions where the integrand becomes singular. In the singular regions the integration over the photon phase space is carried out analytically in the approximation that the photon is soft and/or collinear to a charged fermion.

The singular regions consist of two parts one of which contains a soft photon ($k^0 < \Delta E$) and the other a photon that is collinear but not soft ($k^0 > \Delta E$ and $\theta_{\gamma f} < \Delta\theta$, where $\theta_{\gamma f}$ is the angle between the photon and a charged fermion). Thus, the real corrections are decomposed according to

$$\int \mathrm{d}\sigma^{\gamma\gamma\to 4f\gamma} = \int \mathrm{d}\sigma_{\mathrm{soft}} + \int \mathrm{d}\sigma_{\mathrm{coll}} + \int \mathrm{d}\sigma^{\gamma\gamma\to 4f\gamma}_{\mathrm{finite}}, \tag{4.3.2}$$

where the cutoff parameters ΔE and $\Delta\theta$ are defined in the CM system of the incoming photons. Both in the soft and collinear regions the squared matrix element $|\mathcal{M}^{\gamma\gamma\to 4f\gamma}|^2$ factorizes into the squared lowest-order matrix element $|\mathcal{M}^{\gamma\gamma\to 4f}_{\mathrm{Born}}|^2$ and a universal factor containing the singularity. The five-particle phase space also factorizes into a four-particle phase space and a photon part, so that $\mathrm{d}\sigma_{\mathrm{soft}}$ and $\mathrm{d}\sigma_{\mathrm{coll}}$ can be integrated over the photon momentum. Taking over the results from Ref. [19] yields

$$\begin{aligned}\mathrm{d}\sigma_{\mathrm{soft}} = {} & \mathrm{d}\sigma^{\gamma\gamma\to 4f}_{\mathrm{Born}}\,\Theta(\Phi_{4f})\,\frac{\alpha}{\pi}\sum_{i=1}^{4}\sum_{j=i+1}^{4}(-1)^{i+j}Q_iQ_j\left\{2\ln\left(\frac{2\Delta E}{\lambda}\right)\left[1-\ln\left(\frac{s_{ij}}{m_im_j}\right)\right]\right.\\ & \left. -\ln\left(\frac{4p_i^0p_j^0}{m_im_j}\right)+\ln^2\left(\frac{2p_i^0}{m_i}\right)+\ln^2\left(\frac{2p_j^0}{m_j}\right)+\frac{\pi^2}{3}+\mathrm{Li}_2\left(1-\frac{4p_i^0p_j^0}{s_{ij}}\right)\right\}\end{aligned} \tag{4.3.3}$$

and

$$\mathrm{d}\sigma_{\mathrm{coll}} = \mathrm{d}\sigma^{\gamma\gamma\to 4f}_{\mathrm{Born}}\,\Theta(\Phi_{4f})\,\frac{\alpha}{2\pi}\sum_{i=1}^{4}Q_i^2\left\{\left[\frac{3}{2}+2\ln\left(\frac{\Delta E}{p_i^0}\right)\right]\left[1-2\ln\left(\frac{\Delta\theta\, p_i^0}{m_i}\right)\right]+3-\frac{2\pi^2}{3}\right\}, \tag{4.3.4}$$

where Q_i and m_i denote the relative electric charge and mass of fermion f_i, respectively. The step function $\Theta(\Phi_{4f})$ indicates that both $\mathrm{d}\sigma_{\mathrm{soft}}$ and $\mathrm{d}\sigma_{\mathrm{coll}}$ are defined on the four-particle phase space of the lowest-order cross section, so that the singular part

$$\mathrm{d}\sigma^{\gamma\gamma\to 4f\gamma}_{\mathrm{sing}} = \mathrm{d}\sigma_{\mathrm{soft}} + \mathrm{d}\sigma_{\mathrm{coll}} \tag{4.3.5}$$

can be locally combined with the singular part of the virtual corrections, which are defined on the same phase space. In the result $\mathrm{d}\sigma^{\gamma\gamma\to 4f}_{\mathrm{virt+real,sing}}$ all dependences on the photon and fermion masses cancel.

While $\mathrm{d}\sigma^{\gamma\gamma\to 4f}_{\mathrm{virt+real,sing}}$ depends on the cutoff parameters ΔE and $\Delta\theta$ analytically, the finite real corrections $\int \mathrm{d}\sigma^{\gamma\gamma\to 4f\gamma}_{\mathrm{finite}}$ only show this dependence upon the cuts in the numerical integration. Nevertheless, the cutoff dependence has to cancel in the full result in the limit

$\Delta E, \Delta\theta \to 0$. This is illustrated on the l.h.s. of Figures 4.4 and 4.5 where the relative correction factor $\delta = \sigma/\sigma_{\mathrm{Born}} - 1$ of the $4f$ part ($\int \mathrm{d}\sigma^{\gamma\gamma\to 4f}_{\mathrm{virt,finite,DPA}} + \int \mathrm{d}\sigma^{\gamma\gamma\to 4f}_{\mathrm{virt+real,sing}}$) and of the $4f\gamma$ part $\int \mathrm{d}\sigma^{\gamma\gamma\to 4f\gamma}_{\mathrm{finite}}$ is shown as a function of the cutoff parameters ΔE and $\Delta\theta$. The cancellations of the cutoff dependence of the two contributions is shown on a smaller scale on the r.h.s. of Figures 4.4 and 4.5. While terms of $\mathcal{O}(\Delta E/E_{\mathrm{beam}})$ and $\mathcal{O}(\Delta\theta)$ become visible for large values of the cutoff parameters, for smaller values a plateau is reached. The integration error increases with decreasing cutoff values, until for too small values the integration error is usually underestimated. As a result, we decided to take $\Delta E/E_{\mathrm{beam}} = 10^{-3}$ and $\Delta\theta = 10^{-2}$ as default values.

4.3.1.2 Dipole subtraction method

In a subtraction method an auxiliary function is constructed that contains the same singularities as the real corrections. Subtracting this function from the real corrections, this difference can be integrated numerically. The next step is to perform the singular integration of the auxiliary function over the photon momentum analytically and to readd the result to the virtual corrections. In our case where soft and collinear singularities originate from final-state radiation only, the soft and collinear singularities completely cancel against their counterparts in the virtual corrections for collinear-safe observables.

In the dipole subtraction method [53, 67], which was originally proposed for QCD [68], the auxiliary function consists of different contributions labelled by all ordered combinations of two charged fermions i and j, which are called emitter and spectator. These contributions contain the singularities connected with the emitter i. Since there are only charged particles in the final state in $\gamma\gamma \to 4f$, the situation is simpler than for $\mathrm{e}^+\mathrm{e}^- \to 4f$. Explicitly the auxiliary function, which is subtracted from the spin-summed squared bremsstrahlung matrix element, reads

$$\begin{aligned} |\mathcal{M}_{\mathrm{sub}}|^2 &= \sum_{\substack{i,j=1\\ i\neq j}}^{4} |\mathcal{M}_{\mathrm{sub},ij}|^2, \\ |\mathcal{M}_{\mathrm{sub},ij}(\Phi_{4f\gamma})|^2 &= -(-1)^{i+j} Q_i Q_j e^2 g^{(\mathrm{sub})}_{ij}(p_i,p_j,k) |\mathcal{M}^{\gamma\gamma\to 4f}_{\mathrm{Born}}(\tilde{\Phi}_{4f,ij})|^2. \end{aligned} \tag{4.3.6}$$

Adopting the formulation of Ref. [67][2], the soft and collinear divergences are contained in the function

$$g^{(\mathrm{sub})}_{ij}(p_i,p_j,k) = \frac{1}{(p_i k)(1-y_{ij})}\left[\frac{2}{1-z_{ij}(1-y_{ij})} - 1 - z_{ij}\right] \tag{4.3.7}$$

with

$$y_{ij} = \frac{p_i k}{p_i p_j + p_i k + p_j k}, \qquad z_{ij} = \frac{p_i p_j}{p_i p_j + p_j k}. \tag{4.3.8}$$

The embedding of the $4f$ phase space $\tilde{\Phi}_{4f,ij}$ into the $4f\gamma$ phase space $\Phi_{4f\gamma}$ is defined as

$$\tilde{p}^{\mu}_i = p^{\mu}_i + k^{\mu} - \frac{y_{ij}}{1-y_{ij}} p^{\mu}_j, \qquad \tilde{p}^{\mu}_j = \frac{1}{1-y_{ij}} p^{\mu}_j, \tag{4.3.9}$$

---

[2] The formulation of Ref. [53] differs from that by the regular factor $1/(1-y_{ij})$ in Eq. (4.3.7), so that the readded singular contributions of Refs. [53] and [67] differ by non-singular finite parts.

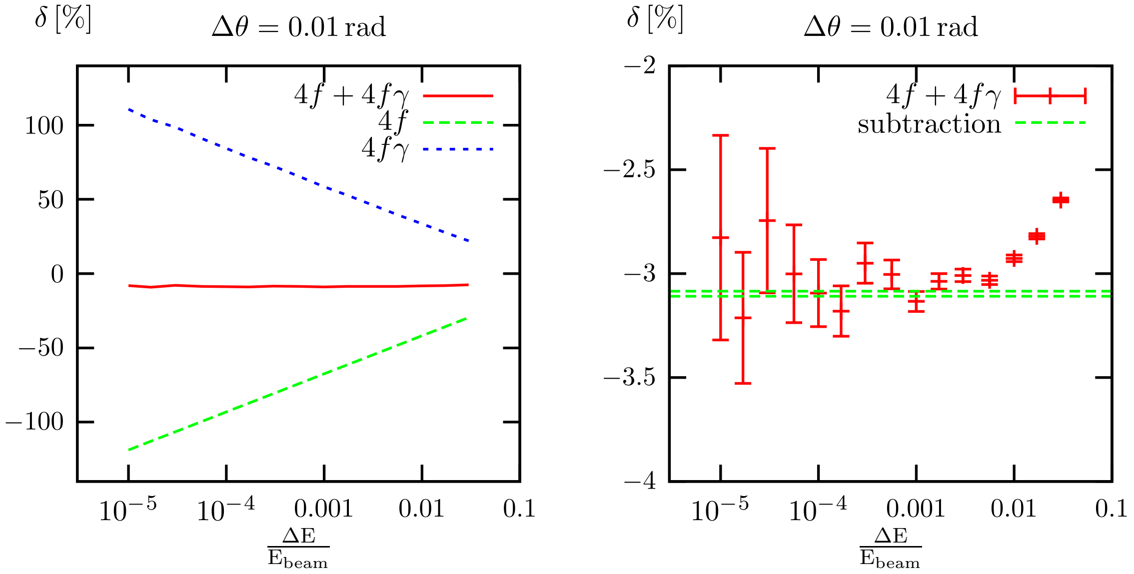

Figure 4.4: Dependence of the corrections on the energy cutoff in the slicing approach for the process $\gamma\gamma \to \nu_e e^+ d\bar{u}$ at $\sqrt{s_{\gamma\gamma}} = 500\,\mathrm{GeV}$. For comparison the corresponding result obtained with the dipole subtraction method is shown as a 1σ band in the plot on the r.h.s.

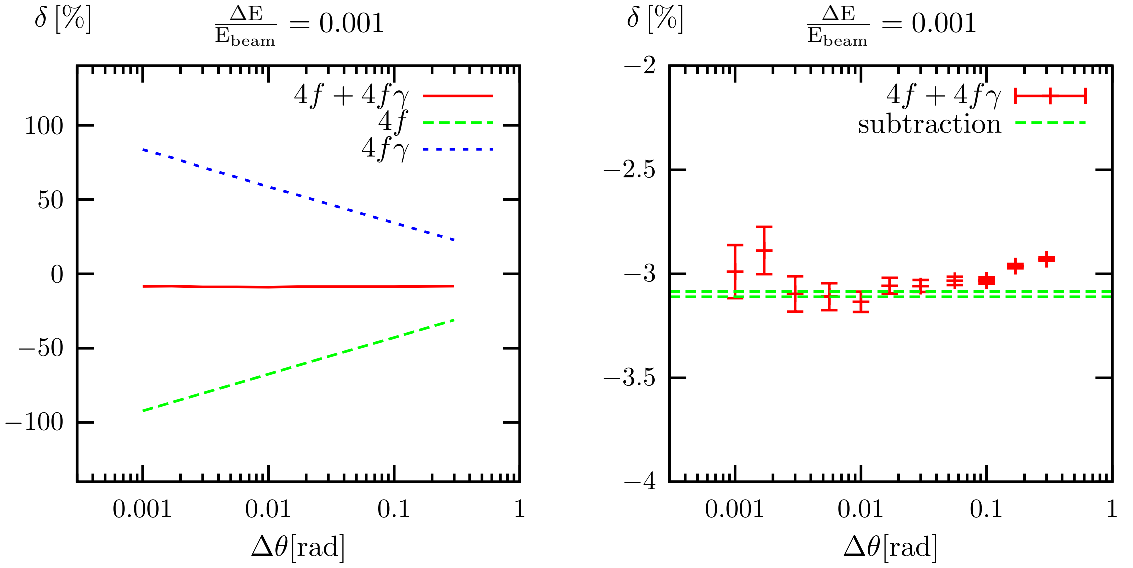

Figure 4.5: Dependence of the corrections on the angular cutoff in the slicing approach for the process $\gamma\gamma \to \nu_e e^+ d\bar{u}$ at $\sqrt{s_{\gamma\gamma}} = 500\,\mathrm{GeV}$. For comparison the corresponding result obtained with the subtraction method is shown as a 1σ band in the plot on the r.h.s.

with all other momenta unchanged, $\tilde{p}_k = p_k, k \neq i, j$. Subtracting the auxiliary function from the real corrections enables us to carry out the numerical integration,

$$\int \mathrm{d}\sigma_{\text{finite}}^{\gamma\gamma\to 4f\gamma} = \frac{1}{2s}\int \mathrm{d}\Phi_{4f\gamma}\left[|\mathcal{M}^{\gamma\gamma\to 4f\gamma}|^2\Theta(\Phi_{4f\gamma}) - \sum_{\substack{i,j=1\\ i\neq j}}^{4} |\mathcal{M}_{\mathrm{sub},ij}|^2\Theta(\tilde{\Phi}_{4f,ij})\right], \qquad (4.3.10)$$

which does not contain any soft or collinear divergences by construction of $|\mathcal{M}_{\mathrm{sub}}|^2$ for collinear-safe observables. In this context, it is important to notice the different arguments of the step functions Θ which account for phase-space cuts. Since for a generic point in $4f\gamma$ phase space each ij contribution corresponds to a different point in phase space, there is in general no correlation between the values of the different step functions. For collinear-safe observables, however, we have $\Theta(\Phi_{4f\gamma}) = \Theta(\tilde{\Phi}_{4f,ij})$ in the soft region ($k \to 0$) and in the region where the photon momentum k is nearly collinear to the emitter momentum p_i ($p_i k \to 0$). The collinear safety can, e.g., be enforced by photon recombination, as discussed in the next section in more detail.

In order to combine the subtraction function with the virtual correction, it has to be integrated over the photon momentum, yielding

$$\int \mathrm{d}\sigma_{\text{sing}}^{\gamma\gamma\to 4f\gamma} = -\frac{\alpha}{2\pi}\sum_{\substack{i,j=1\\ i\neq j}}^{4}(-1)^{i+j}Q_iQ_j\frac{1}{2s}\int \mathrm{d}\Phi_{4f}\, G_{ij}^{(\mathrm{sub})}(s_{ij})|\mathcal{M}_{\mathrm{Born}}^{\gamma\gamma\to 4f}(\Phi_{4f})|^2\Theta(\Phi_{4f}). \qquad (4.3.11)$$

The singularities are contained in the function

$$G_{ij}^{(\mathrm{sub})}(s_{ij}) = \mathcal{L}(s_{ij}, m_i^2) - \frac{\pi^2}{3} + \frac{3}{2} \qquad (4.3.12)$$

with

$$\mathcal{L}(s_{ij}, m_i^2) = \ln\left(\frac{m_i^2}{s_{ij}}\right)\ln\left(\frac{\lambda^2}{s_{ij}}\right) + \ln\left(\frac{\lambda^2}{s_{ij}}\right) - \frac{1}{2}\ln^2\left(\frac{m_i^2}{s_{ij}}\right) + \frac{1}{2}\ln\left(\frac{m_i^2}{s_{ij}}\right). \qquad (4.3.13)$$

We have checked numerically that these soft and collinear divergences are completely cancelled by their counterparts in the virtual correction.

4.3.2 Non-collinear-safe observables

In the previous sections the matching of real and virtual corrections was described for collinear-safe observables. We speak of collinear-safe observables if a nearly collinear system of a charged fermion and a photon is treated inclusively, i.e. if phase-space selection cuts (or histogram bins of distributions) depend only on the sum $p_i + k$ of the nearly collinear fermion and photon momenta. In this case the energy fraction

$$z_i = \frac{p_i^0}{p_i^0 + k^0} \qquad (4.3.14)$$

of a charged fermion f_i after emitting a photon in a sufficiently small cone around its direction of flight is fully integrated over, because it is not constrained by any phase-space cut (or histogram bin selection in distributions). Thus, the KLN theorem [69] guarantees that all singularities connected with final-state radiation cancel between the virtual and real corrections, even though they are defined on different phase spaces. A sufficient inclusiveness is, e.g., achieved by the photon recombination described in Section 4.4.1, which treats outgoing charged fermions and photons as one quasi-particle if they are very close in angle.

In the previous section we could, therefore, integrate the subtraction function $|\mathcal{M}_{\mathrm{sub}}|^2$ and the slicing contribution $\mathrm{d}\sigma_{\mathrm{coll}}$ over z_i analytically. In this section we are concerned with non-collinear-safe observables, i.e. the fermion–photon system is not treated inclusively and fermion-mass singularities can become visible. As the integration over z_i now is constrained by phase-space cuts (or histogram bins), we have to modify the methods described in the previous section in such a way that the integration over z_i is part of the numerical phase-space integration.

4.3.2.1 Phase-space slicing

In the slicing method the procedure is straightforward. The numerical integration over $z = z_i$ in the collinear parts reads

$$\mathrm{d}\sigma_{\mathrm{coll}} = \mathrm{d}\sigma_{\mathrm{Born}}^{\gamma\gamma\to 4f}(\tilde{\Phi}_{4f})\,\frac{\alpha}{2\pi}\sum_{i=1}^{4} Q_i^2 \int_0^{1-\Delta E/\tilde{p}_i^0} \mathrm{d}z\,\Theta\Big(p_i = z\tilde{p}_i, k = (1-z)\tilde{p}_i, \{\tilde{p}_{j\neq i}\}\Big) \times \left\{P_{ff}(z)\left[2\ln\left(\frac{\Delta\theta\,\tilde{p}_i^0}{m_i}z\right) - 1\right] + (1-z)\right\}, \tag{4.3.15}$$

with the splitting function

$$P_{ff}(z) = \frac{1+z^2}{1-z}. \tag{4.3.16}$$

The Born cross section and the logarithm still depend on the momenta of the $4f$ phase space $\tilde{\Phi}_{4f}$ which are labelled $\tilde{p}_i$. In the cut and recombination function Θ, however, the momentum $\tilde{p}_i$ of the fermion i (before photon emission) is distributed to the fermion momentum p_i and the photon momentum k. For collinear-safe observables, as e.g. achieved by photon recombination, the Θ function effectively only depends on the sum $p_i + k = \tilde{p}_i$ of the collinear momenta, which is independent of z. In this case, the Θ function becomes $\Theta(\tilde{\Phi}_{4f})$, and the z-integration can be easily carried out analytically yielding Eq. (4.3.4).

4.3.2.2 Dipole subtraction method

In the case of the dipole subtraction method the generalization to non-collinear-safe observables is more complicated than in the slicing approach, since the integration over the photon momentum is more involved. Here, we collect the formulas relevant for our calculation. Details on their derivation are given in Appendix A of Ref. [2].

In order to keep the information on the energy fraction z in each part of the subtraction function, the finite part of the real corrections is modified to

$$\int \mathrm{d}\sigma_{\mathrm{finite}}^{\gamma\gamma\to 4f\gamma} = \frac{1}{2s}\int \mathrm{d}\Phi_{4f\gamma}\Big[|\mathcal{M}^{\gamma\gamma\to 4f\gamma}|^2\Theta(\Phi_{4f\gamma})$$

$$
- \sum_{\substack{i,j=1\\ i\neq j}}^{4} |\mathcal{M}_{\mathrm{sub},ij}|^2 \Theta\Big(p_i = z_{ij}\tilde{p}_i, k = (1-z_{ij})\tilde{p}_i, \{\tilde{p}_{k\neq i}\}\Big)\Bigg]. \qquad (4.3.17)
$$

It is easily seen that the variable z_{ij}, which is defined in Eq. (4.3.8), plays the role of the energy fraction z_i in the collinear limit for each dipole ij. Again, in the collinear-safe case the Θ functions of the subtraction function depend only on the sums $p_i + k = \tilde{p}_i$ of collinear momenta; in this case we recover Eq. (4.3.10).

In the integration of the subtraction function over the photon phase space, we now have to leave the integrations over z_{ij} open. The resulting z_{ij} dependence of the integrand is most conveniently described with a $[...]_+$ prescription[3], which separates the soft singularity at $z_{ij} = 1$. The endpoint part at $z_{ij} = 1$, which results from the full integration over z_{ij}, exactly corresponds to the contribution of $G_{ij}^{(\mathrm{sub})}(\tilde{s}_{ij})$ for the collinear-safe case, as given in Eq. (4.3.12), where $\tilde{s}_{ij} = 2\tilde{p}_i\tilde{p}_j$. The continuum part in z_{ij} involves an integral over $\Big[\bar{\mathcal{G}}_{ij}^{(\mathrm{sub})}(\tilde{s}_{ij}, z_{ij})\Big]_+$ with

$$
\bar{\mathcal{G}}_{ij}^{(\mathrm{sub})}(\tilde{s}_{ij}, z) = P_{ff}(z)\left[\ln\left(\frac{\tilde{s}_{ij}z}{m_i^2}\right) - 1\right] + (1+z)\ln(1-z) + (1-z). \qquad (4.3.18)
$$

The total integrated subtraction part explicitly reads

$$
\begin{aligned}
\int \mathrm{d}\sigma_{\mathrm{sing}}^{\gamma\gamma\to 4f\gamma} = {} & -\frac{\alpha}{2\pi} \sum_{\substack{i,j=1\\ i\neq j}}^{4} (-1)^{i+j} Q_i Q_j \frac{1}{2s} \int \mathrm{d}\tilde{\Phi}_{4f,ij}\, |\mathcal{M}_{\mathrm{Born}}^{\gamma\gamma\to 4f}(\tilde{\Phi}_{4f,ij})|^2 \bigg\{ G_{ij}^{(\mathrm{sub})}(\tilde{s}_{ij})\Theta(\tilde{\Phi}_{4f,ij}) \\
& + \int_0^1 \mathrm{d}z\, \Big[\bar{\mathcal{G}}_{ij}^{(\mathrm{sub})}(\tilde{s}_{ij}, z)\Big]_+ \Theta\Big(p_i = z\tilde{p}_i, k = (1-z)\tilde{p}_i, \{\tilde{p}_{k\neq i}\}\Big)\bigg\}. \qquad (4.3.19)
\end{aligned}
$$

Owing to the $[...]_+$ prescription, the continuum part is zero if the full integration over z is carried out, thereby recovering the collinear-safe case (4.3.11).

4.4 Numerical results

4.4.1 Input parameters and setup

We use the same input parameters as in the previous chapter. In addition, we have to specify the fermion masses contained in the fermionic loop corrections. The complete list of input parameters is [55]

$$
\begin{array}{lll}
G_\mu = 1.16639\times 10^{-5}\,\mathrm{GeV}^{-2}, & \alpha(0) = 1/137.03599976, & \alpha_{\mathrm{s}} = 0.1172, \\
M_{\mathrm{W}} = 80.423\,\mathrm{GeV}, & \Gamma_{\mathrm{W}} = 2.118\,\mathrm{GeV}, & \\
M_{\mathrm{Z}} = 91.1876\,\mathrm{GeV}, & \Gamma_{\mathrm{Z}} = 2.4952\,\mathrm{GeV}, & \\
m_{\mathrm{e}} = 0.510998902\times 10^{-3}\,\mathrm{GeV}, & m_\mu = 0.105658357\,\mathrm{GeV}, & m_\tau = 1.77699\,\mathrm{GeV}, \\
m_{\mathrm{u}} = 0.066\,\mathrm{GeV}, & m_{\mathrm{c}} = 1.2\,\mathrm{GeV}, & m_{\mathrm{t}} = 174.3\,\mathrm{GeV}, \\
m_{\mathrm{d}} = 0.066\,\mathrm{GeV}, & m_{\mathrm{s}} = 0.15\,\mathrm{GeV}, & m_{\mathrm{b}} = 4.3\,\mathrm{GeV}, \quad (4.4.1)
\end{array}
$$

---

[3] We use the definition $\int_0^1 \mathrm{d}x\, [f(x)]_+\, g(x) \equiv \int_0^1 \mathrm{d}x\, f(x)\, [g(x) - g(1)]$.

where the masses of the light quarks are adjusted to reproduce the hadronic contribution to the photonic vacuum polarization of Ref. [70]. If not stated otherwise, the Higgs mass is $M_{\mathrm{H}} = 170\,\mathrm{GeV}$. In some cases we alternatively use $M_{\mathrm{H}} = 130\,\mathrm{GeV}$. The corresponding values for the Higgs-boson decay width Γ_{H}, which have been obtained with the program HDECAY [56], are given by

$$\Gamma_{\mathrm{H}}\,(M_{\mathrm{H}} = 170\,\mathrm{GeV}) = 0.3834\,\mathrm{GeV}, \qquad \Gamma_{\mathrm{H}}\,(M_{\mathrm{H}} = 130\,\mathrm{GeV}) = 0.004995\,\mathrm{GeV}. \tag{4.4.2}$$

We set the quark-mixing matrix to the unit matrix throughout, but in the limit of massless external fermions a non-trivial quark-mixing matrix can be included by a simple rescaling of the cross sections.

Furthermore, we apply a set of recombination and separation cuts:

(i) Bremsstrahlung photons that are closer than 5° to a charged fermion or have less energy than 1 GeV are recombined with the charged fermion that is closest in angle. This means that in this case before evaluating distributions or applying phase-space cuts the momenta of the photon and the fermion are added and associated with the fermion, while the photon is discarded.

(ii) The separation cuts, which are applied to the momenta defined after a possible recombination, are the same as the cuts we used in the previous chapter for the tree-level cross section of $\gamma\gamma \to 4f$. Explicitly, they read

$$\begin{aligned} &E_l > 10\,\mathrm{GeV}, \qquad \theta(l,\mathrm{beam}) > 5^\circ, \qquad \theta(l,l') > 5^\circ, \qquad \theta(l,q) > 5^\circ, \\ &E_q > 10\,\mathrm{GeV}, \qquad \theta(q,\mathrm{beam}) > 5^\circ, \qquad m(q,q') > 10\,\mathrm{GeV}, \end{aligned} \tag{4.4.3}$$

where an obvious notation for energies $E_{\dots}$, angles $\theta(\dots)$, and invariant masses $m(\dots)$ for leptons l and quarks q is used.

Since the separation cuts and input parameters are the same as in the previous chapter for the processes $\gamma\gamma \to 4f$, the Born cross sections of both chapters coincide. In particular, we exclude forward and backward scattered charged fermions, because they cause collinear singularities. While for final-state quarks these singularities signal a non-perturbative regime, for leptons they are in principle cured by finite-mass effects. However, we exclude this region by demanding that leptons appear in the detector with finite production angle and energy. Compared to Ref. [19] we use different recombination cuts, because, in contrast to $\mathrm{e}^+\mathrm{e}^-$ collisions, the recombination criterion based on invariant masses does not lead to collinear-safe observables. This is due to the collinear singularity that arises if a charged fermion is collinear to the beam. Even though an appropriate cut on the angle between charged fermions and the beam is imposed, it might happen that a photon with relatively high energy is recombined with a low-energy fermion that is close to the beam. Thus, after recombination, the fermion almost follows the direction of the photon and is not affected by the angular cut. Such events are avoided by taking a recombination condition based on the angle.

For the evaluation of the lowest-order matrix elements of $\gamma\gamma \to 4f$ and $\gamma\gamma \to 4f\gamma$, we use the fixed-width scheme as defined in Eq. (3.1.22). The photon spectrum is accounted for by using the parametrization of the program CompAZ [14], as described in Section 3.4. In order to distinguish the cases with and without convolution over the photon spectrum, we write $\sqrt{s_{\mathrm{ee}}}$ and $\sqrt{s_{\gamma\gamma}}$ for the CM energies in these cases, respectively.

In the numerical integration we generate $2 \cdot 10^7$ events for the plots showing the integrated cross sections, and $5 \cdot 10^7$ events for distributions and for the integrated cross sections in Table 4.1. If not stated otherwise, the shown results are based on the subtraction method, but have been cross-checked with the slicing approach.

4.4.2 Integrated cross sections

In Table 4.1 we present a survey of integrated cross sections for a leptonic, a hadronic, and two semi-leptonic final states, as obtained with the subtraction and slicing methods. The cross sections of the semi-leptonic final states differ because of the effective polarizations of the photons resulting from the Compton backscattering (cf. Section 3.5.2.6). Final states that differ only in the fermion generation (i.e. in their mass values) receive the same radiative corrections, since our predictions are based on the massless limit for the external fermions and mass singularities cancel after performing a photon recombination. The results obtained with the two methods for treating the real corrections, subtraction ("sub") and slicing ("sli"), are in good agreement. Note that they both are implemented in the same Monte Carlo generator, which, thus, yields identical results for $\sqrt{s_{\gamma\gamma}} < 170\,\mathrm{GeV}$ where the IBA is used. This is the reason why the "sub" and "sli" numbers are identical in the case of $\sqrt{s_{\mathrm{ee}}} = 200\,\mathrm{GeV}$ with γ spectrum, where only the range $\sqrt{s_{\gamma\gamma}} < 170\,\mathrm{GeV}$ is relevant in the convolution.

In Figure 4.6 the integrated cross section for $\gamma\gamma \to \nu_{\mathrm{e}}\mathrm{e}^+\mathrm{d}\bar{\mathrm{u}}$ including radiative corrections is compared with the Born cross section as a function of the CM energy for monochromatic photon beams. The "best" curves correspond to the $\mathcal{O}(\alpha)$-corrected cross sections. A Higgs boson of $M_{\mathrm{H}} = 170\,\mathrm{GeV}$ produces a sharp peak in the cross section at $\sqrt{s_{\gamma\gamma}} = 170\,\mathrm{GeV}$, while for larger energies the corrections are almost independent of the Higgs mass. The relative corrections $\delta = \sigma/\sigma_{\mathrm{Born}} - 1$ in the four lower plots of Figure 4.6 behave roughly like the corrections to on-shell W-pair production [39, 59, 62]. Close to the W-pair production threshold the corrections are dominated by the Coulomb singularity. For higher energies the corrections decrease until they reach about -7% at $1\,\mathrm{TeV}$. In this region they are dominated by large logarithms from the Regge and Sudakov domains.

In Figure 4.6(c) we also show the comparison with the IBA for a Higgs mass of $M_{\mathrm{H}} = 130\,\mathrm{GeV}$. Since close to the W-pair production threshold the bulk of the corrections is due to the Coulomb singularity and since there are no other pronounced corrections, the agreement between the two curves is quite good. The very good agreement of the DPA and the IBA at $\sqrt{s_{\gamma\gamma}} \sim 170\,\mathrm{GeV}$ both for semi-leptonic and for hadronic final states (in both cases the difference is well below 0.1%) is of course accidental. For the leptonic final state the difference is about 0.7%.

As explained in Section 4.2.5, the intrinsic uncertainty of the IBA is about $\sim \pm 2\%$, while the DPA accuracy is up to $\lesssim 0.5\%$ where it is applicable. Since the convolution of the hard $\gamma\gamma$ cross section, in general, involves both the IBA (in the low-energy tail) and the DPA (for $\sqrt{s_{\gamma\gamma}} > 170\,\mathrm{GeV}$), the uncertainty of our cross-section prediction is in

		σ[fb]		σ_{Born}[fb]	
CM energy	final state	subtraction	slicing		(sub–sli)/sli
$\sqrt{s_{\gamma\gamma}} = 200$ GeV without γ spectrum	$\nu_{\mathrm{e}}\mathrm{e}^+\mu^-\bar{\nu}_\mu$	581.403(67)	581.41(16)	575.628(64)	0.00(3) %
	$\nu_{\mathrm{e}}\mathrm{e}^+\mathrm{d}\bar{\mathrm{u}}$	1734.02(23)	1735.26(43)	1716.10(22)	−0.07(3) %
	$\mathrm{u}\bar{\mathrm{d}}\mathrm{e}^-\bar{\nu}_{\mathrm{e}}$	1734.24(23)	1734.32(43)	1716.06(22)	0.00(3) %
	$\mathrm{u}\bar{\mathrm{d}}\mathrm{s}\bar{\mathrm{c}}$	4931.01(76)	4935.0(1.0)	4878.67(73)	−0.08(3) %
$\sqrt{s_{\gamma\gamma}} = 500$ GeV without γ spectrum	$\nu_{\mathrm{e}}\mathrm{e}^+\mu^-\bar{\nu}_\mu$	801.21(11)	801.57(20)	826.620(91)	−0.05(3) %
	$\nu_{\mathrm{e}}\mathrm{e}^+\mathrm{d}\bar{\mathrm{u}}$	2278.50(34)	2279.96(51)	2351.37(30)	−0.06(3) %
	$\mathrm{u}\bar{\mathrm{d}}\mathrm{e}^-\bar{\nu}_{\mathrm{e}}$	2278.45(34)	2278.84(48)	2351.39(30)	−0.02(3) %
	$\mathrm{u}\bar{\mathrm{d}}\mathrm{s}\bar{\mathrm{c}}$	6452.2(1.0)	6452.8(1.2)	6662.25(96)	−0.01(2) %
$\sqrt{s_{\gamma\gamma}} = 1000$ GeV without γ spectrum	$\nu_{\mathrm{e}}\mathrm{e}^+\mu^-\bar{\nu}_\mu$	696.25(15)	696.68(17)	746.995(93)	−0.06(3) %
	$\nu_{\mathrm{e}}\mathrm{e}^+\mathrm{d}\bar{\mathrm{u}}$	1836.31(43)	1836.96(45)	1979.92(29)	−0.04(3) %
	$\mathrm{u}\bar{\mathrm{d}}\mathrm{e}^-\bar{\nu}_{\mathrm{e}}$	1836.37(42)	1836.95(42)	1979.95(29)	−0.03(3) %
	$\mathrm{u}\bar{\mathrm{d}}\mathrm{s}\bar{\mathrm{c}}$	4892.2(1.2)	4891.4(1.1)	5300.97(90)	0.02(3) %
$\sqrt{s_{\mathrm{ee}}} = 200$ GeV with γ spectrum	$\nu_{\mathrm{e}}\mathrm{e}^+\mu^-\bar{\nu}_\mu$	0.073205(44)	0.073205(44)	0.072009(44)	0
	$\nu_{\mathrm{e}}\mathrm{e}^+\mathrm{d}\bar{\mathrm{u}}$	0.33129(21)	0.33129(21)	0.32601(21)	0
	$\mathrm{u}\bar{\mathrm{d}}\mathrm{e}^-\bar{\nu}_{\mathrm{e}}$	0.39204(25)	0.39204(25)	0.38593(24)	0
	$\mathrm{u}\bar{\mathrm{d}}\mathrm{s}\bar{\mathrm{c}}$	1.24460(79)	1.24460(79)	1.22537(78)	0
$\sqrt{s_{\mathrm{ee}}} = 500$ GeV with γ spectrum	$\nu_{\mathrm{e}}\mathrm{e}^+\mu^-\bar{\nu}_\mu$	190.757(60)	190.835(96)	190.816(45)	−0.04(6) %
	$\nu_{\mathrm{e}}\mathrm{e}^+\mathrm{d}\bar{\mathrm{u}}$	559.18(18)	559.63(24)	558.50(14)	−0.08(5) %
	$\mathrm{u}\bar{\mathrm{d}}\mathrm{e}^-\bar{\nu}_{\mathrm{e}}$	564.58(18)	564.79(25)	565.05(14)	−0.04(5) %
	$\mathrm{u}\bar{\mathrm{d}}\mathrm{s}\bar{\mathrm{c}}$	1604.92(54)	1605.60(59)	1603.80(45)	−0.04(5) %
$\sqrt{s_{\mathrm{ee}}} = 1000$ GeV with γ spectrum	$\nu_{\mathrm{e}}\mathrm{e}^+\mu^-\bar{\nu}_\mu$	165.759(91)	165.604(81)	170.588(41)	0.09(7) %
	$\nu_{\mathrm{e}}\mathrm{e}^+\mathrm{d}\bar{\mathrm{u}}$	461.02(20)	461.34(23)	474.81(12)	−0.07(7) %
	$\mathrm{u}\bar{\mathrm{d}}\mathrm{e}^-\bar{\nu}_{\mathrm{e}}$	472.10(19)	471.61(24)	485.65(13)	0.10(7) %
	$\mathrm{u}\bar{\mathrm{d}}\mathrm{s}\bar{\mathrm{c}}$	1296.49(52)	1295.29(62)	1335.13(38)	0.09(6) %

Table 4.1: Integrated cross sections for different final states and energies with and without convolution over the photon spectrum. The third column shows the result obtained with the subtraction method and the fourth with the slicing method. The last two columns show the Born cross section and the relative difference between subtraction and slicing.

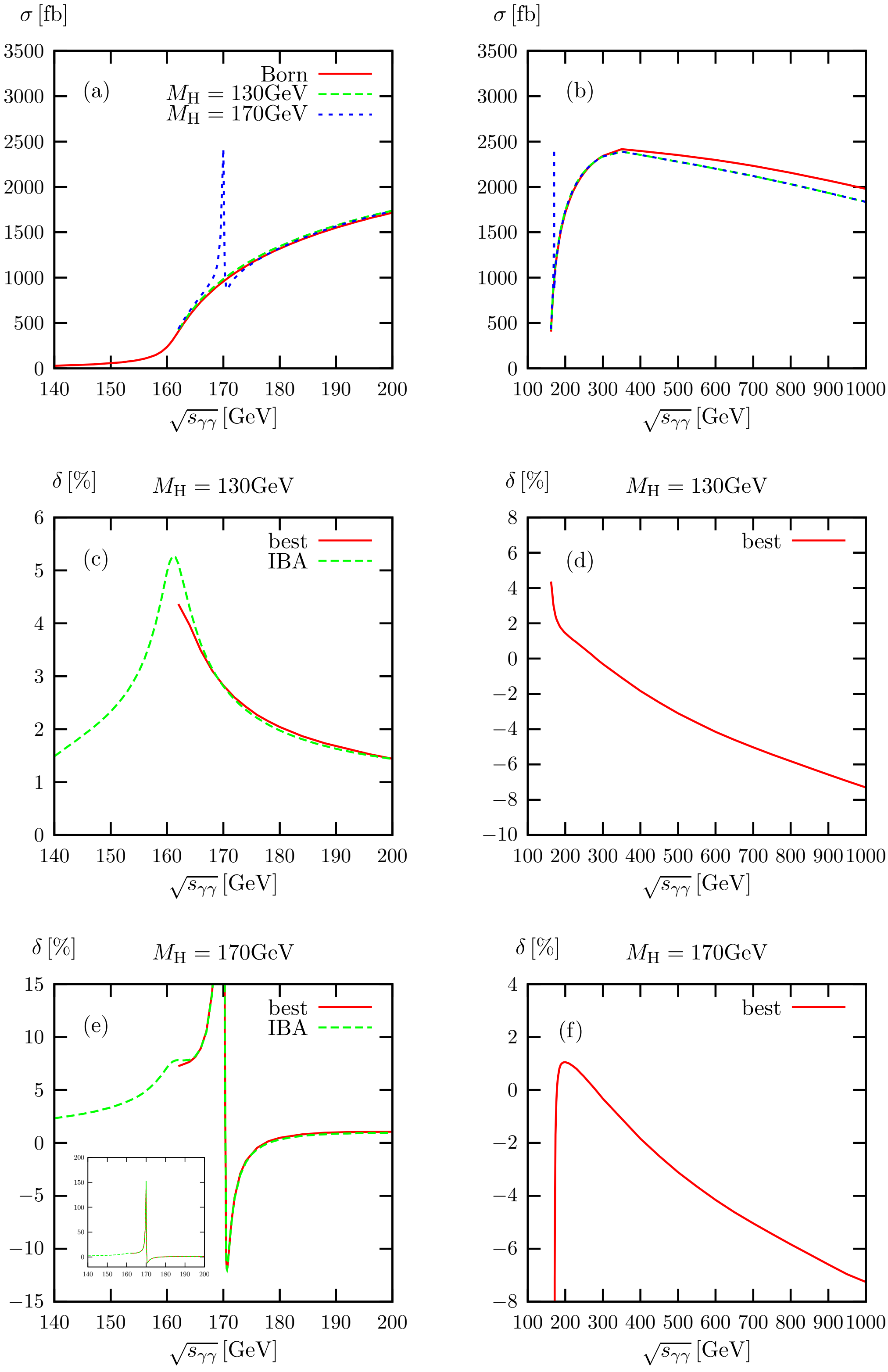

Figure 4.6: Integrated cross section for $\gamma\gamma \to \nu_{\rm e}{\rm e}^+{\rm d}\bar{\rm u}$ (the two upper plots) and relative radiative corrections (the four lower plots) without convolution over the photon spectrum for Higgs masses $M_{\rm H} = 130\,\mathrm{GeV}$ and $170\,\mathrm{GeV}$.

$\sqrt{s_{\mathrm{ee}}}$/ GeV	200	240	260	280	300	500	1000
TU	2.0%	1.9%	1.3%	0.8%	0.7%	0.5%	0.5%

Table 4.2: Estimates of the TU (4.4.4) for the $\mathcal{O}(\alpha)$-corrected cross section of $\gamma\gamma \to \nu_{\mathrm{e}}\mathrm{e}^+\mathrm{d}\bar{\mathrm{u}}$ at various CM energies $\sqrt{s_{\mathrm{ee}}}$.

the range 0.5−2%, depending on the contribution of the IBA part to the full convolution. Denoting the IBA and DPA parts of the full cross section as $\Delta\sigma_{\mathrm{IBA}}$ and $\Delta\sigma_{\mathrm{DPA}}$ (both including the corresponding lowest-order contribution, so that $\Delta\sigma_{\mathrm{IBA}} + \Delta\sigma_{\mathrm{DPA}} = \sigma$), we can estimate the theoretical uncertainty (TU) of the corrected cross section σ to

$$\mathrm{TU} = \frac{\Delta\sigma_{\mathrm{IBA}}}{\sigma} \times 2\% + \frac{\Delta\sigma_{\mathrm{DPA}}}{\sigma} \times 0.5\%. \tag{4.4.4}$$

Table 4.4.2 illustrates this estimate for a few CM energies $\sqrt{s_{\mathrm{ee}}}$ for $\gamma\gamma \to \nu_{\mathrm{e}}\mathrm{e}^+\mathrm{d}\bar{\mathrm{u}}$. For $\sqrt{s_{\mathrm{ee}}} \lesssim 230\,\mathrm{GeV}$ our prediction possesses a TU of $\sim 2\%$, because it is mainly based on the IBA, but already for $\sqrt{s_{\mathrm{ee}}} \gtrsim 300\,\mathrm{GeV}$ (500 GeV) the IBA contribution is widely suppressed so that the DPA uncertainty of $\lesssim 0.7\%$ (0.5%) sets the precision of our calculation. We note, however, that the overall uncertainty of our calculation certainly becomes worse as soon as TeV energies for $\sqrt{s_{\gamma\gamma}}$ are dominating because of the relevance of high-energy logarithms beyond $\mathcal{O}(\alpha)$.

In Figure 4.6(e) the comparison of the full correction with the IBA is shown for a Higgs mass of $M_{\mathrm{H}} = 170\,\mathrm{GeV}$. The IBA includes the Higgs resonance via an effective coupling and reflects the shape of the resonance quite well.

The cross section including the convolution over the photon spectrum as a function of CM energy is shown in Figure 4.7 for a Higgs mass of $M_{\mathrm{H}} = 130\,\mathrm{GeV}$ and in the lower left plot also for $M_{\mathrm{H}} = 170\,\mathrm{GeV}$. In the upper plots the integrated cross sections are shown, and in the lower plots the corrections relative to the Born cross section. Recall that we use the IBA below $\sqrt{s_{\gamma\gamma}} = 170\,\mathrm{GeV}$. This means, in particular, that the Higgs resonance is calculated from the effective coupling and not from the full DPA in this region. The interesting structure in the lower left plot reflects the shape of the photon spectrum convoluted with the Higgs resonance. Since the Higgs resonance is very narrow, a sizable contribution is only possible if $x_1 x_2 s_{\mathrm{ee}} \approx M_{\mathrm{H}}^2$ where x_1 and x_2 are the energy fractions carried by the photons. The correction is very small at low $\sqrt{s_{\mathrm{ee}}}$ where x_1 and x_2 have to be so large in order to match this condition that the corresponding spectrum is extremely small. Increasing $\sqrt{s_{\mathrm{ee}}}$ allows for lower values of x_1 and x_2. For instance, for $M_{\mathrm{H}} = 130\,\mathrm{GeV}$, the rise at $\sqrt{s_{\mathrm{ee}}} \sim 180\,\mathrm{GeV}$ results from a region where both x_1 and x_2 are in the high-energy tail of the spectrum which is produced by multiple photon scattering. The peak at $\sqrt{s_{\mathrm{ee}}} \sim 200\,\mathrm{GeV}$ is caused by events where one photon comes from the high-energy tail and one from the dominant peak in the photon spectrum. Finally, at $\sqrt{s_{\mathrm{ee}}} \gtrsim 210\,\mathrm{GeV}$ both x_1 and x_2 originate from the dominant photon-spectrum peak which causes the steep rise until $\sqrt{s_{\mathrm{ee}}} \sim 220\,\mathrm{GeV}$.

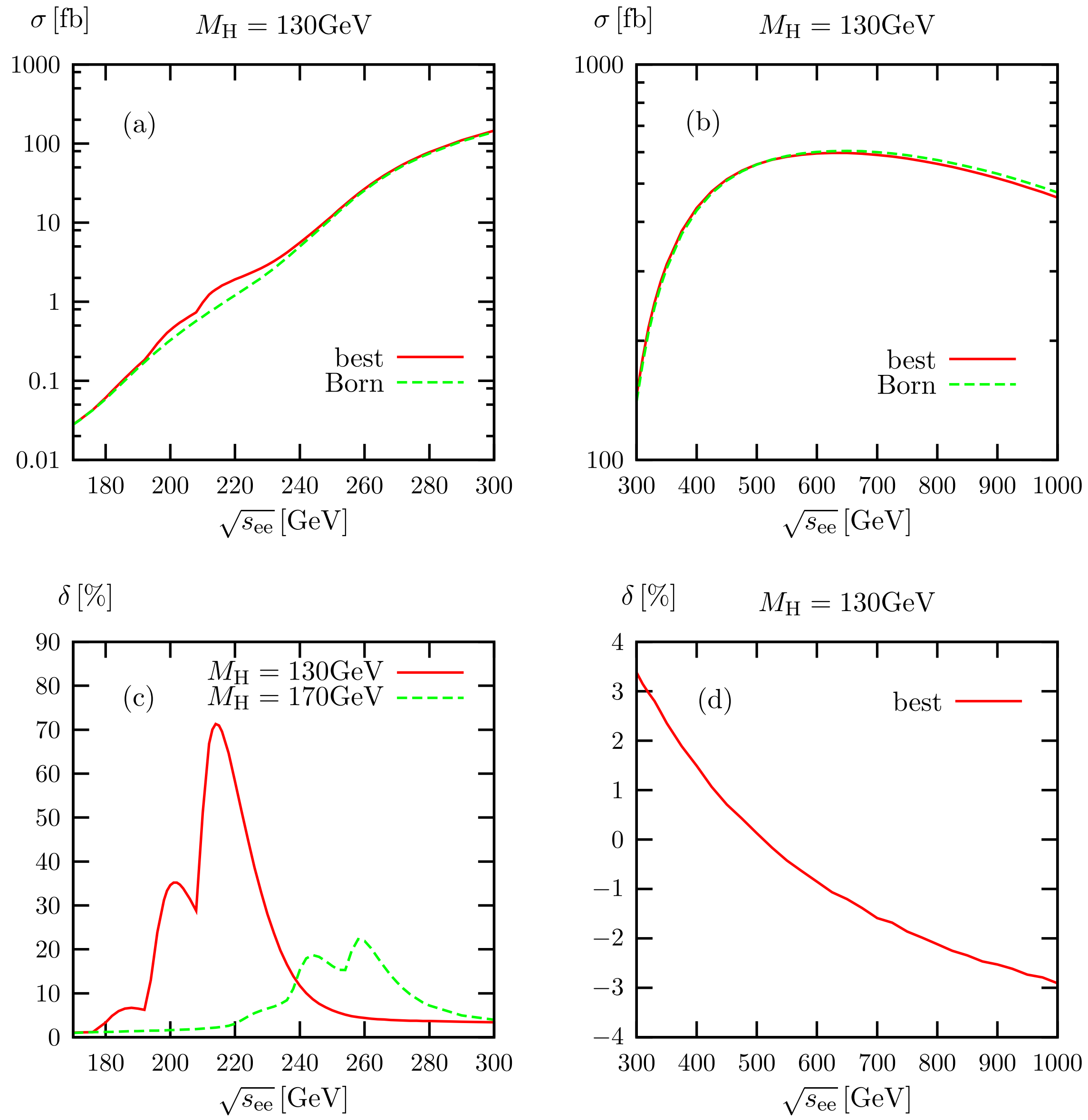

Figure 4.7: Integrated cross section for $\gamma\gamma \to \nu_e e^+ d\bar{u}$ (upper plots) and relative radiative corrections (lower plots) including the convolution over the photon spectrum for Higgs masses of $M_H = 130$ GeV and 170 GeV (lower left plot). For $\sqrt{s_{ee}} > 300$ GeV (shown on the r.h.s.) the "best" curve for $M_H = 170$ GeV practically coincides with the shown curve for $M_H = 130$ GeV.

4.4.3 Differential cross sections

In Figure 4.8 we show the invariant-mass distributions for the $\nu_{\mathrm{e}}\mathrm{e}^+$ and $\mathrm{d}\bar{\mathrm{u}}$ pairs in the process $\gamma\gamma \to \nu_{\mathrm{e}}\mathrm{e}^+\mathrm{d}\bar{\mathrm{u}}$, both with and without convolution over the photon spectrum. The upper plots show the absolute predictions, and the lower plots the corrections normalized to the Born predictions. Since we use $\sqrt{s_{\gamma\gamma}} = 500\,\mathrm{GeV}$ or $\sqrt{s_{\mathrm{ee}}} = 500\,\mathrm{GeV}$, the corrections are shifted upwards when including the photon spectrum, because the effective energy of the photons is lower (cf. Figure 4.6). The shape of the corrections, however, is hardly changed by the convolution over the photon spectrum. As the shape of the corrections determine a possible shift of the peak of the invariant-mass distribution, it is of particular importance in the determination of the W-boson mass. The measurement of the W-boson mass can, e.g., be used for understanding and calibrating the detector of a $\gamma\gamma$ collider.

The distribution in the W-boson production angle is sensitive to anomalous couplings. In order to set bounds on these couplings it is mandatory to know radiative corrections, because both anomalous couplings and radiative corrections typically distort angular distributions. The corresponding angular distribution of the $\mathrm{d}\bar{\mathrm{u}}$ system, which is equal within the statistical error to the distribution of the $\nu_{\mathrm{e}}\mathrm{e}^+$ system, is shown in Figure 4.9. While the correction without the photon spectrum is about -9% for W bosons emitted perpendicular to the beam, the corrections are rather small when including the photon spectrum. As already explained above, the cross section is dominated by a region where the $\gamma\gamma$ CM energy is smaller. In fact, the relative correction δ is accidentally small at $\sqrt{s_{\mathrm{ee}}} \sim 500\,\mathrm{GeV}$ [cf. Figure 4.7(d)] and might also become larger if other cuts or event selection procedures are applied.

Figure 4.10 shows the energy distribution of e^+ and d for the process $\gamma\gamma \to \nu_{\mathrm{e}}\mathrm{e}^+\mathrm{d}\bar{\mathrm{u}}$. The characteristics of the Born cross section, especially the influence of the effective polarization of the photons after Compton backscattering, were explained in detail in Section 3.5.3.2. The relative corrections shown in the lower plots amount to a few per cent. For very low and very high energies, where the Born cross section is very small, the relative corrections in DPA are not reliable anymore. In this region the assumption that doubly-resonant diagrams dominate is not fulfilled. The angular distributions for e^+ and d are shown in Figure 4.11. The shape of the Born cross section and the influence of the photon spectrum were also explained in Section 3.5.3.2. Similar to the angular distributions of the $\nu_{\mathrm{e}}\mathrm{e}^+$ and $\mathrm{d}\bar{\mathrm{u}}$ systems, the corrections are maximal in a region where the fermions are emitted perpendicular to the beam. However, after including the photon spectrum, the corrections almost cancel as can be anticipated from Figure 4.7(d) which shows that the corrections to the integrated cross section are almost zero at $\sqrt{s_{\mathrm{ee}}} \sim 500\,\mathrm{GeV}$.

Finally, the energy distribution of the photon in the process $\gamma\gamma \to \nu_{\mathrm{e}}\mathrm{e}^+\mathrm{d}\bar{\mathrm{u}}+\gamma$ is shown in Figure 4.12. The distribution is dominated by the soft-photon pole at $k^0 \to 0$ and decreases rapidly at higher energies. Comparing the distributions with and without convolution over the photon spectrum, the convolution shifts the curve to lower energies, because the initial-state photons already have less energy.

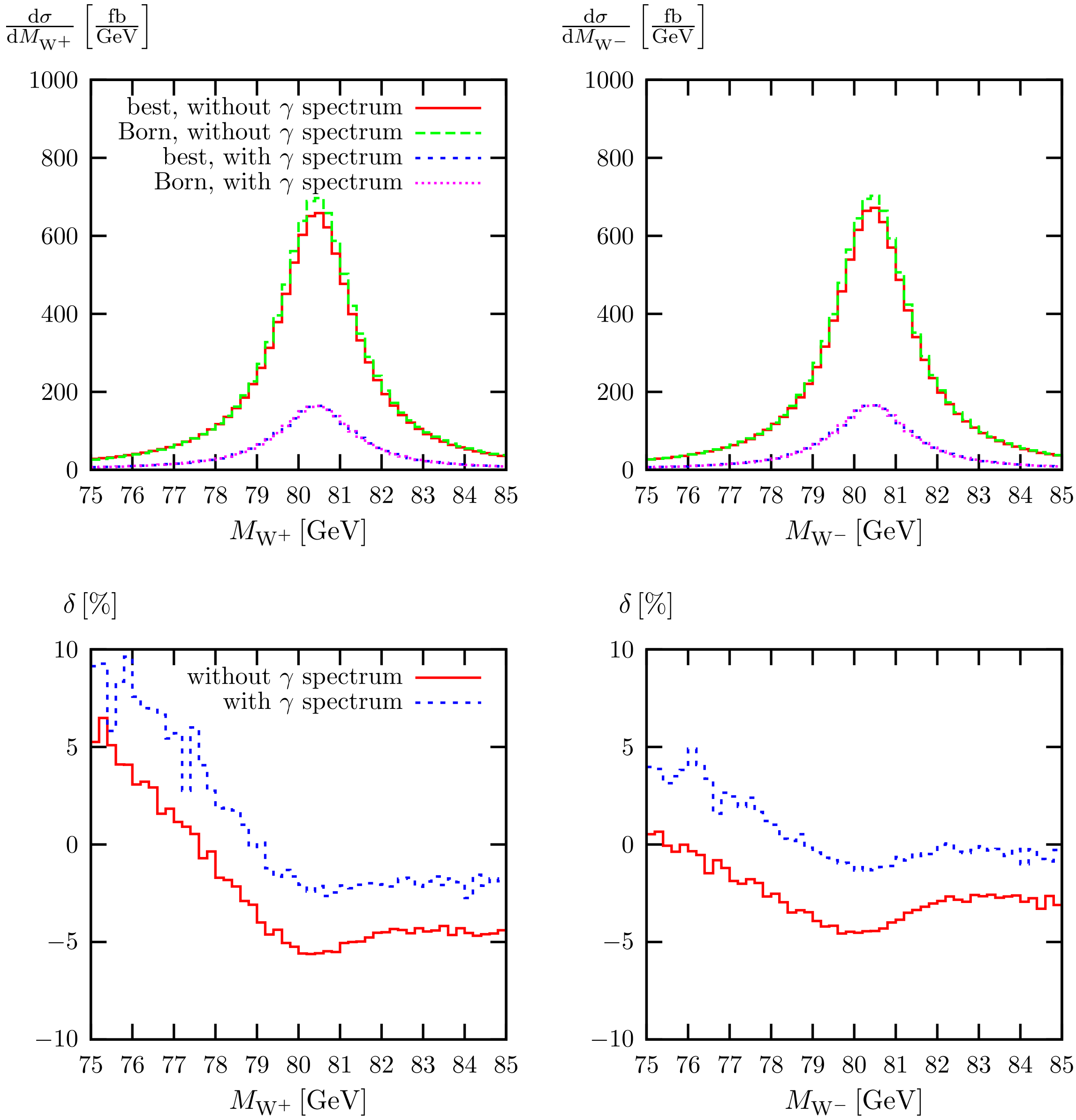

Figure 4.8: Invariant-mass distributions of the W^+ and W^- bosons reconstructed from the $\nu_\mathrm{e}\mathrm{e}^+$ and $\mathrm{d}\bar{\mathrm{u}}$ pairs in the process $\gamma\gamma \to \nu_\mathrm{e}\mathrm{e}^+\mathrm{d}\bar{\mathrm{u}}$ at $\sqrt{s} = 500\,\mathrm{GeV}$.

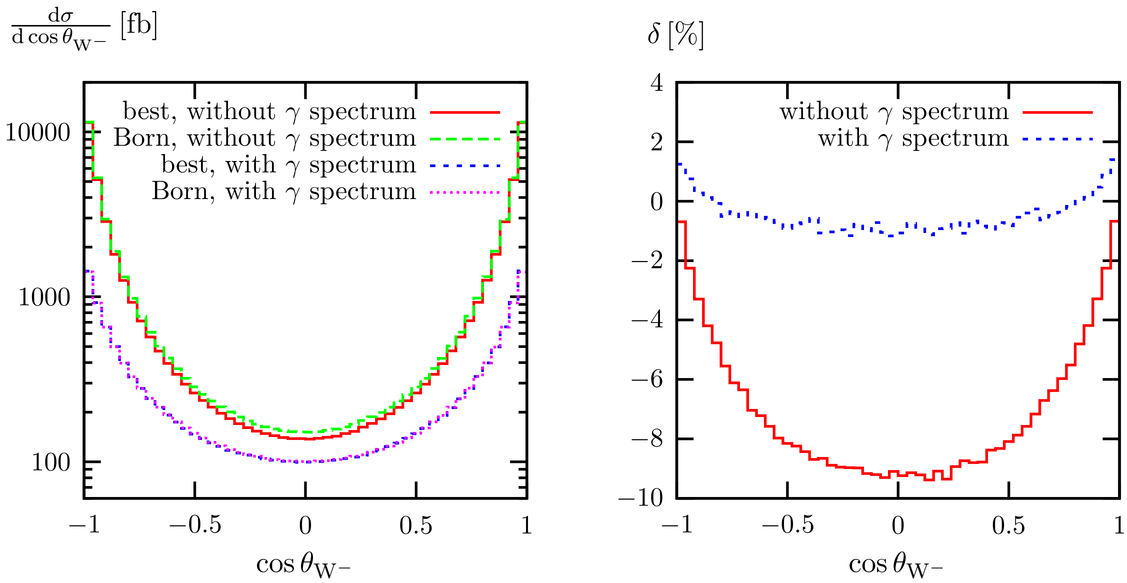

Figure 4.9: Angular distribution of the W^- boson reconstructed from the $d\bar{u}$ pair in the process $\gamma\gamma \to \nu_e e^+ d\bar{u}$ at $\sqrt{s} = 500\,\mathrm{GeV}$.

4.4.4 Non-collinear-safe observables

As explained in Section 4.3.2, the treatment of collinear singularities in non-collinear-safe observables deserves some care. Applying the generalizations of the subtraction and the slicing methods described above, we now turn to observables without photon recombination. Apart from that, the same phase-space cuts are applied as before. In Figure 4.13 we show the distributions of the $\nu_e e^+$, $\nu_\mu \mu^+$, and $d\bar{u}$ pairs in the processes $\gamma\gamma \to \nu_e e^+ d\bar{u}$, $\nu_\mu \mu^+ d\bar{u}$. With photon recombination the leptonic invariant masses of the two processes receive the same radiative corrections since the recombination guarantees the necessary inclusiveness so that all mass singularities cancel. If the recombination is not applied, the distributions change drastically. Note, however, that the recombination is mainly a rearrangement of events, and omitting the recombination affects the integrated cross section by less than 0.5%. With decreasing invariant masses the relative corrections rise, while they are smaller at large invariant masses. The reason is that without recombination final-state radiation (which is enhanced by mass logarithms) reduces the invariant mass of the reconstructed W boson, thereby shifting events from the dominating resonant region to lower invariant mass values. The recombination brings most of these events back to the resonance region, because it prevents momentum loss from final-state radiation. The l.h.s. of Figure 4.13 also shows a hierarchy in the mass effects of the outgoing leptons as the slope for the $\nu_e e^+$ pair is much steeper than the slope for the $\nu_\mu \mu^+$ pair due to the smaller mass of e^+. The plot on the r.h.s. shows that the corrections for the $d\bar{u}$ pair are not as large as for the $\nu_\mu \mu^+$ pair on the l.h.s., because the remaining mass terms behave like $Q_f^2 \ln m_f$, where Q_f denotes the charge of the fermion f. We also note that the cor-

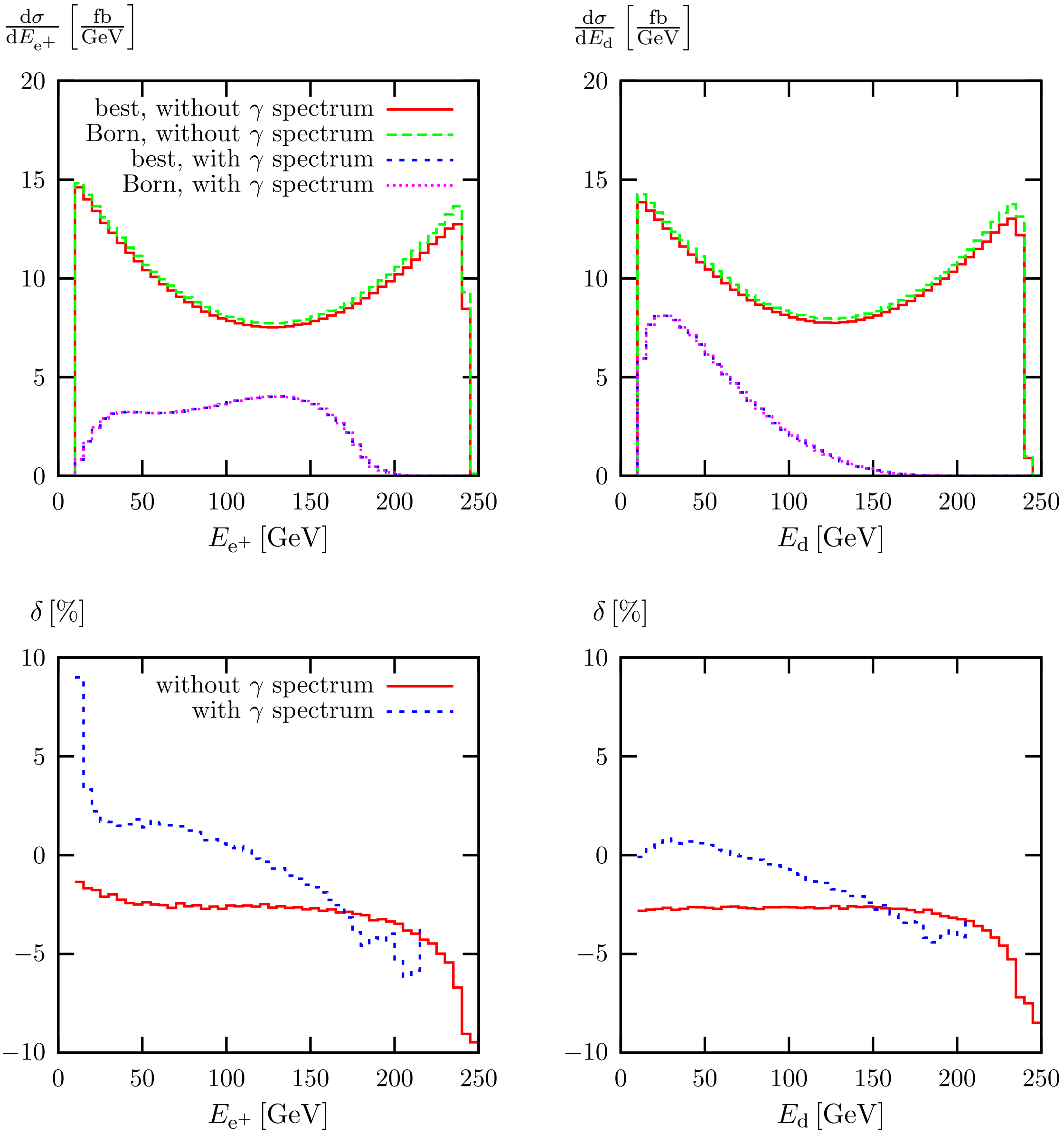

Figure 4.10: Energy distribution of e^+ and d in the process $\gamma\gamma \to \nu_{\mathrm{e}}\mathrm{e}^+\mathrm{d}\bar{\mathrm{u}}$ at $\sqrt{s} = 500\,\mathrm{GeV}$.

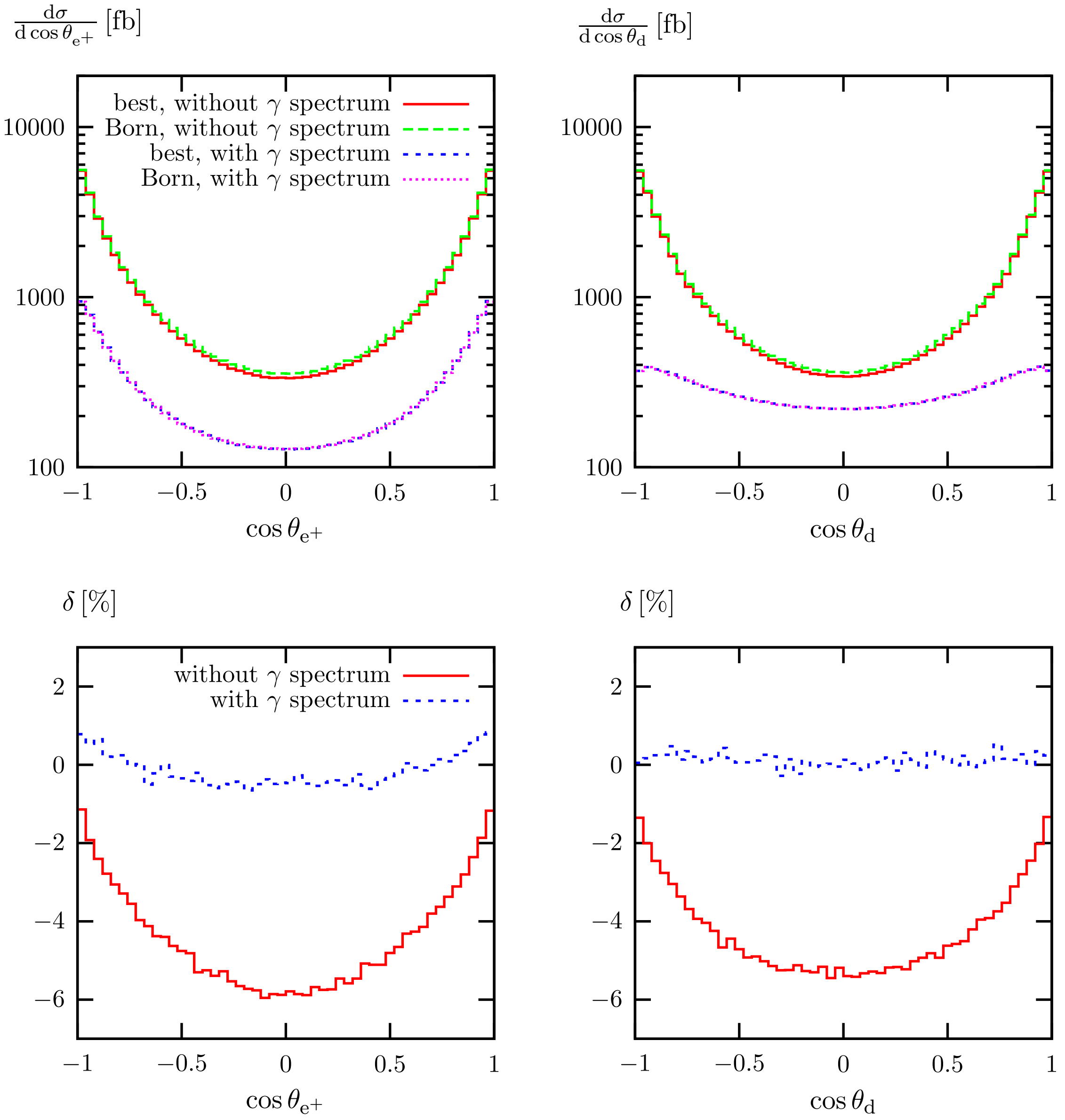

Figure 4.11: Distributions in the production angles of e^+ and d in the process $\gamma\gamma \to \nu_e e^+ d\bar{u}$ at $\sqrt{s} = 500\,\mathrm{GeV}$.

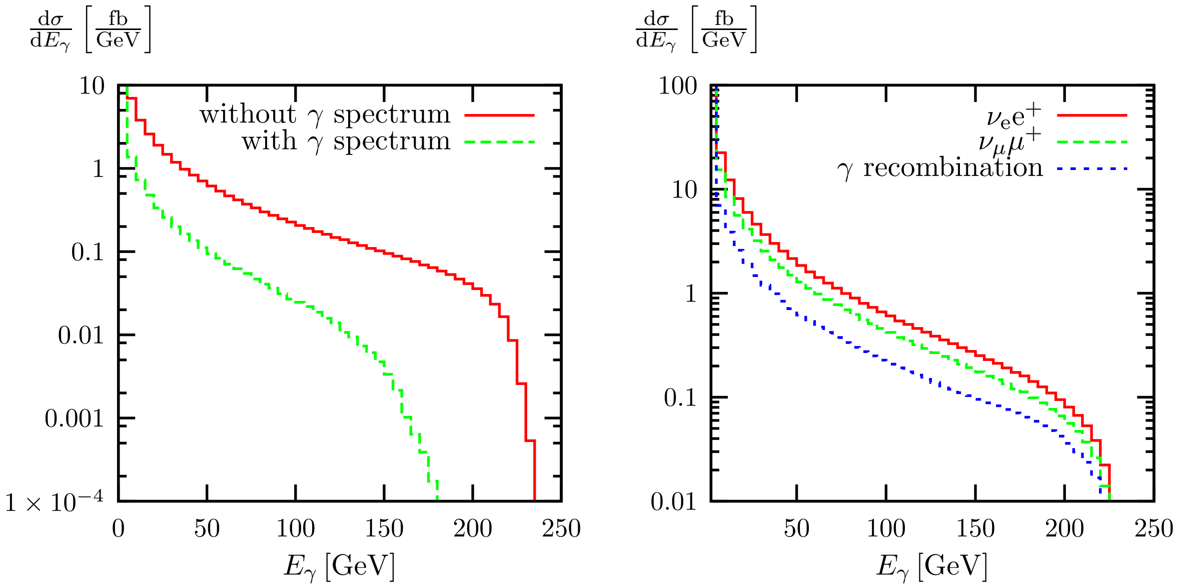

Figure 4.12: Energy distribution of the final-state photon in the processes $\gamma\gamma \to \nu_{\mathrm{e}}\mathrm{e}^{+}\mathrm{d}\bar{\mathrm{u}}+\gamma$ and $\gamma\gamma \to \nu_{\mu}\mu^{+}\mathrm{d}\bar{\mathrm{u}}+\gamma$ at $\sqrt{s} = 500\,\mathrm{GeV}$. The l.h.s. compares the distributions with and without convolution over the photon spectrum (with photon recombination); the r.h.s. compares the cases with and without photon recombination (without convolution over the photon spectrum).

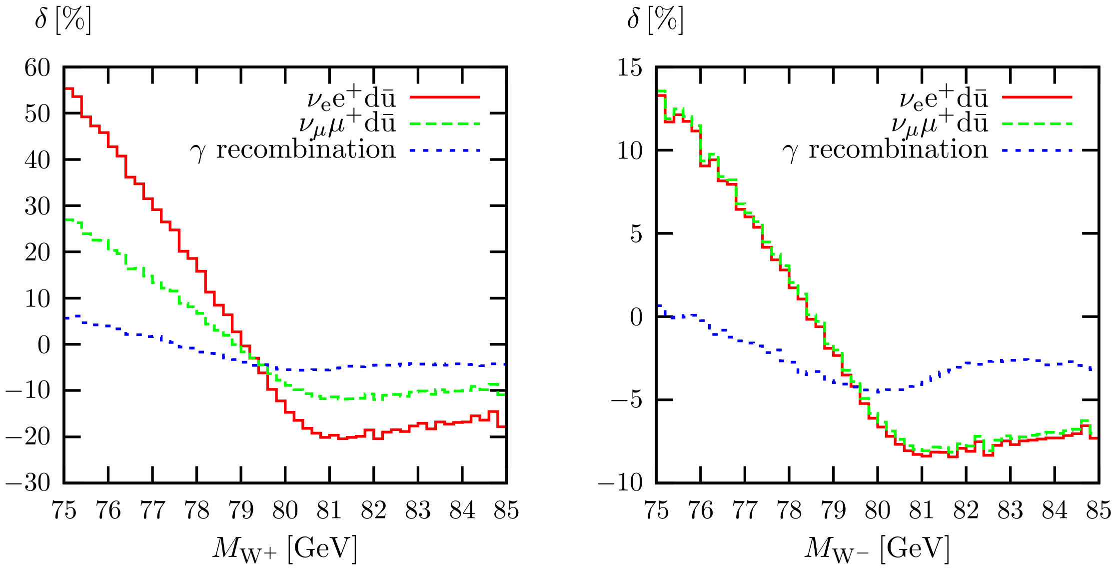

Figure 4.13: Invariant-mass distributions of the W^{+} and W^{-} boson reconstructed from the $\nu_{\mathrm{e}}\mathrm{e}^{+}(\nu_{\mu}\mu^{+})$ pair and $\mathrm{d}\bar{\mathrm{u}}$ pair in the process $\gamma\gamma \to \nu_{\mathrm{e}}\mathrm{e}^{+}\mathrm{d}\bar{\mathrm{u}}$ $(\gamma\gamma \to \nu_{\mu}\mu^{+}\mathrm{d}\bar{\mathrm{u}})$ at $\sqrt{s_{\gamma\gamma}} = 500\,\mathrm{GeV}$, with and without photon recombination.

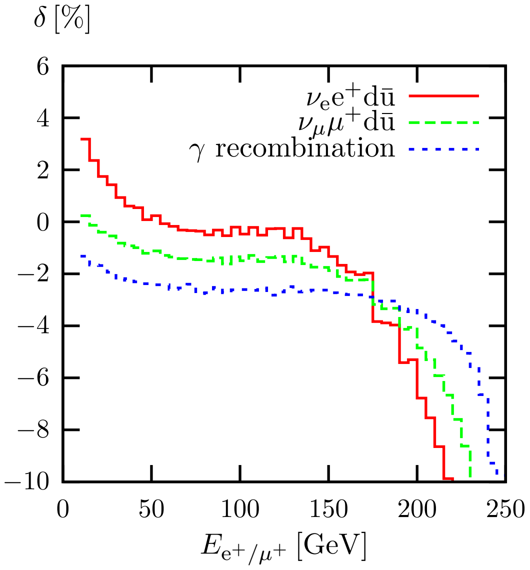

Figure 4.14: Energy distributions of e^+ and μ^+ in the processes $\gamma\gamma \to \nu_\mathrm{e}\mathrm{e}^+\mathrm{d}\bar{\mathrm{u}}$ and $\gamma\gamma \to \nu_\mu\mu^+\mathrm{d}\bar{\mathrm{u}}$ at $\sqrt{s_{\gamma\gamma}} = 500\,\mathrm{GeV}$, with and without photon recombination.

rections are smallest in the case with photon recombination because of the cancellation of all mass singularities.

The photon recombination also affects the energy distributions of the fermions. Figure 4.14 shows this distribution for e^+ and μ^+ in the processes $\gamma\gamma \to \nu_\mathrm{e}\mathrm{e}^+\mathrm{d}\bar{\mathrm{u}}$ and $\gamma\gamma \to \nu_\mu\mu^+\mathrm{d}\bar{\mathrm{u}}$ with and without recombination. In the former case the curves coincide, as explained above. The recombination attributes the photon to a fermion and, thus, shifts events to higher energies of the fermion. The mass-singular effect, which appears without recombination, is again larger for e^+ than for μ^+.

The effect of the photon recombination on the photon-energy spectrum is shown in Figure 4.12. Without recombination the distribution is shifted to higher photon energies because the recombination transfers events to the bin with zero photon energy. The difference is again bigger for the process $\gamma\gamma \to \nu_\mathrm{e}\mathrm{e}^+\mathrm{d}\bar{\mathrm{u}}$ than for $\gamma\gamma \to \nu_\mu\mu^+\mathrm{d}\bar{\mathrm{u}}$, since the mass-singular logarithms of e^+ are larger.

Chapter 5

The Higgs-boson decays $\mathrm{H} \to \mathrm{WW/ZZ} \to 4f$

The primary task of the LHC will be the detection and the study of the Higgs boson. If it is heavier than 140 GeV and behaves as predicted by the Standard Model (SM), it decays dominantly into gauge-boson pairs and subsequently into four light fermions. From a Higgs-boson mass M_H of about 130 GeV up to the Z-boson-pair threshold $2M_\mathrm{Z}$, the decay signature $\mathrm{H}(\to \mathrm{WW}) \to 2\,\mathrm{leptons} + \mathrm{missing}\ p_\mathrm{T}$ [71] has the highest discovery potential for the Higgs boson at the LHC [72]. For higher Higgs masses, the leading role is taken over by the famous "gold-plated" channel $\mathrm{H} \to \mathrm{ZZ} \to 4\,\mathrm{leptons}$, which will allow for the most accurate measurement of M_H above 130 GeV [73]. More details and recent developments concerning Higgs studies at the LHC can be found in the literature [74, 75, 76]. At a future $\mathrm{e}^+\mathrm{e}^-$ linear collider [77, 78, 79], the decays $\mathrm{H} \to 4f$ will enable measurements of the $\mathrm{H} \to \mathrm{WW/ZZ}$ branching ratios at the level of a few to 10% [80].

A kinematical reconstruction of the Higgs boson and of the virtual W and Z bosons requires the study of distributions defined from the kinematics of the decay fermions. In doing so, it is important to include radiative corrections, in particular real photon radiation. In addition, the verification of the spin and of the CP properties of the Higgs boson relies on the study of angular, energy, and invariant-mass distributions [81, 82]. In particular, the sensitivity of the angle between the two Z-decay planes in $\mathrm{H} \to \mathrm{ZZ} \to 4\,\mathrm{leptons}$ has been frequently emphasized in the literature. As a consequence a Monte Carlo generator for $\mathrm{H} \to \mathrm{WW/ZZ} \to 4\,\mathrm{fermions}$ including electroweak corrections is needed.

The theoretical description of the decays of a SM Higgs boson into W- or Z-boson pairs started with lowest-order formulas for the partial decay widths. The first calculations [83] that include off-shell effects of the gauge bosons made the approximation that one of the W or Z bosons was still on shell, an approximation that turns out to be not sufficient. Later calculations [84] dealt with the situation of two intermediate off-shell gauge bosons. The various approaches are compared, e.g., in Ref. [85]. We note that the program HDECAY [56], which is frequently used in practice, calculates the partial decay widths for $\mathrm{H} \to \mathrm{WW/ZZ}$ with on- or off-shell gauge bosons depending on M_H. Distributions of the decay fermions have been considered in Refs. [81, 82], but still in lowest order of perturbation theory.

In the past the electroweak $\mathcal{O}(\alpha)$ corrections to decays into gauge bosons, H → WW/ZZ, were known [86, 87] only in narrow-width approximation (NWA), i.e. for on-shell W and Z bosons. In this case, also leading two-loop corrections enhanced by powers of the top-quark mass [88] or of the Higgs-boson mass [89, 90] have been calculated. However, near and below the gauge-boson-pair thresholds the NWA is not applicable, so that only the lowest-order results exist in this M_{H} range.

In this chapter we describe the calculation of the electroweak $\mathcal{O}(\alpha)$ corrections to the full processes $\mathrm{H} \to \mathrm{WW/ZZ} \to 4f$ with off-shell gauge bosons and of the included improvements beyond this order. The involved Feynman diagrams are closely related to the ones of the production process $\mathrm{e^+e^-} \to \nu\bar{\nu}\mathrm{H}$, whose electroweak $\mathcal{O}(\alpha)$ corrections have been evaluated in Refs. [91, 92]. Therefore, concerning the algebraic reduction of the one-loop diagrams we proceed as described in Ref. [92]. On the other hand, the resonance structure of the decays $\mathrm{H} \to \mathrm{WW/ZZ} \to 4f$ is practically the same as in $\mathrm{e^+e^-} \to \mathrm{WW} \to 4f$, which was treated at the one-loop level in Ref. [24]. Thus, we apply the "complex-mass scheme" [24], where gauge-boson masses are consistently treated as complex quantities. This procedure fully maintains gauge invariance at the price of having complex gauge-boson masses everywhere, i.e. also in couplings and loop integrals. For a numerically stable evaluation of the latter we employ the methods described in Refs. [93, 94]. Since the final state coincides with the final state of $\gamma\gamma \to \mathrm{WW} \to 4f$ and since there are no infrared singularities connected with the initial state, the combination of virtual and real photon corrections is performed in the same way as described in Section 4.3.

5.1 Lowest-order results

We consider the lowest-order processes

$$\mathrm{H}(p) \longrightarrow f_1(k_1,\sigma_1) + \bar{f}_2(k_2,\sigma_2) + f_3(k_3,\sigma_3) + \bar{f}_4(k_4,\sigma_4), \tag{5.1.1}$$

where the momenta and helicities of the external particles are indicated in parentheses. The helicities take the values $\sigma_i = \pm 1/2$, but we often use only the sign to indicate the helicity. The masses of the external fermions are neglected whenever possible; they are only taken into account in the mass-singular logarithms originating from collinear final-state radiation (FSR). The matrix elements can be constructed from the generic diagram shown in Figure 5.1.

The relevant couplings were already introduced in Eqs. (1.2.18) and (1.2.22). However, using the complex-mass scheme we have to replace real gauge-boson masses by complex masses everywhere,

$$M_V^2 \to \mu_V^2 = M_V^2 - \mathrm{i} M_V \Gamma_V, \qquad V = \mathrm{W}, \mathrm{Z}, \tag{5.1.2}$$

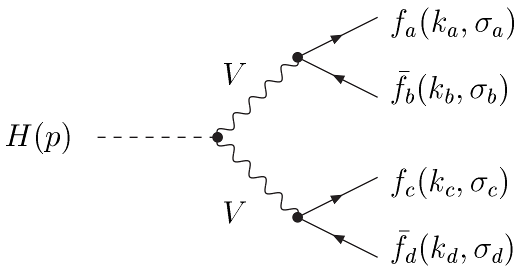

Figure 5.1: Generic lowest-order diagram for $\mathrm{H} \to 4f$ where $V = \mathrm{W},\mathrm{Z}$.

where M_V and Γ_V denote the real pole-mass and width parameters. Accordingly the sine and cosine of the weak mixing angle are fixed by

$$c_{\mathrm{w}}^2 = 1 - s_{\mathrm{w}}^2 = \frac{\mu_{\mathrm{W}}^2}{\mu_{\mathrm{Z}}^2}. \tag{5.1.3}$$

More details about the complex-mass scheme are described in Section 5.2.2.2.

The generic lowest-order amplitude reads

$$\mathcal{M}_0^{VV,\sigma_a\sigma_b\sigma_c\sigma_d}(k_a,k_b,k_c,k_d) = 2e^3 g^{\sigma_a}_{Vf_af_b} g^{\sigma_c}_{Vf_cf_d} g_{HVV}\,\delta_{\sigma_a,-\sigma_b}\delta_{\sigma_c,-\sigma_d} A^{VV}_{\sigma_a\sigma_c}(k_a,k_b,k_c,k_d), \tag{5.1.4}$$

or more specifically for the case of Z-mediated and W-mediated decays

$$\begin{aligned}\mathcal{M}_0^{\mathrm{ZZ},\sigma_a\sigma_b\sigma_c\sigma_d}(k_a,k_b,k_c,k_d) &= \frac{2e^3 g^{\sigma_a}_{\mathrm{Z}f_af_b} g^{\sigma_c}_{\mathrm{Z}f_cf_d}\mu_{\mathrm{W}}}{c_{\mathrm{w}}^2 s_{\mathrm{w}}}\,\delta_{\sigma_a,-\sigma_b}\delta_{\sigma_c,-\sigma_d}\, A^{\mathrm{ZZ}}_{\sigma_a\sigma_c}(k_a,k_b,k_c,k_d),\\ \mathcal{M}_0^{\mathrm{WW},\sigma_a\sigma_b\sigma_c\sigma_d}(k_a,k_b,k_c,k_d) &= \frac{e^3\mu_{\mathrm{W}}}{s_{\mathrm{w}}^3}\,\delta_{\sigma_a,-}\delta_{\sigma_b,+}\delta_{\sigma_c,-}\delta_{\sigma_d,+}\, A^{\mathrm{WW}}_{--}(k_a,k_b,k_c,k_d).\end{aligned} \tag{5.1.5}$$

The auxiliary functions are expressed in terms of WvdW spinors following the notation of Section 3.1.3.1,

$$\begin{aligned}A^{VV}_{--}(k_a,k_b,k_c,k_d) &= \frac{\langle k_bk_d\rangle^*\langle k_ak_c\rangle}{[(k_a+k_b)^2-\mu_V^2][(k_c+k_d)^2-\mu_V^2]},\\ A^{VV}_{+-}(k_a,k_b,k_c,k_d) &= A^{VV}_{--}(k_b,k_a,k_c,k_d),\\ A^{VV}_{-+}(k_a,k_b,k_c,k_d) &= A^{VV}_{--}(k_a,k_b,k_d,k_c),\\ A^{VV}_{++}(k_a,k_b,k_c,k_d) &= A^{VV}_{--}(k_b,k_a,k_d,k_c),\end{aligned} \tag{5.1.6}$$

and obey the relations

$$\begin{aligned}A^{VV}_{-\sigma_a,-\sigma_c}(k_a,k_b,k_c,k_d) &= \left(A^{VV}_{\sigma_a\sigma_c}(k_a,k_b,k_c,k_d)\right)^*\Big|_{\mu_V\to\mu_V^*,g\to g^*},\\ A^{VV}_{-\sigma_a,\sigma_c}(k_a,k_b,k_c,k_d) &= A^{VV}_{\sigma_a\sigma_c}(k_b,k_a,k_c,k_d),\\ A^{VV}_{\sigma_a,-\sigma_c}(k_a,k_b,k_c,k_d) &= A^{VV}_{\sigma_a\sigma_c}(k_a,k_b,k_d,k_c),\\ A^{VV}_{\sigma_a,\sigma_c}(k_a,k_b,k_c,k_d) &= \left(A^{VV}_{\sigma_c\sigma_a}(k_d,k_c,k_b,k_a)\right)^*\Big|_{\mu_V\to\mu_V^*,g\to g^*},\\ A^{VV}_{\sigma_a\sigma_c}(k_a,k_b,k_c,k_d) &= A^{VV}_{\sigma_c\sigma_a}(k_c,k_d,k_a,k_b).\end{aligned} \tag{5.1.7}$$

The relations between the $A^{\cdots}_{\cdots}$ functions that differ in all helicities result from a P transformation. Those where only one fermion helicity is reversed are related to C symmetry. The last but one is due to CP symmetry, and the last one results from a symmetry under the exchange of the two fermion pairs. The replacements $\mu_V \to \mu_V^*$ in (5.1.7) ensure that the vector-boson masses remain unaffected by complex conjugation, and $g \to g^*$ indicates that this substitution implicitly also applies to coupling constants that may become complex via mass factors.

From the generic matrix element $\mathcal{M}_0^{VV,\sigma_a\sigma_b\sigma_c\sigma_d}(k_a,k_b,k_c,k_d)$ the matrix elements for the specific processes can be constructed as follows. To write down the explicit matrix elements for the different final states, we denote different fermions ($f \neq F$) by f and F, and their weak-isospin partners by f' and F', respectively.

- $H \to f\bar{f}F\bar{F}$:

$$\mathcal{M}_0^{\sigma_1\sigma_2\sigma_3\sigma_4}(k_1,k_2,k_3,k_4) = \mathcal{M}_0^{\mathrm{ZZ},\sigma_1\sigma_2\sigma_3\sigma_4}(k_1,k_2,k_3,k_4). \tag{5.1.8}$$

- $H \to f\bar{f}'F\bar{F}'$:

$$\mathcal{M}_0^{\sigma_1\sigma_2\sigma_3\sigma_4}(k_1,k_2,k_3,k_4) = \mathcal{M}_0^{\mathrm{WW},\sigma_1\sigma_2\sigma_3\sigma_4}(k_1,k_2,k_3,k_4). \tag{5.1.9}$$

- $H \to f\bar{f}f\bar{f}$:

$$\begin{aligned}\mathcal{M}_0^{\sigma_1\sigma_2\sigma_3\sigma_4}(k_1,k_2,k_3,k_4) = {}& \mathcal{M}_0^{\mathrm{ZZ},\sigma_1\sigma_2\sigma_3\sigma_4}(k_1,k_2,k_3,k_4)\\ &- \mathcal{M}_0^{\mathrm{ZZ},\sigma_1\sigma_4\sigma_3\sigma_2}(k_1,k_4,k_3,k_2).\end{aligned} \tag{5.1.10}$$

- $H \to f\bar{f}f'\bar{f}'$:

$$\begin{aligned}\mathcal{M}_0^{\sigma_1\sigma_2\sigma_3\sigma_4}(k_1,k_2,k_3,k_4) = {}& \mathcal{M}_0^{\mathrm{ZZ},\sigma_1\sigma_2\sigma_3\sigma_4}(k_1,k_2,k_3,k_4)\\ &- \mathcal{M}_0^{\mathrm{WW},\sigma_1\sigma_4\sigma_3\sigma_2}(k_1,k_4,k_3,k_2).\end{aligned} \tag{5.1.11}$$

The relative signs between contributions of the basic subamplitudes to the full matrix elements account for the sign changes resulting from interchanging external fermion lines.

The matrix elements of (5.1.8) and (5.1.9) can be extended to the case of semi-leptonic or hadronic final states by simply multiplying the squared matrix element by a colour factor 3 or 9, respectively. Note that care has to be taken in the cases of (5.1.10) and (5.1.11) for hadronic final states (semi-leptonic final states do not exist) owing to the non-trivial colour interferences. Summing over the colour degrees of freedom, we have

- $H \to q\bar{q}q\bar{q}$:

$$\begin{aligned}&|\mathcal{M}_0^{\sigma_1\sigma_2\sigma_3\sigma_4}(k_1,k_2,k_3,k_4)|^2 =\\ &\quad 9\left|\mathcal{M}_0^{\mathrm{ZZ},\sigma_1\sigma_2\sigma_3\sigma_4}(k_1,k_2,k_3,k_4)\right|^2 + 9\left|\mathcal{M}_0^{\mathrm{ZZ},\sigma_1\sigma_4\sigma_3\sigma_2}(k_1,k_4,k_3,k_2)\right|^2\\ &\quad -6\,\mathrm{Re}\left\{\mathcal{M}_0^{\mathrm{ZZ},\sigma_1\sigma_2\sigma_3\sigma_4}(k_1,k_2,k_3,k_4)\left(\mathcal{M}_0^{\mathrm{ZZ},\sigma_1\sigma_4\sigma_3\sigma_2}(k_1,k_4,k_3,k_2)\right)^*\right\}.\end{aligned} \tag{5.1.12}$$

- $H \to q\bar{q}q'\bar{q}'$:

$$\begin{aligned}
&|\mathcal{M}_0^{\sigma_1\sigma_2\sigma_3\sigma_4}(k_1,k_2,k_3,k_4)|^2 = \\
&\qquad 9\left|\mathcal{M}_0^{\mathrm{ZZ},\sigma_1\sigma_2\sigma_3\sigma_4}(k_1,k_2,k_3,k_4)\right|^2 + 9\left|\mathcal{M}_0^{\mathrm{WW},\sigma_1\sigma_4\sigma_3\sigma_2}(k_1,k_4,k_3,k_2)\right|^2 \\
&\qquad -6\,\mathrm{Re}\left\{\mathcal{M}_0^{\mathrm{ZZ},\sigma_1\sigma_2\sigma_3\sigma_4}(k_1,k_2,k_3,k_4)\left(\mathcal{M}_0^{\mathrm{WW},\sigma_1\sigma_4\sigma_3\sigma_2}(k_1,k_4,k_3,k_2)\right)^*\right\}. \quad (5.1.13)
\end{aligned}$$

Having constructed the matrix elements, we can write the lowest-order decay width Γ_0 as

$$\Gamma_0 = \frac{1}{2M_\mathrm{H}}\int \mathrm{d}\Phi_0 \sum_{\sigma_1,\sigma_2,\sigma_3,\sigma_4=\pm\frac{1}{2}} |\mathcal{M}_0^{\sigma_1,\sigma_2,\sigma_3,\sigma_4}|^2, \qquad (5.1.14)$$

where the phase-space integral is defined by

$$\int \mathrm{d}\Phi_0 = \left(\prod_{i=1}^4 \int \frac{\mathrm{d}^3\mathbf{k}_i}{(2\pi)^3 2k_i^0}\right)(2\pi)^4\delta^{(4)}\left(p - \sum_{i=1}^4 k_i\right). \qquad (5.1.15)$$

5.2 Virtual corrections

5.2.1 Survey of one-loop diagrams

The virtual corrections receive contributions from self-energy, vertex, box, and pentagon diagrams. The structural diagrams containing the generic contributions of vertex functions are summarized in Figure 5.2. Here and in the following we omit all diagrams that vanish in the limit of vanishing external fermion masses from the beginning. For charged-current processes the generic field V stands for the W-boson field, for neutral-current processes we have $V = Z, \gamma$, where the photon is of course absent in couplings to the Higgs boson. The generic diagrams cover all structures relevant for electroweak corrections to arbitrary four-fermion final states, including quarks. Note, however, that some four-quark final states receive corrections from diagrams with intermediate gluons on tree-like lines (quark-loop-induced Hgg vertex). Possible QCD corrections for quarks in the final state will not be considered in the following lists of diagrams.

The pentagon diagrams are shown in Figures 5.3 and 5.4, respectively. The specific subdiagrams of loop-induced 4-point functions have been shown in Ref. [92], where the process class $\mathrm{e}^+\mathrm{e}^- \to \nu\bar{\nu}\mathrm{H}$ was analyzed at one loop. They involve 4-point vertex functions of the type $\nu_l\bar{\nu}_l\mathrm{ZH}$, $\nu_l\bar{\nu}_l\gamma\mathrm{H}$, $l^-l^+\mathrm{ZH}$, $l^-l^+\gamma\mathrm{H}$, and $l^\mp \overset{(-)}{\nu}_l \mathrm{W}^+\mathrm{H}$ with $l = \mathrm{e}, \mu, \tau$ denoting any charged lepton. The 3-point loop insertions in the $\mathrm{H}\nu_l\bar{\nu}_l$, $\mathrm{H}l^-l^+$, HWW, and HZZ vertices have also been listed there; the one-loop diagrams for the $\mathrm{HZ}\gamma$ and $\mathrm{H}\gamma\gamma$ vertices follow from the HZZ case by obvious substitutions and omissions. Most of the diagrams for the self-energies and the $\nu_l\bar{\nu}_l\mathrm{Z}$, $\mathrm{e}^-\mathrm{e}^-\mathrm{Z}$, and $l^\pm\overset{(-)}{\nu}_\mathrm{e}\mathrm{W}$ vertex functions can be found in Ref. [95].

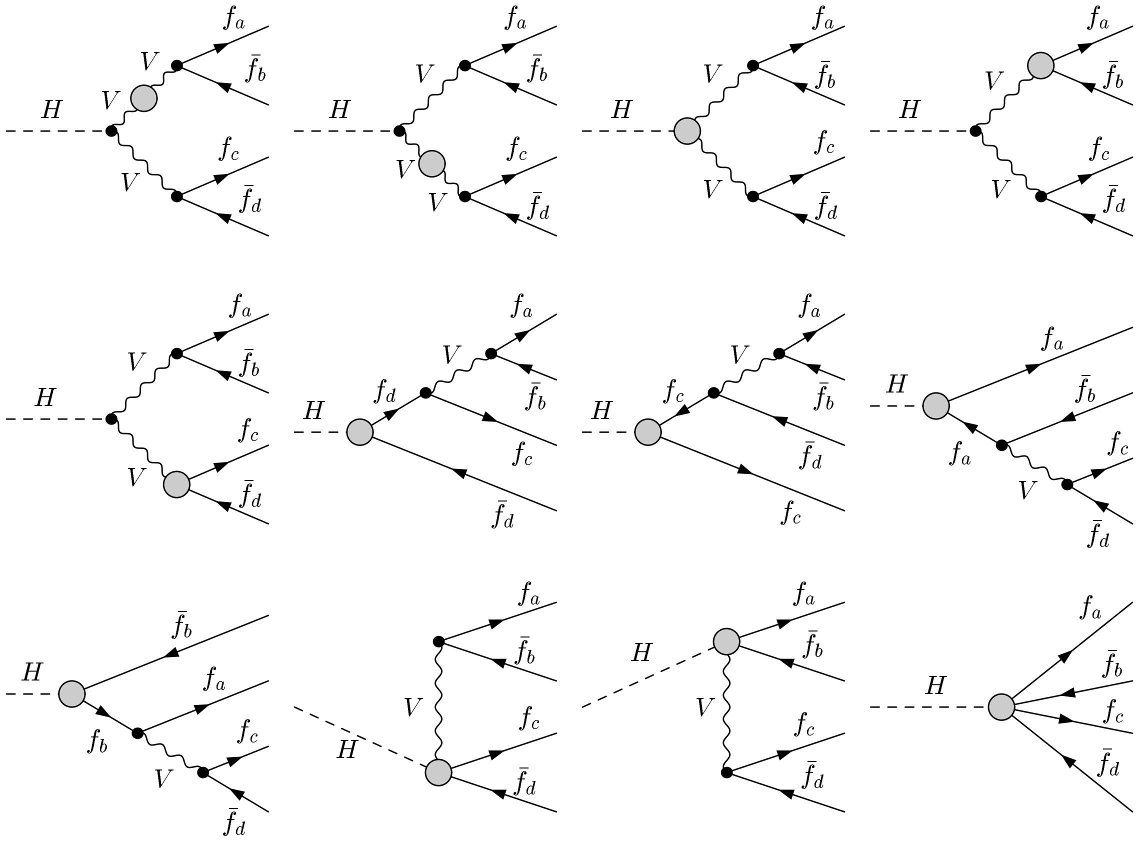

Figure 5.2: Generic contributions of different vertex functions to H → WW/ZZ → $4f$.

5.2.2 Calculation of the one-loop corrections

5.2.2.1 *Algebraic reduction of diagrams and standard matrix elements*

The algebraic part of the two calculations has been carried out in the same way as in the one-loop calculation of $\mathrm{e^+e^-} \to \nu\bar{\nu}\mathrm{H}$ described in Ref. [92]. This means that we separate the fermion spinor chains from the rest of the amplitude by defining standard matrix elements (SME). To introduce a compact notation for the SME, the tensors

$$\begin{aligned}\Gamma^{ab,\sigma}_{\{\alpha,\alpha\beta\gamma\}} &= \bar{v}_{f_a}(k_a)\,\{\gamma_\alpha, \gamma_\alpha\gamma_\beta\gamma_\gamma\}\,\omega_\sigma u_{\bar{f}_b}(k_b),\\ \Gamma^{cd,\tau}_{\{\alpha,\alpha\beta\gamma\}} &= \bar{v}_{f_c}(k_c)\,\{\gamma_\alpha, \gamma_\alpha\gamma_\beta\gamma_\gamma\}\,\omega_\tau u_{\bar{f}_d}(k_d)\end{aligned} \qquad (5.2.1)$$

are defined with obvious notations for the Dirac spinors $\bar{v}_{f_a}(k_a)$, etc., and $\omega_\pm = (1 \pm \gamma_5)/2$ denote the right- and left-handed chirality projectors. Here and in the following, each entry in the set within curly brackets refers to a single object, i.e. from the first line in

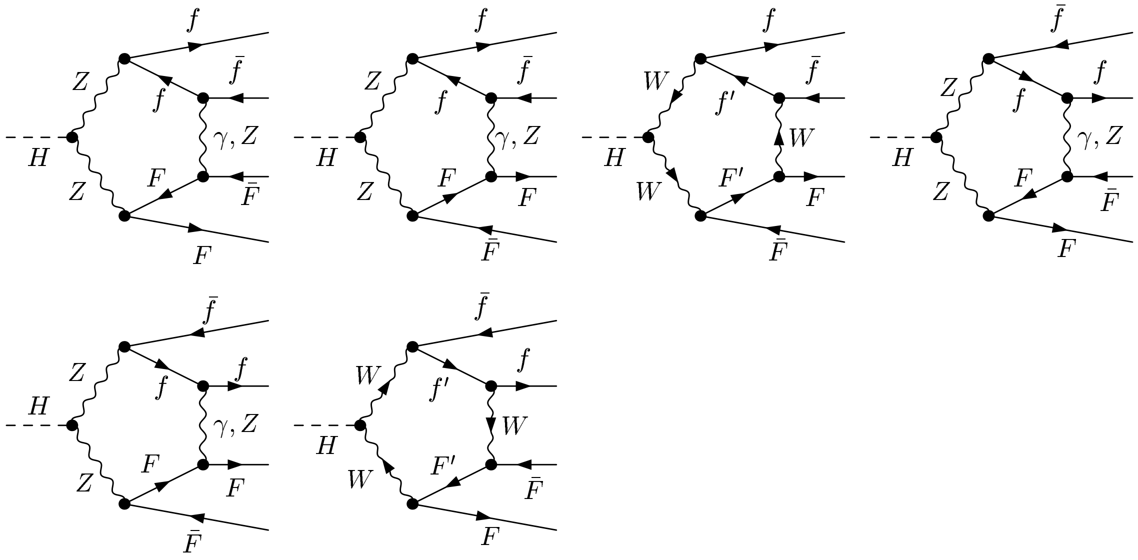

Figure 5.3: Pentagon diagrams for $\mathrm{H} \to \mathrm{ZZ} \to f\bar{f}F\bar{F}$, where f and F are different fermions with respective weak-isospin partners f' and F'.

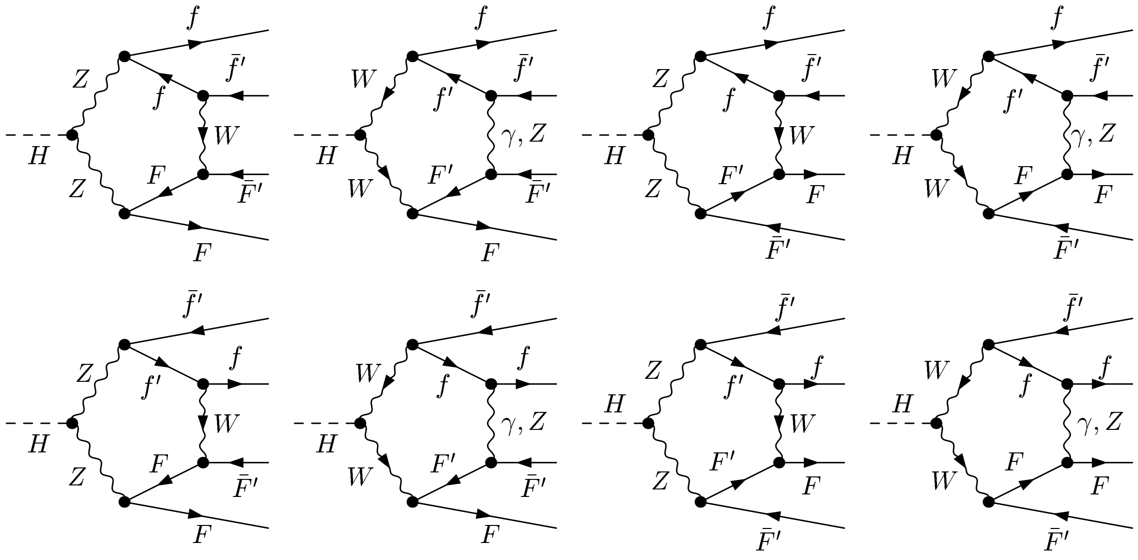

Figure 5.4: Pentagon diagrams for $\mathrm{H} \to \mathrm{WW} \to f\bar{f}'F\bar{F}'$, where f and F are different fermions with respective weak-isospin partners f' and F'.

the equation above we have $\Gamma^{ab,\sigma}_{\alpha} = \bar{v}_{f_a}(k_a)\gamma_\alpha\omega_\sigma u_{\bar{f}_b}(k_b)$, etc. Furthermore, symbols like Γ_p are used as shorthand for the contraction $\Gamma_\mu\, p^\mu$. We define the 52 SME

$$
\begin{aligned}
\hat{\mathcal{M}}^{abcd,\sigma\tau}_{\{1,2\}} &= \Gamma^{ab,\sigma}_{\alpha}\;\Gamma^{cd,\tau,\{\alpha,\alpha k_a k_b\}}, &\qquad \hat{\mathcal{M}}^{abcd,\sigma\tau}_{\{3,4\}} &= \Gamma^{ab,\sigma}_{\alpha k_c k_d}\;\Gamma^{cd,\tau,\{\alpha,\alpha k_a k_b\}},\\
\hat{\mathcal{M}}^{abcd,\sigma\tau}_{\{5,6\}} &= \Gamma^{ab,\sigma}_{k_c}\;\Gamma^{cd,\tau,\{k_a,k_b\}}, & \hat{\mathcal{M}}^{abcd,\sigma\tau}_{\{7,8\}} &= \Gamma^{ab,\sigma}_{k_d}\;\Gamma^{cd,\tau,\{k_a,k_b\}},\\
\hat{\mathcal{M}}^{abcd,\sigma\tau}_{\{9,10\}} &= \Gamma^{ab,\sigma}_{\alpha\beta k_c}\;\Gamma^{cd,\tau,\{\alpha\beta k_a,\alpha\beta k_b\}}, & \hat{\mathcal{M}}^{abcd,\sigma\tau}_{\{11,12\}} &= \Gamma^{ab,\sigma}_{\alpha\beta k_d}\;\Gamma^{cd,\tau,\{\alpha\beta k_a,\alpha\beta k_b\}},\\
\hat{\mathcal{M}}^{abcd,\sigma\tau}_{13} &= \Gamma^{ab,\sigma}_{\alpha\beta\gamma}\;\Gamma^{cd,\tau,\alpha\beta\gamma}. & & \qquad (5.2.2)
\end{aligned}
$$

The SME are evaluated within the WvdW spinor technique, similar to the lowest-order amplitudes described in the previous section. The tree-level and one-loop amplitudes $\mathcal{M}^{abcd,\sigma\tau}_0$ and $\mathcal{M}^{abcd,\sigma\tau}_1$, respectively, for the generic four-fermion final state $f_a\bar{f}_b f_c\bar{f}_d$ can be expanded in terms of linear combinations of SME,

$$
\mathcal{M}^{abcd,\sigma\tau}_n = \sum_{i=1}^{13} F^{abcd,\sigma\tau}_{n,i}\,\hat{\mathcal{M}}^{abcd,\sigma\tau}_i, \qquad n = 0,1, \tag{5.2.3}
$$

with Lorentz-invariant functions $F^{abcd,\sigma\tau}_{n,i}$. In this notation the lowest-order amplitudes (5.1.5) read

$$
\begin{aligned}
\mathcal{M}^{\mathrm{ZZ},\sigma_a\sigma_b\sigma_c\sigma_d}_0(k_a,k_b,k_c,k_d) &= \frac{e^3 g^{\sigma_a}_{\mathrm{Z}f_af_b} g^{\sigma_c}_{\mathrm{Z}f_cf_d}\mu_{\mathrm{W}}}{c^2_{\mathrm{W}} s_{\mathrm{W}}}\,\delta_{\sigma_a,-\sigma_b}\delta_{\sigma_c,-\sigma_d}\\
&\quad\times\frac{1}{[(k_a+k_b)^2-\mu^2_{\mathrm{Z}}][(k_c+k_d)^2-\mu^2_{\mathrm{Z}}]}\,\hat{\mathcal{M}}^{abcd,\sigma_a\sigma_c}_1,\\
\mathcal{M}^{\mathrm{WW},\sigma_a\sigma_b\sigma_c\sigma_d}_0(k_a,k_b,k_c,k_d) &= \frac{e^3\mu_{\mathrm{W}}}{2s^3_{\mathrm{W}}}\,\delta_{\sigma_a,-}\delta_{\sigma_b,+}\delta_{\sigma_c,-}\delta_{\sigma_d,+}\\
&\quad\times\frac{1}{[(k_a+k_b)^2-\mu^2_{\mathrm{W}}][(k_c+k_d)^2-\mu^2_{\mathrm{W}}]}\,\hat{\mathcal{M}}^{abcd,--}_1.
\end{aligned} \tag{5.2.4}
$$

For the one-loop amplitudes in general all invariant functions receive contributions. In particular, they contain the loop integrals. The one-loop amplitudes for the various final states are constructed from the amplitudes for $H \to f\bar{f}F\bar{F}$ and $H \to f\bar{f}'F\bar{F}'$ as described in (5.1.8) to (5.1.11) for the lowest order. The one-loop correction to the partial decay widths, finally, reads

$$
\Gamma_{\mathrm{virt}} = \frac{1}{2M_{\mathrm{H}}}\int \mathrm{d}\Phi_0 \sum_{\sigma_1,\sigma_2,\sigma_3,\sigma_4=\pm\frac{1}{2}} 2\,\mathrm{Re}\,\{\mathcal{M}^{\sigma_1,\sigma_2,\sigma_3,\sigma_4}_1(\mathcal{M}^{\sigma_1,\sigma_2,\sigma_3,\sigma_4}_0)^*\}\,. \tag{5.2.5}
$$

The calculation of the one-loop diagrams, which have been generated with *FeynArts* [96], has been carried out in the 't Hooft–Feynman gauge and has been repeated using the background-field method [7], where the individual contributions from self-energy, vertex, and box corrections differ from their counterparts in the conventional formalism. The total one-loop corrections of the conventional and of the background-field approach were found to be in perfect numerical agreement.

5.2.2.2 Gauge-boson resonances and complex-mass scheme

As described in Section 2.3 the description of resonances in (standard) perturbation theory requires a Dyson summation of self-energy insertions in the resonant propagator in order to introduce the imaginary part provided by the finite decay width into the propagator denominator. This procedure in general violates gauge invariance, i.e. destroys Slavnov–Taylor or Ward identities and disturbs the cancellation of gauge-parameter dependences, because different perturbative orders are mixed.

In our calculation we employ the so-called "complex-mass scheme", which was introduced in Ref. [18] for lowest-order calculations and generalized to the one-loop level in Ref. [24]. In this approach the W- and Z-boson masses are consistently considered as complex quantities, defined as the locations of the propagator poles in the complex plane. To this end, bare real masses are split into complex renormalized masses and complex counterterms. Since the bare Lagrangian is not changed, double counting does not occur. Perturbative calculations can be performed as usual, only parameters and counterterms, in particular the electroweak mixing angle defined from the ratio of the W- and Z-boson masses, become complex. Since we only perform an analytic continuation of the parameters, all relations that follow from gauge invariance, such as Ward identities, remain valid. As a consequence the amplitudes are gauge independent, and unitarity cancellations are respected. Moreover, the on-shell renormalization scheme can straightforwardly be transferred to the complex-mass scheme [24].

The use of complex gauge-boson masses necessitates the consistent use of these complex masses also in loop integrals. The scalar master integrals are evaluated for complex masses using the methods and results of Refs. [97, 98, 99].

5.2.2.3 Numerically stable evaluation of one-loop integrals

The one-loop calculation of the decay $\mathrm{H} \to 4f$ requires the evaluation of 5-point one-loop tensor integrals. We calculate the 5-point integrals by directly reducing them to five 4-point functions, as described in Refs. [93, 94]. Note that this reduction does not involve inverse Gram determinants composed of external momenta, which naturally occur in the Passarino–Veltman reduction [100] of tensor to scalar integrals. The latter procedure leads to serious numerical problems when the Gram determinants become small.

Tensor 4-point and 3-point integrals are reduced to scalar integrals with the Passarino–Veltman algorithm [100] as long as no small Gram determinant appears in the reduction. If small Gram determinants occur, the methods that were developed in Ref. [94] are applied. In particular, we evaluate a specific tensor coefficient, the integrand of which is logarithmic in Feynman parametrization, by numerical integration. Then the remaining coefficients as well as the standard scalar integral are algebraically derived from this coefficient.

The whole procedure for the evaluation of the scalar and tensor one-loop integrals has been taken over from the one-loop calculation of $\mathrm{e}^+\mathrm{e}^- \to 4\,\mathrm{fermions}$ [24].

5.2.3 Leading two-loop corrections

Since corrections due to the self-interaction of the Higgs boson become important for large Higgs masses, we have included the dominant two-loop corrections to the decay $\mathrm{H} \to VV$ in the large-Higgs mass limit which were calculated in Refs. [89, 90]. They are of order $\mathcal{O}(G_\mu^2 M_\mathrm{H}^4)$ and read

$$\Gamma_{G_\mu^2 M_\mathrm{H}^4} = 62.0308(86) \left(\frac{G_\mu M_\mathrm{H}^2}{16\pi^2\sqrt{2}}\right)^2 \Gamma_0, \tag{5.2.6}$$

where the numerical prefactor has been taken from Ref. [90]. The error of this factor is far beyond other uncertainties and, thus, ignored in the numerics.

5.3 Real photon corrections

5.3.1 Matrix element for $\mathbf{H} \to 4f\gamma$

The real photonic corrections are induced by the process

$$\mathrm{H}(p) \longrightarrow f_1(k_1,\sigma_1) + \bar{f}_2(k_2,\sigma_2) + f_3(k_3,\sigma_3) + \bar{f}_4(k_4,\sigma_4) + \gamma(k,\lambda), \tag{5.3.1}$$

where the momenta and helicities of the external particles are indicated in parentheses.

As for the lowest-order process, we consistently neglect fermion masses whenever possible. However, we restore the mass-singular logarithms appearing in collinear photon emission as described in Section 4.3 improved by higher-order final-state radiation as described in Section 5.3.3.

The matrix elements for the radiative process can be constructed in the same way as for the lowest-order process (5.1.1) from the set of generic diagrams that is obtained from Figure 5.1 by adding a photon line in all possible ways to the charged particles. We have evaluated the generic helicity matrix elements $\mathcal{M}_\gamma^{\sigma_a\sigma_b\sigma_c\sigma_d\lambda}(k_a,k_b,k_c,k_d,k)$ of this process again using the WvdW spinor technique in the formulation of Ref. [42]. The amplitudes generically read

$$\begin{aligned}&\mathcal{M}_\gamma^{VV,\sigma_a\sigma_b\sigma_c\sigma_d\lambda}(Q_a,Q_b,Q_c,Q_d,k_a,k_b,k_c,k_d,k) = \\ &\qquad 2\sqrt{2}e^4\, g_{Vf_af_b}^{\sigma_a} g_{Vf_cf_d}^{\sigma_c} g_{HVV}\, \delta_{\sigma_a,-\sigma_b}\delta_{\sigma_c,-\sigma_d}\, A_{\sigma_a\sigma_c\lambda}^{VV}(Q_a,Q_b,Q_c,Q_d,k_a,k_b,k_c,k_d,k),\end{aligned} \tag{5.3.2}$$

or more specifically for the case of Z-mediated and W-mediated decays

$$\begin{aligned}&\mathcal{M}_\gamma^{\mathrm{ZZ},\sigma_a\sigma_b\sigma_c\sigma_d\lambda}(Q_a,Q_b,Q_c,Q_d,k_a,k_b,k_c,k_d,k) = \\ &\qquad \frac{2\sqrt{2}e^4 g_{\mathrm{Z}f_af_b}^{\sigma_a} g_{\mathrm{Z}f_cf_d}^{\sigma_c} M_\mathrm{W}}{c_\mathrm{W}^2 s_\mathrm{W}}\, \delta_{\sigma_a,-\sigma_b}\delta_{\sigma_c,-\sigma_d}\, A_{\sigma_a\sigma_c\lambda}^{\mathrm{ZZ}}(Q_a,Q_b,Q_c,Q_d,k_a,k_b,k_c,k_d,k), \\ &\mathcal{M}_\gamma^{\mathrm{WW},\sigma_a\sigma_b\sigma_c\sigma_d\lambda}(Q_a,Q_b,Q_c,Q_d,k_a,k_b,k_c,k_d,k) = \\ &\qquad \frac{\sqrt{2}e^4 M_\mathrm{W}}{s_\mathrm{W}^3}\, \delta_{\sigma_a,-}\delta_{\sigma_b,+}\delta_{\sigma_c,-}\delta_{\sigma_d,+}\, A_{--\lambda}^{\mathrm{WW}}(Q_a,Q_b,Q_c,Q_d,k_a,k_b,k_c,k_d,k).\end{aligned} \tag{5.3.3}$$

The auxiliary functions are given by

$$
\begin{aligned}
&A^{VV}_{---}(Q_a,Q_b,Q_c,Q_d,k_a,k_b,k_c,k_d,k) = \\
&\quad \langle k_b k_d\rangle^* \Biggl[\frac{\langle k_a k_b\rangle^* \langle k_a k_c\rangle + \langle k k_b\rangle^* \langle k k_c\rangle}{[(k_a+k_b+k)^2 - M_V^2][(k_c+k_d)^2 - M_V^2]} \\
&\qquad \times \left(\frac{Q_a}{\langle k k_a\rangle^* \langle k k_b\rangle^*} + \frac{Q_a - Q_b}{(k_a+k_b)^2 - M_V^2} \frac{\langle k k_a\rangle}{\langle k k_b\rangle^*} \right) \\
&\quad - \frac{\langle k_c k_d\rangle^* \langle k_c k_a\rangle + \langle k k_d\rangle^* \langle k k_a\rangle}{[(k_a+k_b)^2 - M_V^2][(k_c+k_d+k)^2 - M_V^2]} \\
&\qquad \times \left(\frac{Q_c}{\langle k k_c\rangle^* \langle k k_d\rangle^*} + \frac{Q_c - Q_d}{(k_c+k_d)^2 - M_V^2} \frac{\langle k k_c\rangle}{\langle k k_d\rangle^*} \right) \\
&\quad + \frac{Q_a - Q_b}{[(k_a+k_b)^2 - M_V^2][(k_c+k_d)^2 - M_V^2]} \frac{\langle k_b k_d\rangle^* \langle k_a k_c\rangle}{\langle k k_b\rangle^* \langle k k_d\rangle^*} \Biggr], \\
&A^{VV}_{+--}(Q_a,Q_b,Q_c,Q_d,k_a,k_b,k_c,k_d) = A^{VV}_{---}(-Q_b,-Q_a,Q_c,Q_d,k_b,k_a,k_c,k_d), \\
&A^{VV}_{-+-}(Q_a,Q_b,Q_c,Q_d,k_a,k_b,k_c,k_d) = A^{VV}_{---}(Q_a,Q_b,-Q_d,-Q_c,k_a,k_b,k_d,k_c), \\
&A^{VV}_{++-}(Q_a,Q_b,Q_c,Q_d,k_a,k_b,k_c,k_d) = A^{VV}_{---}(-Q_b,-Q_a,-Q_d,-Q_c,k_b,k_a,k_d,k_c), \\
&A^{VV}_{\sigma_a\sigma_c+}(Q_a,Q_b,Q_c,Q_d,k_a,k_b,k_c,k_d,k) = \\
&\quad \Bigl(A^{VV}_{-\sigma_a,-\sigma_c,-}(Q_a,Q_b,Q_c,Q_d,k_a,k_b,k_c,k_d,k) \Bigr)^* \Big|_{M_V \to M_V^*},
\end{aligned}
\tag{5.3.4}
$$

and obey the relations

$$
\begin{aligned}
&A^{VV}_{-\sigma_a,-\sigma_c,-\lambda}(Q_a,Q_b,Q_c,Q_d,k_a,k_b,k_c,k_d,k) = \\
&\quad \Bigl(A^{VV}_{\sigma_a\sigma_c\lambda}(Q_a,Q_b,Q_c,Q_d,k_a,k_b,k_c,k_d,k) \Bigr)^* \Big|_{M_V \to M_V^*}, \\
&A^{VV}_{-\sigma_a,\sigma_c,\lambda}(Q_a,Q_b,Q_c,Q_d,k_a,k_b,k_c,k_d,k) = \\
&\quad A^{VV}_{\sigma_a\sigma_c\lambda}(-Q_b,-Q_a,Q_c,Q_d,k_b,k_a,k_c,k_d,k), \\
&A^{VV}_{\sigma_a,-\sigma_c,\lambda}(Q_a,Q_b,Q_c,Q_d,k_a,k_b,k_c,k_d,k) = \\
&\quad A^{VV}_{\sigma_a\sigma_c\lambda}(Q_a,Q_b,-Q_d,-Q_c,k_a,k_b,k_d,k_c,k), \\
&A^{VV}_{\sigma_a,\sigma_c,-\lambda}(Q_a,Q_b,Q_c,Q_d,k_a,k_b,k_c,k_d) = \\
&\quad -\Bigl(A^{VV}_{\sigma_c\sigma_a\lambda}(Q_d,Q_c,Q_b,Q_a,k_d,k_c,k_b,k_a,k) \Bigr)^* \Big|_{M_V \to M_V^*}, \\
&A^{VV}_{\sigma_a,\sigma_c,\lambda}(Q_a,Q_b,Q_c,Q_d,k_a,k_b,k_c,k_d) = \\
&\quad A^{VV}_{\sigma_c\sigma_a\lambda}(Q_c,Q_d,Q_a,Q_b,k_c,k_d,k_a,k_b,k).
\end{aligned}
\tag{5.3.5}
$$

The relations between the $A^{\cdots}_{\cdots}$ functions that differ in all helicities result from a P transformation. Those, where only one fermion helicity is reversed are related to C symmetry. The last but one is due to CP symmetry, and the last one results from a symmetry under the exchange of the two fermion pairs. The charges of the fermions are related by

$$
Q_a - Q_b + Q_c - Q_d = 0. \tag{5.3.6}
$$

For the Z-mediated decays, where $Q_a = Q_b$ and $Q_c = Q_d$, the auxiliary function (5.3.4) simplifies to

$$
\begin{aligned}
&A^{\mathrm{ZZ}}_{---}(Q_a, Q_a, Q_c, Q_c, k_a, k_b, k_c, k_d, k) = \\
&\quad \langle k_b k_d\rangle^* \Biggl[\frac{\langle k_a k_b\rangle^*\langle k_a k_c\rangle + \langle k k_b\rangle^*\langle k k_c\rangle}{[(k_a+k_b+k)^2 - M_V^2][(k_c+k_d)^2 - M_V^2]}\frac{Q_a}{\langle k k_a\rangle^*\langle k k_b\rangle^*} \\
&\quad - \frac{\langle k_c k_d\rangle^*\langle k_c k_a\rangle + \langle k k_d\rangle^*\langle k k_a\rangle}{[(k_a+k_b)^2 - M_V^2][(k_c+k_d+k)^2 - M_V^2]}\frac{Q_c}{\langle k k_c\rangle^*\langle k k_d\rangle^*}\Biggr]. \qquad (5.3.7)
\end{aligned}
$$

From the generic matrix element $\mathcal{M}^{VV,\sigma_a\sigma_b\sigma_c\sigma_d\lambda}(k_a, k_b, k_c, k_d, k)$ the matrix elements for the specific processes can be constructed in complete analogy to the process without photon as in (5.1.8)–(5.1.11).

The squares of the matrix elements (5.3.2) have been successfully checked against the result obtained with the package MADGRAPH [43] numerically.

The contribution Γ_γ of the radiative decay to the total decay width is given by

$$
\Gamma_\gamma = \frac{1}{2M_{\mathrm{H}}}\int \mathrm{d}\Phi_\gamma \sum_{\sigma_1,\sigma_2,\sigma_3,\sigma_4=\pm\frac{1}{2}} \; \sum_{\lambda=\pm 1} |\mathcal{M}_\gamma^{\sigma_1,\sigma_2,\sigma_3,\sigma_4,\lambda}|^2, \qquad (5.3.8)
$$

where the phase-space integral is defined by

$$
\int \mathrm{d}\Phi_\gamma = \int \frac{\mathrm{d}^3\mathbf{k}}{(2\pi)^3 2k^0}\left(\prod_{i=1}^{4}\int \frac{\mathrm{d}^3\mathbf{k}_i}{(2\pi)^3 2k_i^0}\right)(2\pi)^4\delta^{(4)}\biggl(p - k - \sum_{i=1}^{4} k_i\biggr). \qquad (5.3.9)
$$

5.3.2 Treatment of soft and collinear divergences

The structure of soft and collinear singularities of the decay H → $4f$ is exactly the same as in the process $\gamma\gamma \to \mathrm{WW} \to 4f$, because both processes involve the same pattern of charged particles in the initial and final states. Consequently, apart from obvious substitutions for the flux factors all formulas given in Section 4.3 for cross sections literally carry over to the decay widths. The agreement of the dipole-subtraction method and the phase-space slicing method is illustrated in Figures 5.5 and 5.6 for the widths of the two decay channels $\mathrm{H} \to \nu_{\mathrm{e}}\mathrm{e}^+\mu^-\bar{\nu}_\mu$ and $\mathrm{H} \to \mathrm{e}^-\mathrm{e}^+\mu^-\mu^+$. For decreasing auxiliary parameters ΔE and $\Delta\theta$, the slicing result reaches a plateau, as it should be, until the increasing statistical errors become large and are eventually underestimated. In the plateau region the slicing and subtraction results are compatible within statistical errors, but the subtraction result shows smaller integration errors although the same number of events is used.

5.3.3 Higher-order final-state radiation

Photons that are emitted collinear from a charged fermion give rise to corrections that are enhanced by large logarithms of the form $\alpha\log m_f^2/Q^2$, where m_f is a fermion mass and Q is some typical energy scale. If the photons are treated fully inclusively, as it is the case if the photons are recombined with the corresponding fermion, these logarithms cancel due to the KLN theorem [69]. If, however, distributions like in the

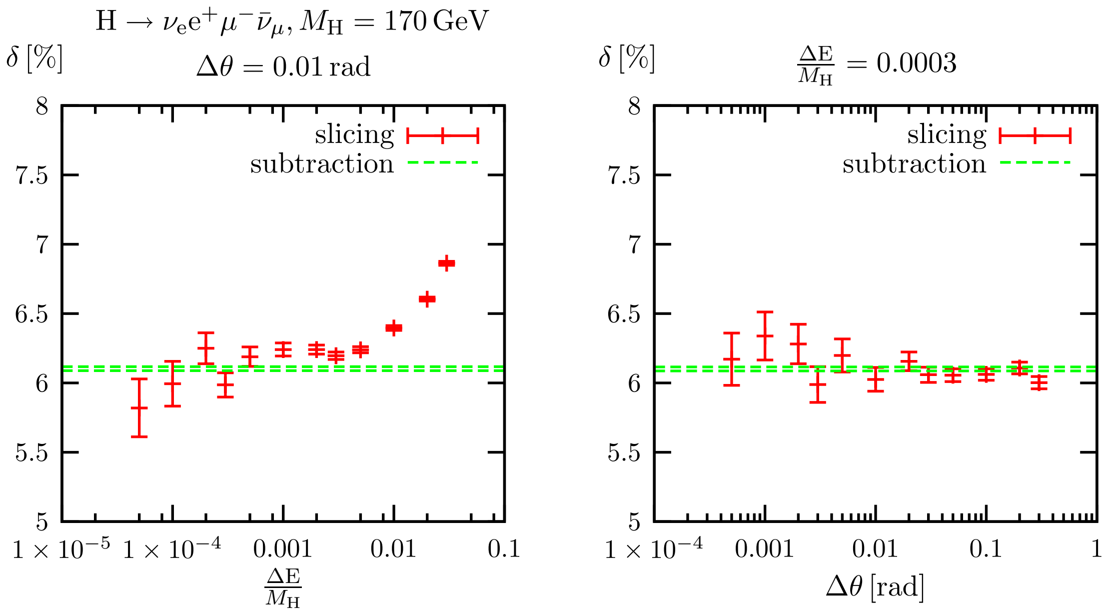

Figure 5.5: Dependence of the relative corrections δ to the partial decay width on the energy cutoff ΔE (l.h.s.) and on the angular cutoff $\Delta\theta$ (r.h.s.) in the slicing approach for the process $\mathrm{H}\to\nu_\mathrm{e}\mathrm{e}^+\mu^-\bar{\nu}_\mu$ with $M_\mathrm{H} = 170\,\mathrm{GeV}$. For comparison the corresponding result obtained with the dipole subtraction method is shown as a 1σ band in the plots.

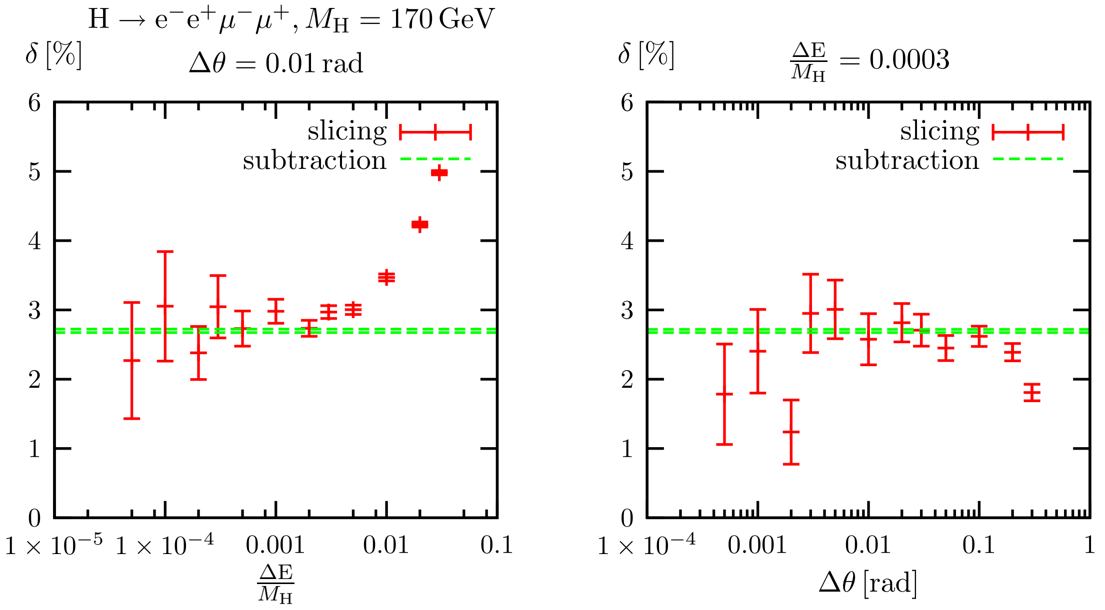

Figure 5.6: Same as in Figure 5.5 but for the decay $\mathrm{H}\to\mathrm{e}^-\mathrm{e}^+\mu^-\mu^+$.

invariant mass of two fermions, as discussed in Section 5.5.3, are to be considered without recombining collinear photons, then these logarithms do not cancel and yield large effects. Thus, corrections of this origin beyond $\mathcal{O}(\alpha)$ should be taken into account. This can be achieved in the structure-function approach [101] which is based on the mass-factorization theorem. According to this theorem the decay width including the leading-logarithmic FSR terms can be written as

$$\int \mathrm{d}\Gamma_{\mathrm{LLFSR}} = \prod_{\substack{i \\ Q_i \neq 0}} \left[\int_0^1 \mathrm{d}z_i \, \Gamma_{ii}^{\mathrm{LL}}(z_i, Q^2) \right] \int \mathrm{d}\Gamma_0 \, \Theta_{\mathrm{cut}}(\{z_j k_j\}). \tag{5.3.10}$$

The function $\Theta_{\mathrm{cut}}(\{z_j k_j\})$ generically denotes all histogram routines or phase-space cuts. It depends on the fermion momenta $z_j k_j$ which, in the case of charged fermions, may be reduced by the factor z_j due to collinear photon emission. For neutral fermions we have $z_j = 1$. The structure functions including terms up to $\mathcal{O}(\alpha^3)$, improved by the exponentiation of the soft-photonic parts, read

$$\begin{aligned}
\Gamma_{ii}^{\mathrm{LL,exp}}(z, Q^2) = {} & \frac{\exp\left(-\frac{1}{2}\beta_i \gamma_{\mathrm{E}} + \frac{3}{8}\beta_i\right)}{\Gamma\left(1 + \frac{1}{2}\beta_i\right)} \frac{\beta_i}{2}(1-z)^{\frac{\beta_i}{2}-1} - \frac{\beta_i}{4}(1+z) \\
& - \frac{\beta_i^2}{32}\left\{ \frac{1+3z^2}{1-z}\ln(z) + 4(1+z)\ln(1-z) + 5 + z \right\} \\
& - \frac{\beta_i^3}{384}\left\{ (1+z)\left[6\,\mathrm{Li}_2(z) + 12\ln^2(1-z) - 3\pi^2\right] \right. \\
& \qquad + \frac{1}{1-z}\left[\frac{3}{2}(1+8z+3z^2)\ln(z) + 6(z+5)(1-z)\ln(1-z) \right. \\
& \qquad + 12(1+z^2)\ln(z)\ln(1-z) - \frac{1}{2}(1+7z^2)\ln^2(z) \\
& \qquad \left.\left. + \frac{1}{4}(39 - 24z - 15z^2) \right] \right\}
\end{aligned} \tag{5.3.11}$$

with γ_{E} and $\Gamma(y)$ denoting Euler's constant and the Gamma function, respectively. The mass-singular logarithm

$$\beta_i = \frac{2\alpha(0)}{\pi}\left[\ln\left(\frac{Q^2}{m_i^2}\right) - 1\right] \tag{5.3.12}$$

involves a scale Q^2, which is not fixed in leading logarithmic order and should be set to a scale typical for the process under consideration. We use $Q^2 = M_{\mathrm{H}}^2$ in our evaluations. As the function $(1-z)^{\frac{\beta_i}{2}-1}$ is difficult to integrate numerically, an appropriate mapping has to be chosen in practice.

In order to study the influence of the higher-order terms we alternatively expanded the exponential up to terms of $\mathcal{O}(\alpha^3)$, yielding

$$\begin{aligned}
\Gamma_{ii}^{\mathrm{LL}}(z, Q^2) = {} & \left[1 + \beta^2\left(\frac{9}{128} - \frac{\pi^2}{48}\right) + \beta^3\left(\frac{\zeta(3)}{24} - \frac{\pi^2}{128} + \frac{9}{1024}\right) \right] \delta(1-z) \\
& + \left[\frac{\beta_i}{4}\frac{1+z^2}{1-z} + \frac{\beta_i^2}{16}\left(\frac{3}{1-z} + 4\frac{\ln(1-z)}{1-z}\right) \right.
\end{aligned}$$

$$
\begin{aligned}
&\left.\quad + \frac{\beta_i^3}{768}\frac{1}{1-z}(27 - 8\pi^2 + 72\ln(1-z) + 48\ln^2(1-z))\right]_+ \\
&- \frac{\beta_i^2}{32}\left\{\frac{1+3z^2}{1-z}\ln(z) + 4(1+z)\ln(1-z) + 5 + z\right\} \\
&- \frac{\beta_i^3}{384}\left\{(1+z)\left[6\,\mathrm{Li}_2(z) + 12\ln^2(1-z) - 3\pi^2\right]\right. \\
&\quad + \frac{1}{1-z}\left[\frac{3}{2}(1+8z+3z^2)\ln(z) + 6(z+5)(1-z)\ln(1-z)\right. \\
&\quad + 12(1+z^2)\ln(z)\ln(1-z) - \frac{1}{2}(1+7z^2)\ln^2(z) \\
&\quad \left.\left. + \frac{1}{4}(39 - 24z - 15z^2)\right]\right\},
\end{aligned}
\tag{5.3.13}
$$

where ζ labels the Riemann ζ-function.

Since we already accounted for the lowest-order term and the $\mathcal{O}(\alpha)$ term which is contained in the complete $\mathcal{O}(\alpha)$ corrections, we have to subtract

$$
\int \mathrm{d}\Gamma_{\mathrm{LLFSR},1} = \int \mathrm{d}\Gamma_0 + \int \mathrm{d}\Gamma_0 \sum_i \int_0^1 \mathrm{d}z_i\, \Gamma_{ii}^{\mathrm{LL},1}(z_i, Q^2)\Theta_{\mathrm{cut}}(z_i k_i, \{k_{j\neq i}\}),
\tag{5.3.14}
$$

i.e. the leading logarithmic terms up to $\mathcal{O}(\alpha)$, from $\int \mathrm{d}\Gamma_{\mathrm{LLFSR}}$. They are defined by

$$
\Gamma_{ii}^{\mathrm{LL},1}(z, Q^2) = \frac{\beta_{i,G_\mu}}{4}\left(\frac{1+z^2}{1-z}\right)_+ .
\tag{5.3.15}
$$

Note that the leading-logarithmic terms scale with $\alpha(0)$. Therefore, we have to subtract the $\mathcal{O}(\alpha)$ terms according to the scheme that is applied for the virtual corrections. Since we work in the G_μ scheme, β_{i,G_μ} is proportional to α_{G_μ}, as defined in Eq. (3.5.3).

5.4 Improved Born Approximation

Some loop diagrams involving top quarks lead to corrections that are enhanced by a large coupling factor $G_\mu m_\mathrm{t}^2$ in the limit of a large top-quark mass m_t. For the generic amplitudes of $\mathrm{H} \to 4f$ the leading m_t-dependent corrections in the heavy-top limit read (in the G_μ-scheme)

$$
\begin{aligned}
\mathcal{M}_1^{\mathrm{ZZ},\sigma_1\sigma_3}\Big|_{G_\mu\text{-scheme}} \;\widetilde{m_\mathrm{t}\to\infty}\;& \frac{\alpha}{4\pi s_\mathrm{w}^2}\left[\left(\frac{1}{8} - \frac{3c_\mathrm{w}}{4s_\mathrm{w}}\left(\frac{Q_{f_1}}{g_{\mathrm{Z}f_1f_1}^{\sigma_1}} + \frac{Q_{f_3}}{g_{\mathrm{Z}f_3f_3}^{\sigma_3}}\right)\right)\frac{m_\mathrm{t}^2}{M_\mathrm{W}^2}\right. \\
&\left. - \left(\frac{Q_{f_1}}{g_{\mathrm{Z}f_1f_1}^{\sigma_1}} + \frac{Q_{f_3}}{g_{\mathrm{Z}f_3f_3}^{\sigma_3}}\right)\frac{3-2s_\mathrm{w}^2}{3c_\mathrm{w}s_\mathrm{w}}\ln\frac{m_\mathrm{t}}{M_\mathrm{W}}\right]\mathcal{M}_0^{\mathrm{ZZ},\sigma_1\sigma_3} + \mathcal{O}(m_\mathrm{t}^0), \\
\mathcal{M}_1^{\mathrm{WW}}\Big|_{G_\mu\text{-scheme}} \;\widetilde{m_\mathrm{t}\to\infty}\;& -\frac{5\alpha}{32\pi s_\mathrm{w}^2}\frac{m_\mathrm{t}^2}{M_\mathrm{W}^2}\mathcal{M}_0^{\mathrm{WW}} + \mathcal{O}(m_\mathrm{t}^0),
\end{aligned}
\tag{5.4.1}
$$

where we use the real W-boson mass M_W, and the terms proportional to a charge factor Q_f are absent if f is a neutrino. The leading m_t^2-enhanced terms of the WW channel agree with the terms derived for the HWW vertex [88], since in the G_μ-scheme all leading m_t^2 contributions related to the W-boson coupling to fermions are absorbed in α_{G_μ}. In the ZH channel, m_t^2-enhanced terms do not only result from the HZZ vertex, but there are also remnants originating from the renormalization of the Z-boson couplings to fermions. In contrast to the WW channel, in the ZZ channel there are also logarithmic terms $\ln m_\mathrm{t}$ for a large top-quark mass. For the WW channel and for the ZZ channel with one Z boson decaying into neutrinos and the other into charged leptons, the correction terms in (5.4.1) agree with the corresponding results given in Ref. [92] for the production process $\mathrm{e}^+\mathrm{e}^- \to \nu\bar{\nu}\mathrm{H}$.

Including also the one-loop corrections $\propto G_\mu M_\mathrm{H}^2$ and the two-loop corrections $\propto (G_\mu M_\mathrm{H}^2)^2$ from Refs. [89, 90] we define the matrix elements for an improved-Born approximation (IBA) for the non-photonic contributions as

$$\begin{aligned}
\mathcal{M}^{\mathrm{ZZ},\sigma_1\sigma_3}_{\mathrm{IBA,non\text{-}photonic}} &= \mathcal{M}_0^{\mathrm{ZZ},\sigma_1\sigma_3}\Biggl[1 - \frac{G_\mu m_\mathrm{t}^2}{2\sqrt{2}\pi^2}\left(\frac{1}{8} - \frac{3c_\mathrm{w}}{4s_\mathrm{w}}\left(\frac{Q_{f_1}}{g^{\sigma_1}_{\mathrm{Z}f_1f_1}} + \frac{Q_{f_3}}{g^{\sigma_3}_{\mathrm{Z}f_3f_3}}\right)\right) \\
&\quad - \frac{G_\mu M_\mathrm{W}^2}{2\sqrt{2}\pi^2}\left(\frac{Q_{f_1}}{g^{\sigma_1}_{\mathrm{Z}f_1f_1}} + \frac{Q_{f_3}}{g^{\sigma_3}_{\mathrm{Z}f_3f_3}}\right)\frac{3-2s_\mathrm{w}^2}{3c_\mathrm{w}s_\mathrm{w}}\ln\frac{m_\mathrm{t}}{M_\mathrm{W}} \\
&\quad + \frac{G_\mu M_\mathrm{H}^2}{16\pi^2\sqrt{2}}\left(\frac{5\pi^2}{6} - 3\sqrt{3}\pi + \frac{19}{2} + \mathrm{i}\pi(2\ln 2 - 5)\right) \\
&\quad - \left(\frac{G_\mu M_\mathrm{H}^2}{16\pi^2\sqrt{2}}\right)^2\Bigl(34.4082(43) + 21.0031(62)\,\mathrm{i}\Bigr)\Biggr], \\
\mathcal{M}^{\mathrm{WW}}_{\mathrm{IBA,non\text{-}photonic}} &= \mathcal{M}_0^{\mathrm{WW}}\Biggl[1 - \frac{5G_\mu m_\mathrm{t}^2}{16\sqrt{2}\pi^2} \\
&\quad + \frac{G_\mu M_\mathrm{H}^2}{16\pi^2\sqrt{2}}\left(\frac{5\pi^2}{6} - 3\sqrt{3}\pi + \frac{19}{2} + \mathrm{i}\pi(2\ln 2 - 5)\right) \\
&\quad - \left(\frac{G_\mu M_\mathrm{H}^2}{16\pi^2\sqrt{2}}\right)^2\Bigl(34.4082(43) + 21.0031(62)\,\mathrm{i}\Bigr)\Biggr], \qquad (5.4.2)
\end{aligned}$$

where we suppress some polarization indices in the lowest-order matrix elements that were defined in Section 5.1. Since our lowest-order matrix element $\mathcal{M}_0$ is complex, owing to the propagator width, both the imaginary part of the $G_\mu M_\mathrm{H}^2$ term and the imaginary part of the $(G_\mu M_\mathrm{H}^2)^2$ term contribute when taking the absolute square of the matrix elements.

Finally, we define the IBA for the partial decay widths $\mathrm{H} \to \mathrm{WW} \to f_1\bar{f}_2f_3\bar{f}_4$ and $\mathrm{H} \to \mathrm{ZZ} \to f_1\bar{f}_2f_3\bar{f}_4$ as

$$\begin{aligned}
\Gamma^{\mathrm{H}\to\mathrm{ZZ}\to4f}_{\mathrm{IBA}} &= \frac{1}{2M_\mathrm{H}}\int \mathrm{d}\Phi_0 \sum_{\sigma_1,\sigma_3=\pm} |\mathcal{M}^{\mathrm{ZZ},\sigma_1\sigma_3}_{\mathrm{IBA,non\text{-}photonic}}|^2, \\
\Gamma^{\mathrm{H}\to\mathrm{WW}\to4f}_{\mathrm{IBA}} &= \frac{1}{2M_\mathrm{H}}\int \mathrm{d}\Phi_0\, |\mathcal{M}^{\mathrm{WW}}_{\mathrm{IBA,non\text{-}photonic}}|^2 \\
&\quad \times \Bigl[1 + \delta_{\mathrm{Coul}}\Bigl(M_\mathrm{H}^2, (k_1+k_2)^2, (k_3+k_4)^2\Bigr)\, g(\bar{\beta})\Bigr], \qquad (5.4.3)
\end{aligned}$$

which is then convoluted with the FSR as given in (5.3.10). The phase-space integral was defined in (5.3.9), and the effect of the Coulomb singularity is incorporated in

$$\begin{aligned}
\delta_{\mathrm{Coul}}(s,k_+^2,k_-^2) &= \frac{\alpha(0)}{\bar\beta}\,\mathrm{Im}\left\{\ln\left(\frac{\beta-\bar\beta+\Delta_M}{\beta+\bar\beta+\Delta_M}\right)\right\},\\
\bar\beta &= \frac{\sqrt{s^2+k_+^4+k_-^4-2sk_+^2-2sk_-^2-2k_+^2k_-^2}}{s},\\
\beta &= \sqrt{1-\frac{4\mu_{\mathrm{W}}^2}{s}}, \qquad \Delta_M = \frac{|k_+^2-k_-^2|}{s},
\end{aligned} \tag{5.4.4}$$

with the fine-structure constant $\alpha(0)$. The auxiliary function

$$g(\bar\beta) = \left(1-\bar\beta^2\right)^2 \tag{5.4.5}$$

restricts the impact of δ_{Coul} to the threshold region where it is valid.

The IBA for the final states $f\bar f f \bar f$ and $f\bar f f'\bar f'$ are defined via the corresponding matrix elements as in (5.1.10) and (5.1.11), respectively. However, the correction factor δ_{Coul} is only multiplied to the squared charged-current matrix element $|\mathcal{M}^{\mathrm{WW}}_{\mathrm{IBA,non\text{-}photonic}}|^2$, because the interference term turns out to be very small.

5.5 Numerical results

5.5.1 Input parameters and setup

We use the following set of input parameters [9]

$$\begin{aligned}
G_\mu &= 1.16637\times10^{-5}\,\mathrm{GeV}^{-2}, & \alpha(0) &= 1/137.03599911, & \alpha_{\mathrm{s}} &= 0.1172,\\
M_{\mathrm{W}} &= 80.425\,\mathrm{GeV}, & M_{\mathrm{Z}} &= 91.1876\,\mathrm{GeV}, & &\\
m_{\mathrm{e}} &= 0.51099892\,\mathrm{MeV}, & m_\mu &= 105.658369\,\mathrm{MeV}, & m_\tau &= 1.77699\,\mathrm{GeV},\\
m_{\mathrm{u}} &= 0.066\,\mathrm{GeV}, & m_{\mathrm{c}} &= 1.2\,\mathrm{GeV}, & m_{\mathrm{t}} &= 178\,\mathrm{GeV},\\
m_{\mathrm{d}} &= 0.066\,\mathrm{GeV}, & m_{\mathrm{s}} &= 0.15\,\mathrm{GeV}, & m_{\mathrm{b}} &= 4.3\,\mathrm{GeV}.
\end{aligned} \tag{5.5.1}$$

For the top-quark mass m_{t} we have taken the value from Ref. [102].

By applying the G_μ scheme a large part of the $\mathcal{O}(\alpha)$ corrections is absorbed into the lowest order prediction as described in Section 3.5.1. In particular, the electromagnetic coupling constant is derived from the Fermi constant according to Eq. (3.5.3), so that our lowest-order results scale with $\alpha^3_{G_\mu}$ and the radiative corrections with $\alpha^4_{G_\mu}$

The widths of the gauge bosons W and Z, Γ_{W} and Γ_{Z}, are calculated from the above input including $\mathcal{O}(\alpha)$ corrections, but using real mass parameters everywhere. Alternatively, the experimental widths could be used, but the procedure pursued here ensures that the "effective branching ratios" of the W's and Z's, which result from the integration over their decays, add up to one if all decay channels are summed over. The gauge-boson widths depend on the Higgs mass only weakly. For the Higgs masses $M_{\mathrm{H}} = 140, 170, 200\,\mathrm{GeV}$

the corresponding values are given in Table 5.1. These values are used everywhere, i.e. we also apply the $\mathcal{O}(\alpha)$-corrected W and Z widths for the lowest-order predictions.

The angular distributions in Section 5.5.4 are defined in the rest frame of the Higgs boson. All observables are calculated without applying phase-space cuts, and, if not stated otherwise, a photon recombination is performed. More precisely, if the invariant mass of a photon and a charged fermion is smaller than 5 GeV, the photon momentum is added to the fermion momentum in the histograms. If this condition applies to more than one fermion the photon is recombined with the fermion that yields the smallest invariant mass.

All but the lowest-order predictions contain the higher-order FSR, as described in Section 5.3.3, as well as the two-loop corrections proportional to $G_\mu^2 M_\mathrm{H}^4$ given in Section 5.2.3. The phase-space integration is performed using the multi-channel Monte Carlo technique, which is described in App. A. The numerical results presented below have been obtained using $5 \cdot 10^7$ events except for the plots showing the decay width as a function of the Higgs mass which were calculated using $2 \cdot 10^7$ events per point. Since the virtual corrections (rendered finite by adding the soft and collinear singularities from the real corrections), and also their statistical error, are at least a factor 10 smaller than the lowest-order values for moderate Higgs masses, we only evaluated the virtual corrections every 100th time, which improves the run-time of the program but does not deteriorate the overall statistical error.

5.5.2 Results for the partial decay width

In Table 5.1 the partial decay width including $\mathcal{O}(\alpha)$ corrections is shown for different decay channels and different values of the Higgs mass. In brackets the statistical error of the phase-space integration is shown, and $\delta = \Gamma/\Gamma_0 - 1$ labels the relative corrections. The first two channels, $\mathrm{e}^-\mathrm{e}^+\mu^-\mu^+$ and $\mathrm{e}^-\mathrm{e}^+\mathrm{e}^-\mathrm{e}^+$ result from the decay $\mathrm{H} \to \mathrm{ZZ} \to 4f$. The corresponding lowest-order matrix elements are given in (5.1.8) and (5.1.10), respectively. The width corresponding to the latter channel is typically smaller by a factor 2, because the decay $\mathrm{H} \to \mathrm{e}^-\mathrm{e}^+\mathrm{e}^-\mathrm{e}^+$ proceeds via two Feynman diagrams with small interference in lowest order and requires a factor 1/4 for identical particles in the final state. The channel $\nu_\mathrm{e}\mathrm{e}^+\mu^-\bar{\nu}_\mu$ (5.1.9) results from the decay $\mathrm{H} \to \mathrm{WW} \to 4f$, while the last channel $\nu_\mathrm{e}\mathrm{e}^+\mathrm{e}^-\bar{\nu}_\mathrm{e}$ (5.1.11) receives contributions from the decay into W and into Z bosons. The larger the Higgs mass, the larger is the decay width, because the available phase space grows.

In the two upper plots of Figure 5.7 we show the partial decay width for the final state $\nu_\mathrm{e}\mathrm{e}^+\mu^-\bar{\nu}_\mu$ as a function of the Higgs mass. The lower plots show the corrections relative to the lowest-order result. As already explained, we always normalize to the lowest-order result that already includes the $\mathcal{O}(\alpha)$-corrected width of the gauge bosons. A large fraction of the $\mathcal{O}(\alpha)$ corrections is transferred to the lowest-order decay width by applying the G_μ scheme. Thus, the corrections are at the order of 2–8% for moderate Higgs masses. However, for large Higgs masses the corrections become larger and reach about 13% at $M_\mathrm{H} = 700\,\mathrm{GeV}$. In this region the leading two-loop corrections already amount to about 4%. Around 160 GeV the Coulomb singularity, which originates from soft-photon exchange between the two slowly moving W bosons, is reflected in the shape

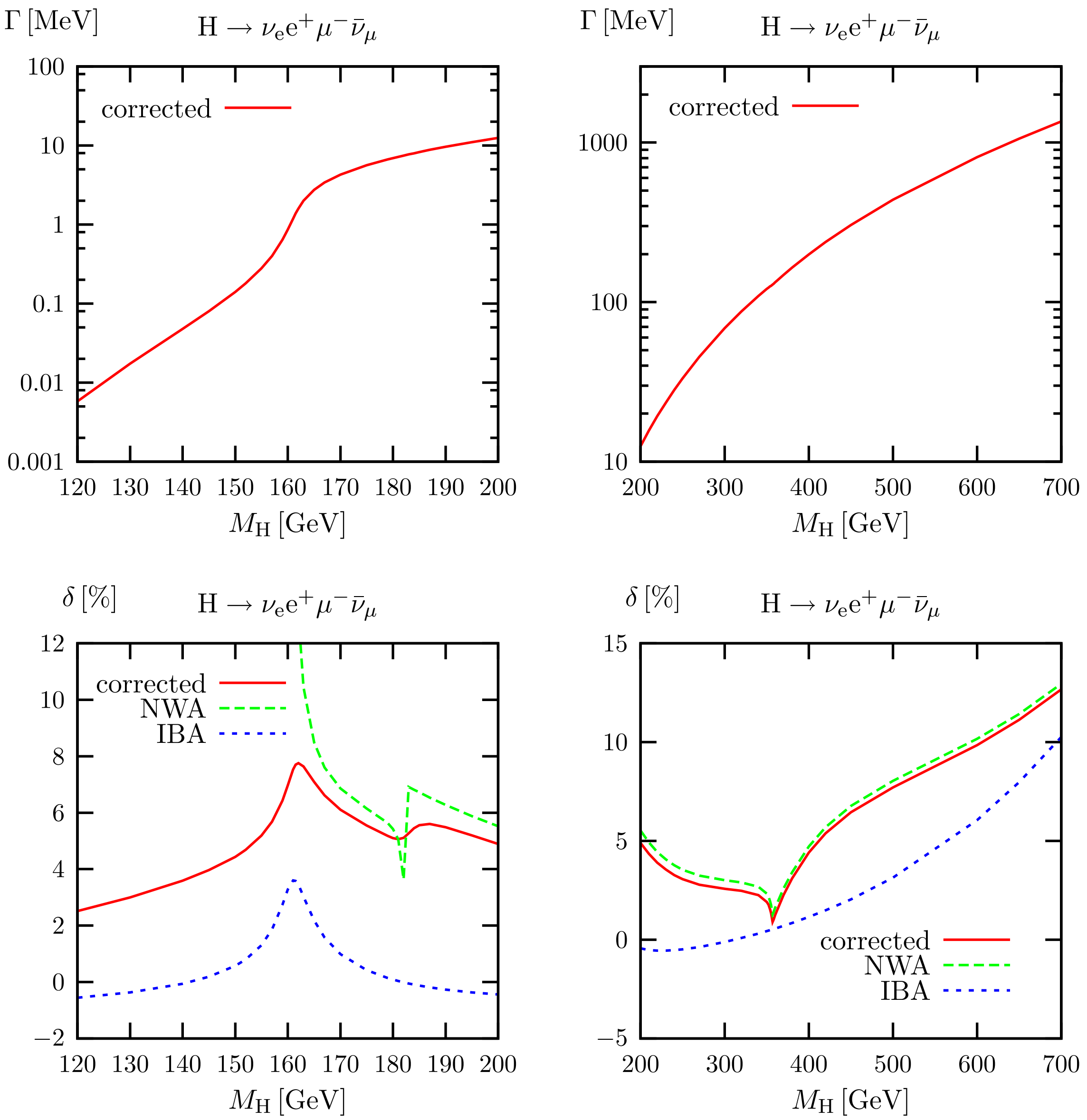

Figure 5.7: Partial decay width for $\mathrm{H} \to \nu_\mathrm{e}\mathrm{e}^+\mu^-\bar{\nu}_\mu$ as a function of the Higgs mass. The upper plots show the absolute prediction including $\mathcal{O}(\alpha)$ and $\mathcal{O}(G_\mu^2 M_\mathrm{H}^4)$ corrections, and the lower plots show the comparison of the relative $\mathcal{O}(\alpha)$ and $\mathcal{O}(G_\mu^2 M_\mathrm{H}^4)$ corrections with the NWA and IBA.

	$M_{\mathrm{H}}[\,\mathrm{GeV}]$	140		170		200	
	$\Gamma_{\mathrm{W}}[\,\mathrm{GeV}]$	2.09273...		2.09275...		2.09276...	
	$\Gamma_{\mathrm{Z}}[\,\mathrm{GeV}]$	2.50548...		2.50557...		2.50563...	
$\mathrm{H} \to$		$\Gamma[\,\mathrm{MeV}]$	$\delta[\%]$	$\Gamma[\,\mathrm{MeV}]$	$\delta[\%]$	$\Gamma[\,\mathrm{MeV}]$	$\delta[\%]$
$\mathrm{e}^-\mathrm{e}^+\mu^-\mu^+$	corrected	0.0012582(5)	2.2	0.020056(7)	2.7	0.8183(2)	4.4
	lowest order	0.0012310(4)		0.019529(5)		0.78408(8)	
$\mathrm{e}^-\mathrm{e}^+\mathrm{e}^-\mathrm{e}^+$	corrected	0.0006667(2)	2.0	0.010292(3)	2.7	0.40930(8)	4.4
	lowest order	0.0006534(2)		0.010026(2)		0.39217(4)	
$\nu_{\mathrm{e}}\mathrm{e}^+\mu^-\bar{\nu}_\mu$	corrected	0.04789(2)	3.6	4.2962(9)	6.1	12.484(3)	4.9
	lowest order	0.04623(1)		4.0491(7)		11.899(2)	
$\nu_{\mathrm{e}}\mathrm{e}^+\mathrm{e}^-\bar{\nu}_{\mathrm{e}}$	corrected	0.04896(2)	3.7	4.329(1)	6.1	14.114(3)	5.0
	lowest order	0.04722(2)		4.0804(8)		13.446(2)	

Table 5.1: Partial decay widths for H → 4 leptons including $\mathcal{O}(\alpha)$ corrections and relative correction for various decay channels and different Higgs masses.

of the curve. The influence of diagrams with a Higgs boson splitting into Z-boson pair ("normal ZZ threshold") is visible at $M_{\mathrm{H}} \sim 2M_{\mathrm{Z}}$. At about $2m_{\mathrm{t}}$ the $\mathrm{t\bar{t}}$ threshold is visible.

For stable W or Z bosons, i.e. in the limit $\Gamma_V \to 0$ $(V = \mathrm{W},\mathrm{Z})$, it is possible to define a narrow-width approximation (NWA) where the matrix elements factorize into the decay $\mathrm{H} \to VV$ and the subsequent decay of the gauge bosons into fermions. By definition the NWA is only applicable above the WW or ZZ threshold. However, its analytical structure and evaluation is considerably simpler than in the case of the full decay $\mathrm{H} \to \mathrm{WW/ZZ} \to 4f$ with off-shell gauge bosons. Therefore, above threshold the NWA allows for an economic way of calculating $\mathcal{O}(\alpha)$ corrections to the integrated decay width, while the lowest-order contribution may, of course, still take into account unstable gauge bosons. Following this line of thought, we define

$$\Gamma^{\mathrm{NWA}} = \Gamma_0\,\frac{\Gamma_1^{\mathrm{NWA}}}{\Gamma_0^{\mathrm{NWA}}}, \tag{5.5.2}$$

with

$$\Gamma_1^{\mathrm{NWA}} = \Gamma_{\mathrm{H}VV,1}\,\frac{\Gamma_{Vf_1\bar{f}_2,1}\Gamma_{Vf_3\bar{f}_4,1}}{\Gamma_{V,1}\Gamma_{V,1}}, \tag{5.5.3}$$

and

$$\Gamma_0^{\mathrm{NWA}} = \Gamma_{\mathrm{H}VV,0}\,\frac{\Gamma_{Vf_1\bar{f}_2,0}\Gamma_{Vf_3\bar{f}_4,0}}{\Gamma_{V,1}\Gamma_{V,1}}. \tag{5.5.4}$$

The indices "0" and "1" label lowest-order and $\mathcal{O}(\alpha)$-corrected results, respectively. The Higgs-mass-enhanced two-loop terms, described in Section 5.2.3, have also been included in $\Gamma_{\mathrm{H}VV,1}$. In order to be consistent we again use the $\mathcal{O}(\alpha)$-corrected total width for the gauge bosons in Γ_0^{NWA}. We note that we have rederived all necessary $\mathcal{O}(\alpha)$ corrections entering the NWA; the hard photonic corrections to the decay $\mathrm{H} \to \mathrm{WW}$ have been checked against the expression given in Ref. [87].

A few GeV above the corresponding gauge-boson-pair threshold the NWA agrees with the complete $\mathcal{O}(\alpha)$ corrections within 1%. Near $M_\mathrm{H} = 180\,\mathrm{GeV}$ the loop-induced ZZ threshold can be seen in the relative corrections to $\mathrm{H} \to \mathrm{WW} \to \nu_\mathrm{e}\mathrm{e}^+\mu^-\bar{\nu}_\mu$ shown in Figure 5.7. In the NWA this threshold leads to a singularity visible as a sharp peak; in the off-shell calculation in the complex-mass scheme this singular structure is smeared out, because the Z-boson width is taken into account. Since the ZZ threshold corresponds to the situation where two Z bosons become on shell in the loop, the latter description with the singularity regularized by a finite Γ_Z should be closer to physical reality. A similar situation can be seen near $\mathrm{H} = 2m_\mathrm{t}$ for the $\mathrm{t\bar{t}}$ threshold with top quarks in the loops, where we observe a sharp peak also for the complete $\mathcal{O}(\alpha)$ corrections, because we have not taken into account the top decay width Γ_t. In principle, this is straightforward and represents an option for a future improvement of the calculation.

Although the IBA, which is also shown in Figure 5.7 reflects the shape of the Coulomb singularity around $M_\mathrm{H} = 160\,\mathrm{GeV}$ and the rise of the corrections for large Higgs masses quite well, it does not provide a good overall description of the complete $\mathcal{O}(\alpha)$ corrections. Apparently, the m_t^2-enhanced terms do not yield the dominant effect, but bosonic corrections contribute a substantial part of the $\mathcal{O}(\alpha)$ corrections.

The plots in Figure 5.8 show the decay width and the relative correction for the final state $\mathrm{e}^-\mathrm{e}^+\mu^-\mu^+$. The correction are between 2% and 4% for moderate Higgs masses and rise to more than 10% for large Higgs masses. At a Higgs mass of about 160 GeV the influence of the diagram where a W-boson loop is coupled to the Higgs boson can be observed. As explained above, the behaviour of the corrections as a function of the Higgs mass is smooth, because the gauge-boson width is also used in the loop integrals. In contrast to the decay $\mathrm{H} \to \nu_\mathrm{e}\mathrm{e}^+\mu^-\bar{\nu}_\mu$, there is no Coulomb singularity at around 180 GeV because the Z boson is electrically neutral. The NWA reproduces the complete result up to 0.5% not too close to the threshold, while the IBA is only good within 2%, and deviates even more in the region $M_\mathrm{H} \sim 2m_\mathrm{t}$, where the assumption of large top mass is not valid.

Predictions for the partial decay widths of the Higgs boson can also be obtained with various program packages, such as HDECAY [56], which contains the lowest-order decay width for $\mathrm{H} \to V^{(*)}V^{(*)}$, and also the leading one-loop corrections $\propto G_\mu M_\mathrm{H}^2$ and two-loop corrections $\propto G_\mu^2 M_\mathrm{H}^4$. In order to obtain the decay width for $\mathrm{H} \to \mathrm{WW/ZZ} \to 4f$, we define

$$\Gamma^\mathrm{HD} = \Gamma^\mathrm{HD}_{\mathrm{H}VV} \frac{\Gamma_{Vf_1f_2,0}}{\Gamma_{V,1}} \frac{\Gamma_{Vf_3f_4,0}}{\Gamma_{V,1}}, \tag{5.5.5}$$

where $\Gamma^\mathrm{HD}_{\mathrm{H}VV}$ is the decay width from HDECAY. In (5.5.5) the branching ratios of the gauge bosons are normalized in the same way (lowest order in the numerator, corrected total width in the denominator) as the effective branching ratios of our lowest-order predictions for the $\mathrm{H} \to VV \to 4f$ partial widths; otherwise a comparison would not be very conclusive.

The comparison in Figure 5.9, where Γ^HD is shown relative to our complete lowest-order prediction, shows that HDECAY agrees with our lowest-order prediction below the decay threshold quite well. In this region $\Gamma^\mathrm{HD}_{\mathrm{H}VV}$ consistently takes into account the off-shell

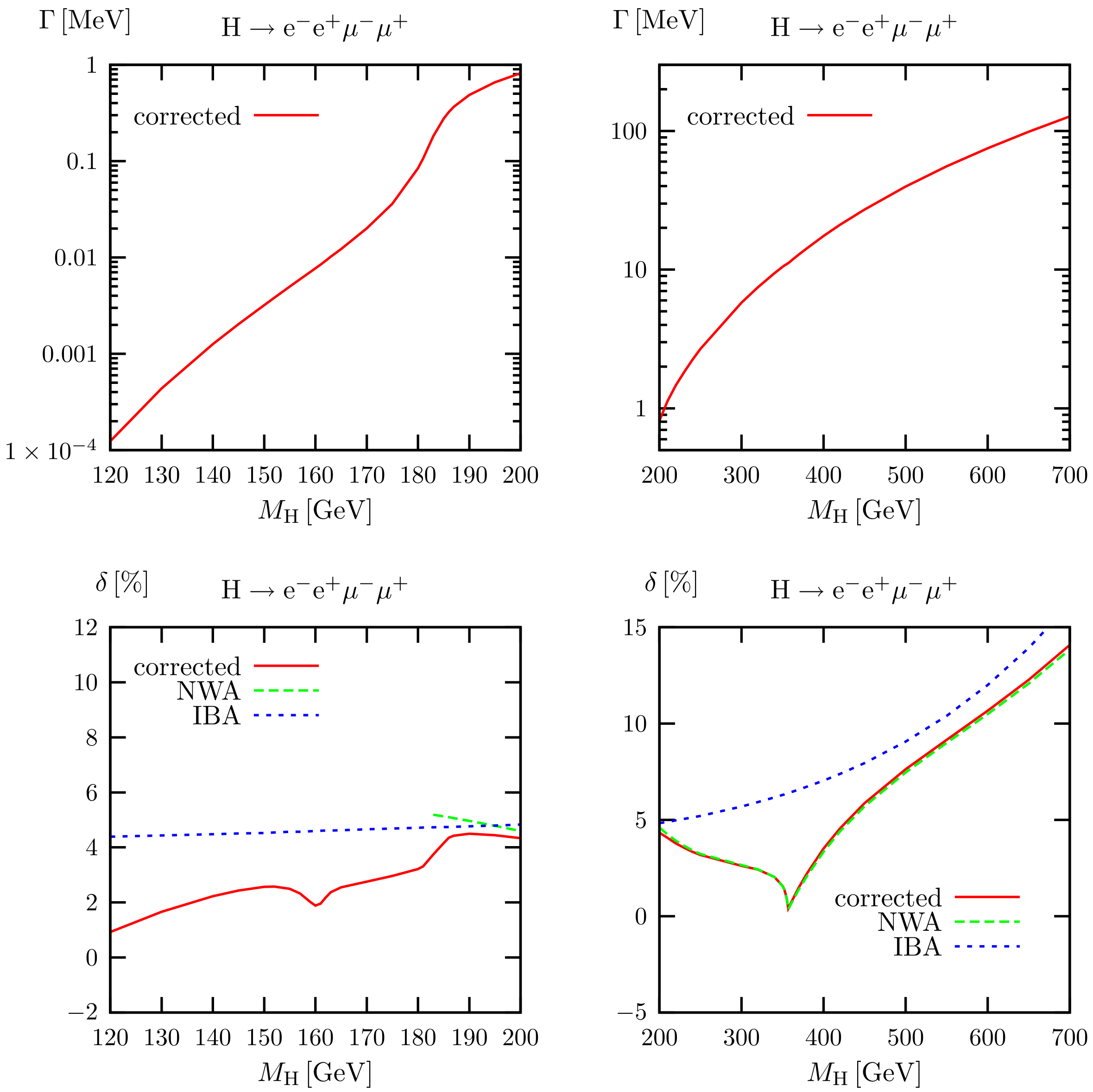

Figure 5.8: Partial decay width for $H \to e^-e^+\mu^-\mu^+$ as a function of the Higgs mass. The upper plots show the absolute prediction including $\mathcal{O}(\alpha)$ and $\mathcal{O}(G_\mu^2 M_H^4)$ corrections, and the lower plots show the comparison of the relative $\mathcal{O}(\alpha)$ and $\mathcal{O}(G_\mu^2 M_H^4)$ corrections with the NWA and IBA.

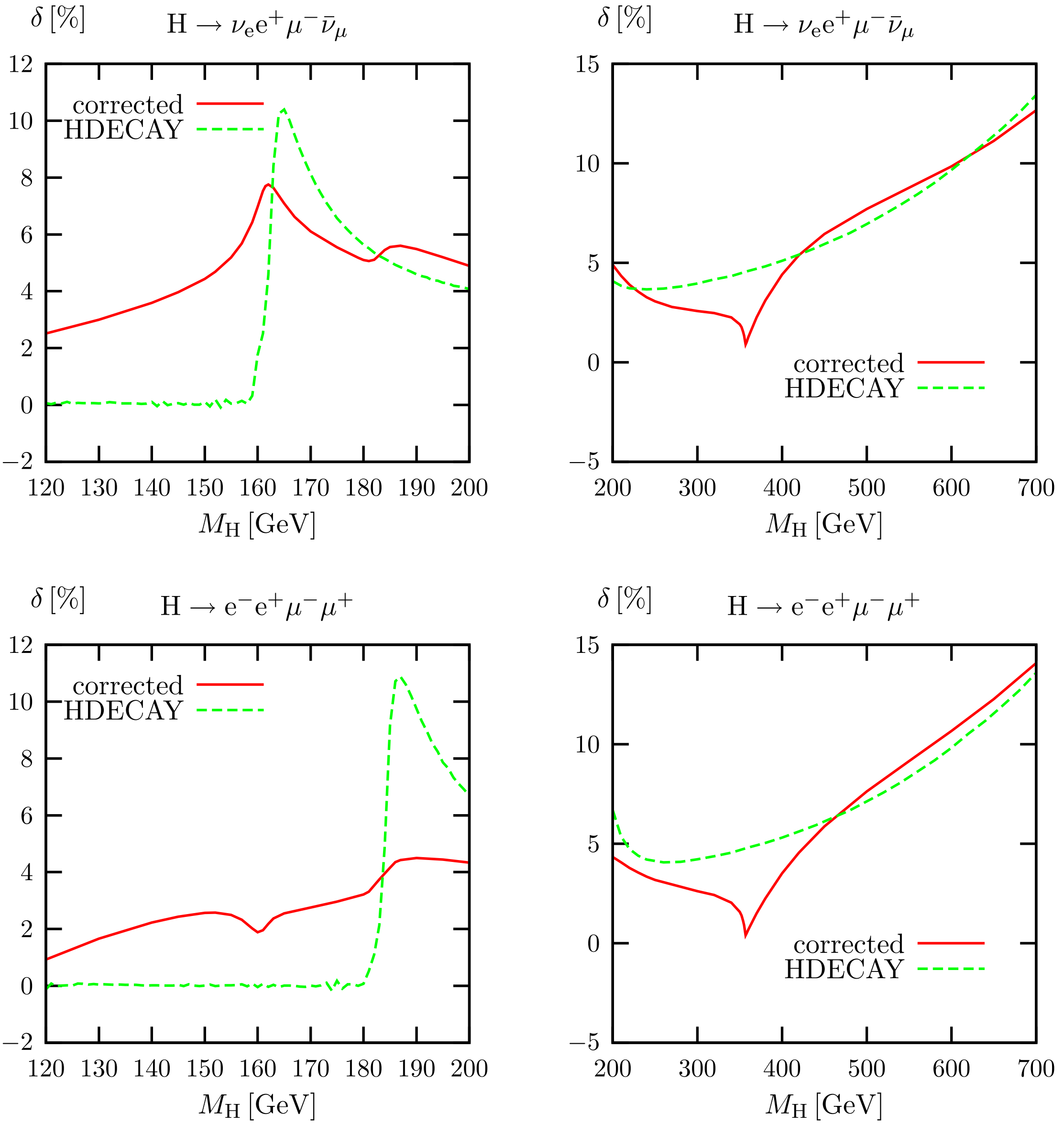

Figure 5.9: Predictions for the partial decay widths for $\mathrm{H} \to \nu_\mathrm{e}\mathrm{e}^+\mu^-\bar{\nu}_\mu$ and $\mathrm{H} \to \mathrm{e}^-\mathrm{e}^+\mu^-\mu^+$ obtained with the program HDECAY normalized to the complete lowest-order decay width. The corrections shown in Figures 5.7 and 5.8 are included for comparison.

effects of the gauge bosons. Above the threshold HDECAY neglects off-shell effects of the gauge bosons. In the threshold region, off-shell effects are, however, very important. Here, the difference between the complete off-shell result and the Higgs width for on-shell gauge bosons amounts to about 10%. In detail, HDECAY interpolates between the off-shell and on-shell results within a window of $\pm 2\,\mathrm{GeV}$ around threshold. The maxima in the HDECAY curves near the WW and ZZ thresholds in the upper and lower left plots of Figure 5.9, respectively, are artefacts originating from the on-shell phase space of the W or Z bosons above threshold. These maxima have nothing to do with the maximum of the correction near the WW threshold in the upper left plot, which is due to the Coulomb singularity. For large M_{H} HDECAY follows our corrected result within a few per cent, because the dominant radiative corrections $\propto G_\mu M_{\mathrm{H}}^2$ and $\propto G_\mu^2 M_{\mathrm{H}}^4$, which grow fast with increasing M_{H}, are included in both calculations.

5.5.3 Invariant-mass distributions

In Figure 5.10 we study the invariant-mass distribution of the two fermions resulting from the decay of the W bosons in the decay $\mathrm{H} \to \nu_{\mathrm{e}}\mathrm{e}^+\mu^-\bar{\nu}_\mu$. The plots on the l.h.s. show the distribution for $\mu^-\bar{\nu}_\mu$ including corrections for $M_{\mathrm{H}} = 140\,\mathrm{GeV}$ and $M_{\mathrm{H}} = 170\,\mathrm{GeV}$, i.e. for one value of M_{H} below and one above the WW threshold. The plots on the r.h.s. compare the relative corrections for $\nu_{\mathrm{e}}\mathrm{e}^+$ and $\mu^-\bar{\nu}_\mu$ both with and without photon recombination. The invariant mass $M_{f\bar{f}'}$ is calculated from the sum of the momenta of the fermions f and f'. If no photon recombination is applied, the bare momenta are taken. In the case of photon recombination the momentum of collinear photons is included in the invariant mass.

For $M_{\mathrm{H}} = 170\,\mathrm{GeV}$, where both intermediate W bosons can be simultaneously resonant, the physical situation in Figure 5.10 is very similar to the situation for the process $\gamma\gamma \to \mathrm{WW} \to 4f$ depicted in Figures 4.8 and Figure 4.13. Again, the shape of the curve can be understood as follows. Resonant gauge bosons give a large contribution to the width. If one of the decay fermions emits a photon, the invariant mass $M_{f\bar{f}'}$ is reduced, giving rise to an enhancement for small invariant masses. Without photon recombination these positive corrections are large due to the appearance of logarithms of the small fermion masses. As the electron mass is smaller, the corresponding logarithms yield a larger contribution. If photon recombination is applied, events are rearranged from small invariant masses to large invariant masses. In this case, the observable is inclusive,i.e. the fermion mass logarithms cancel due to the KLN theorem, and the $\nu_{\mathrm{e}}\mathrm{e}^+$ and $\mu^-\bar{\nu}_\mu$ distributions do not differ.

For $M_{\mathrm{H}} = 140\,\mathrm{GeV}$, i.e. below the threshold, only one W boson can become on shell. Thus, there is still a resonance around $M_{f\bar{f}'} \sim M_{\mathrm{W}}$, but also an enhancement below an invariant mass of about 60 GeV, where the other decaying W boson can become resonant. Near the resonance at $M_{f\bar{f}'} \sim M_{\mathrm{W}}$ the corrections look similar to the doubly-resonant case discussed for $M_{\mathrm{H}} = 170\,\mathrm{GeV}$ above. The same redistribution of events from higher to lower invariant mass due to FSR happens as explained above. Between 70 GeV and 60 GeV in $M_{f\bar{f}'}$ the large positive corrections decrease until the broad maximum near $M_{f\bar{f}'} \sim 54\,\mathrm{GeV}$ is seen. In the region of this maximum the same qualitative FSR effects

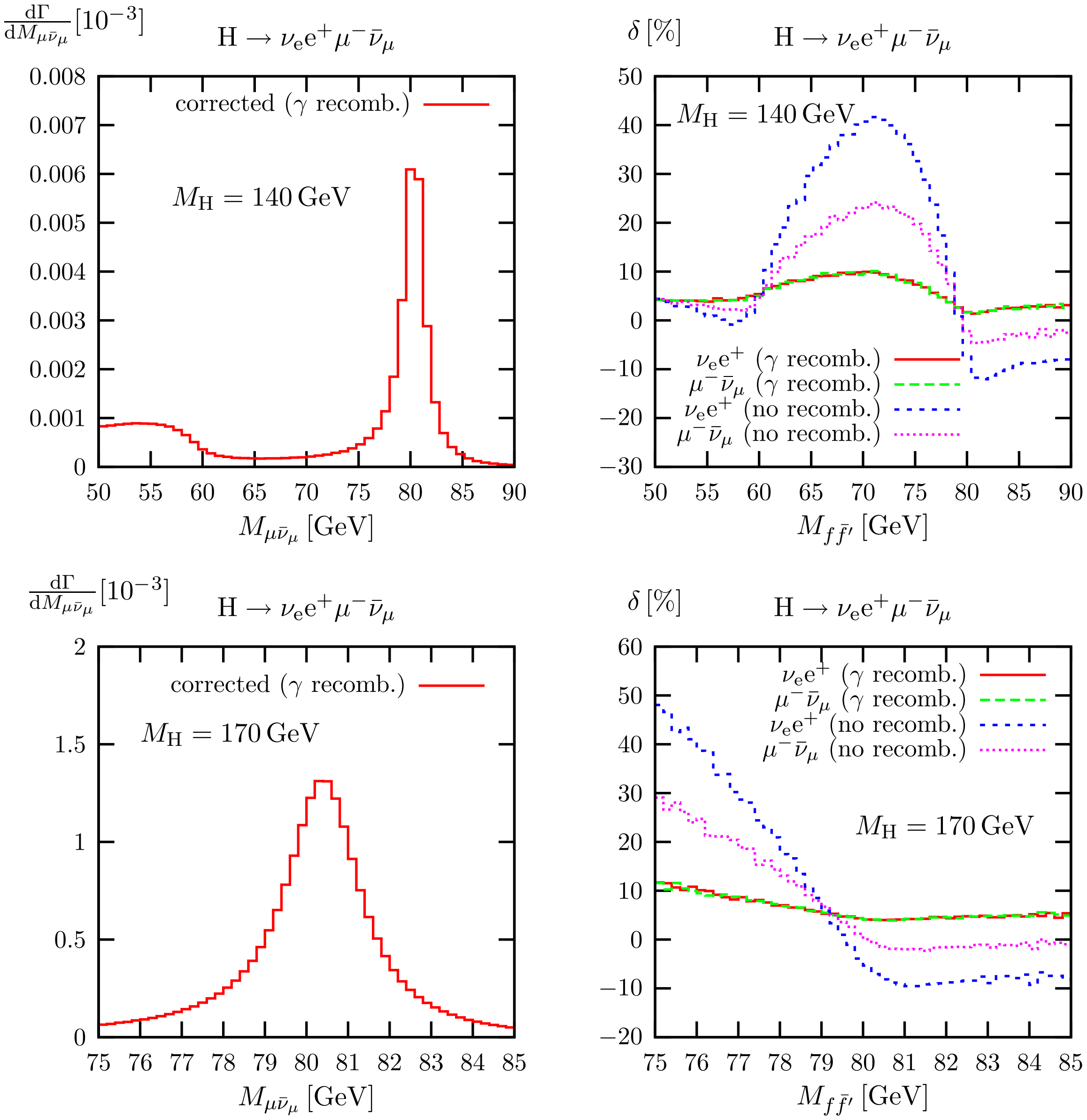

Figure 5.10: Invariant-mass distribution of $\mu^-\bar{\nu}_\mu$ (l.h.s.) and relative correction for the invariant-mass distribution of $\nu_\mathrm{e}\mathrm{e}^+$ and $\mu^-\bar{\nu}_\mu$ (r.h.s.) in the decay $\mathrm{H} \to \nu_\mathrm{e}\mathrm{e}^+\mu^-\bar{\nu}_\mu$ for $M_\mathrm{H} = 140\,\mathrm{GeV}$ and $M_\mathrm{H} = 170\,\mathrm{GeV}$.

(but of course much less pronounced) are visible as in the vicinity of the resonance at M_{W}: apart from a constant positive off-set in the relative corrections, events a distributed from the right to the left of the maximum.

Figure 5.11 shows the corresponding invariant-mass distributions for the decay $\mathrm{H} \to \mathrm{e}^{-}\mathrm{e}^{+}\mu^{-}\mu^{+}$ with $M_{\mathrm{H}} = 170\,\mathrm{GeV}$ and $M_{\mathrm{H}} = 200\,\mathrm{GeV}$. The generic features of the plots are similar to the decay into W bosons. Above the ZZ threshold ($M_{\mathrm{H}} = 200\,\mathrm{GeV}$), there is one resonance region around M_{Z}, and the corrections become large in the non-collinear-safe case. Photon recombination rearranges the events, so that the fermion logarithms cancel. Below the ZZ threshold ($M_{\mathrm{H}} = 170\,\mathrm{GeV}$), there is an additional resonance region for $M_{f\bar{f}} \lesssim 80\,\mathrm{GeV}$. The shape and the large size of the corrections are due to collinear FSR as explained above. In Ref. [82] it was pointed out that the kinematical threshold where the other Z boson can become on shell, which is at $M_{f\bar{f}} \lesssim 80\,\mathrm{GeV}$ in this case, can be used to verify the spin of the Higgs boson. A particle of spin 1, e.g., would at least involve one power of momentum in the coupling to vector bosons. Thus, the invariant-mass spectrum would decrease more rapidly at the kinematical threshold compared to the SM case. Figure 5.11 shows that the radiative corrections influence the slope at the kinematical threshold significantly.

Finally, in Figure 5.12 we investigate the influence of higher-order FSR on the invariant-mass distribution of $\mu^{-}\nu_{\mu}$ and $\mu^{-}\mu^{+}$ in the decays $\mathrm{H} \to \nu_{\mathrm{e}}\mathrm{e}^{+}\mu^{-}\bar{\nu}_{\mu}$ and $\mathrm{H} \to \mathrm{e}^{-}\mathrm{e}^{+}\mu^{-}\mu^{+}$. The invariant mass is defined via the momenta of the fermions alone, i.e. without photon recombination. If photon recombination was applied, the leading logarithmic FSR corrections, as described in Section 5.3.3, would vanish completely. Subtracting the $\mathcal{O}(\alpha)$ terms (5.3.14) from the structure functions yields the contribution that is beyond $\mathcal{O}(\alpha)$. In Figure 5.12 the impact of this contribution is studied revealing corrections of up to 4% in regions where the lowest-order result is relatively small. Figure 5.12 also shows the comparison between the structure function with and without the exponentiation of the soft-photonic parts in (5.3.11) and (5.3.13), respectively. The difference is beyond $\mathcal{O}(\alpha^3)$ and turns out to be tiny.

5.5.4 Angular distributions

The investigation of angular correlations between the fermionic decay products is an essential means of testing the properties of the Higgs boson. In Ref. [81, 82] it was demonstrated how the spin of the Higgs boson can be determined by looking at the angle between the decay planes of the Z bosons in the decay $\mathrm{H} \to \mathrm{ZZ}$. This angle can be defined as

$$\begin{aligned} \cos\phi' &= \frac{(\mathbf{k}_{+} \times \mathbf{k}_1)(\mathbf{k}_{+} \times \mathbf{k}_3)}{|\mathbf{k}_{+} \times \mathbf{k}_1||\mathbf{k}_{+} \times \mathbf{k}_3|}, \\ \mathrm{sgn}(\sin\phi') &= \mathrm{sgn}\{\mathbf{k}_{+} \cdot [(\mathbf{k}_{+} \times \mathbf{k}_1) \times (\mathbf{k}_{+} \times \mathbf{k}_3)]\}, \end{aligned} \qquad (5.5.6)$$

where $\mathbf{k}_{+} = \mathbf{k}_1 + \mathbf{k}_2$. The l.h.s. of Figure 5.13 shows the decay width for $\mathrm{H} \to \mathrm{e}^{-}\mathrm{e}^{+}\mu^{-}\mu^{+}$ as a function of ϕ' revealing a $\cos 2\phi'$ term. As was noticed in Ref. [81, 82], this term would be proportional to $(-\cos 2\phi')$ if the Higgs boson was a pseudo-scalar.

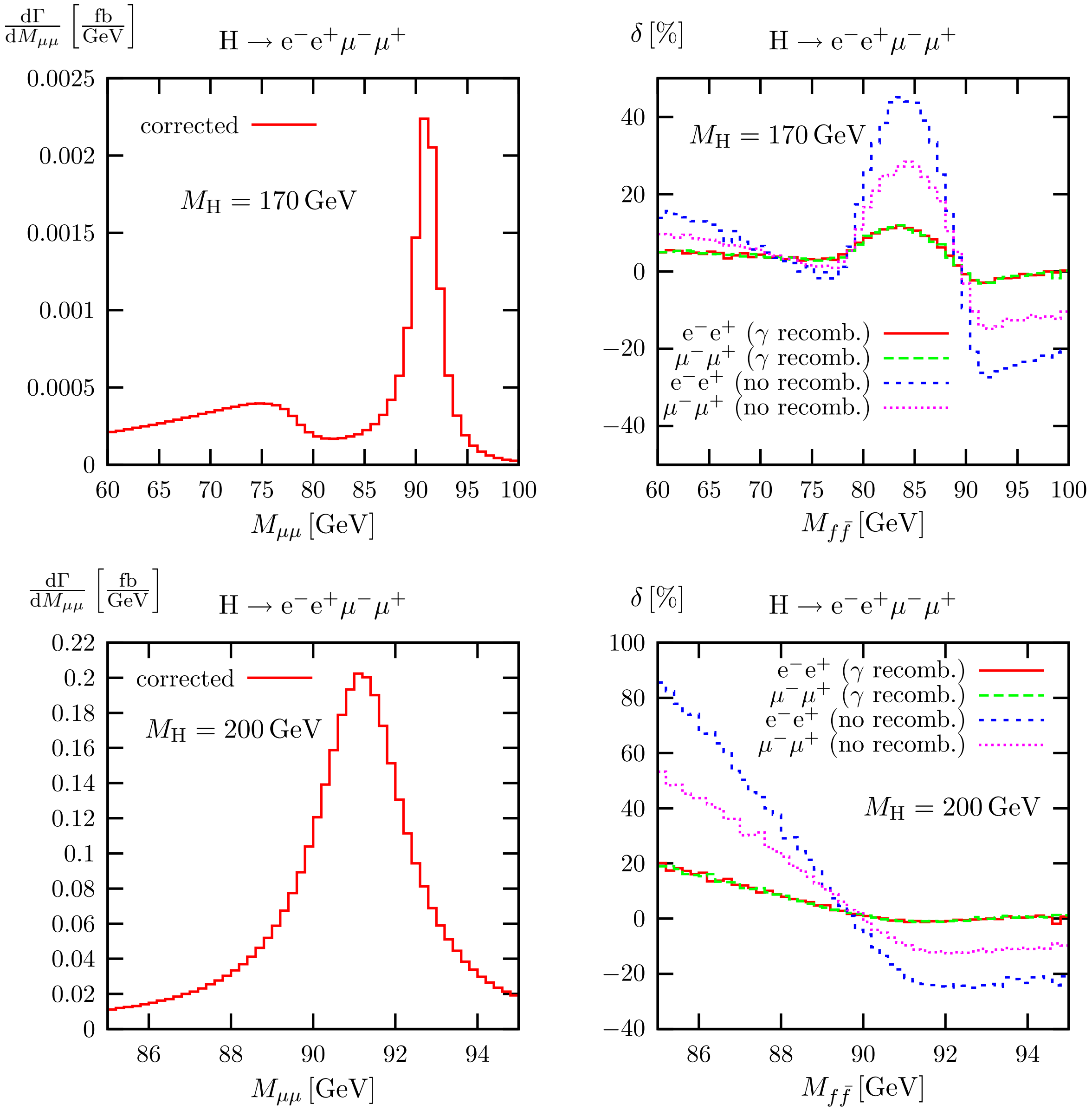

Figure 5.11: Invariant-mass distribution of $\mu^-\mu^+$ (l.h.s.) and relative correction for the invariant-mass distribution of e^-e^+ and $\mu^-\mu^+$ (r.h.s.) in the decay $H \to e^-e^+\mu^-\mu^+$ for $M_H = 170\,GeV$ and $M_H = 200\,GeV$.

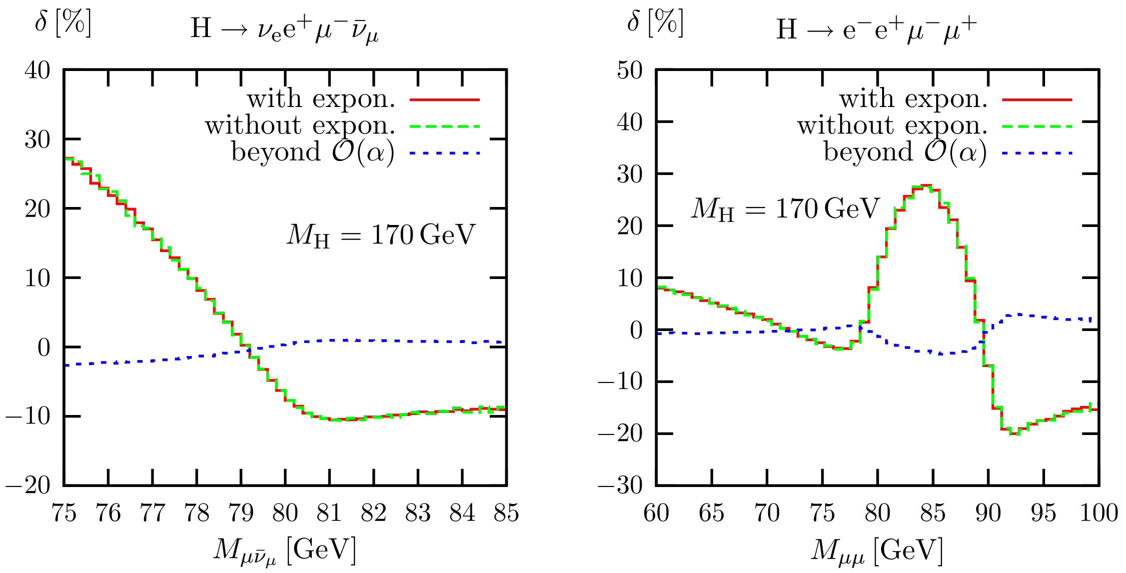

Figure 5.12: Influence of the leading logarithmic terms of FSR on the invariant-mass distribution of $\mu^-\nu_\mu$ and $\mu^-\mu^+$ in the decays $H \to \nu_e e^+ \mu^- \bar{\nu}_\mu$ and $H \to e^- e^+ \mu^- \mu^+$. The different curves correspond to the result with exponentiation, without exponentiation, and to the sum of α^2 and α^3 terms, which are labelled "beyond $\mathcal{O}(\alpha)$".

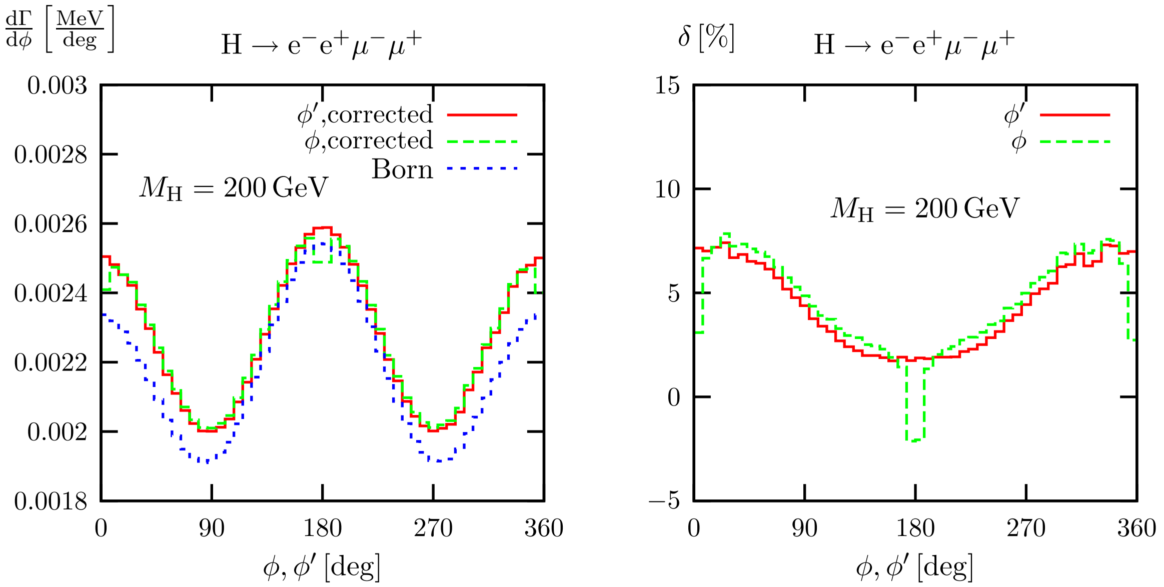

Figure 5.13: Distribution in the angle between the $Z \to l^- l^+$ decay planes in the decay $H \to e^- e^+ \mu^- \mu^+$ and relative corrections (with photon recombination) for $M_H = 200$ GeV.

Note that for non-photonic events the definition of ϕ' coincides with the definition given in Ref. [19] where $(-\mathbf{k}_- \times \mathbf{k}_3)$ with $\mathbf{k}_- = \mathbf{k}_3 + \mathbf{k}_4$ was used instead of $(\mathbf{k}_+ \times \mathbf{k}_3)$. Explicitly, ϕ was defined as

$$\begin{aligned} \cos\phi &= \frac{(\mathbf{k}_+ \times \mathbf{k}_1)(-\mathbf{k}_- \times \mathbf{k}_3)}{|\mathbf{k}_+ \times \mathbf{k}_1||-\mathbf{k}_- \times \mathbf{k}_3|}, \\ \mathrm{sgn}(\sin\phi) &= \mathrm{sgn}\{\mathbf{k}_+ \cdot [(\mathbf{k}_+ \times \mathbf{k}_1) \times (-\mathbf{k}_- \times \mathbf{k}_3)]\}. \end{aligned} \tag{5.5.7}$$

However, this definition yields large negative contributions at $\phi = 0°$ and $\phi = 180°$. As was explained in Ref. [19], this is an effect of the suppressed phase space of the real corrections. At $\phi = 0°$ and $\phi = 180°$ the phase space for photonic events shrinks to the configurations where the photon is either soft or lies in the decay plane of the gauge bosons. Thus, the negative contributions from the virtual corrections are not fully compensated by the real corrections. Using $\mathbf{k}_+ \times \mathbf{k}_3$ as in (5.5.6) avoids this suppression and gives rise to a smooth dependence of the corrections on ϕ as can be seen on the r.h.s. of Figure 5.13 which shows the relative corrections for ϕ and ϕ' in the decay $\mathrm{H} \to \mathrm{e}^-\mathrm{e}^+\mu^-\mu^+$. Since the difference of ϕ and ϕ' is only due to photons, this, again, emphasizes the large influence of the photon treatment.

In contrast to the invariant-mass distribution of Figure 5.10, photon recombination does not produce any significant effect for the observable ϕ. This is because adding a soft or collinear photon to a fermion momentum does not change its direction very much and, thus, has only a small influence on the angle ϕ.

The decay angle of the μ^- relative to the corresponding Z boson in the decay $\mathrm{H} \to \mathrm{e}^-\mathrm{e}^+\mu^-\mu^+$ is shown in Figure 5.14. The angle is defined in the rest frame of the Z boson so that the distribution is symmetric w.r.t. $\cos\theta_{\mathrm{Z}\mu^-}$. The relative corrections which are shown in the plot on the r.h.s. reveal a strong enhancement in the forward and backward direction if no recombination is applied. These corrections are due to events where the μ^+ has only a small energy and emits a collinear photon. Since the momentum of the Z boson is defined via its decay fermions, it has almost the same momentum as the μ^-. After applying photon recombination, the momentum of the Z boson is defined via the sum of the fermion and photon momenta. Thus, the μ^- is not necessarily collinear to the Z boson anymore, and large events are rearranged to smaller $|\cos\theta_{\mathrm{Z}\mu^-}|$ giving rise to a flatter distribution.

Next, we consider the angle between two fermions. In the case of $\mathrm{H} \to \mathrm{WW}$ the angle between the charged fermions can be used to discriminate the Higgs signal events from background events, because the fermions are emitted preferably in the same direction. This can be understood as follows. At leading order, the only non-vanishing helicity amplitudes for $\mathrm{H} \to \mathrm{WW}$ are those with equal helicity W bosons. Since W bosons only couple to left-handed particles and due to angular momentum conservation, particles (anti-particles) are emitted preferably in the forward direction of transverse W bosons with negative (positive) helicity, and anti-particles (particles) in the backward direction. As, close to threshold, 2/3 of the W bosons are transverse and as the W bosons fly in opposite directions, a particle and an anti-particle of their decay products will be emitted in the same direction.

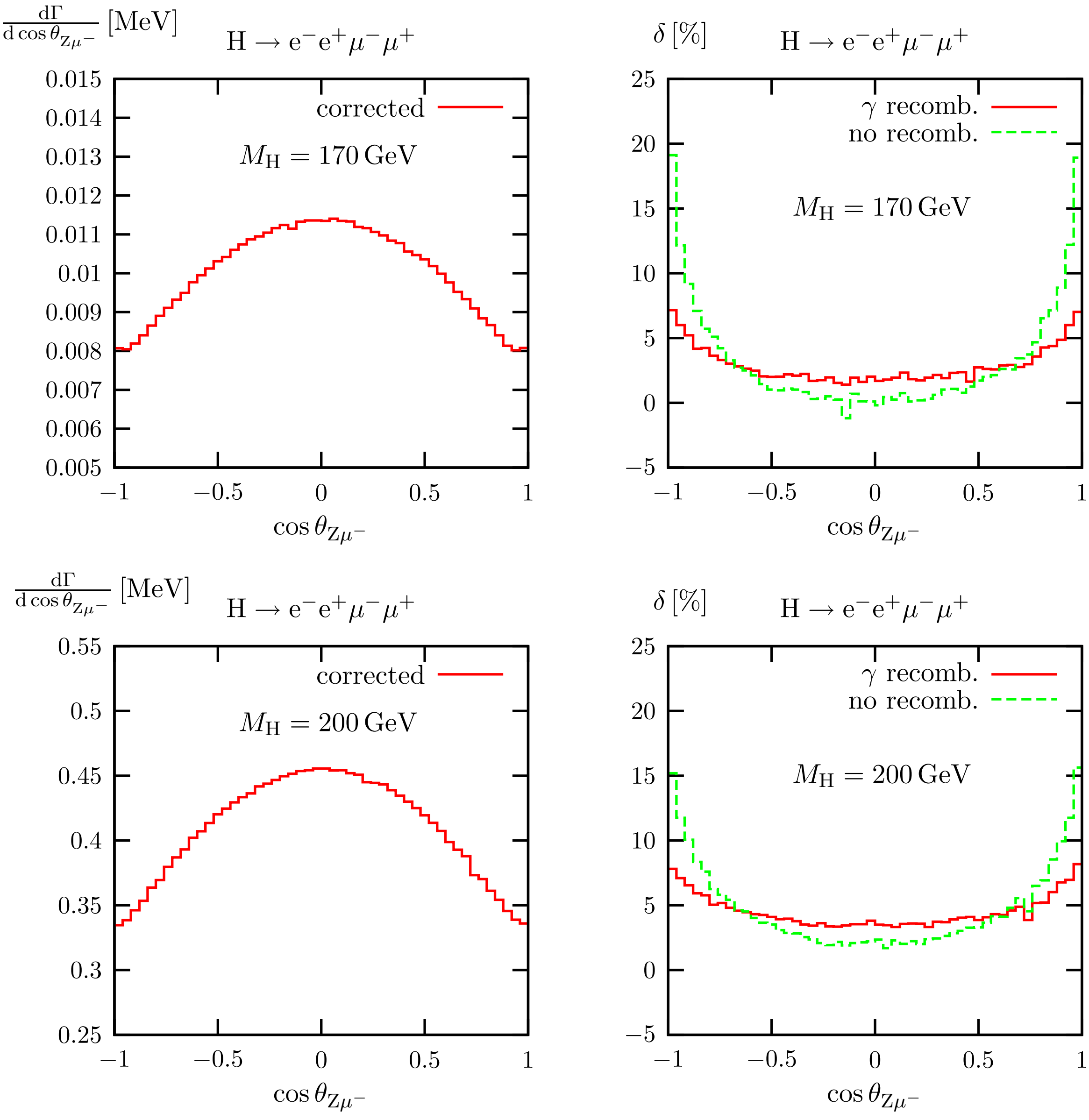

Figure 5.14: Distribution of the angle between the μ^- and the corresponding Z boson in the rest frame of the Z for the decay $H \to e^-e^+\mu^-\mu^+$. The plot on the l.h.s. shows the corrected result and the plot on the r.h.s. the relative corrections with and without applying photon recombination for $M_H = 170\,\text{GeV}$ and $M_H = 200\,\text{GeV}$.

In the decay $\mathrm{H} \to \nu_\mathrm{e}\mathrm{e}^+\mu^-\bar{\nu}_\mu$ neither the Higgs-boson nor the W-boson momenta can be reconstructed from the decay products. The distribution in the angle between the e^+ and μ^- can, thus, only be studied upon including the Higgs-production process. If the Higgs boson was, however, produced without transverse momentum, or if the transverse momentum is known, the angle between e^+ and μ^- in the plane perpendicular to the beam axis could be studied without knowledge of the production process. For gluon–gluon and $\gamma\gamma$ fusion into a Higgs boson, this is to some approximation the case. We define the transverse angle between e^+ and μ^- as

$$\begin{aligned} \phi_{\mathrm{e}^+\mu^-,\mathrm{T}} &= \frac{\mathbf{k}_{2,\mathrm{T}} \cdot \mathbf{k}_{3,\mathrm{T}}}{|\mathbf{k}_{2,\mathrm{T}}||\mathbf{k}_{3,\mathrm{T}}|}, \\ \mathrm{sgn}(\sin\phi_{\mathrm{e}^+\mu^-,\mathrm{T}}) &= \mathrm{sgn}\{\mathbf{e}_z \cdot (\mathbf{k}_2 \times \mathbf{k}_3)\}, \end{aligned} \tag{5.5.8}$$

where $\mathbf{k}_{i,\mathrm{T}}$ are the transverse components of the fermion momenta w.r.t. the unit vector $\mathbf{e}_z$.

The corresponding distribution, together with the influence of the corrections, is shown in Figure 5.15. The enhancement for small angles, which was explained above, is transferred to the distribution of the transverse angle $\phi_{\mathrm{e}^+\mu^-,\mathrm{T}}$. Since the photon recombination does not change the direction of the fermions, it does not have any visible effect on the relative corrections.

Finally, we investigate the distribution of the angle between e^- and μ^- in the decay $\mathrm{H} \to \mathrm{e}^-\mathrm{e}^+\mu^-\mu^+$. We prefer to choose the angle between two fermions with the same charge because this constitutes an unambiguous choice in the decay $\mathrm{H} \to \mu^-\mu^+\mu^-\mu^+$. Figure 5.16 shows the tendency that the fermions are emitted in opposite directions for the same reason as explained above. However, this feature is not as pronounced as in $\mathrm{H} \to \nu_\mathrm{e}\mathrm{e}^+\mu^-\bar{\nu}_\mu$ because Z bosons do not only couple to left-handed particles so that one Z boson might decay into a left-handed particle and the other into a right-handed particle.

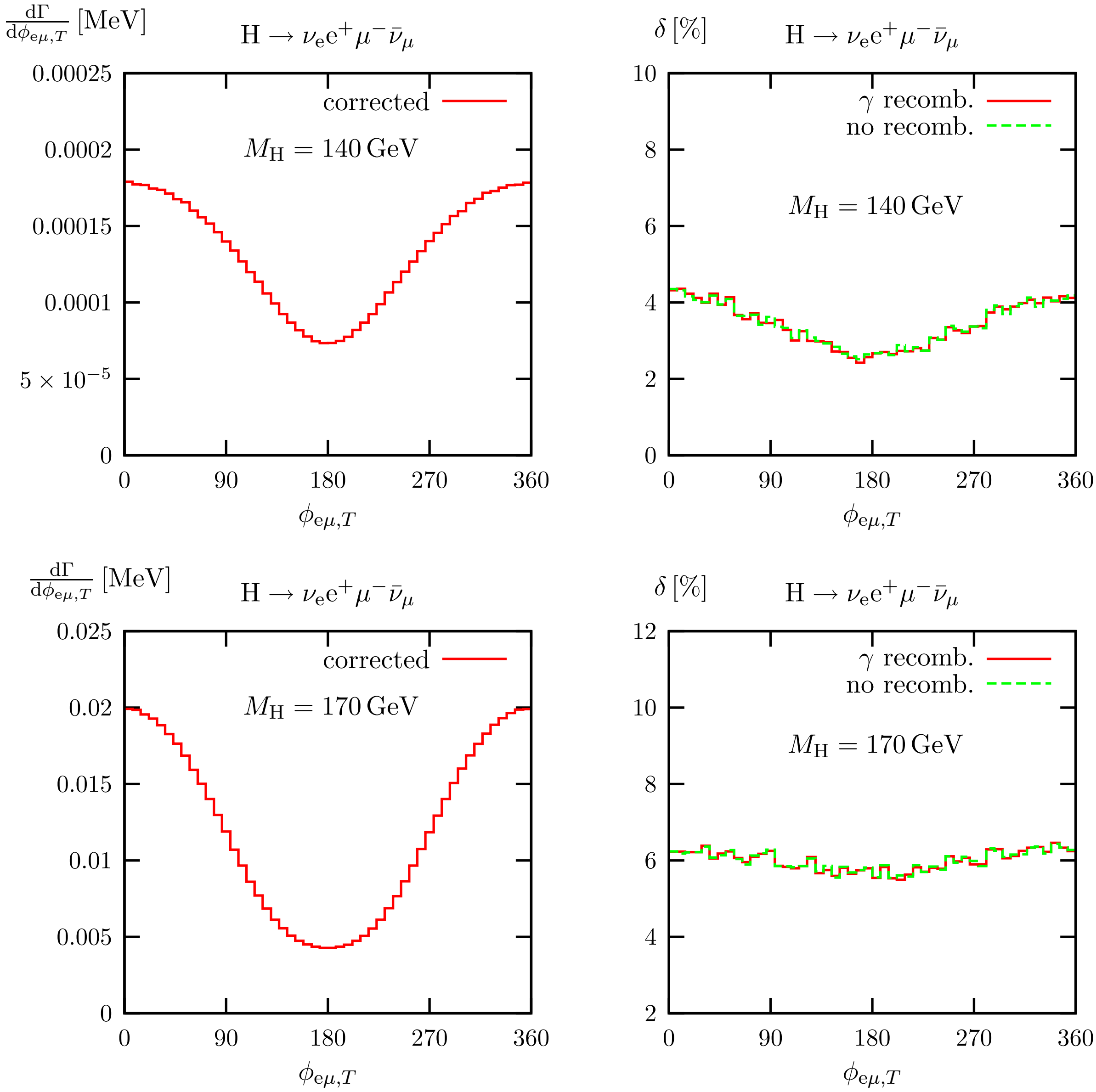

Figure 5.15: Distribution of the transverse angle between e^+ and μ^- including corrections (l.h.s) and relative corrections (r.h.s.) with and without applying photon recombination for $M_H = 140\,GeV$ and $M_H = 170\,GeV$.

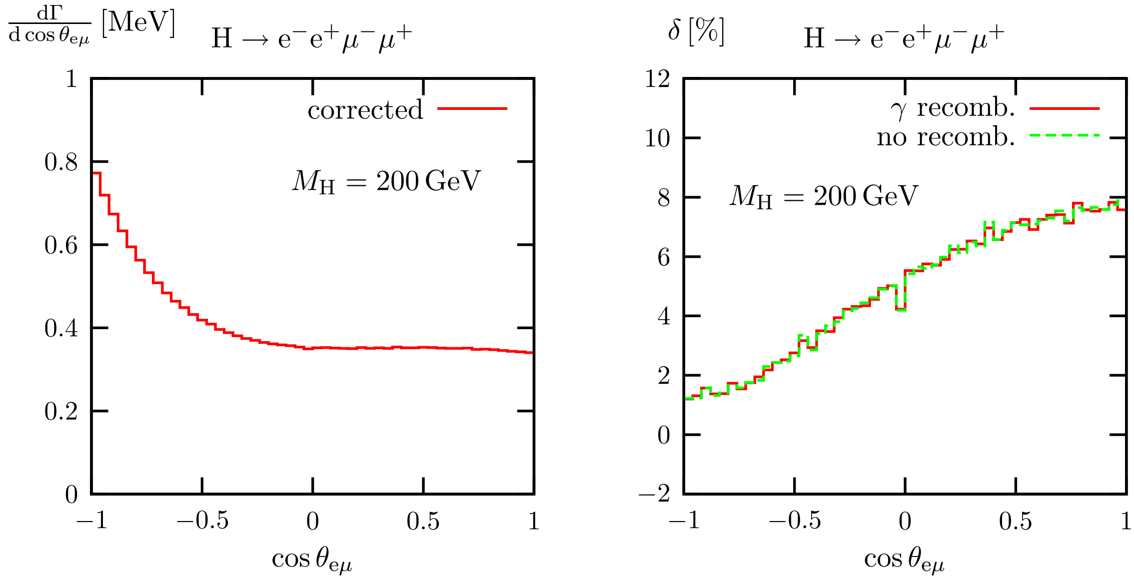

Figure 5.16: Distribution of the angle between e^- and μ^- including corrections (l.h.s) and relative corrections (r.h.s.) with and without applying photon recombination for $M_{\mathrm{H}} = 200\,\mathrm{GeV}$.

Chapter 6

Summary and conclusions

We have performed precision calculations for the processes $\gamma\gamma \to 4f$ and $\mathrm{H} \to \mathrm{WW/ZZ} \to 4f$. Starting with the predictions in lowest order of perturbation theory, we presented compact results for the transition amplitudes in terms of Weyl–van-der-Waerden spinor products. In the next step, radiative corrections in $\mathcal{O}(\alpha)$, which can be classified into real and virtual corrections, were calculated. The real corrections, originating from photon emission, are based on the complete lowest-order matrix elements for $\gamma\gamma \to 4f\gamma$ and $\mathrm{H} \to \mathrm{WW/ZZ} \to 4f\gamma$. In the case of $\gamma\gamma \to \mathrm{WW} \to 4f$ virtual corrections to doubly-resonant terms were calculated in the double-pole approximation and decomposed into factorizable and non-factorizable corrections. For $\mathrm{H} \to \mathrm{WW/ZZ} \to 4f$ we calculated the complete $\mathcal{O}(\alpha)$ corrections. The infrared divergences appearing in the virtual and real corrections due to soft or collinear photon emission were treated in two different ways, using the dipole-subtraction method or the phase-space slicing method. In order to cover also non-collinear-safe observables, where mass-singularities from collinear photon emission do not cancel, extensions of these methods were used. Finally, the phase-space integration over the final-state momenta was carried out with the adaptive multi-channel Monte Carlo method.

Special attention was paid to the treatment of the gauge-boson width, which has to be implemented in order to describe resonances. For the lowest-order predictions for $\gamma\gamma \to 4f(\gamma)$ we compared different schemes, revealing good agreement between the gauge-invariant complex-mass scheme and the fixed-width scheme. However, we encountered problems with the running-width scheme for $\gamma\gamma \to 4f\gamma$, because it does not preserve gauge invariance. For the radiative corrections to $\gamma\gamma \to \mathrm{WW} \to 4f$ the double-pole approximation represents a gauge-invariant way of introducing the width. In the case of $\mathrm{H} \to \mathrm{WW/ZZ} \to 4f$ the corrections were calculated using a generalization of the complex-mass scheme to the one-loop level, which respects gauge invariance.

Monte Carlo generators have been constructed, called COFFER$\gamma\gamma$ ($\gamma\gamma \to 4f$) and PROPHECY4F ($\mathrm{H} \to \mathrm{WW/ZZ} \to 4f$), which can be used in experimental studies. We have presented a variety of numerical results that were obtained with these generators:

For the lowest-order processes $\gamma\gamma \to 4f$ and $\gamma\gamma \to 4f\gamma$ and for the processes $\gamma\gamma \to \mathrm{WW} \to 4f$ including $\mathcal{O}(\alpha)$ corrections we presented a representative list of integrated cross sections. For some of these processes we showed the dependence of cross sections on the centre-of-mass energy, thereby studying the influence of a realistic photon-beam spectrum and the size of the radiative corrections. In the W-pair threshold region the corrections are dominated by the Coulomb singularity and are, thus, positive and of the order of a few per cent. For increasing $\gamma\gamma$ scattering energies the corrections become more and more negative and reach about -10% in the TeV range for integrated cross sections.

Various distributions were shown, especially in the invariant mass and in the production angle of the reconstructed W bosons and in the invariant mass of a resonant Higgs boson in the loop-induced reaction $\gamma\gamma \to \mathrm{H} \to \mathrm{WW} \to 4f$. Moreover, it is shown that the convolution over the photon spectrum significantly distorts energy and angular distributions due to an effective photon polarization. Typically, collinear-safe observables (i.e. where mass-singular logarithms cancel due an inclusive treatment of final-state radiation) receive corrections of a few per cent for energies of the $\mathrm{e}^-\mathrm{e}^-$ system before Compton backscattering up to 1 TeV. As expected, non-collinear-safe observables receive very large corrections (tens of per cent) because of the existence of logarithmic mass singularities. Also for large scattering angles, where the Born cross section is relatively small, the impact of the corrections is usually larger.

In addition, we examined the effects of anomalous triple and quartic gauge-boson couplings on integrated $\gamma\gamma \to 4f$ cross sections. Since contributions of anomalous couplings to cross sections can cancel in specific configurations, it is necessary to take into account results from other observables (such as differential distributions) or from other experiments (such as $\mathrm{e}^+\mathrm{e}^-$ or $\mathrm{e}^-\gamma$ collisions) in order to constrain individual anomalous couplings. However, our results suggest that an analysis of the processes $\gamma\gamma \to 4f$ can constrain anomalous $\gamma\gamma\mathrm{WW}$ couplings about an order of magnitude better than studying $\mathrm{e}^+\mathrm{e}^- \to 4f\gamma$. The Monte Carlo generator COFFER$\gamma\gamma$ can serve as a tool for more realistic studies.

At the LHC the Higgs boson decays $\mathrm{H} \to \mathrm{WW/ZZ} \to 4f$ lead to signatures that can be exploited for its detection and for the subsequent study of its properties. In order to achieve the required accuracy of theoretical predictions, off-shell effects of the gauge bosons and radiative corrections have to be taken into account. Since we calculated the $\mathcal{O}(\alpha)$ corrections in the complex-mass scheme, which does not employ any type of expansion or on-shell approximation, our results are equally valid above, in the vicinity and below the WW and ZZ thresholds. Comparing our results to an on-shell (narrow-width) approximation, we found that in the threshold region off-shell effects amount to about 10%. Treating only one gauge boson as off-shell also leads to deviations of some 10% far below this threshold. The radiative corrections to partial decay widths typically amount to several per cent and increase with growing Higgs masses reaching about 10% at $M_\mathrm{H} \sim 500\,\mathrm{GeV}$. In this regime also corrections beyond $\mathcal{O}(\alpha)$ originating from heavy-Higgs effects, which we included in our calculation, are relevant. For angular distributions that are important in the verification of the discrete quantum numbers of the Higgs boson, we found corrections of the order of 5–10%. To conclude, the Monte Carlo generator PROPHECY4F will be a useful tool for the Higgs reconstruction and related studies.

Appendix

A Phase-space integration

The squared matrix elements of the processes $\gamma\gamma \to 4f(\gamma)$ with $n = 4(5)$ final-state particles are integrated over the phase space yielding the cross section

$$\int \mathrm{d}\sigma = \frac{1}{2s} \int \mathrm{d}\Phi_n \, |\mathcal{M}|^2,$$
$$\int \mathrm{d}\Phi_n = \left(\prod_{i=1}^{n} \int \frac{\mathrm{d}^3\mathbf{p}_i}{(2\pi)^3 2p_i^0} \right) (2\pi)^4 \delta^{(4)}\left(k_1 + k_2 - \sum_{i=1}^{n} p_i\right) \tag{A.1}$$

with the incoming momenta k_1, k_2, the outgoing momenta $p_i (i = 1,..,4(5))$, and the CM energy $\sqrt{s}$. The corresponding relation for the decay width of $\mathrm{H} \to 4f(\gamma)$ was given in Sections 5.1 and 5.3.1. We basically follow the strategy described in Refs. [18, 26, 53], which is based on multi-channel Monte Carlo integration.

A.1 Phase-space mappings and multi-channel Monte Carlo integration

In a Monte Carlo integration the integration region is covered by mapping pseudo-random numbers into the phase space of the outgoing particles. Each phase-space configuration, called event, gives a contribution to the integral with a certain weight. The main challenge of the integration arises due to the complex peaking structure of the integrand in eight ($\gamma\gamma/\mathrm{H} \to 4f$) or eleven ($\gamma\gamma/\mathrm{H} \to 4f\gamma$) dimensions. This structure is induced by various diagram types with time- and space-like propagators that peak at different points in phase space. As a consequence, the statistical error of the numerical integration increases, and the numerical results may even become unstable. As a first step to a solution, we employ phase-space mappings. To this end, the integration variables are chosen such that they contain the kinematical invariants of the propagators. The mappings of the pseudo-random numbers into the momenta of the outgoing particles are then constructed in such a way that their Jacobian cancels or compensates the denominator of the propagator. Thus, more events are generated in regions where the squared matrix element is large, so that the integrand is flattened. For time-like Breit–Wigner resonances of a particle with mass M_V and width Γ_V, an appropriate mapping to the square of the propagator momentum p^2 is

$$p^2(r) = M_V \Gamma_V \tan\Big(y_1 + (y_2 - y_1) r\Big) + M_V^2, \qquad y_{1/2} = \arctan\left(\frac{p^2_{\mathrm{min/max}} - M_V^2}{M_V \Gamma_V}\right). \tag{A.2}$$

The corresponding Jacobian,

$$\frac{1}{g(p^2)} = \Big[(p^2 - M_V^2)^2 + M_V^2\Gamma_V^2\Big]\,\frac{(y_2 - y_1)}{M_V\Gamma_V}, \tag{A.3}$$

cancels the denominator of the squared propagator. For a propagator without width we choose the mapping

$$p^2(r) = \Big[r(p^2_{\mathrm{max}} - m^2)^{1-\nu} + (1-r)(p^2_{\mathrm{min}} - m^2)^{1-\nu}\Big]^{\frac{1}{1-\nu}} + m^2, \tag{A.4}$$

with the Jacobian

$$\frac{1}{g(p^2)} = (p^2 - m^2)^{\nu}\,\frac{[(p^2_{\mathrm{max}} - m^2)^{1-\nu} - (p^2_{\mathrm{min}} - m^2)^{1-\nu}]}{1-\nu}, \tag{A.5}$$

which cancels the square of the denominator of a propagator with vanishing width for $\nu = 2$. The choice of ν and m^2 will be discussed in the next section.

Combining the mappings for the propagators of a given Feynman diagram we can build up the phase space. This is done successively from the subprocesses of the diagram. First, time-like invariants are generated according to Eqs. (A.2) or (A.4). Second, the $2 \to 2$ particle subprocesses are generated. The corresponding space-like invariants are only mapped for particles with vanishing width, and the corresponding azimuthal angle is generated uniformly. Finally, the azimuthal angle and the polar angle of the $1 \to 2$ particle decays are generated without any mapping. In the construction of the phase space, detector cuts are taken into account as much as possible in order to increase the efficiency of the Monte Carlo generator. For further details, we refer to Ref. [18, 53].

Obviously, it is not possible to construct mappings of the pseudo-random numbers that are adjusted for all Feynman diagrams at the same time. What can be done is to construct a mapping for each squared diagram following the procedure described above. The naive approach would be to choose one of these mappings randomly at each iteration of the integration. However, it might happen that one mapping produces a phase-space point where another diagram becomes resonant, but the Jacobian of this mapping is small and does not smooth the integrand. As a solution the multi-channel Monte Carlo technique [54] was developed. In this approach the mappings for the various diagrams, which are called "channels", are combined in such a way that the integrand is smoothed everywhere in phase space (for squared propagators; interferences of different diagrams are not taken into account). To this end, the integration over the phase space of $n = 4(5)$ final-state particles is rewritten

$$\int \mathrm{d}\Phi_n \, \frac{\sum_i \alpha_i g_i}{g_{\mathrm{tot}}} |\mathcal{M}|^2 = \sum_i \alpha_i \int_0^1 \mathrm{d}r^{8(11)}\, \frac{|\mathcal{M}|^2}{g_{\mathrm{tot}}}, \qquad g_{\mathrm{tot}} = \sum_i \alpha_i g_i, \tag{A.6}$$

in terms of the pseudo-random numbers $\mathbf{r}$. The densities g_i, which are the product of the inverse jacobians in Eqs. (A.3) and (A.5), are combined in the total density g_{tot}. This density smoothes the squared matrix element $|\mathcal{M}|^2$. The parameters $\alpha_i \gtrsim 0$, with $\sum_i \alpha_i = 1$, denote the probability that a certain channel is chosen. This means that for each event a single channel is chosen with probability α_i, and the phase-space configuration is determined according to the mapping of the channel. In addition to the density of this channel, also the densities of all other channels at the given phase-space point have to be calculated in order to obtain g_{tot}. The probability α_i is optimized according to Ref. [103] to minimize the statistical error as much as possible. This procedure, called "adaptive optimization", is repeated several times during the integration.

For the process $\gamma\gamma \to 4f(\gamma)$ the number of channels ranges from 13(72) for $\gamma\gamma \to \nu_{\mathrm{e}}\mathrm{e}^+\mu^-\bar{\nu}_\mu(\gamma)$ to 71(468) for $\gamma\gamma \to \mathrm{u}\bar{\mathrm{u}}\mathrm{d}\bar{\mathrm{d}}(\gamma)$. Generally, the number of Feynman diagrams coincides with the number of channels. Only the diagrams with gluon exchange receive the same mapping as the corresponding diagrams with photon exchange. In the integration over the matrix elements for $\mathrm{H} \to \mathrm{WW/ZZ} \to 4f(\gamma)$, there are much less diagrams, resulting in 1-10 channels. However, below the WW and ZZ thresholds, only one propagator can become on shell. Therefore, we introduce additional channels, in which one of the propagators receives a flat mapping instead of the Breit-Wigner mapping (A.2).

For both processes additional channels are constructed according to Ref. [53] for the integration of the subtraction terms defined in Section 4.3.1.2. These terms are integrated over the $4f\gamma$ phase space $\Phi_{4f\gamma}$ but also depend on the $4f$ phase space $\Phi_{4f,ij}$. Therefore, the $4f$ phase space is generated first, and from this the $4f\gamma$ phase space is constructed with the mappings corresponding to different emitter/spectator pairs i/j.

A.2 Technical parameters

In the Monte Carlo generator several technical parameters are introduced for different purposes. First, we discuss the parameters of the mappings for propagators with vanishing width introduced in the previous section. Although the squared matrix element contains a factor $(p^2)^{-2}$, the choice $\nu \lesssim 1$ turns out to be more appropriate, because the propagator is partly cancelled in the collinear limit where p^2 becomes small. The mass could be chosen $m^2 = 0$, because the mapping is used for photons and for fermions, whose mass is neglected. However, the density g_i in Eqs. (A.5) and (A.6) could get arbitrarily large in this case, and the mapping (A.4) produces many events with small p^2 increasing the number of events that have to be discarded due to numerical instabilities. Therefore, it is useful to choose $m^2 = -a$ with a positive a. This mitigates the strong increase of g_i for $p^2 \to 0$. We choose $a \sim 10^{-5}\,\mathrm{GeV}^2$ for the subtraction method, but changing a over several orders of magnitude has almost no visible numerical impact. For the slicing method, however, a should be chosen smaller, because many events are needed in the soft and collinear regions due to the large squared matrix elements in this region.

Second, the cut-off parameters used in the phase-space slicing method are chosen $\frac{\Delta E}{E_{\mathrm{CM}}} \sim 3\cdot 10^{-4}$, with CM energy E_{CM}, and $\Delta\theta \sim 10^{-2}$ (corresponding to $1-\cos\theta > 5\cdot 10^{-5}$ for non-singular events). For a sufficiently large number of events this results in an accuracy of $\mathcal{O}(10^{-3})$ or better as can be seen in Figures 4.4, 4.5, 5.5, and 5.6. In the singular regions defined by ΔE and $\Delta\theta$ the matrix elements are integrated analytically in the soft or collinear approximation, respectively. In order to reduce the corresponding error, the cuts have to be chosen smaller. Thus, one of the weaknesses of the slicing method is that for given ΔE and $\Delta\theta$, the accuracy of the calculation cannot be improved

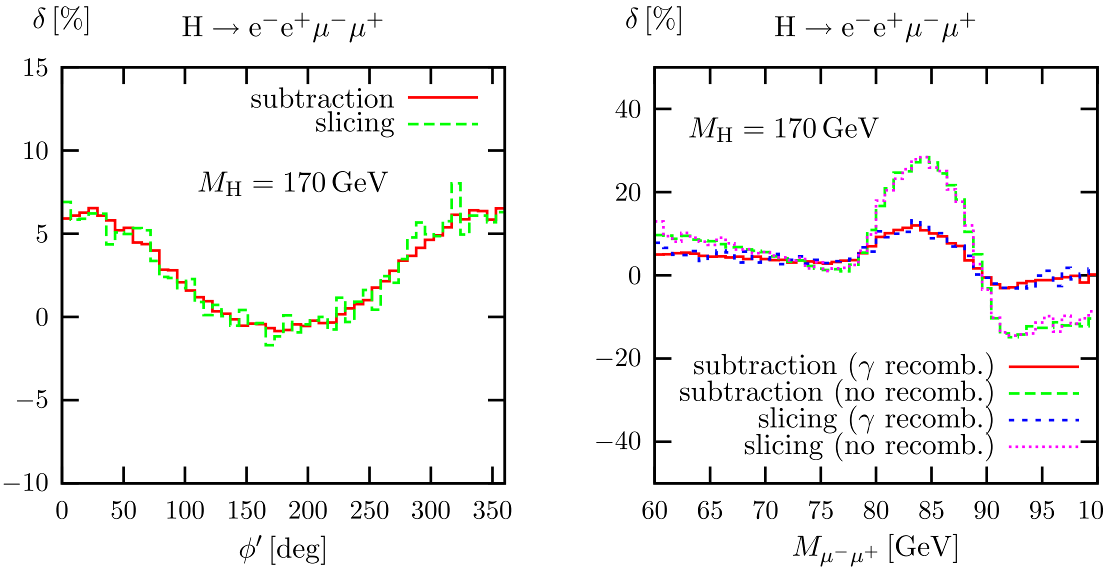

Figure 6.1: Comparison of the relative corrections obtained with the subtraction and the slicing methods. The plot on the l.h.s. shows the distribution in the angle between the decay planes of the Z boson in the process $\mathrm{H} \to \mathrm{ZZ} \to \mathrm{e}^-\mathrm{e}^+\mu^-\mu^+$ and the plot on the r.h.s. shows the invariant mass distribution of the $\mu^-\mu^+$ pair with and without photon recombination for $M_\mathrm{H} = 170\,\mathrm{GeV}$.

simply by increasing the number of events. The above choice of parameters is such that the statistical error of the integration with the slicing method is generally larger than the corresponding error in the subtraction method. If the desired accuracy is at the order of several per mille, it suffices to calculate with larger slicing cuts. For example, the histograms contained in this work agree between the subtraction method and the slicing method with $\frac{\Delta E}{E_\mathrm{CM}} = 10^{-3}$ and $\Delta\theta = 3 \cdot 10^{-2}$ within the statistical error of the integration, which is smaller in this case. In Figure 6.1 we show the comparison for the angle between the decay planes defined in Eq. (5.5.6) and the invariant mass distribution of the $\mu^-\mu^+$ pair in the process $\mathrm{H} \to \mathrm{ZZ} \to \mathrm{e}^-\mathrm{e}^+\mu^-\mu^+$.

Third, we introduce parameters in order to overcome numerical instabilities. Since the precision of variables in a numerical integration on a computer is limited, it might happen that in certain kinematical regions the weight of an event is not calculated correctly. For example, time-like invariants can become smaller than zero. With $\mathcal{O}(10^7)$ events this may happen a few times. In this case, we discard the event. In the subtraction method, the bremsstrahlung matrix elements are completely integrated over, i.e. also over the singular region. The subtraction terms are constructed in such a way that they cancel the singularities. Hence, the weight should vanish in the soft and collinear limit. However, as the terms get very large, the cancellation is not accurate anymore due to the limited numerical accuracy. Therefore, events with an invariant mass of a photon and a charged fermion of $m^2_\mathrm{inv} < m^2_\mathrm{inv,min}$ are discarded. We choose $m^2_\mathrm{inv,min} = (10^{-4}E_\mathrm{CM})^2$, but the integration is stable for a variation of $m^2_\mathrm{inv,min}$ over a relatively large range, because the events that are discarded have a negligible weight. This cut affects up to $\mathcal{O}(10^{-2})$ of the events.

Finally, numerical instabilities can occur in the generation of histograms. In the subtraction method, which was introduced in Sections 4.3.1.2 and 4.3.2.2, the cancellation between the bremsstrahlung matrix elements and the subtraction terms is non-local. The bremsstrahlung matrix elements are defined on the $4f\gamma$ phase space $\Phi_{4f\gamma}$, while the subtraction terms are defined via the mapping to the $4f$ phase space $\tilde{\Phi}_{4f,ij}$. For non-collinear-safe observables the events of the subtraction terms are distributed to the histogram bins according to $\Theta\Bigl(p_i = z_{ij}\tilde{p}_i, k = (1-z_{ij})\tilde{p}_i, \{\tilde{p}_{k\neq i}\}\Bigr)$ as defined in Eq. (4.3.17). In the soft limit the momenta of both phase spaces coincide. Nevertheless, it may happen that close to the singularity the two corresponding large weights, which compensate each other, are distributed into neighbouring bins of the histogram. This means that the integral for a specific bin shows large fluctuations. For the processes $\gamma\gamma \to 4f$, however, numerical problems of this kind are smaller than the overall statistical uncertainty. In the case of $\mathrm{H} \to \mathrm{WW/ZZ} \to 4f$ the statistical error of the histograms is deteriorated considerably due to this non-local cancellations. Therefore, we distribute weights of the subtraction terms into the histograms according to $\Theta(\Phi_{4f\gamma})$, if the photon momentum is $k < 10^{-3}E_{\mathrm{CM}}$ and $y_{ij} < 10^{-3}$. Equation (4.3.9) implies that the momenta $\tilde{p}_i$ of $\Phi_{4f,ij}$ and p_i of $\Phi_{4f\gamma}$ are almost the same under this condition. The number of events that are affected by this cut is of $\mathcal{O}(10^{-3})$. Another situation where the definition of the histogram bins is problematic occurs in Eq. (4.3.19). For $z \to 1$, $\bar{\mathcal{G}}^{(\mathrm{sub})}_{ij}(\tilde{s}_{ij}, z)$ becomes very large. Due to the $[...]_+$ prescription two events with large weight, which cancel each other in the integrated cross section, might be distributed to different bins. Again, for the processes $\gamma\gamma \to 4f$ the numerical effect is obscured by statistical uncertainty of the integration. For the processes $\mathrm{H} \to \mathrm{WW/ZZ} \to 4f$ it turns out that a cut of $(1-z) < 10^{-3}$ does not change the distributions but improves the statistical uncertainty.

B Soft and collinear divergences

In this appendix we describe different contributions to the soft and collinear divergences that appear in the calculation of the one-loop corrections to $\gamma\gamma \to \mathrm{WW} \to 4f$ and $\mathrm{H} \to \mathrm{WW/ZZ} \to 4f$.

Soft divergences in the real corrections arise if a photon with very small energy is emitted from an external particle, while collinear divergences arise due to collinear photon emission from a light external particle. The corresponding soft divergences in the virtual corrections appear when a massless particle is exchanged between two external particles. This situation is illustrated in diagram (a) of Figure 6.2, where a photon is exchanged between two on-shell fermions with small masses m_1 and m_2. If the momentum transfer of the photon tends to zero, the propagator denominators, which can be written as q^2, q^2+2qp_1, and q^2-2qp_2, cause a logarithmic singularity of the corresponding loop integral. Collinear singularities in virtual corrections arise if a massless external particle couples to two massless particles. In this case the singularity originates from a region in the loop integral, where the momenta in the massless propagators are collinear to the momentum of the external particle. In fact, diagram (a) of Figure 6.2 also contains a collinear singularity.

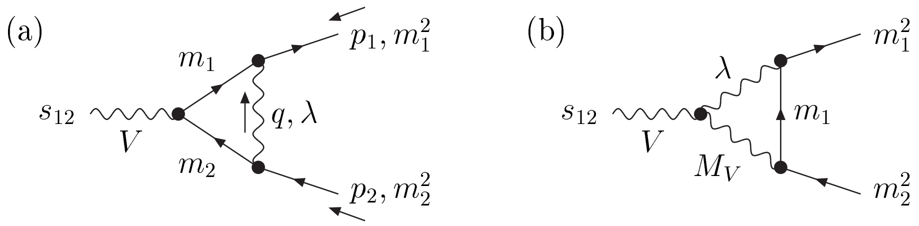

Figure 6.2: Two vertex subdiagrams of the processes $\gamma\gamma \to \mathrm{WW} \to 4f$ and $\mathrm{H} \to \mathrm{WW/ZZ} \to 4f$, where a gauge boson $V = \mathrm{W/Z}$ couples to two fermions, containing soft and collinear ($m_i \ll s_{12}, M_V^2$) singularities.

For $q \sim xp_1$ with a constant x, the photon is collinear to the fermion with mass m_1, and the two corresponding propagator denominators are $x^2p_1^2$ and $(x+1)^2p_1^2$ in the limit of vanishing fermion mass ($p_1^2 = m_1^2 \to 0$). Consequently, the loop integral also develops a logarithmic singularity for this configuration.

In Ref. [104] an explicit formula for the soft and collinear singularities of a general tensor one-loop N-point integral was presented. The application to the diagrams of Figure 6.2 is, of course, particularly simple. Decomposing the tensors and reducing them to scalar integrals, the matrix element for diagram (a) can be written in the conventions of Ref. [6] as

$$\begin{aligned}
\mathcal{M}^{(a)} &\sim -\frac{\alpha}{2\pi}Q_1Q_2\mathcal{M}_B s_{12}(C_0 + C_1 + C_1) \\
&\sim -\frac{\alpha}{2\pi}Q_1Q_2\mathcal{M}_B\Big\{s_{12}C_0 - B_0(m_1^2, m_1, \lambda) - B_0(m_2^2, m_2, \lambda)\Big\} \\
&\sim -\frac{\alpha}{2\pi}Q_1Q_2\mathcal{M}_B\Big\{\ln\left(\frac{\lambda^2}{-\bar{s}_{12}}\right)\ln\left(\frac{m_1m_2}{-\bar{s}_{12}}\right) \\
&\qquad -\frac{1}{4}\ln^2\left(\frac{m_1^2}{-\bar{s}_{12}}\right) - \frac{1}{4}\ln^2\left(\frac{m_2^2}{-\bar{s}_{12}}\right) + \ln\left(\frac{m_1^2m_2^2}{s_{12}^2}\right)\Big\}, \qquad \text{(B.1)}
\end{aligned}$$

where Q_i denote the relative fermion charges, $\mathcal{M}_B$ denotes the corresponding Born matrix element, and $\bar{s}_{12} = s_{12} + i\epsilon$. The sign $\sim$ indicates that non-singular parts were omitted. The singularities are regulated with mass parameters for the photon, λ, and for the fermions, m_1 and m_2 ($|s_{12}| \gg m_{1,2}^2 \gg \lambda \to 0$). The collinear singularity of diagram (b) can be derived as

$$\begin{aligned}
\mathcal{M}^{(b)} &\sim -\frac{\alpha}{2\pi}Q_1(Q_1 - Q_2)\mathcal{M}_B s_{12}C_1 \\
&\sim +\frac{\alpha}{2\pi}Q_1(Q_1 - Q_2)\mathcal{M}_B\Big\{B_0(m_1^2, m_1, \lambda) + M_V^2C_0\Big\} \\
&\sim -\frac{\alpha}{2\pi}Q_1(Q_1 - Q_2)\mathcal{M}_B\ln\left(\frac{m_1^2}{s_{12}}\right)\left\{1 + \frac{M_V^2}{s_{12}}\ln\left(1 - \frac{\bar{s}_{12}}{M_V^2}\right)\right\}. \qquad \text{(B.2)}
\end{aligned}$$

The singularities of the diagram where the photon couples to the fermion with mass m_2 is obtained by appropriate substitutions.

The calculation of radiative corrections to $\gamma\gamma \to \mathrm{WW} \to 4f$ in DPA included the corrections to the decay of on-shell W bosons. In this case diagram (b) also develops a soft singularity, as can be seen from Eq. (B.2), which is not defined for $s_{12} \to M_{\mathrm{W}}^2$. In this limit the singularity of diagram (b) can be written as

$$\mathcal{M}^{(b)}_{s_{12}\to M_{\mathrm{W}}^2} \sim -\frac{\alpha}{2\pi} Q_1(Q_1-Q_2)\mathcal{M}_B\Big\{\ln\left(\frac{m_1^2}{M_{\mathrm{W}}^2}\right) - \ln\left(\frac{m_1 M_{\mathrm{W}}}{\lambda^2}\right)\ln\left(\frac{m_1}{M_{\mathrm{W}}}\right)\Big\}. \tag{B.3}$$

The singularities of the corresponding counterterm, which originates from the field renormalization constants of the W boson and of the fermions, read

$$\mathcal{M}_{\mathrm{count}} \sim -\frac{\alpha}{4\pi}\mathcal{M}_B\Big\{\ln\left(\frac{\lambda^2}{M_{\mathrm{W}}^2}\right) + \sum_{i=1}^{2} Q_i^2\Big[\ln\left(\frac{\lambda^2}{m_i^2}\right) - \frac{1}{2}\ln\left(\frac{m_i^2}{M_{\mathrm{W}}^2}\right)\Big]\Big\}. \tag{B.4}$$

Summing up all contributions for both W-boson decays in $\gamma\gamma \to \mathrm{WW} \to 4f$ and taking also the limit $s_{12} \to M_W^2$ for diagram (a), the singularities can be written as a factor to the squared lowest-order matrix element for $\gamma\gamma \to \mathrm{WW} \to 4f$,

$$\begin{aligned}\delta^{4f}_{\mathrm{W}f\bar{f}'} \sim -\frac{\alpha}{2\pi}\Big\{&2\ln\left(\frac{\lambda^2}{M_{\mathrm{W}}^2}\right) + \ln\left(\frac{\lambda^2}{M_{\mathrm{W}}^2}\right)\sum_{i=1}^{4} Q_i^2\left[1+\ln\left(\frac{m_i^2}{M_{\mathrm{W}}^2}\right)\right]\\ &+\frac{1}{2}\sum_{i=1}^{4} Q_i^2\Big[\ln\left(\frac{m_i^2}{M_{\mathrm{W}}^2}\right) - \ln^2\left(\frac{m_i^2}{M_{\mathrm{W}}^2}\right)\Big]\Big\}.\end{aligned} \tag{B.5}$$

Similarly, the production process of the on-shell W bosons acquires a soft singularity [39],

$$\delta^{4f}_{\gamma\gamma\mathrm{WW}} \sim -\frac{\alpha}{\pi}\ln\left(\frac{\lambda^2}{M_{\mathrm{W}}^2}\right)\Big\{1 + \frac{s-2M_{\mathrm{W}}^2}{s\beta}\ln\left(\frac{1-\beta}{1+\beta}\right)\Big\}, \qquad \beta \sim \sqrt{1-\frac{4M_{\mathrm{W}}^2}{s}} \tag{B.6}$$

with the CM energy $\sqrt{s}$. As explained in Section 4.2.3 the soft singularities for photon emission off on-shell W bosons were artificially introduced in the decomposition of the virtual corrections in DPA. They cancel together with the non-factorizable corrections,

$$\begin{aligned}\delta^{4f}_{\mathrm{nf}} \sim \frac{\alpha}{\pi}\ln\left(\frac{\lambda^2}{M_{\mathrm{W}}^2}\right)\Big\{&2 + \frac{s-2M_{\mathrm{W}}^2}{s\beta}\ln\left(\frac{1-\beta}{1+\beta}\right) - Q_1Q_3\ln\left(\frac{s_{13}}{M_{\mathrm{W}}^2}\right)\\ &+Q_1Q_4\ln\left(\frac{s_{14}}{M_{\mathrm{W}}^2}\right) + Q_2Q_3\ln\left(\frac{s_{23}}{M_{\mathrm{W}}^2}\right) - Q_2Q_4\ln\left(\frac{s_{24}}{M_{\mathrm{W}}^2}\right)\Big\},\end{aligned} \tag{B.7}$$

where s_{ij} was defined in (4.1.3). The first term stems from the diagrams of type (mm) depicted in Figure 4.2, the second term from the diagram of type (mm′), and the last terms from diagrams of type (ff′). The sum $\delta^{4f}_{\mathrm{W}f\bar{f}'} + \delta^{4f}_{\gamma\gamma\mathrm{WW}} + \delta^{4f}_{\mathrm{nf}}$ yields the complete singularities of the virtual corrections to $\gamma\gamma \to \mathrm{WW} \to 4f$,

$$\begin{aligned}\delta^{4f}_{\mathrm{sing,virt}} \sim \frac{\alpha}{2\pi}\sum_{\substack{i,j=1\\ i\neq j}}^{4}(-1)^{i+j}Q_iQ_j\Big\{&\ln\left(\frac{m_i^2}{s_{ij}}\right)\ln\left(\frac{\lambda^2}{s_{ij}}\right) + \ln\left(\frac{\lambda^2}{s_{ij}}\right)\\ &-\frac{1}{2}\ln^2\left(\frac{m_i^2}{s_{ij}}\right) + \frac{1}{2}\ln\left(\frac{m_i^2}{s_{ij}}\right)\Big\},\end{aligned} \tag{B.8}$$

where we used $Q_i = \sum_{\substack{j=1 \\ j\neq i}}^4 Q_j(-1)^{(i+j)}$ and the fact that in DPA after the on-shell projection the invariants obey $s_{12} = s_{34} = M_\mathrm{W}^2$. Even though Eq. (B.8) was derived in DPA, it is valid also for the complete $\gamma\gamma \to 4f$ process without on-shell projection, as can be seen from the construction of the dipole-subtraction terms in Eq. (4.3.11). In order to avoid a mismatch between the singularities of the virtual corrections, which are calculated in DPA, and the singularities of the real corrections, which are calculated without on-shell projection, we proceed as explained in Section 4.1. We subtract the singular part of the virtual corrections, defined via the negative of Eq. (4.3.11) in DPA, and readd the same expression with off-shell kinematics. The error introduced by this procedure is of the order of the accuracy of the DPA. Note that the singularities that are subtracted and readded in this way, should not be defined from the corresponding Eqs. (4.3.3) and (4.3.4) of the slicing method, because these expressions involve the small slicing parameters ΔE and $\Delta\theta$. Hence, these parameters would not drop out in the final result.

The process $\mathrm{H} \to \mathrm{WW/ZZ} \to 4f$ is calculated with off-shell gauge bosons. Hence, the singularities from vertex diagrams are given by Eqs. (B.1) and (B.2). In addition, collinear divergences arise from box diagrams, where a photon couples to an external fermion and an internal gauge boson, and soft and collinear divergences arise from pentagon diagrams, where a photon couples to two fermions originating from different gauge bosons. Since the processes $\gamma\gamma \to \mathrm{WW} \to 4f$ and $\mathrm{H} \to \mathrm{WW/ZZ} \to 4f$ involve the same final state, the sum of all contributions is also given by Eq. (B.8).

C Transformation of the coefficient functions F_j

In this appendix we describe the transformation of the coefficient functions F_j for the factorizable virtual corrections (4.2.9) that transforms all F_j into the helicity amplitudes of the on-shell process $\gamma\gamma \to \mathrm{WW}$.

The 36 SME $\mathcal{M}_j^{\gamma\gamma\mathrm{WW}}$ of Ref. [39], which fix the coefficient functions F_j by Eq. (4.2.6), are defined for 36 different helicity configurations which can be enumerated with a single index l,

$$\mathcal{M}_j^{\gamma\gamma\mathrm{WW}}(\lambda_1,\lambda_2;\lambda_+,\lambda_-) \equiv M_{jl}, \quad l = (\lambda_1,\lambda_2,\lambda_+,\lambda_-), \tag{C.1}$$

where $j, l = 1,\dots,36$. The 36×36 matrix M is explicitly obtained by inserting momenta and polarization vectors into the 36 independent SME $\mathcal{M}_j^{\gamma\gamma\mathrm{WW}}$ of the 83 structures defined in Eqs. (5)–(9) of Ref. [39].

If we transform the F_j according to

$$\hat{F}_l = \sum_{j=1}^{36} F_j M_{jl}, \tag{C.2}$$

the function $\hat{F}_l$ is the helicity amplitude for the on-shell process $\gamma\gamma \to \mathrm{WW}$ corresponding to the helicity configuration $l = (\lambda_1,\lambda_2,\lambda_+,\lambda_-)$. As such, it can be well approximated by the generalized Fourier series described in Section 4.2.2.2. It is important to notice that in Ref. [39] the scattering plane spanned by the beam axes and the produced W bosons was rotated into the (x^1, x^3)-plane, so that the SME $\mathcal{M}_j^{\gamma\gamma\mathrm{WW}}$ depend only on s and $\cos\theta$, or equivalently on s and $\hat{t}$. Since, thus, the matrix M is a function of s and $\hat{t}$, also the new functions $\hat{F}_l$ depend only on s and $\hat{t}$, but not on the azimuthal angle of the scattering plane or other on kinematical variables. According to Eq. (C.2), the SME $\mathcal{M}_j$ transform as

$$\hat{\mathcal{M}}_l = \sum_{j=1}^{36} (M^{-1})_{lj} \mathcal{M}_j, \tag{C.3}$$

where M^{-1} denotes the inverse matrix of M. By construction, the transformation decouples the different helicity channels of $\gamma\gamma \to$ WW. When including the W decays in the SME, as done in Eq. (C.3), this decoupling is somewhat disguised for the W-boson polarizations, but still valid for the photon helicities. This means that the new SME $\hat{\mathcal{M}}_l$ consist of four subsets, each of which contributes only for one of the four different polarization combinations (λ_1, λ_2) of the photons. In practice, we have evaluated and simplified the matrix M and the new SME $\hat{\mathcal{M}}_l$ analytically as much as possible.

Bibliography

[1] A. Bredenstein, S. Dittmaier and M. Roth, Eur. Phys. J. C **36** (2004) 341 [hep-ph/0405169].

[2] A. Bredenstein, S. Dittmaier and M. Roth, Eur. Phys. J. C **44** (2005) 27 [hep-ph/0506005].

[3] A. Bredenstein, A. Denner, S. Dittmaier and M. M. Weber, MPP-2005-24, in preparation.

[4] M. Böhm, A. Denner and H. Joos, "Gauge theories of the strong and electroweak interaction,"
M. E. Peskin and D. V. Schroeder, "An Introduction To Quantum Field Theory,"
S. Weinberg, "The Quantum theory of fields. Vol. 1: Foundations," "The quantum theory of fields. Vol. 2: Modern applications".

[5] G. 't Hooft, Nucl. Phys. B **33** (1971) 173 and Nucl. Phys. B **35** (1971) 167.

[6] A. Denner, Fortsch. Phys. **41** (1993) 307.

[7] A. Denner, S. Dittmaier and G. Weiglein, Nucl. Phys. B **440** (1995) 95 [hep-ph/9410338].

[8] R. Barate *et al.* [LEP Working Group for Higgs boson searches Collaboration], Phys. Lett. B **565** (2003) 61 [hep-ex/0306033].

[9] S. Eidelman *et al.* [Particle Data Group Collaboration], Phys. Lett. B **592** (2004) 1.

[10] M. J. G. Veltman, Acta Phys. Polon. B **8** (1977) 475;
C. E. Vayonakis, Lett. Nuovo Cim. **17** (1976) 383;
B. W. Lee, C. Quigg and H. B. Thacker, Phys. Rev. D **16** (1977) 1519.

[11] I. F. Ginzburg *et al.*, Nucl. Instrum. Meth. **205** (1983) 47 and Nucl. Instrum. Meth. A **219** (1984) 5;
V. I. Telnov, Nucl. Instrum. Meth. A **294** (1990) 72;
R. Brinkmann *et al.*, Nucl. Instrum. Meth. A **406** (1998) 13 [hep-ex/9707017];
I. Watanabe *et al.*, "$\gamma\gamma$ collider as an option of JLC," KEK-REPORT-97-17;
B. Badelek *et al.* "TESLA Technical Design Report, Part VI, Chapter 1: Photon collider at TESLA," hep-ex/0108012;

T. Abe *et al.* [American Linear Collider Working Group Collaboration], in *Proc. of the APS/DPF/DPB Summer Study on the Future of Particle Physics (Snowmass 2001)* ed. R. Davidson and C. Quigg, SLAC-R-570, *Resource book for Snowmass 2001* [hep-ex/0106055, hep-ex/0106056, hep-ex/0106057, hep-ex/0106058].

[12] A. De Roeck, hep-ph/0311138;
M. Krawczyk, hep-ph/0312341;
S. J. Brodsky, hep-ph/0404186.

[13] V. Telnov, Nucl. Instrum. Meth. A **355**, 3 (1995);
P. Chen, T. Ohgaki, A. Spitkovsky, T. Takahashi and K. Yokoya, Nucl. Instrum. Meth. A **397**, 458 (1997) [physics/9704012].

[14] A. F. Zarnecki, Acta Phys. Polon. B **34** (2003) 2741 [hep-ex/0207021].

[15] I. Božović-Jelisavčić, K. Mönig and J. Šekarić, hep-ph/0210308.

[16] M. Moretti, Nucl. Phys. B **484** (1997) 3 [hep-ph/9604303] and hep-ph/9606225;
E. Boos and T. Ohl, Phys. Lett. B **407** (1997) 161 [hep-ph/9705374].

[17] M. Baillargeon, G. Belanger and F. Boudjema, Phys. Lett. B **404** (1997) 124 [hep-ph/9701368].

[18] A. Denner, S. Dittmaier, M. Roth and D. Wackeroth, Nucl. Phys. B **560** (1999) 33 [hep-ph/9904472].

[19] A. Denner, S. Dittmaier, M. Roth and D. Wackeroth, Nucl. Phys. B **587** (2000) 67 [hep-ph/0006307].

[20] A. Denner, S. Dittmaier, M. Roth and D. Wackeroth, Phys. Lett. B **475** (2000) 127 [hep-ph/9912261]; Eur. Phys. J. direct C **2** (2000) 4 [hep-ph/9912447]; hep-ph/0101257 and Comput. Phys. Commun. **153** (2003) 462 [hep-ph/0209330].

[21] S. Jadach *et al.*, Phys. Rev. D **61** (2000) 113010 [hep-ph/9907436]; Phys. Rev. D **65** (2002) 093010 [hep-ph/0007012]; Comput. Phys. Commun. **140** (2001) 432 [hep-ph/0103163] and Comput. Phys. Commun. **140** (2001) 475 [hep-ph/0104049].

[22] W. Beenakker, F. A. Berends and A. P. Chapovsky, Nucl. Phys. B **548** (1999) 3 [hep-ph/9811481].

[23] Y. Kurihara, M. Kuroda and D. Schildknecht, Phys. Lett. B **509** (2001) 87 [hep-ph/0104201].

[24] A. Denner, S. Dittmaier, M. Roth and L. H. Wieders, Phys. Lett. B **612**, 223 (2005) [hep-ph/0502063] and Nucl. Phys. B **724** (2005) 247 [hep-ph/0505042].

[25] E. N. Argyres *et al.*, Phys. Lett. B **358** (1995) 339 [hep-ph/9507216];
W. Beenakker *et al.*, Nucl. Phys. B **500** (1997) 255 [hep-ph/9612260].

[26] S. Dittmaier and M. Roth, Nucl. Phys. B **642** (2002) 307 [hep-ph/0206070].

[27] M. Baillargeon, G. Bélanger and F. Boudjema, Nucl. Phys. B **500** (1997) 224 [hep-ph/9701372].

[28] G. Tupper and M. A. Samuel, Phys. Rev. D **23** (1981) 1933;
S. Y. Choi and F. Schrempp, Phys. Lett. B **272** (1991) 149;
E. Yehudai, Phys. Rev. D **44** (1991) 3434.

[29] G. Bélanger and F. Boudjema, Phys. Lett. B **288** (1992) 210.

[30] I. B. Marfin, V. A. Mossolov and T. V. Shishkina, hep-ph/0304250.

[31] G. Bélanger and G. Couture, Phys. Rev. D **49** (1994) 5720;
S. Y. Choi, K. Hagiwara and M. S. Baek, Phys. Rev. D **54** (1996) 6703 [hep-ph/9605334].

[32] M. Herrero and E. Ruiz-Morales, Phys. Lett. B **296** (1992) 397 [hep-ph/9208220];
P. Poulose and L. M. Sehgal, Phys. Lett. B **552** (2003) 57 [hep-ph/0211179].

[33] A. Denner, lecture notes on "Unstable particles in gauge theories", Second Graduate School in Physics at Colliders, Torino, July 2003.

[34] M. J. G. Veltman, Physica **29** (1963) 186.

[35] A. Denner and S. Dittmaier, Phys. Rev. D **54** (1996) 4499 [hep-ph/9603341].

[36] A. Sirlin, Phys. Rev. Lett. **67** (1991) 2127;
G. Stuart, Phys. Lett. B **262** (1991) 113;
A. Sirlin, Phys. Lett. B **267** (1991) 240;
T. Bhattacharya and S. Willenbrock, Phys. Rev. D **47** (1993) 4022.

[37] A. Aeppli, G. J. van Oldenborgh and D. Wyler, Nucl. Phys. B **428** (1994) 126 [hep-ph/9312212].

[38] V. S. Fadin, V. A. Khoze and A. D. Martin, Phys. Lett. B **320** (1994) 141 [hep-ph/9309234].

[39] A. Denner, S. Dittmaier and R. Schuster, Nucl. Phys. B **452** (1995) 80 [hep-ph/9503442].

[40] K. Fujikawa, Phys. Rev. D **7** (1973) 393;
M. Bace and N. D. Hari Dass, Annals Phys. **94** (1975) 349;
B. W. Lee and R. E. Shrock, Phys. Rev. D **16** (1977) 1444;
M. B. Gavela, G. Girardi, C. Malleville and P. Sorba, Nucl. Phys. B **193** (1981) 257;
N. G. Deshpande and M. Nazerimonfared, Nucl. Phys. B **213** (1983) 390;
F. Boudjema, Phys. Lett. B **187** (1987) 362.

[41] D. Bardin et al, in *Physics at LEP2*, eds. G. Altarelli, T. Sjöstrand, F. Zwirner, CERN 96-01, Vol. 2, p. 3, hep-ph/9709270.

[42] S. Dittmaier, Phys. Rev. D **59** (1999) 016007 [hep-ph/9805445].

[43] T. Stelzer and W. F. Long, Comput. Phys. Commun. **81** (1994) 357 [hep-ph/9401258]; H. Murayama, I. Watanabe and K. Hagiwara, "HELAS: HELicity amplitude subroutines for Feynman diagram evaluations," KEK-91-11.

[44] M. W. Grünewald *et al.*, in *Reports of the Working Groups on Precision Calculations for LEP2 Physics*, eds. S. Jadach, G. Passarino and R. Pittau (CERN 2000-009, Geneva, 2000), p. 1 [hep-ph/0005309].

[45] W. Beenakker *et al.*, in *Physics at LEP2*, eds. G. Altarelli, T. Sjöstrand and F. Zwirner (CERN 96-01, Geneva, 1996), Vol. 1, p. 79 [hep-ph/9602351].

[46] K. J. F. Gaemers and G. J. Gounaris, Z. Phys. C **1** (1979) 259;
K. Hagiwara, R. D. Peccei, D. Zeppenfeld and K. Hikasa, Nucl. Phys. B **282** (1987) 253;
M. S. Bilenky, J. L. Kneur, F. M. Renard and D. Schildknecht, Nucl. Phys. B **409** (1993) 22.

[47] G. Gounaris *et al.*, in *Physics at LEP2*, eds. G. Altarelli, T. Sjöstrand, F. Zwirner, CERN 96-01, Vol. 1, p. 525, hep-ph/9601233.

[48] G. J. Gounaris, J. Layssac and F. M. Renard, Phys. Rev. D **61** (2000) 073013 [hep-ph/9910395] and Phys. Rev. D **62** (2000) 073012 [hep-ph/0005269].

[49] G. Bélanger and F. Boudjema, Phys. Lett. B **288** (1992) 201;
O. J. Eboli, M. C. Gonzalez-Garcia and S. F. Novaes, Nucl. Phys. B **411** (1994) 381 [hep-ph/9306306];
G. Abu Leil and W. J. Stirling, J. Phys. G**21** (1995) 517 [hep-ph/9406317];
W. J. Stirling and A. Werthenbach, Eur. Phys. J. C **12** (2000) 441 [hep-ph/9905341] and Eur. Phys. J. C **14** (2000) 103 [hep-ph/9903315].

[50] A. Denner, S. Dittmaier, M. Roth and D. Wackeroth, Eur. Phys. J. C **20** (2001) 201 [hep-ph/0104057].

[51] G. Bélanger, F. Boudjema, Y. Kurihara, D. Perret-Gallix and A. Semenov, Eur. Phys. J. C **13** (2000) 283 [hep-ph/9908254].

[52] M. A. Shifman, A. I. Vainshtein, M. B. Voloshin and V. I. Zakharov, Sov. J. Nucl. Phys. **30** (1979) 711 [Yad. Fiz. **30** (1979) 1368].

[53] M. Roth, PhD thesis, ETH Zürich No. 13363 (1999), hep-ph/0008033.

[54] F. A. Berends, R. Pittau and R. Kleiss, Nucl. Phys. B **424** (1994) 308 [hep-ph/9404313] and Comput. Phys. Commun. **85** (1995) 437 [hep-ph/9409326];
F. A. Berends, P. H. Daverveldt and R. Kleiss, Nucl. Phys. B **253** (1985) 441;
J. Hilgart, R. Kleiss and F. Le Diberder, Comput. Phys. Commun. **75** (1993) 191.

[55] K. Hagiwara *et al.* [Particle Data Group Collaboration], Phys. Rev. D **66** (2002) 010001.

[56] A. Djouadi, J. Kalinowski and M. Spira, Comput. Phys. Commun. **108** (1998) 56 [hep-ph/9704448].

[57] D. Y. Bardin, S. Riemann and T. Riemann, Z. Phys. C **32** (1986) 121;
F. Jegerlehner, Z. Phys. C **32** (1986) 425 [Erratum-ibid. C **38** (1988) 519];
A. Denner and T. Sack, Z. Phys. C **46** (1990) 653.

[58] W. Kilian, "WHIZARD 1.0: A generic Monte-Carlo integration and event generation package for multi-particle processes. Manual," LC-TOOL-2001-039.

[59] G. Jikia, Nucl. Phys. B **494** (1997) 19 [hep-ph/9612380].

[60] K. Melnikov and O. I. Yakovlev, Nucl. Phys. B **471** (1996) 90 [hep-ph/9501358];
W. Beenakker, A. P. Chapovsky and F. A. Berends, Phys. Lett. B **411** (1997) 203 [hep-ph/9706339] and Nucl. Phys. B **508** (1997) 17 [hep-ph/9707326].

[61] A. Denner, S. Dittmaier and M. Roth, Nucl. Phys. B **519** (1998) 39 [hep-ph/9710521].

[62] A. Denner, S. Dittmaier and R. Schuster, Phys. Rev. D **51** (1995) 4738 [hep-ph/9411268].

[63] G. Passarino and M. J. G. Veltman, Nucl. Phys. B **160** (1979) 151.

[64] A. Djouadi, M. Spira, J. J. van der Bij and P. M. Zerwas, Phys. Lett. B **257** (1991) 187.
A. Djouadi, M. Spira and P. M. Zerwas, Phys. Lett. B **311** (1993) 255 [hep-ph/9305335].
K. Melnikov and O. I. Yakovlev, Phys. Lett. B **312** (1993) 179 [hep-ph/9302281].
M. Inoue, R. Najima, T. Oka and J. Saito, Mod. Phys. Lett. A **9** (1994) 1189.
J. Fleischer, O. V. Tarasov and V. O. Tarasov, Phys. Lett. B **584** (2004) 294 [hep-ph/0401090];
U. Aglietti, R. Bonciani, G. Degrassi and A. Vicini, Phys. Lett. B **595** (2004) 432 [hep-ph/0404071].
G. Degrassi and F. Maltoni, hep-ph/0504137.

[65] A. Sirlin, Phys. Rev. D **22** (1980) 971;
W. J. Marciano and A. Sirlin, Phys. Rev. D **22** (1980) 2695 [Erratum-ibid. D **31** (1985) 213] and Nucl. Phys. B **189** (1981) 442.

[66] D. Y. Bardin, W. Beenakker and A. Denner, Phys. Lett. B **317** (1993) 213.

[67] S. Dittmaier, Nucl. Phys. B **565** (2000) 69 [hep-ph/9904440].

[68] S. Catani and M. H. Seymour, Phys. Lett. B **378** (1996) 287 [hep-ph/9602277] and Nucl. Phys. B **485** (1997) 291 [Erratum-ibid. B **510** (1997) 291] [hep-ph/9605323].

[69] T. Kinoshita, J. Math. Phys. **3** (1962) 650.
T. D. Lee and M. Nauenberg, Phys. Rev. **133** (1964) B1549.

[70] F. Jegerlehner, hep-ph/0105283.

[71] E. W. N. Glover, J. Ohnemus and S. S. D. Willenbrock, Phys. Rev. D **37** (1988) 3193;
V. D. Barger, G. Bhattacharya, T. Han and B. A. Kniehl, Phys. Rev. D **43** (1991) 779;
V. D. Barger, R. J. N. Phillips and D. Zeppenfeld, Phys. Lett. B **346** (1995) 106 [hep-ph/9412276];
M. Dittmar and H. K. Dreiner, Phys. Rev. D **55** (1997) 167 [hep-ph/9608317];
D. L. Rainwater and D. Zeppenfeld, Phys. Rev. D **60** (1999) 113004 [Erratum-ibid. D **61** (2000) 099901] [hep-ph/9906218];
N. Kauer, T. Plehn, D. L. Rainwater and D. Zeppenfeld, Phys. Lett. B **503** (2001) 113 [hep-ph/0012351].

[72] S. Asai *et al.*, Eur. Phys. J. C **32S2** (2004) 19 [hep-ph/0402254];
S. Abdullin *et al.*, Eur. Phys. J. C **39S2** (2005) 41.

[73] L. Zivkovic, Czech. J. Phys. **54** (2004) A73.

[74] ATLAS Collaboration, Technical Design Report, CERN–LHCC 99–14 (May 1999);
CMS Collaboration, Technical Proposal, CERN–LHCC 94–38 (Dec. 1994).

[75] K. A. Assamagan *et al.* [Higgs Working Group Collaboration], proceedings of the 3rd Les Houches Workshop: "Physics at TeV Colliders", Les Houches, 2003, hep-ph/0406152.

[76] Standard Model working group report of the workshop "Physics at TeV Colliders", Les Houches, May 2005.

[77] J. A. Aguilar-Saavedra *et al.*, TESLA Technical Design Report Part III: Physics at an e^+e^- Linear Collider, hep-ph/0106315.

[78] T. Abe *et al.* [American Linear Collider Working Group Collaboration], in *Proc. of the APS/DPF/DPB Summer Study on the Future of Particle Physics (Snowmass 2001)* ed. R. Davidson and C. Quigg, SLAC-R-570, *Resource book for Snowmass 2001*, [hep-ex/0106055, hep-ex/0106056, hep-ex/0106057, hep-ex/0106058].

[79] K. Abe *et al.* [ACFA Linear Collider Working Group Collaboration], ACFA Linear Collider Working Group report, [hep-ph/0109166].

[80] N. Meyer and K. Desch, Eur. Phys. J. C **35** (2004) 171.

[81] C. A. Nelson, Phys. Rev. D **37** (1988) 1220;
D. Chang, W. Y. Keung and I. Phillips, Phys. Rev. D **48** (1993) 3225 [hep-ph/9303226];
A. Skjold and P. Osland, Phys. Lett. B **311** (1993) 261 [hep-ph/9303294];
V.D. Barger, K.M. Cheung, A. Djouadi, B.A. Kniehl and P.M. Zerwas, Phys. Rev. D **49** (1994) 79 [hep-ph/9306270];
C. P. Buszello, I. Fleck, P. Marquard and J. J. van der Bij, Eur. Phys. J. C **32** (2004) 209 [hep-ph/0212396];
T. Arens and L. M. Sehgal, Z. Phys. C **66** (1995) 89 [hep-ph/9409396].

[82] S. Y. Choi, D. J. Miller, M. M. Mühlleitner and P. M. Zerwas, Phys. Lett. B **553** (2003) 61 [hep-ph/0210077].

[83] G. Pocsik and T. Torma, Z. Phys. C **6** (1980) 1;
T. G. Rizzo, Phys. Rev. D **22** (1980) 722;
W. Y. Keung and W. J. Marciano, Phys. Rev. D **30** (1984) 248.

[84] A. Grau, G. Panchieri and R. J. N. Phillips, Phys. Lett. B **251** (1990) 293;
E. Gross, G. Wolf and B. A. Kniehl, Z. Phys. C **63** (1994) 417 [Erratum-ibid. C **66** (1995) 321] [hep-ph/9404220].

[85] A. Djouadi, hep-ph/0503172.

[86] J. Fleischer and F. Jegerlehner, Phys. Rev. D **23** (1981) 2001;
B. A. Kniehl, Nucl. Phys. B **352** (1991) 1;
D.Y. Bardin, P.K. Khristova and B.M. Vilensky, Sov. J. Nucl. Phys. **54** (1991) 833 [Yad. Fiz. **54** (1991) 1366].

[87] B. A. Kniehl, Nucl. Phys. B **357** (1991) 439.

[88] B. A. Kniehl and M. Spira, Z. Phys. C **69** (1995) 77 [hep-ph/9505225];
B. A. Kniehl and M. Steinhauser, Phys. Lett. B **365** (1996) 297 [hep-ph/9507382] and Nucl. Phys. B **454** (1995) 485 [hep-ph/9508241];
A. Djouadi, P. Gambino and B. A. Kniehl, Nucl. Phys. B **523** (1998) 17 [hep-ph/9712330].

[89] A. Ghinculov, Nucl. Phys. B **455** (1995) 21 [hep-ph/9507240].

[90] A. Frink, B. A. Kniehl, D. Kreimer and K. Riesselmann, Phys. Rev. D **54** (1996) 4548 [hep-ph/9606310].

[91] G. Belanger, F. Boudjema, J. Fujimoto, T. Ishikawa, T. Kaneko, K. Kato and Y. Shimizu, hep-ph/0211268 and hep-ph/0212261.

[92] A. Denner, S. Dittmaier, M. Roth and M. M. Weber, Phys. Lett. B **560** (2003) 196 [hep-ph/0301189] and Nucl. Phys. B **660** (2003) 289 [hep-ph/0302198].

[93] A. Denner and S. Dittmaier, Nucl. Phys. B **658** (2003) 175 [hep-ph/0212259].

[94] A. Denner and S. Dittmaier, Nucl. Phys. B **734** (2006) 62 [hep-ph/0509141].

[95] W. F. L. Hollik, Fortsch. Phys. **38** (1990) 165.

[96] J. Küblbeck, M. Böhm and A. Denner, Comput. Phys. Commun. **60** (1990) 165;
H. Eck and J. Küblbeck, *Guide to FeynArts 1.0*, University of Würzburg, 1992.

[97] G. 't Hooft and M. Veltman, Nucl. Phys. B **153** (1979) 365.

[98] W. Beenakker and A. Denner, Nucl. Phys. B **338** (1990) 349.

[99] A. Denner, U. Nierste and R. Scharf, Nucl. Phys. B **367** (1991) 637.

[100] G. Passarino and M. Veltman, Nucl. Phys. B **160** (1979) 151.

[101] E. A. Kuraev and V. S. Fadin, Sov. J. Nucl. Phys. **41** (1985) 466 [Yad. Fiz. **41** (1985) 733];
G. Altarelli and G. Martinelli, in *Physics at LEP*, eds. J. Ellis and R. Peccei, (CERN 86-02, Geneva, 1986), Vol. 1, p. 47;
O. Nicrosini and L. Trentadue, Phys. Lett. B **196** (1987) 551 and Z. Phys. C **39** (1988) 479;
F. A. Berends, W. L. van Neerven and G. J. H. Burgers, Nucl. Phys. B **297** (1988) 429 [Erratum-ibid. B **304** (1988) 921];
A. B. Arbuzov, Phys. Lett. B **470** (1999) 252 [hep-ph/9908361].

[102] P. Azzi *et al.* [CDF Collaboration], arXiv:hep-ex/0404010.

[103] R. Kleiss and R. Pittau, Comput. Phys. Commun. **83** (1994) 141 [hep-ph/9405257].

[104] S. Dittmaier, Nucl. Phys. B **675** (2003) 447 [hep-ph/0308246].

Acknowledgements

I am indebted to all the people who supported me in the last years. First of all, there is Stefan Dittmaier, who suggested this investigation. Not only did I learn a lot about field theory from him, but I always got the decisive advice or hint from him when I got stuck. Moreover, I owe him the experience of the peculiar world of Bavaria.

Markus Roth introduced me to the mysteries of Monte Carlo integration. Working with him was a great pleasure. For a very fruitful collaboration I would also like to thank Ansgar Denner and Marcus Weber.

I am grateful to Gerhard Buchalla for his interest in my work and to Wolfgang Hollik for giving me the opportunity to work in a very stimulating environment in his group at the Max-Planck-Institut für Physik.

Many thanks go to my friends and colleagues at the MPI who made life so enjoyable during the last years.

Last but not least, I would like to thank my parents for their never-ending support and Naoko Kobayashi on whom I could rely at any time and who gave me many insights beyond physics.